SENSORDEVICES 2014

The Fifth International Conference on Sensor Device Technologies and Applications

ISBN: 978-1-61208-375-9

November 16 - 20, 2014

Lisbon, Portugal

SENSORDEVICES 2014 Editors

Sergey Yurish, Excelera, S. L., Spain

Vítor Carvalho, Minho University, Portugal

SENSORDEVICES 2014

Foreword

The Fifth International Conference on Sensor Device Technologies and Applications (SENSORDEVICES 2014), held between November 16-20, 2014 in Lisbon, Portugal, continued a series of events focusing on sensor devices themselves, the technology-capturing style of sensors, special technologies, signal control and interfaces, and particularly sensors-oriented applications. The evolution of the nano-and microtechnologies, nanomaterials, and the new business services make the sensor device industry and research on sensor-themselves very challenging.

We take here the opportunity to warmly thank all the members of the SENSORDEVICES 2014 Technical Program Committee, as well as the numerous reviewers. The creation of such a high quality conference program would not have been possible without their involvement. We also kindly thank all the authors who dedicated much of their time and efforts to contribute to SENSORDEVICES 2014. We truly believe that, thanks to all these efforts, the final conference program consisted of top quality contributions.

Also, this event could not have been a reality without the support of many individuals, organizations, and sponsors. We are grateful to the members of the SENSORDEVICES 2014 organizing committee for their help in handling the logistics and for their work to make this professional meeting a success. We hope that SENSORDEVICES 2014 was a successful international forum for the exchange of ideas and results between academia and industry and for the promotion of progress in the area of sensor device technologies and applications.

We are convinced that the participants found the event useful and communications very open. We hope Lisbon provided a pleasant environment during the conference and everyone saved some time for exploring this beautiful city.

SENSORDEVICES 2014 Chairs:

SENSORDEVICES Advisory Chairs
Sergey Yurish, IFSA - Barcelona, Spain
Petre Dini, Concordia University, Canada / China Space Agency Center, China
Elena Gaura, Coventry University, UK
Vittorio Ferrari, Università di Brescia, Italy

SENSORDEVICES 2014 Research/Industry Chairs
Raluca - Ioana Stefan-van Staden, National Institute of Research for Electrochemistry and Condensed Matter, Bucharest, Romania
Alberto Yúfera, Centro Nacional de Microelectronica (CNM-CSIC) - Sevilla, Spain

SENSORDEVICES 2014

Committee

SENSORDEVICES Advisory Chairs

Sergey Y. Yurish, International Frequency Sensor Association (IFSA), Spain
Petre Dini, Concordia University, Canada / China Space Agency Center, China
Elena Gaura, Coventry University, UK
Vittorio Ferrari, Università di Brescia, Italy

SENSORDEVICES 2014 Research/Industry Chairs

Raluca - Ioana Stefan-van Staden, National Institute of Research for Electrochemistry and Condensed
Matter, Bucharest, Romania
Alberto Yúfera, Centro Nacional de Microelectronica (CNM-CSIC) - Sevilla, Spain

SENSORDEVICES Special Area Chairs

Ultrasonic and piezoelectric sensors
Thomas Herzog, Fraunhofer Institute for Non-Destructive Testing IZFP - Dresden, Germany
Henning Heuer, Fraunhofer Institute for Non-Destructive Testing IZFP - Dresden, Germany

Optical sensors
Vítor Carvalho, Minho University, Portugal
Irinela Chilibon, National Institute of Research and Development for Optoelectronics - Bucharest,
Romania

Gas sensors
Dongfang Yang, National Research Council Canada - London, Canada

Nanosensors
Marco Tartagni, University of Bologna - Cesena, Italy

Testing and validation
Ksenia V. Sapozshnikova D.I. Mendeleyev Institute for Metrology - St. Petersburg, Russia

Vibration sensors
Subodh Kumar Singhal, National Physical Laboratory, New Delhi, India

SENSORDEVICES 2014 Technical Program Committee

Farid Amirouche, University of Illinois at Chicago, USA
Ammar Aryan, Université de Caen Basse-Normandie, France
Selcuk Atalay, Inonu University - Malatya, Turkey
Francisco Javier Arcega Solsona, University of Zaragoza, Spain
Debjyoti Banerjee, Texas A&M University, U.S.A.

Matthias Bartholmai, BAM Federal Institute for Materials Research and Testing, Germany
Sukumar Basu, Jadavpur University - Kolkata, India
Juarez Bento da Silva, Universidade Federal de Santa Catarina, Brazil
Daniel Berckmans, Katholieke Universiteit Leuven, Belgium
Partha Bhattacharyya, Bengal Engineering and Science University, West Bengal, India
Virginie Blondeau-Patissier, Université de Franche-Comté, France
Michal Borecki, Warsaw University of Technology, Poland
Jaime Calvo-Gallego, University of Salamanca - Zamora, Spain
Cristina Carmona-Duarte, University of Las Palmas de Gran Canaria, Spain
Vítor Carvalho, Minho University, Portugal
Gustavo Cerda-Villafaña, University of Guanajuato, Mexico
Sudhir Chandra, Indian Institute of Technology Delhi - New Delhi, India
Irinela Chilibon, National Institute of R&D for Optoelectronics - Bucharest-Magurele, Romania
Jeong-Woo Choi, Sogang University - Seoul, Korea
Caterina Ciminelli, Politecnico of Bari, Italy
Alberto Corigliano, Politecnico di Milano, Italy
Rodrigo P.B. Costa-Felix, INMETRO, Brazil
Anna Cysewska-Sobusiak, Poznan University of Technology, Poland
Boris Zaitsev Davydovich, Russian Academy of Sciences - Saratov Branch, Russia
Francesco De Leonardis, Politecnico di Bari, Italy
Matthieu Denoual, GREYC-ENSICAEN, France
Dermot Diamond, Dublin City University, Ireland
Alexandar Djordjevich, City University of Hong Kong, Hong Kong
Alessandro Fantoni, UNINOVA-CTS, Portugal
Miguel Fernandes, UNINOVA - Caparica, Portugal
Vittorio Ferrari, Università di Brescia, Italy
Masato Futagawa, Toyohashi University of Technology, Japan
Noureddine Gabouze, CRTSE (exUDTS), Algeria
Juan Carlos García García, University of Alcalá, Spain
Arfan Ghani, University of Bolton, UK
Friederike Gruhl, Karlsruhe Institute of Technology (KIT), Germany
Vinod Kumar Gupta, Indian Institute of Technology Roorkee, India
Jong-in Hahm, Georgetown University - Washington DC, USA
Jan Havlík, Czech Technical University in Prague, Czech Republic
Thomas Herzog, Fraunhofer Institute for Non-Destructive Testing IZFP - Dresden, Germany
Henning Heuer, Fraunhofer Institute for Non-Destructive Testing IZFP - Dresden, Germany
Eiji Higurashi, University of Tokyo, Japan
Gotan Hiralal Jain, KTHM College, India
Sandeep K. Jha, Indian Institute of Technology Delhi, India
Vladan Koncar, ENSAIT Research, France
Vladimir Laukhin, Institució Catalana de Recerca i Estudis Avançats (ICREA / Institut de Ciencia de Materials de Barcelona (ICMAB-CSIC) - Barcelona, Spain
Elena Laukhina, Networking Research Center on Bioenginering, Biomaterials and Nanomedicine (CIBER-BBN) - Bellaterra, Spain
Yann-Aël Le Borgne, Université Libre de Bruxelles, Belgium
Kevin Lee, Murdoch University, Australia
Aihua Liu, Qingdao Institute of Bioenergy & Bioprocess Technology, Chinese Academy of Sciences, China
Kenneth J. Loh, University of California - Davis, USA

Dan Zhang, University of Ontario Institute of Technology, Canada
Weiping Zhang, Shanghai Jiao Tong University, P. R. China
Ya-Pu Zhao, Chinese Academy of Sciences - Beijing, China
Daniele Zonta, University of Trento, Italy

Copyright Information

For your reference, this is the text governing the copyright release for material published by IARIA.

The copyright release is a transfer of publication rights, which allows IARIA and its partners to drive the dissemination of the published material. This allows IARIA to give articles increased visibility via distribution, inclusion in libraries, and arrangements for submission to indexes.

I, the undersigned, declare that the article is original, and that I represent the authors of this article in the copyright release matters. If this work has been done as work-for-hire, I have obtained all necessary clearances to execute a copyright release. I hereby irrevocably transfer exclusive copyright for this material to IARIA. I give IARIA permission or reproduce the work in any media format such as, but not limited to, print, digital, or electronic. I give IARIA permission to distribute the materials without restriction to any institutions or individuals. I give IARIA permission to submit the work for inclusion in article repositories as IARIA sees fit.

I, the undersigned, declare that to the best of my knowledge, the article is does not contain libelous or otherwise unlawful contents or invading the right of privacy or infringing on a proprietary right.

Following the copyright release, any circulated version of the article must bear the copyright notice and any header and footer information that IARIA applies to the published article.

IARIA grants royalty-free permission to the authors to disseminate the work, under the above provisions, for any academic, commercial, or industrial use. IARIA grants royalty-free permission to any individuals or institutions to make the article available electronically, online, or in print.

IARIA acknowledges that rights to any algorithm, process, procedure, apparatus, or articles of manufacture remain with the authors and their employers.

I, the undersigned, understand that IARIA will not be liable, in contract, tort (including, without limitation, negligence), pre-contract or other representations (other than fraudulent misrepresentations) or otherwise in connection with the publication of my work.

Exception to the above is made for work-for-hire performed while employed by the government. In that case, copyright to the material remains with the said government. The rightful owners (authors and government entity) grant unlimited and unrestricted permission to IARIA, IARIA's contractors, and IARIA's partners to further distribute the work.

Table of Contents

Innovative Procedures to Analyze Data of Gas Sensor Systems and Gas Sensor Nets: a Review

Rolf Seifert, Hubert Keller, Jörg Matthes

Karlsruhe Institute of Technology

D-76344 Eggenstein-Leopoldshafen, Germany

e-mail: rolf.seifert@kit.edu, Hubert.keller@kit.edu, joerg.matthes@kit.edu

Abstract—**Economic online and in-situ field analyses applications like discriminated alarming of smoldering fire or toxic gas leakages, monitoring of volatile components in chemical and biochemical processes, quality monitoring in food processing etc., wait for reliable and economic analytical solutions by sensor systems. This paper presents various innovative mathematical procedures to analyze data from gas sensor systems and gas sensor nets: ProSens - an efficient mathematical procedure for calibration and evaluation of tin oxide gas sensor data, ProCal - a program for batch-wise calibration of multi gas sensors and ProSource - a procedure for source localization. Applications to real data demonstrate the performance of the procedures.**

Keywords: calibration and evaluation procedure; batchwise calibration; source location

I. INTRODUCTION

There is a growing need of economic online and in-situ field analysis applications like online monitoring of volatile components in chemical and biochemical processes, quality monitoring in food processing, discriminated monitoring of toxic gas leakages, etc. In the last application, it is often necessary to find and locate the source of the leakage. In this context, isothermally operated metal oxide gas sensors (MOGs) with tin oxide as base material are manifold introduced due to their high sensitivity, long-term stability and low price. Their sensitivity to specific gas components, however, cannot be cultivated with high discrimination to others. Therefore, other approaches are necessary like a multi gas sensor array of MOGs [1][2] or thermo-cyclic operation of the MOG.

For evaluation of the sensor data, powerful mathematical evaluation procedures for substance identification and concentration determination, even in the case of variable environmental conditions like varying humidity, are necessary. The calibration of sensor elements is very time consuming and expensive. Even sensor elements which are fabricated batch-wise have to be individually calibrated for good analysis performance. Therefore, economic mathematical calibration procedures are useful to reduce the costs and the scope of calibration measurements. Last but not least, mathematical procedures are needed to locate the source of a leakage.

At the Karlsruhe Institute of Technology (KIT) mathematical procedures are developed to meet the above mentioned requirements: ProSens – a mathematical procedure for calibration and evaluation, ProCal – a mathematical procedure for batch-wise calibration of sensor elements and ProSource – a mathematical procedure to locate the source of a leakage. After some remarks to thermo-cyclic operation of the MOG, these procedures will be briefly described in this paper and their performance will be demonstrated in applications with real data.

In Section 2, the principles of thermo-cyclic operation are briefly discussed. A short outline of the program ProSens with two applications to real data is given in Section 3. In Section 4, the program ProCal is briefly introduced and its performance is demonstrated in an example. In Section 5, the program ProSource for source localization is briefly described and in Section 6, the results of the paper are summarized.

II. THERMO-CYCLIC OPERATION

Thermo-cyclic operation means, that the working temperature of the sensor element is periodically increased and decreased over the time in a triangular shape. Simultaneous sampling of the conductance values over the time leads to so-called Conductance over Time Profiles (CTP) [3][4][5]. These profiles give a fingerprint of the surface processes with the gas and represent the gas mixture under consideration. The gas specific features of the CTPs can be used for component identification and concentration determination.
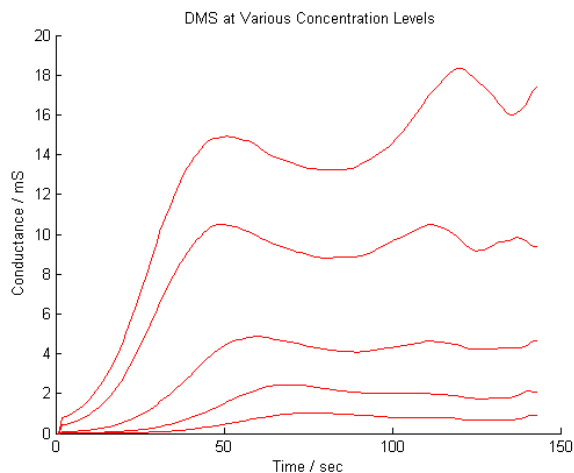
Figure 1. CTPs of dimethyl sulphate (DMS) at various concentration levels
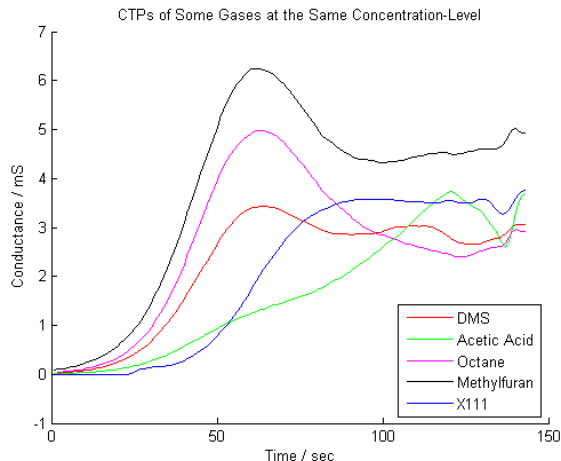
Figure 2. CTPs of some gases at a certain concentration level

Figure 1 shows the CTPs of dimethyl sulphate (DMS) at various concentration levels with the characteristic shape. The working temperature of the sensor element is in the range of 100 to 400 degree Celsius. The conductance values are recorded only over the growing part of the triangular shape.

Figure 2 shows the CTPs of some gases at a certain concentration level. It can be seen that the shapes of the various gases are quite different. Therefore, they can be used for substance identification using innovative calibration and evaluation procedures.

III. PROSENS – A MATHEMATICAL PROCEDURE FOR CALIBRATION AND EVALUATION

As mentioned above, MOGs can be used for ambitious analysis applications, if they are thermo-cyclically operated. A mathematical procedure for data evaluation has to identify an unknown gas sample (classification) to avoid misleading results like false alarms. Furthermore, it has to determine the concentration of the components of the gas sample. Varying environmental conditions like varying humidity or varying environmental temperature often influence the measurement results. These variations must be incorporated in the evaluation model of the mathematical procedure.

The program ProSens developed at KIT was designed to meet the above mentioned requirements. ProSens consists of two parts: a calibration part and an evaluation part.

In the calibration part, ProSens provides the mathematical calibration model which is the basis for routine data evaluation. The determination of the mathematical calibration model is based on calibration measurements performed by MOG with thermo-cyclic operation. These mathematical calibration models are parametric models. Their parameters are transferred to the evaluation part for the analysis of unknown gas samples.

In the evaluation part of ProSens, an unknown gas sample is analyzed. That means that a substance identification and a concentration determination is performed.

For gas component or compound identification, ProSens calculates the so-called theoretical CTP for the calibrated gas under consideration and compares this CTP with the measured CTP.

If the measured CTP and the theoretical CTP are close together, i.e., a difference value calculated from the sum of quadratic differences of every sample point of the measured CTP and the theoretical CTP is smaller than a predetermined decision value, ProSens identifies the unknown gas sample with the related calibrated gas.

Otherwise ProSens recognizes that the gas sample is not the calibrated gas.

In the case of a successful identification, ProSens calculates the concentration of the gas sample.

In order to demonstrate the performance of the mathematical evaluation procedure ProSens, the CTP-data of two evaluation experiments of chemical analysis were used, first ammonia under various water vapor partial pressures and second binary toluene/ethanol-mixtures dissolved in water. The experimental details of data acquisition are described in [5][6].

In the first investigation ammonia was analyzed. To perform the mathematical calibration model the CTP was measured at different ammonia concentrations (100 ppm, 200 ppm, 500 ppm, 1000 ppm) and at different water vapour partial pressures (529, 1322, 2334 Pa) as well. These 12 calibration points are visualized in Figure 3. This low number of calibration points is important, because it keeps the calibration costs low. The graphs of measured and theoretical CTP are compared when testing an ammonia sample (750 ppm) in Figure 4(a) and in case of a non-ammonia sample (carbon monoxide with 1000 ppm) in Figure 4(b). It is evident that ProSens is able to identify the ammonia sample. Table I demonstrates that ProSens can determine the concentration of ammonia samples quite well, even in the case of varying water vapour partial pressures.
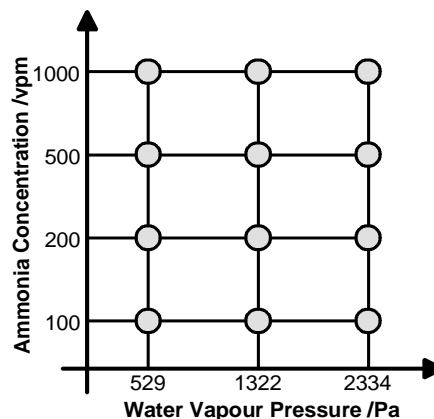
Figure 3. Calibration field of only 12 calibration points
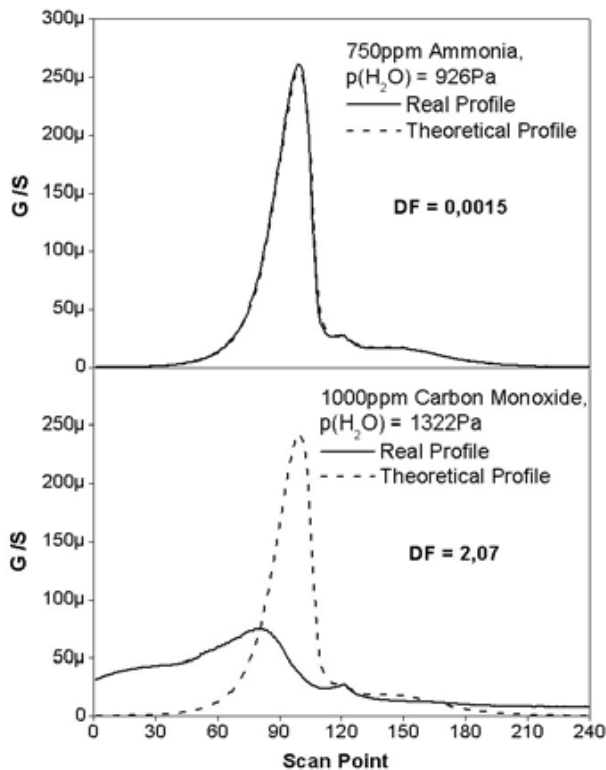
Figure 4. Comparison of measured/theoretical CTP (a) ammonia sample, (b) non-ammonia sample

TABLE I. AMMONIA ANALYSIS RESULTS OF TEST EXPERIMENTS AT DIFFERENT WATER PARTIAL PRESSURES

Dosed concentration	p(H2O)/Pa	Determined concentration
150 ppm	1058	159 ppm
150 ppm	1587	171 ppm
350 ppm	1058	329 ppm
350 ppm	1587	373 ppm

In a second example, the CTP-data of binary toluene/ethanol mixtures dissolved in water were used for chemical analysis. Also in this case only 12 calibration points were used in the calibration procedure (Figure 5). Three further binary toluene/ethanol-mixtures (analysis test points, Figure 5) and a non-toluene/ethanol-mixture were analyzed for demonstration of the performance of ProSens.

The analysis proves that the evaluation procedure is able to identify toluene/ethanol binary mixtures and to detect non-toluene/ethanol-mixtures as well. This is due to the fact that in the second case the difference between the theoretical CTP and the measured CTP is significantly big (Figure 6) in comparison with the negligible difference in the first case (Figure 7).
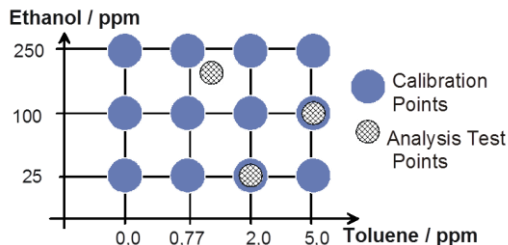
Figure 5. Calibration field and analysis test points of toluene/ethanol mixtures dissolved in water at constant temperature. Sensor signals were sampled using a gas carrier sample.
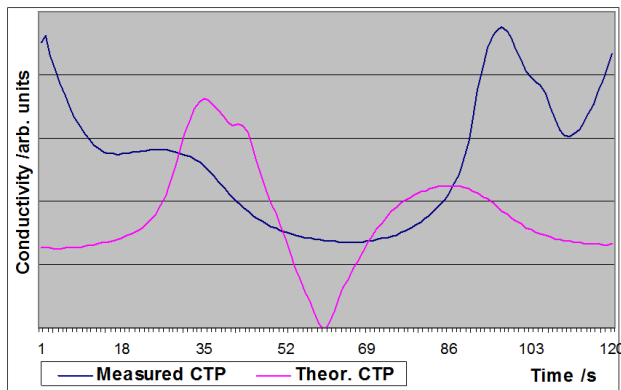
Figure 6. Comparison of measured and theoretical CTP of a non-toluene/ethanol-mixture
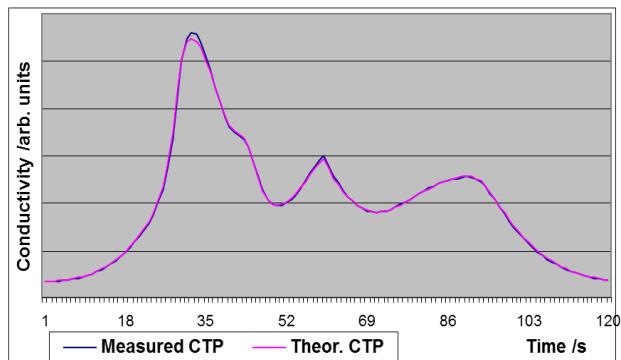
Figure 7. Comparison of measured and theoretical CTP of a toluene/ethanol binary mixture

TABLE II. RESULTS OF THE ANALYSIS TESTS

Dosed concentrations	Determined concentrations	Time delay*/days
25/2	23.4/2.1	1.25
100/5	95.3/5.4	1.0
200/1	200.1/0.9	1.5

*Time delay of the analysis test experiment after having finished the calibration data sampling

The CTP-analysis resulted in rather accurate estimations of the VOC-components (error < 10%), see Table II.

IV. PROCAL – A MATHEMATICAL PROCEDURE FOR BATCH-WISE CALIBRATION

For economic reasons, MOGs are typically fabricated in batch production. For technological reasons, production fluctuations are unavoidable which lead to fluctuations of the gas sensors specific features, e.g., manifested in CTP shape variations in the case of thermo-cyclic sensor operation.

Although the signal patterns (e.g., CTPs) of the various sensor chips of a production line are similar, each sensor chip has to be costly calibrated, in order to yield a high analytic performance. The same is true if a sensor chip has to be exchanged in case of a defect or if a sensor chip has to be recalibrated in case of long-term drifting.

The basic idea of ProCal is that only one single sensor chip (the so-called class reference chip) of the production line is measured at all calibration points (typically 5 calibration points for a single gas analysis application) and its signal patterns are sampled. Every other chips of the production line are measured at only one calibration point (the so-called reference point).

Next, for every sensor chip a mathematical function (the so-called approximation function) is determined which fits the signal pattern of the reference point, yield by the reference chip, to the signal pattern yield by the corresponding sensor chip in a best manner. That means that for each sensor chip excluding the reference chip a sensor specific approximation function is obtained.

With these approximation functions, the signal patterns of the reference chip are numerically calculated for all the other calibration points of the corresponding chips of the batch. This means that the signal patterns for the other calibration points do not have to be measured but can be approximated by numerical calculation. This results in a significant reduction of the calibration measurements by approximately factor 5.

The whole procedure is sketched in Table III with sensor s1 as the reference chip and concentration con3 as the reference point.

Furthermore, ProCal is able to find the "optimal" reference chip and to recognize a priori which sensor chips of the production line cannot be calibrated with this procedure.

To demonstrate the effectiveness of ProCal, an application was performed with eight thermo-cyclically operated gas sensors which were exposed to 0 ppm, 250 ppm, 500 ppm, 1000 ppm and 2000 ppm CO in humidified synthetic air (50% rH, 21°C), as described in [7].

In ProCal, only the CTPs of the reference concentration point (here at 500 ppm CO) of every sensor (Figure 8) are used to calculate sensor specific approximation functions.

ProCal recognizes that sensor S4 is the best choice for the class-reference chip.

Furthermore, ProCal a priori determines sensor S3 as an outlier which cannot be calibrated with this procedure.

TABLE III. SCHEME OF THE CALIBRATION PROCEDURE

	s1	si	
			s1: class reference chip
con1	m	n	*si = 2,3,..(other sensors)*
con2	m	n	*m:meas. signal pattern*
con3	m →	m	→*:approx. function f_i*
con4	m	n	*n: num. calcul. with f_i*
con5	m	n	*con3: ref. calibr. point*

f_i:CTP(**s1,con3**) -> CTP(**si,con3**) "optimal"

f_i: CTP(**s1,conj**) -> CTP(si,conj), j = 1,..,5
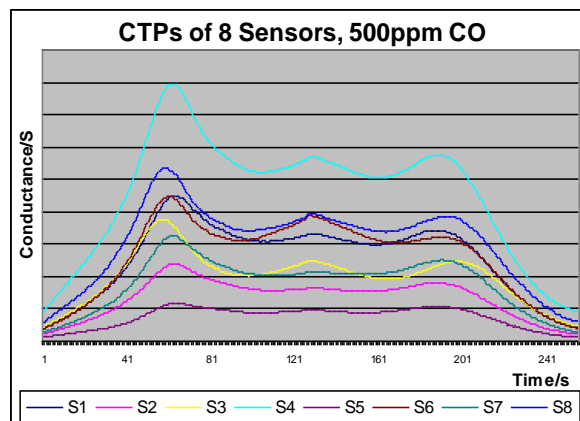
Figure 8. CTPs of eight sensors at reference point 500ppm CO. Sx means sensor x
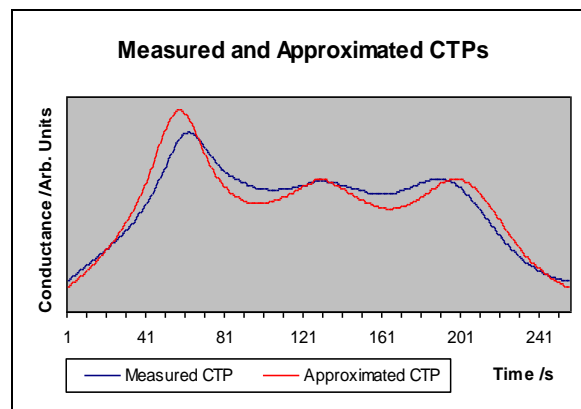
Figure 9. Measured and approximated CTP of S3 at reference point 500 ppm CO

Indeed, Figure 9 shows that the difference between numerically calculated CTP (using the relevant approximation function) and the sampled CTP is strikingly big for sensor S3 at reference point 500 ppm CO.

To demonstrate how well the numerically measured CTP fits the sampled CTP, the data of S2 at 1000 ppm CO are visualized in Figure 10. Similar results are obtained at all calibration points of the other sensors except the a priori excluded sensor S3.

Measured CTP and Approximated CTP
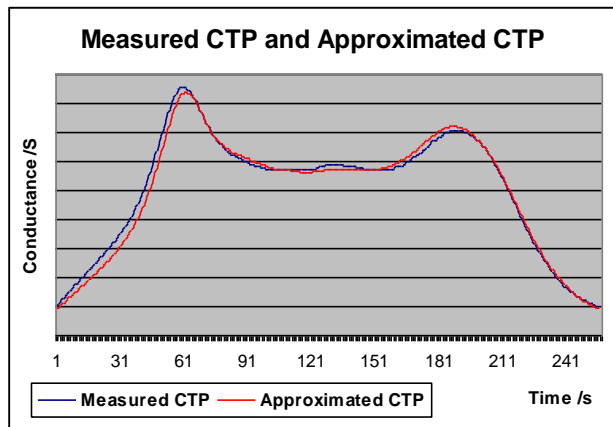
Figure 10. Comparison of measured CTP and approximated CTP of sensor S2 at exposure of 1000ppm CO

TABLE IV. ANALYSIS RESULTS IN PPM CO

DC	S1	S2	S3	S5	S6	S7	S8
0	13	11	-4	5	10	15	2
250	258	250	205	234	247	262	240
500	495	495	495	495	495	495	495
1000	948	988	1180	1007	1014	951	1004
2000	1801	1984	2559	1943	1977	1788	1937
MD	9.95	1.2	27.9	6.4	1.4	10.6	4.0

*DC: Dosed concentration, MD: Maximum deviation from DC in % (DC≠0)

For the determination of the mathematical calibration model with ProSens, only the measured CTPs at the reference point 500ppm were used. All the other CTPs needed for the determination of the calibration model were not measured but calculated. Table IV shows the analysis results achieved by ProSens. The relative analysis errors in all considered cases are less than 11%, except for the a priori excluded sensor S3. These errors are comparable with those obtained when using sampled data.

V. PROSOURCE - A PROCEDURE FOR SOURCE LOCALIZATION

Based on concentration measurements from spatially distributed gas sensors s_i (gas sensor network), the location of a gas source (e.g., from a leakage) is to be determined. To solve this problem it is assumed that the emitted substance is transported by advection caused by a known homogeneous wind field in x-direction and by diffusion.

The basic idea of the procedure ProSource [8][9] is to use a two-step approach for the source localization.

In the first step, for each sensor s_i, located at x_i, the set of points P_i is determined, on which the source can lie, taking only the specific concentration measurement C_i of sensor s_i into account.

In the second step, an estimate for the source position x_0 is evaluated by intersecting the sets P_i.

A. Determining P_i

Each set P_i is given by:

$$\mathcal{P}_i = \left\{ \mathbf{x}_0 \in \mathbb{R}^2 : \|\mathbf{x}_i - \mathbf{x}_0\|_2 = d_i(C_i, x_0, q_0) \right\} \quad (1)$$

Here, for a fixed but unknown source rate q_0 and the measured concentration C_i, the set P_i forms an oval in the x-direction. For different assumed source rates q_0 the oval sets P_i for one sensor s_i are plotted in Figure 11.
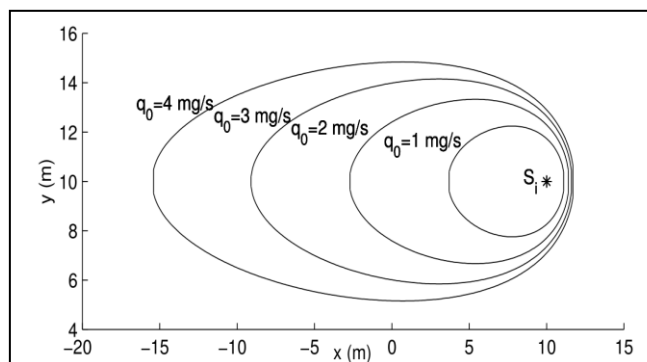
Figure 11. Potential source positions for sensor s_i for different source rates q_0

B. Estimating the source position x_0

Like for one sensor in Figure 11, ovals can be calculated for all m sensors of the sensor network. Thus, all m ovals intersect at the source position x_0, if the source rate, used to generate the ovals, equals the true value q_0. This is demonstrated in Figure 12. In this case, four gas sensors are applied.
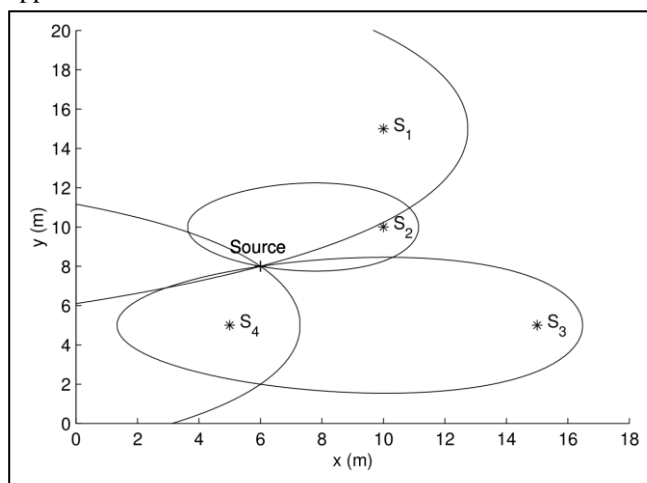
Figure 12. Intersection of all m sets P_i at the source position x_0 for the undisturbed case and the true value of q_0

Figure 12 demonstrates that in the undisturbed case the intersection of the curves is the source position of the gas

leakage with the corresponding source rate. In the disturbed case, ProSource calculates an estimated source position and a corresponding estimated source rate that minimize the geometric error of all ovals.

VI. CONCLUSIONS

In this paper the mathematical procedures ProSens, ProCal and ProSource have been shortly described and their performances have been demonstrated with examples using real measurement data.

The examples demonstrate that the procedures developed at KIT are powerful tools for economic online and in-situ field analyses applications. ProSens is an efficient mathematical procedure for evaluation of tin oxide gas sensor data, even in the case of variable environmental conditions like varying humidity. ProCal is an economic mathematical procedure for batch-wise calibration of multi gas sensors, useful to reduce the costs and the scope of calibration measurements. ProSource is a robust and fast procedure for source localization based on spatially distributed concentration measurements.

ProSens is designed to analyze only one gas mixture under consideration. But in many applications a multitude of different gases may occur, for example in detecting cable fire in a cable slot at a very early point of time but with high discrimination to other gases. Depending on the various coating materials of the cables, a variety of gases or gas mixtures can be emitted which have to be simultaneously identified and analyzed for early detection of such a developing risk. For this reason, ProSens has to be extended in a next step to meet these requirements.

REFERENCES

[1] P. Althainz, J. Goschnick, S. Ehrmann, and H.J. Ache, "Multisensor Microsystem for Contaminants in Air", Sensors and Actuators B 33 (1996) pp. 72-76.

[2] V.V. Sysoev, I. Kiselev, M. Frietsch, and J. Goschnick, "Discrimination Power of a Metal- Oxide Thin-Film Sensor Microarray", Sensors 2004, 4, pp. 37-46.

[3] A. Jerger, H. Kohler, F. Becker, H. B. Keller, and R. Seifert, "New applications of tin oxide gas sensors II. Intelligent Sensor System for Reliable Monitoring of Ammonia Leakages", Sens. Actuators, B 81, pp. 301-307 (2002).

[4] K. Frank, A. Hetznecker, V. Schindler, H. Kohler, H.B. Keller, and R. Seifert, "Metal Oxide Gas Sensors: A new approach for high quality field analysis applications using a dynamically operated sensor array",11th Internat.Meeting on Chemical Sensors (ICMS-11), Brescia, I, July 16-19, 2006.

[5] K. Frank, V. Magapu, V. Schindler, H. Kohler, H. B. Keller, and R. Seifert, "Chemical Analysis with Tin Oxide Gas Sensors: Choice of Additives, Method of Operation and Analysis of Numerical Signal", Sensors Letters 6, pp. 908-911 (2008).

[6] K. Frank, V. Magapu, V. Schindler, Y. Arnanthigo, H. Kohler, H. B. Keller, and R. Seifert, "Improving the analysis capability of tin oxide gas sensors by dynamic operation, appropriate additives and an advanced evaluation procedure", Sensor 2007: 13th Internat.Conf., Nürnberg, May, 2007, Proc. Vol. 1, pp. 139–144, AMA Service GmbH, Wunstorf (2007).

[7] K. Frank, H. Kohler, and U. Guth, "Influence of the measurement conditions on the sensitivity of SnO2 gas sensors operated thermo-cyclically", Sens. Actuators, B 141/2 pp. 361-369 (2009).

[8] J. Matthes, L. Gröll, and H. B. Keller, "Source localization based on pointwise concentration measurements", Sensors and Actuators A: Physical, Volume 115, Issue 1, 15 September 2004, pp. 32-37, ISSN 0924-4247, ttp://dx.doi.org/10.1016/j.sna.2004.03.016.

[9] J. Matthes, L. Gröll and H. B. Keller, "Source localization by spatially distributed electronic noses for advection and diffusion," IEEE Transactions on Signal Processing, vol.53, no.5, pp.1711-1719, May 2005

Development of Fast Response Humidity Sensors Based on Carbon Nanotubes

Marcos C. Moraes, Elisabete Galeazzo, Henrique E.M. Peres, and Francisco J. Ramirez-Fernandez

Departamento de Engenharia de Sistemas Eletrônicos
Universidade de São Paulo
São Paulo, Brazil
e-mail: bete@lme.usp.br

Michel O. S. Dantas

Centro de Engenharia, Modelagem e Ciências Sociais
Universidade Federal do ABC
Santo André, Brazil
michel.dantas@ufabc.edu.br

Abstract — **Current search on miniaturized humidity sensors primarily emphasizes issues related to integration and technological aspects. In this context, research efforts have been focused on developing sensors with Carbon Nanotubes (CNT) because of their promising sensing characteristics. However, there are challenges related to their application in commercial devices such as sensitivity, compatibility, and complexity of miniaturization, among others. In this work, we report the study of the electrical behavior of Multi-Walled Carbon Nanotubes (MWCNT) material deposited between interdigitated electrode structures by means of Dielectrophoresis (DEP), which is a simple and cost-effective method for deposition in micrometric regions. A fast and remarkable increase of electric resistance (up to 2.3 times) was noticed in the tested devices as a function of the concentration of water vapor, thus, these devices play an important and promising role for the development of integrated humidity sensors.**

Keywords: Carbon Nanotubes, Dielectrophoretic Deposition, Humidity Sensors.

I. INTRODUCTION

Nanomaterials have been drawing a lot of attention from scientific community to their potential applications in several areas. Many efforts are focused on obtaining nanomaterials in large scale, or on the analysis of their physical and chemical properties, as well as their application in the technological area. Because of their interesting properties, they have stimulated the development of new gas sensors [1].

Among the various kinds of nanomaterials for humidity and gas sensing applications, Carbon Nanotubes (CNT) are interesting alternatives due to their remarkable characteristics such as high specific area, good electric conductivity, high mechanical and chemical stability [2]. In addition, their capability to change electrical characteristics at room temperature in contact with low concentration gases has been published in several works [3] [4]. Moreover, a lot of research has been focused on answering open questions about electrical conduction and sensing mechanisms of CNT [5] [6].

CNT can be divided essentially into two categories: Single-Walled (SWCNT) and Multi-Walled (MWCNT) carbon nanotubes. Although SWCNT present advantageous characteristics for electrical devices and gas sensors development due to their purity, experimentally MWCNT have been more attractive because they can be produced in large industrial scale, reducing the production cost in comparison with SWCNT. Various methods have been developed for integration or deposition of CNT over the surface of devices [7]-[9]. In particular, Dielectrophoresis (DEP) is a simple, versatile and cost-effective method to deposit and to align CNT on pre-fabricated electrodes immersed in solutions without post-processing procedures. Another advantage of DEP is its compatibility with existing microfabrication capabilities, because this process is conducted at room temperature, in noncorrosive solutions, and at low voltage. The Dielectrophoretic Force (F_{DEP}) arises when an external non-uniform electric field is applied between electrodes immersed in a CNT solution, inducing dipole moment in the nanotubes. The polarized CNT will suffer the action of the F_{DEP}, promoting their motion toward regions of higher electric field gradient, aligning them in parallel with the electric field lines when their permittivity (ε_p) exceeds the permittivity of the suspending medium (ε_m), otherwise they will be repelled. The CNT deposition by DEP method depends on other parameters such as amplitude, frequency, total time of the external applied voltage, CNT morphology, electrode geometries, and solution properties [10].

In this work, we investigate the electrical response of CNT deposited by DEP on interdigitated electrodes towards the development of integrated humidity gas sensors considering that commercial humidity sensors are usually big and slow. The search for fast and reliable sensors, integrated and compatible with microelectronic circuits is a current need. This paper is organized in four sections: Section I presents the advantages of CNT and the DEP process for humidity sensors development; Section II details the experimental procedure for devices fabrication and characterization; Section III shows and discusses the results of CNT deposition by DEP and the electrical characterization of the sensors in humidity environment; the conclusions and perspectives are described in Section IV.

II. EXPERIMENTAL PROCEDURE

A. Devices Fabrication

The fabricated devices were based on interdigitated electrode geometries [11]. Our devices are composed of two interdigitated aluminum (Al) electrodes (A and B), with five fingers each, deposited by sputtering over a planar glass

substrate. As seen in the inset of Figure 1, each finger is composed of triangular geometries to concentrate the electric field during the DEP process and, consequently, to obtain CNT "bridges" between them. The minimum separation distance between electrodes is around 6 µm, and the CNT bridges will form parallel resistive elements between electrodes along the fingers.
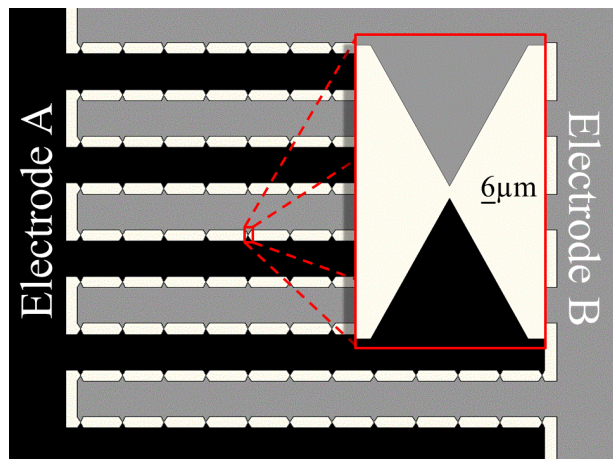
Figure 1.   Interdigitated electrodes for CNT deposition. The inset shows the minimum distance between electrodes where CNT are deposited to form bridges.

The CNT used in this work were CVD-grown MWCNT (catalog n. PD15L520, from Nanolab Inc, USA), which were functionalized for DEP according to the protocols described in [12]. The CNT solution was applied directly onto the samples. The DEP CNT deposition was carried out with the setup illustrated in Figure 2, as follows: a sinusoidal signal with $V = 10 \ V_{pp}$ and $f = 2 \ MHz$ was applied for 60 minutes in the circuit by a function generator. A 1 $k\Omega$ shunt resistor was included to allow monitoring the DEP current and protecting the generator in case of short circuit in the electrochemical cell. The oscilloscope monitored the applied voltage and the current in the process.
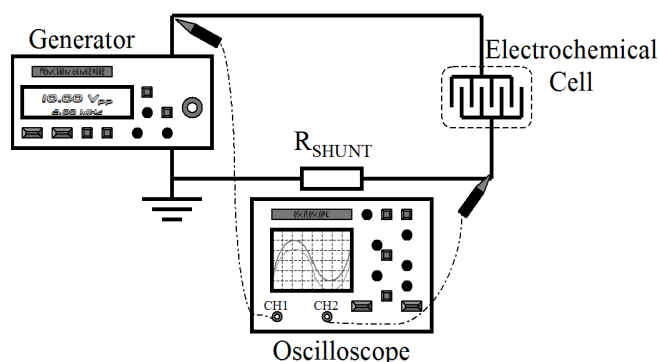
Figure 2.   Setup applied for CNT dielectrophoretic deposition.

After the deposition process, the samples were rinsed in ethanol and left to dry in air. The fabricated devices were observed by Scanning Electron Microscopy (SEM) with a FEI NOVA NanoSEM 400 microscope.

B.   Electric Characterization

All the samples were characterized before and after CNT deposition inside a controlled environment (from dry N_2 to N_2 saturated with H_2O vapor), by using the experimental setup illustrated in Figure 3 [13]. The N_2 was chosen as "background" environment to verify the sensitivity of the devices only for water vapor, avoiding the influence of other gas species. In this setup, the devices were inserted in a small-volume test chamber (300 µL), and the electrical measurements were performed with a Semiconductor Parameter Analyzer, model HP 4156A. The humidity levels into the chamber were established by adjusting simultaneously the fluxes of dry N_2 and N_2 saturated with H_2O through the needle valves and flowmeters. The electromagnetic valve allowed controlling the time intervals of dry and wet injections.
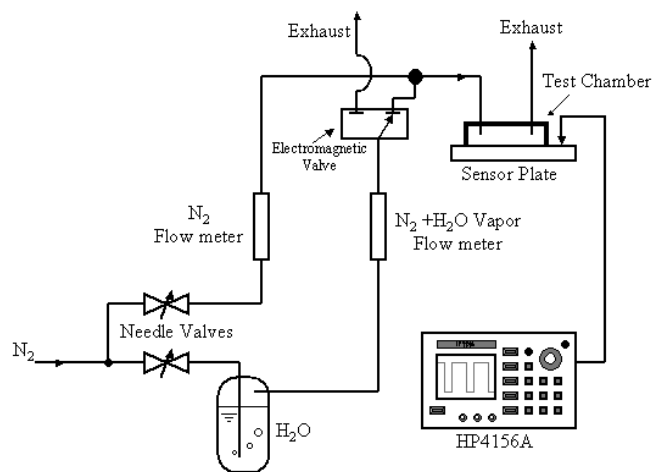
Figure 3.   Experimental setup for electrical characterization of the devices under controlled humidity environments.

Before the humidity tests, the devices were dried into dry N_2 for several minutes. The influence of the deposited CNT was characterized by measuring the electrical resistance between the interdigitated electrode fingers. These characterizations were conducted as follows: first, the electrical resistances of the devices were monitored along the time by varying the humidity from 0 to 100% in N_2 environment (with steps of dry N_2 for 200 s and wet N_2 for 20 s). Second, they were submitted to injection steps of saturated wet N_2 to evaluate the response repeatability. It is important to remark that the devices were also submitted to the same electrical characterization procedures before the CNT deposition [13], with the aim to stabilize the Al electrode surfaces and avoid additional oxidation during the tests with CNT.

III.   RESULTS AND DISCUSSION

Figure 4 shows DEP deposition aspects obtained on the devices. The results indicate the presence of CNT in several regions of the devices, but preferentially deposited at the apex of triangular geometries where the DEP electric field is stronger (Figures 4a and 4b). The applied DEP parameters allowed the formation of nanotube "chains" linked to each

other; however, an inhomogeneous deposition among the electrodes was noticed (Figures 4c and 4d). The hypothesis for this inhomogeneity can be related to the nanotubes deposited in the beginning of DEP which could generate distortions in the applied electric field along the process. Then, the more CNT deposition, the more inhomogeneity could occur.
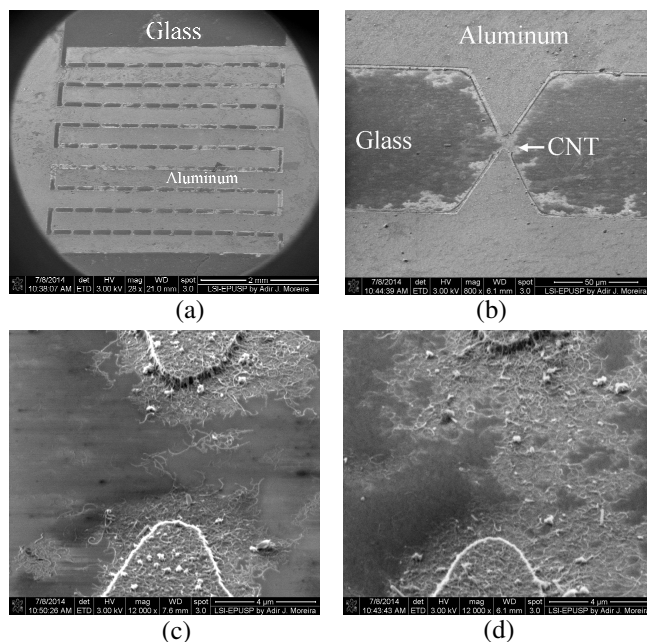
Figure 4. (a) Interdigitated electrodes after DEP CNT deposition; (b, c, d) Detail of CNT bridge between electrodes.

The devices presented a remarkable sensitivity to detect water vapor within a wide range of concentration. As shown in Figure 5, the device presented very fast increase and decrease of the resistance for humidity and for dry environment, respectively.
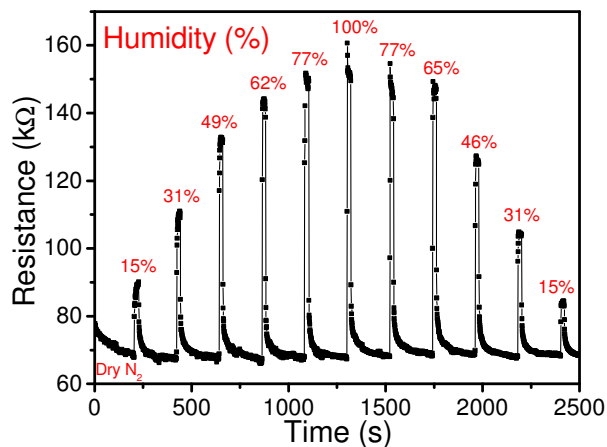
Figure 5. Device resistance along the time for several humidity conditions.

The response and recovery times are about only 3 s, i.e., the time necessary to reach 63 % of total resistance variation

for each humidity level tested. This result indicates that the interaction between water vapor and CNT is mainly dominated by physiosorption with weak bonds. As it takes some time to break these weak bonds, probably due to the water molecules trapped into the agglomerated of the CNT, the total recovery time was about 90 s. The devices recovered their original characteristics, and they did not show evidences of changes occurred by permanent oxidation or poisoning, thus, there was no need to heat or to expose the devices into vacuum environment, as reported in other works [14]. The Al oxidation [15] was considered negligible in our analysis because the devices were also exposed and characterized into oxidant environment before the CNT deposition, and no significant changes were noticed.

The overall electrical response of these devices is the result of several CNT resistors in parallel configuration. Under dry N_2 environment, the resistance measured is related mainly to the existence of metal-CNT and CNT-CNT interface contact resistances [13]. The increase of this resistance in humidity environment occurs because the CNT have p-type semiconductor behavior, and its resistivity tends to increase due to charge transfer from H_2O molecules to CNT, thereby depleting the hole density in the CNT [16]-[18].

The devices showed repeatability of relative resistance measurements in the humidity range tested, with a well-defined trend. The relation between relative resistance R/R_0 and humidity shows no linear behavior (Figure 6), but the hysteresis is very low (about 7 %), which allow the devices to measure environments with increase or decrease of humidity levels with low dispersion. Results depicted in Figure 5 and summarized in Figure 6 show a clear correspondence between the device resistance and the environmental humidity. Naturally, additional careful measurements are needed to determine the accuracy and precision of the sensor.
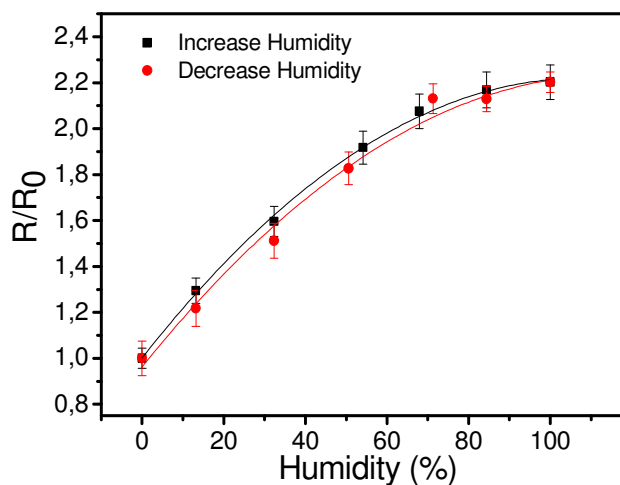
Figure 6. Relative resistance vs humidity for CNT device.

Figure 7 shows the response of the device for successive injections of water saturated N_2.
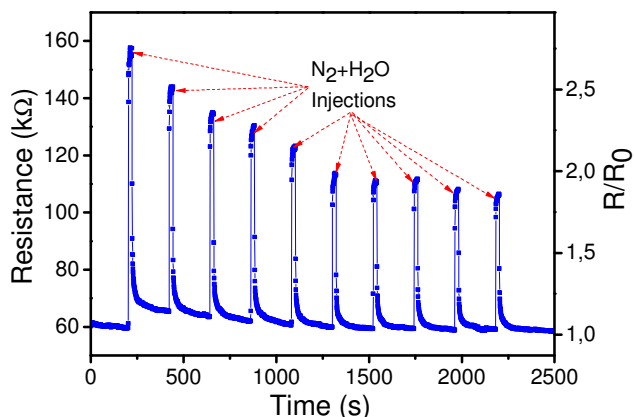
Figure 7. Electrical response for successive injections of humidity saturated N_2. Test steps: dry N_2 (200 s) and N_2 saturated with H_2O vapor (20 s).

One can verify a drift in the response, but it tends to stabilize after some injections. Moreover, the electrical resistance returns to the initial level because there is no sensor poisoning or significant oxidation of the electrodes after wet environment exposure, as described before.

IV. CONCLUSIONS

Miniaturized CNT resistive sensor devices were fabricated by applying DEP deposition. The electrode geometries and DEP parameters allowed CNT deposition preferentially localized. However, reduced DEP times must be experimented to promote CNT deposition only in the regions with stronger electric field. Water molecules adsorbed on CNT surface increase the electrical resistivity of this nanomaterial, and its value is dependent on water vapor concentration in the environment Experiments with other oxidant environments (including a background with synthetic air instead N_2) will be carried out aiming to obtain the selectivity of the sensors for practical applications. Although additional studies must be carried out to improve the sensors, they showed fast response, sensitivity even for low humidity level, and no evidence of poisoning, which is promising for the development of integrated sensors for industrial, agricultural and environment control applications.

REFERENCES

[1] J. P. Colinge et al., "Junctionless nanowire transistor (JNT): properties and design guidelines", Solid-State Electronics, vol. 65–66, July 2011, pp. 33–37.

[2] W. Bai, D. Zhuo, X. Xiao, J. Xie, and J. Lin, "Conductive, mechanical, and chemical resistance properties of polyurushiol/multiwalled carbon nanotube composite coatings", Polymer Composites, vol. 33, no. 5, March 2012, pp. 711-715.

[3] H. Liu, H. Ma, W. Zhou, W. Liu, Z. Jie, and X. Li, "Synthesis and gas sensing characteristic based on metal oxide modification multi wall carbon nanotubes composites", Applied Surface Science, vol. 258, January 2012, pp. 1991-1994.

[4] F. Inam, H. Yan, M. J. Reece, and T. Peijs, "Structural and chemical stability of multiwall carbon nanotubes in sintered ceramic nanocomposite", Advances in Applied Ceramics, vol. 109, no.4, April 2010, pp. 240-245.

[5] O. K. Varghese, P. D. Kichambre, D. Gong, K. G. Ong, E.C. Dickey, and C. A. Grimes, "Gas sensing characteristics of multi-wall carbon nanotubes", Sensors and Actuators B, vol. 81, August 2001, pp. 32-41.

[6] P. Bondavallia, P. Legagneuxa, and D. Pribat, "Carbon nanotubes based transistors as gas sensors: State of the art and critical review", Sensors and Actuators B, vol. 140, May 2009, pp. 304–318.

[7] C. Bower, O. Zhou, W. Zhu, D. J. Werder, and S. Jin, "Nucleation and growth of carbon nanotubes by microwave plasma chemical vapor deposition", Applied Physics Letters, vol. 77, no. 17, October 2000, pp. 2767-2769.

[8] I. G. Assovskii and G. I. Kozlov, "Synthesis of Single-Walled Carbon Nanotubes by the Laser Ablation of Graphite under Normal Conditions", Physical Chemistry, vol. 388, no. 1–3, January 2003, pp. 13–17.

[9] M. Chhowalla et al., "Growth process conditions of vertically aligned carbon nanotubes using plasma enhanced chemical vapor deposition", Journal of Applied Physics, vol. 90, no. 10, November 2001, pp. 5308-5317.

[10] A. K. Naieni and A. Nojeh, "Dielectrophoretic deposition of carbon nanotubes: The role of field frequency and its dependence on solution conductivity", Microelectronic Engineering, vol. 114, September 2013, pp. 26-30.

[11] L. H. D. Skjolding, C. Spegel, A. Ribayrol, J. Emnéus, and L. Montelius, "Characterisation of nano-interdigitated electrodes", Journal of Physics: Conference Series, vol. 100, no. 5, March 2008, pp. 1-4.

[12] S. Minnikanti, P. Skeath, and N. Peixoto, "Electrochemical characterization of multi-walled carbon nanotubes coated electrodes for biological applications", Carbon, vol. 47, no. 3, March 2009, pp. 884-893.

[13] M. C. Moraes, E. Galeazzo, H. E. M. Peres, M. O. S. Dantas, and F. J. Ramirez-Fernandez, "Electrical behavior of devices composed by dielectrophoretically deposited carbon nanotubes for gas sensing applications". IEEE Proceedings, in press.

[14] W. Kim, A. Javey, O. Vermesh, Q. Wang, Y. Li, and H. Dai, "Hysteresis caused by water molecules in carbon nanotube field-effect transistors", Nano Letters, vol. 3, no. 2, January 2003, pp. 193-198.

[15] I. Olefjord and A. Nylund, "Surface analysis of oxidized aluminum. 2. Oxidation of aluminum in dry and humid atmosphere studied by ESCA, SEM, SAM and EDX", Surface and Interface Analysis, vol. 21, no. 5, May 1994, pp. 290-297.

[16] A. Zahab, L. Spina, P. Poncharal, and C. Marlière, "Water-vapor effect on the electrical conductivity of a single-walled carbon nanotube mat", Physical Review B, vol. 62, no. 15, October 2000, pp. 10000-10003

[17] P. R. Bandaru, "Electrical properties and applications of carbon nanotube structures", Journal of Nanoscience and Nanotechnology, vol. 7, January 2007, pp. 1–29

[18] R. Pati, Y. Zhang, S. K. Nayak, and P. M. Ajayan, "Effect of H_2O adsorption on electron transport in carbon nanotubes", Applied Physics Letter, vol.81, no.14, September 2002, pp. 2638-2640.

Bridge Type Hydrogen Sensor Using Platinum Ultrathin film

Yuki Ushita, Shuzo Takeichi, Ryosuke Sugai, Shota Inami, Kenji Sakai, Toshihiko Kiwa, Keiji Tsukada

Graduate School of Natural Science and Technology, Okayama University

Okayama, Japan

e-mail : (en421411, pgrx83ea, en422426, p5x20coc)@s.okayama-u.ac.jp

(sakai-k, kiwa, tsukada)@okayama-u.ac.jp

Abstract—**The resistance of platinum thin-film was reduced by carrier density increment in the presence of hydrogen gas. The resistance change depended on the thickness of the platinum. Using these phenomena, a bridge-type hydrogen sensor, which converted this resistance change into a voltage change, was developed. The developed sensor was able to detect hydrogen at room temperature. Furthermore, we suggest a method in which the response and recovery time is accelerated by applying a pulse voltage to the sensor. The developed sensor can use DC and AC voltage as the driving power source.**

Keywords-platinum; hydrogen sensor; bridge circuit; thin-film.

I. INTRODUCTION

A large amount of energy is being consumed and fossil fuel is mainly used as the energy resource. However, the use of fossil fuel is exacerbating the greenhouse effect and there is a finite supply of fossil fuel. Therefore, a new energy resource as an alternative to fossil fuel is required. Recently, hydrogen has been attracting attention as a new source of energy. However, when the concentration of hydrogen is more than 4.1%, it is liable to explode. Therefore, the development of a hydrogen sensor that can detect low concentrations of hydrogen is required. Several types of hydrogen sensor have been reported, including those based on catalytic, thermal conductivity, electrochemical reaction, resistance change, work function change and optical change [1]-[10]. A metallic resistance change type sensor (resistance based) can operate at room temperature and the structure of this sensor is simple. Generally, this hydrogen sensor uses Palladium (Pd) as the hydrogen storage metal. While Pd has a good response toward hydrogen, its durability is weak. To address this issue, we developed a hydrogen sensor using

Platinum (Pt) instead of Pd [11] and the resistance of the Pt thin-film was reduced by the carrier density increment in the presence of hydrogen gas. Moreover, it was clarified that the resistance change depended on the thickness of the Pt [12] because of the carrier density change caused at only the Pt surface. To develop a practicable hydrogen sensor made of Pt thin-film, a bridge circuit using four Pt thin-film resistances was investigated. It is advantageous that the bridge circuit sensor can reduce environmental noise and off-set signal. Moreover, it can convert resistance change to voltage change and can detect hydrogen concentration by voltage change. In this study, two bride types of sensor, which consist of one or two hydrogen sensitive thin-film resistances (Type 1 and Type 2), were developed. Then, the hydrogen response of these two sensors was evaluated. Moreover, the effect of pulse voltage applied to the sensor was investigated in order to improve the response and recovery time (time taken to achieve a 90% response to a step change). Section II describes schematic of sensing chip and experimental procedure. Section III describes the result and discussion. Section IV addresses the conclusion.

II. EXPERIMENTAL PROCEDURE

A. Schematic of sensing chip

Figure 1 shows a schematic diagram of the sensing chip. The sensing area consists of four resistances ($R_1 - R_4$) and these resistances can be regarded as a bridge circuit. In this study, two types of thin film having different resistances, were fabricated. When the sensor is exposed to hydrogen, the thin layer, which has high resistance, is greatly reduced and the thick layer, which has low resistance, decreases slightly.
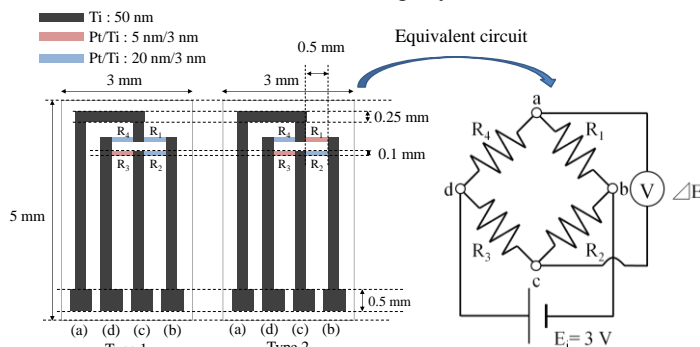
Figure 1. Schematic diagram of the hydrogen sensor.

Therefore, the resistance change can be measured by the bridge circuit and this resistance change depends on the hydrogen concentration. The whole sensor is 3 mm × 5 mm, and each resistance size is 0.5 mm × 0.1 mm. This sensor can also reduce environmental noise using the same material.

B. Production procedure of sensing chip

Figure 2 shows the production procedure of this sensor. First, glass substrate is cleaned by ultrasonic cleaning in acetone and ethanol alternately. Next, the surface of the glass substrate is coated by photoresist using a spin coating machine and baked for 90 s at 110 °C. After that, the glass substrate is irradiated with ultraviolet rays through a mask pattern of the circuit and immersed in a developer solution. Subsequently, the glass substrate is baked in 5 min at 60 °C and a metal film is deposited on glass substrate by sputtering. Finally, the fabricated circuit is cleaned by ultrasonic cleaning. From the above procedure, only metal remains on the circuit (Figure 1 (a) ~ (f)).These processes are repeated three times. In the first process, an electrode layer is formed by titanium (Ti) (50 nm) (Figure 1 (1)). Next, the reaction layer is formed by Pt (5 nm) on Ti (3 nm) (Figure 1 (2), (3)). Finally, the low reaction layer is formed by Pt (20 nm) (Figure 1 (4)). In this study, two types of bridge sensor, Type 1 and 2, were fabricated as shown in Table 1.

TABLE I.   THE THICKNESS OF EACH RESISTANCE

	R_1 (Pt/Ti)	R_2 (Pt/Ti)	R_3 (Pt/Ti)	R_4 (Pt/Ti)
Type 1	20 nm/3 nm	20 nm/3 nm	5 nm/3 nm	20 nm/3 nm
Type 2	5 nm/3 nm	20 nm/3 nm	5 nm/3 nm	20 nm/3 nm

C. Measurement condition

The hydrogen sensor must be able to detect a hydrogen concentration of less than 4.1% because the hydrogen concentration range of explosion is between 4.1% and 74.2%. In this study, gases of air (80%-nitrogen and 20% oxygen) and 1%-H_2 (1%-hydrogen and 99%-air gas) were prepared in order to evaluate the hydrogen response. Three volts are applied to input terminals (Figure 1 (b)-(d)) of the sensor as the driving power source. Then, when gases are injected into the chamber for 5 minutes alternately, the voltage between the output terminals (Figure 1 (a)-(c)) is measured. When DC voltage is applied to the sensor as the driving power source, the wiring affects the output. To reduce the effect of the wiring, AC voltage ($6V_{p-p}$, 1Hz) is applied to two terminals (Figure 1 (b)-(d)) of the sensor as the driving power source. In this case, the terminal voltage of the other two terminals (Figure 1 (a)-(c)) is measured as well as the DC measurement.

D. Improvement of response time

The conventional hydrogen sensor has the problem of slow response time. In this study, in order to accelerate the response time, it was attempted to accelerate the reaction by increasing the temperature of the sensor. Therefore, pulse voltage (40 V) was applied to the sensor for 3 s. As mentioned above, the gas is changed from air gas to 1%-H_2 gas to fill the chamber with 1%-H_2 and the pulse voltage is applied to the sensor to reduce the response time by 30 s after changing the gas (waiting time to fill gas). In the same way, the pulse voltage is also applied to the sensor to reduce the recovery time as well as the response time by 30 s after changing the switch from H_2-1% gas to the air gas to fill the chamber with the air gas.

III.   RESULT AND DISCUSSION

Figure 3 shows the hydrogen response of the developed sensor using DC measurement. Output of Type 1 and Type 2 increased in the presence of hydrogen gas. Here, R_1, R_2 and R_4 of Type 1 are the same because the film thickness is the same. Therefore, the output of ΔE is given by (1).

$$\Delta E = [E_i (R_2 - R_3)] / [2(R_2 + R_3)] \qquad (1)$$

Moreover, in the case of Type 2, R_1 is equal to R_3, and R_2 is equal to R_4 because the film thickness is the same. Consequently, the output voltage is given by (2)

(a) Coating photoresist — Photoresist

Glass substrate

(b) Exposure

Ultraviolet ray

Circuit pattern mask

(c) Development

(d) 1.Sputter

(e) 2.Sputter

(f) Lift-off

(1)Electrode of Ti

(2) Adhesion layer of Ti

(3) Reactive layer of Pt

(4) Low reactive layer of Pt
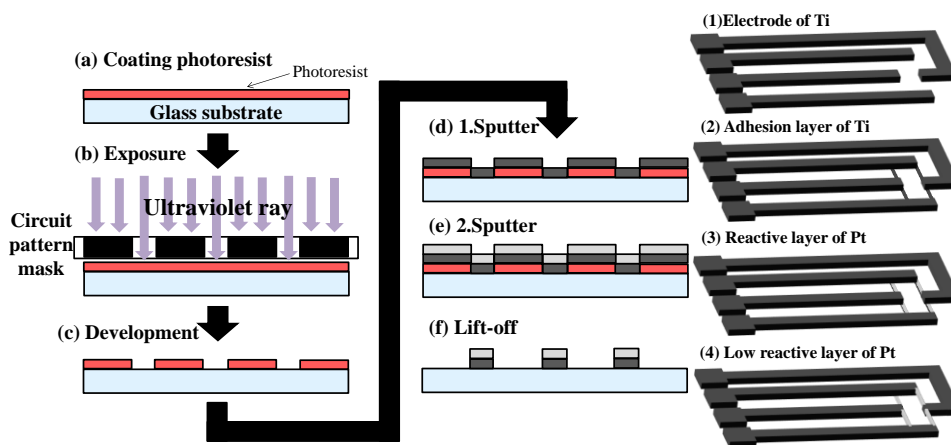
Figure 2. Schematic diagram of fabrication process for the hydrogen sensor.

$$\Delta E = [E_i (R_2 - R_3)] / (R_2 + R_3) \qquad (2)$$

When the sensor is exposed to the hydrogen gas, R_2 (Pt/Ti =20 nm/3 nm) and R_3 (Pt/Ti = 5 nm/3 nm) are reduced by carrier density increment. Moreover, the resistance change depends on the thickness of the platinum. The results of reference [12] show that Pt/Ti (20 nm/3 nm) decreased 0.14 Ω and Pt/Ti (5 nm/3 nm) decreased 5.8 Ω. Therefore, the output increased because the change of R_2 and R_3 is different. Compared with Type 1, output of Type 2 is larger. Type 2 is useful as a sensor. As for the response time, the 90% response time in the case of no pulse voltage was about 210 s. When the pulse voltage is applied, the total response time and waiting time (30 s) is about 50 s. After pulse voltage is applied, the output becomes saturated in 20 s because high voltage was applied to the sensor and the temperature of the sensor increased by joule heat. Moreover, the recovery time is more than 12 h when the pulse voltage is not applied. However, when the pulse voltage is applied, total recovery time and waiting time (30 s) is about 50 s. After the pulse voltage is applied, the output became about 0 V and was saturated in 20 s. The reason for accelerating the response and recovery time is described below.

This sensor uses the chemical change of (3), (4).

$$H_2 \rightleftarrows 2H^+ + 2e^- \qquad (3)$$

$$4H^+ + O^{2-} + 2e^- \rightleftarrows 2H_2O \qquad (4)$$

Therefore, heating a sensor is a simple method of increasing the speed of the reaction rate. The Arrhenius equation (5) shows the reason for this,

$$k = A \times \exp(-E_a/RT) \qquad (5)$$

where k, A, E_a, R, T are the rate constant, constant, activation energy, gas constant, and absolute temperature, respectively. The more T is increased by heating and the k of (5) is increased, the greater the reaction of (3), (4) is accelerated. For these reasons, the response and recovery times are accelerated. Therefore, the pulse voltage application is useful for accelerating the response. Moreover, in this study, the sensor is heated by pulse voltage only when the heating is required. In such a way, power consumption can be reduced. Figure 4 (a) shows the hydrogen response of the developed sensor using AC measurement. As shown in Figure 4 (a), it is difficult to show the hydrogen response because of the offset effect. To solve this problem, the instrumentation amplifier (AD627AN) was used. The offset is canceled by the antiphase of the sensor output. The gain of instrumentation amplifier is 5. Figure 4 (b) shows the hydrogen response of AC measurement using the instrumentation amplifier. The output increased by the presence of hydrogen gas and the hydrogen response could be detected clearly. Moreover, the response and recovery time is accelerated, as well as the use of DC voltage as the driving power source.

(a) Type 1   (b) Type 2
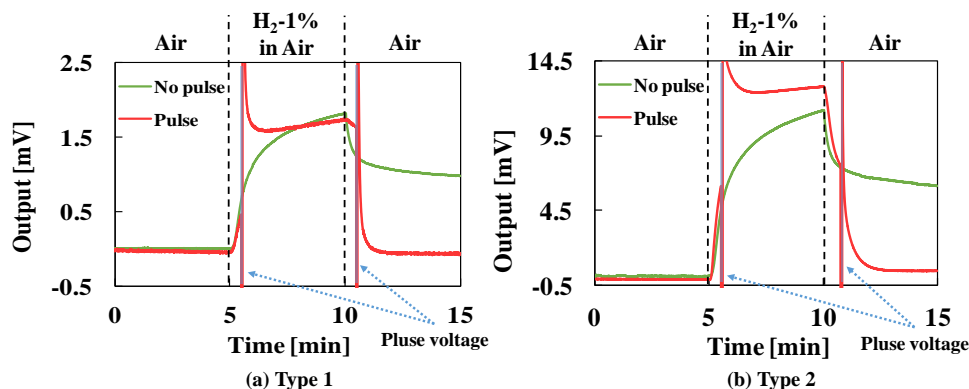
Figure 3. Hydrogen response characteristics of Type 1 and Type 2 operated with DC power supply.

(a) Raw waveform of sensor   (b) Waveform of sensor using Instrumentation amplifier
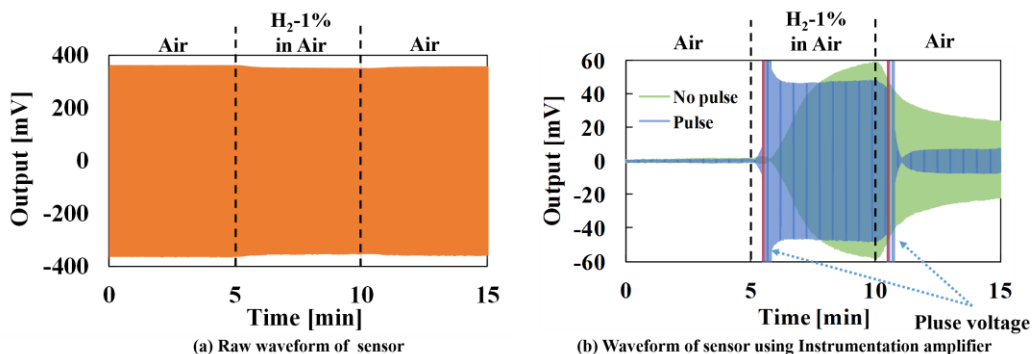
Figure 4. Hydrogen response characteristic of Type 1 and Type 2 operated with AC power supply, and pulse heating effect.

IV. CONCLUSION

A bridge circuit type hydrogen sensor was developed utilizing the principle of electrical resistance change in Pt thin-film. This sensor can detect hydrogen concentration at room temperature. In addition, DC and AC voltage was used as the driving power source and the voltage change caused by the hydrogen sensor was detected when using AC voltage, which can reduce the effect of the wiring. Moreover, the response and recovery times became shorter by applying pulse voltage to the sensor. In future research, the developed sensor will be evaluated under various condition to apply to practical use such as hydrogen station and fuel cell vehicles.

REFERENCES

[1] T. Hubert, L. Boon-Brett, G. Black and U. Banach, "Hydrogen sensor - A Review" Sensors and Actuators B, Chemical, Volume 157 , Issue 2, pp. 329-352, 2011.

[2] M. Matsumiya, W. Shin, N. Izu and N. Murayama, "Nano-structured thin-film Pt catalyst for thermoelectric hydrogen gas sensor" Sensors and Actuators B, Chemical Volume 93, Issues 1–3, pp. 309–315, 2003.

[3] M. Lang, *et al.*, "Long-term stability of a MEIS low energy hydrogen sensor" Sensors and Actuators B, Chemical Volume 187, pp. 395–400, 2013.

[4] S. Horch, *et al.*, "Enhancement of surface self-diffusion of platinum atoms by adsorbed hydrogen" nature 398, pp. 134-136, 1999.

[5] C. Liewhiran, N. Tamaekong, A. Wisitsoraat, A. Tuantranont and S. Phanichphant, "Ultra-sensitive H_2 sensors based on flame-spray-made Pd-loaded SnO_2 sensing films" Sensors and Actuators B 176, pp. 893– 905, 2013.

[6] M. Nishibori, *et al.*, "Robust hydrogen detection system with a thermoelectric hydrogen sensor for hydrogen station application" international journal of hydrogen energy 34, pp. 2834–2841, 2009.

[7] I. Simon and M. Amdt, "Thermal and gas-sensing properties of a micromachined thermal conductivity sensor for the detection of hydrogen in automotive applications", Sensors and Actuators A 97-98, pp. 104-108, 2002.

[8] G. Korotcenkov, S. D. Han and J. R. Stetter, "Review of Electrochemical Hydrogen Sensors" Chem. Rev. 109, pp. 1402–1433, 2009.

[9] T. Xua, M. P. Zach, Z. L. Xiao, D. Rosenmann, U. Welp, W. K. Kwok, and G. W. Crabtree, "Self-assembled monolayer-enhanced hydrogen sensing with ultrathin palladium films" Applied Physics Letters 86, p. 203104 , 2005.

[10] X. Wang, Y. Tang, C. Zhou and B. Liao, "Design and optimization of the optical fiber surface plasmon resonance hydrogen sensor based on wavelength modulation" Optics Communications 298–299, pp. 88–94, 2013.

[11] K. Tsukada, H. Inoue, F. Katayama, K. Sakai and T. Kiwa, "Changes in Work Function and Electrical Resistance of Pt Thin Films in the Presence of Hydrogen Gas", Japanese Journal of Applied Physics, 51, p. 015701, 2012.

[12] K. Tsukada, S. Takeichi, K. Sakai and T. Kiwa, "Ultrathin-film hydrogen gas sensor with nanostructurally modified surface" Japanese Journal of Applied Physics 53, p. 076701, 2014.

Ultrathin Film Hydrogen Sensor with Self-Temperature Compensation

Shuzo Takeichi, Yuki Ushita, Ryosuke Sugai, Kenji Sakai, Toshihiko Kiwa, Keiji Tsukada

Graduate School of Natural Science and Technology, Okayama University

Okayama, Japan

e-mail: (pgrx83ea, en421411, en422426) @s.okayama-u.ac.jp

(sakai-k, kiwa, tsukada) @cc.okayama-u.ac.jp

Abstract—**An ultrathin film sensor, consisting of two serially connected Pt/Ti films with different sensitivity to obtain the output voltage, was developed. The hydrogen sensor, based on the electrical resistance change of Pt thin films upon exposure to hydrogen gas, is operable at room temperature. However, two different Pt/Ti films showed different temperature coefficient of resistance, so the output voltage changed by temperature change. In order to solve this problem, we developed a self-temperature compensation technique by optimized combination of Pt thickness and Ti thickness. As a result, the hydrogen sensor showed good stability against temperature change.**

Keywords-hydrogen sensor; platinum thin film; catalysis.

I.   INTRODUCTION

Hydrogen energy is attracting attention as a clean energy in fuel cells, and the number of applications is growing. However, hydrogen has a wide range of explosive concentrations (4-75% in air) and hydrogen atoms are very small. Therefore, there is a risk of leakage and a method of detecting hydrogen leakage is required. Generally, sensors for detecting hydrogen leakages in multipoint should have high sensitivity, be low cost and have low power consumption. Many types of hydrogen sensors, such as semiconductor sensors [1][2], Field-Effect Transistors (FET) sensors [3]-[7], and metallic resistance change type sensors [8]-[10] have been studied. Semiconductor sensors operated above 300 °C are conventionally used, while FET and the metallic resistance change type sensors can detect hydrogen gas by using the work function change and electrical resistance change in catalytic metals at room temperature, respectively. Moreover, the metallic resistance change type sensors that use Palladium (Pd) are simple, so this sensor is suitable for mass production. However, a serious durability problem is caused by large expansion of Pd after exposure to high concentration hydrogen gas [11]. In order to address this problem, we previously reported a metallic resistance change type hydrogen sensor using Platinum (Pt) thin films instead of Pd [12]. This sensor can detect hydrogen gas by reducing the resistance upon exposure to hydrogen gas at room temperature. However, the resistance also changed by changes in the ambient temperature. Therefore, precise detection of hydrogen gas requires temperature compensation. In this study, we developed and evaluated a hydrogen sensor with self-temperature compensation.

Section II describes experimental procedure. Section III describes the result and discussion. Section IV addresses the conclusion.

II.   EXPERIMENTAL PROCEDURE

Pt/Titanium (Ti) films (Pt thickness: 30 nm, 20 nm, 10 nm, 5 nm/Ti thickness 3 nm), were deposited on a glass substrate (0.55-mm thick) by DC sputtering to investigate the resistance change upon exposure to hydrogen gas. Generally, a Ti layer is used for improvement of poor adhesion. We previously confirmed that Ti shows no response to hydrogen gas [6]. However, the resistance change ratio, when exposed to hydrogen gas, reduced by addition of a Ti layer, because the resistance of Ti is added in parallel to that of the Pt [12]. Therefore, a thinner Ti film that has higher resistance is suitable, and a Ti (3-nm thick) layer was selected. Each Pt/Ti film on glass substrate was cut to dimensions of 3×10 mm^2, respectively (Figure 1). These films were placed in a chamber that was designed to measure the response characteristics at a constant gas exchange rate. The resistance was measured by a four-terminal sensing method using pairs of separated current-carrying and voltage-sensing wires. In order to assess the basic characteristics, the sensitivities of each sample were evaluated with respect to air and hydrogen gas of 1% concentration (1%-H$_2$) at room temperature. The gas was changed from air to 1%-H$_2$ and back to air, and the sensitivity was calculated by the following equation.

$$\Delta R / R = (R_{H2} - R) / R \times 100 \ (\%) \qquad (1)$$

where R and R$_{H2}$ are the resistance of Pt/Ti film in air and hydrogen gas.

However, Pt/Ti film also changed by temperature change, so hydrogen detection was severely affected. Generally, hydrogen sensor with a robustness to temperature in the range of -30 to 80 °C is required for detecting hydrogen gas [13], and it is necessary to detect hydrogen gas precisely in the temperature range. Therefore, we developed the hydrogen sensor with self-temperature compensation, which has two different Pt/Ti films were serially connected (Figure 2). This sensor, utilizing resistance change of Pt/Ti film, can detect hydrogen gas as output voltage change. In this sensor, hydrogen response and temperature dependence were measured. As samples, Pt (5 nm thick) on Ti (3 nm thick) and Pt (30 nm thick) on Ti (3 nm thick) were prepared, and
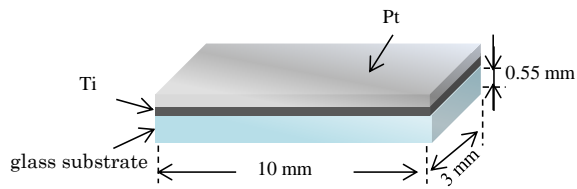
Figure 1.   Schematic diagram of Pt/Ti thin film.
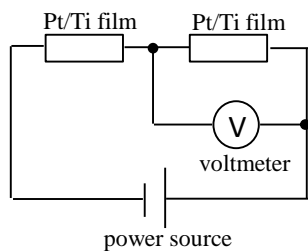
Figure 2.   Schematic diagram of serially connected hydrogen sensor with different Pt/Ti thickness.

Figure 3.   Hydrogen response curve of Pt/Ti thin films with different thickness.
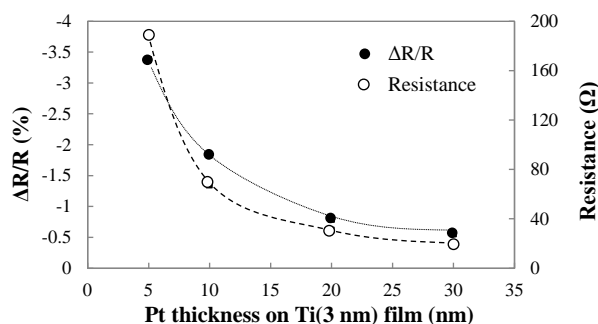
Figure 4.   Pt thickness (5, 10, 20 and 30 nm on Ti(3 nm)) dependence for sensitivities to hydrogen gas when exposed to 1% concentration and the resistance in air.

the output voltage of Pt (5 nm thick) on Ti (3 nm thick) was measured in air and 1%-H_2. The temperature dependence in air was also evaluated in the temperature range from 50 °C to 80 °C in steps of 10 °C. Moreover, to eliminate temperature effect more precisely, combination of Pt thickness and Ti thickness was optimized. First, resistance temperature coefficient of samples, which are Pt films (thickness: 30 nm, 20 nm, 10 nm and 5 nm) on Ti films (thickness: 0 nm, 3 nm and 20 nm), was measured in the range from 50°C to 100°C in the steps of 10 °C. Then, based on the results of temperature dependence, a hydrogen sensor with two Pt/Ti films, which was optimized to have the same temperature coefficient of resistance, was fabricated. The hydrogen response and temperature dependence of the optimized hydrogen sensor was also evaluated under the same conditions as previously mentioned.

III.   RESULTS AND DISCUSSION

The measured resistances of Pt/Ti films when exposed to hydrogen gas are shown in Figure 3. The results show the resistances of Pt/Ti films decreased for all measured samples when gas was switched from air to 1%-H_2. This decrease was caused by the catalytic action of Pt. When hydrogen molecule is adsorbed on the Pt surface, the hydrogen molecule is decomposed into hydrogen ions and electrons by the catalytic action of Pt as expressed in (2). Basically, the decomposed electrons diffuse into the platinum as the carriers, and platinum electrical resistance decreases.

$$\frac{1}{2} H_2 \leftrightarrow H^+ + e^- \qquad (2)$$

Moreover, when hydrogen concentration is decreased, the resistance recovers, because the absorbed hydrogen desorbs and the carrier concentration decreases. Figure 4 shows the sensitivities and the resistances to 1%-H_2 as a function of Pt thickness. With decreasing the thickness of Pt film, sensitivity increased. This is because the surface-to-volume ratio of platinum increases with reducing the thickness. In brief, the number of carriers, generated by the catalytic reaction, increases in relation to the thinness of the Pt film, because the catalytic reaction occurs primarily on the surface without depending on film thickness. Also, the sensitivity as a function of Pt thickness is inversely proportional, similar to the resistance. The sensitivity depends on resistance and carrier caused by catalytic reaction. In this measurement, generated carrier is constant regardless of Pt thickness, so it is considered that the relationship of the sensitivity and Pt thickness is similar to the resistance. From these results, the sensitivity was increased with decreasing Pt thickness. However, the resistance did not completely recover when the gas was switched from 1%-H_2 to air. This indicates that all absorbed hydrogen ions and electrons were not desorbed, and a long time is needed for complete desorption. To solve this problem, we reported hydrogen desorption using instantaneous large pulsed heating in a previous study [12].
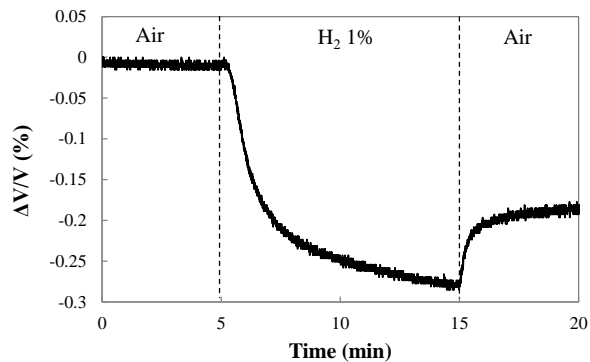
Figure 5.   Hydrogen response curve of the hydrogen sensor that was serially connected Pt (5 nm)/Ti (3 nm) and Pt (30 nm)/Ti (3 nm) films.
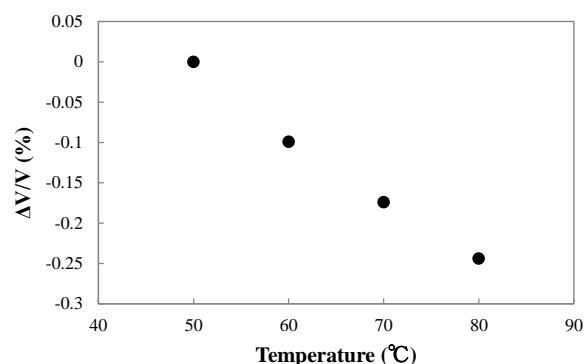
Figure 6.   Temperature dependence for output voltage change of the serially connected Pt (5 nm)/Ti (3 nm) and Pt (30 nm)/Ti (3 nm) films.

TABLE I.   TEMPERATURE COEFFICIENT OF PT/TI FILMS

Pt \ Ti	0 (nm)	3 (nm)	20 (nm)
5 (nm)	0.00065	0.00102	0.00064
10 (nm)	0.00098	0.00154	0.00094
20 (nm)	0.00132	0.00193	0.0017
30 (nm)	0.00171	0.00201	0.00181
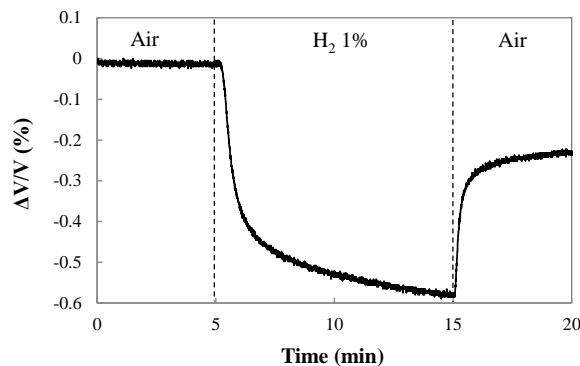
Figure 7.   Hydrogen response curve of the serially connected Pt (5 nm)/Ti (3 nm) and Pt (10 nm)/Ti (20 nm) films.
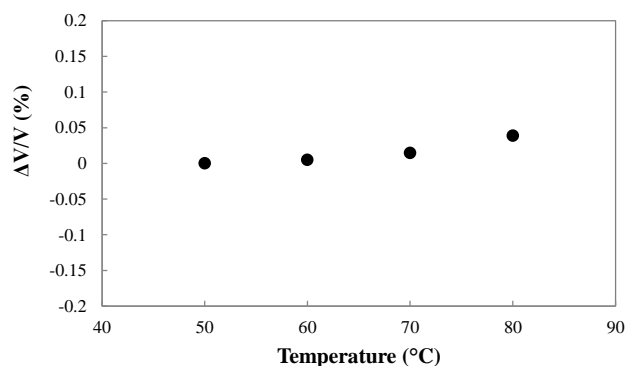
Figure 8.   Temperature dependence for output voltage change of the serially connected Pt (5 nm)/Ti (3 nm) and Pt (10 nm)/Ti (20 nm) films.

$|\Delta R/R|$ in Pt (5 nm)/Ti (3 nm) film was about 3.4% after exposure to hydrogen gas. However, $|\Delta R/R|$ of 3% occurred by temperature change in the range from 50°C to 80°C, so the temperature effect cannot be ignored. To compensate for this temperature effect, a sensor consisting of two different serially connected Pt/Ti films, which are Pt (5-nm thick) on Ti (3-nm thick) and Pt (30-nm thick) on Ti (3-nm thick), was fabricated. The time response curve of the hydrogen sensor when exposed to air and 1%-H_2 is shown in Fig. 5. This sensor utilizes the difference in sensitivities of the two Pt/Ti films, and the rate of voltage change ($|\Delta V/V|$) when exposed to 1%-H_2 was about 0.28%. Next, the temperature dependence in the range of temperature from 50°C to 80°C in increments of 10 °C was evaluated (Fig. 6) and $|\Delta V/V|$ was about 0.24%. This result shows the temperature effect is reduced compared with the single Pt/Ti film. However, $|\Delta V/V|$ with respect to 1%-H_2 also reduced, so it did not improve the temperature effect compared with the hydrogen reaction.

To compensate for the temperature effect more precisely, the resistance temperature coefficient of Pt/Ti films, having a combination of different Pt thickness and Ti thickness, was measured in the temperature range from 50°C to 100°C and the temperature coefficient α was derived from (3) as follows.

$$\alpha = (R_{T2} / R_{T1} - 1) / \Delta T \qquad (3)$$

where R_{T1}, and R_{T2} are the resistance of Pt/Ti film at temperature of T_1 and T_2 respectively, and ΔT is the temperature difference. As shown in Table I, it was found that the temperature coefficient of Pt (10 nm thick)/Ti (20 nm thick) film is almost the same as that of Pt (5 nm thick)/Ti (3 nm thick) film. Therefore, Pt (5 nm thick)/Ti (3 nm thick) film and Pt (10 nm thick)/Ti (20 nm thick) film were suitable for obtaining a sensor that is highly stable to temperature change. The hydrogen sensitivity and temperature dependence of the hydrogen sensor with optimized thickness were evaluated (Figures 7, 8). $|\Delta V/V|$ when exposed to 1%-H_2 was 0.58%. On the other hand, $|\Delta V/V|$ in the temperature range from 50°C to 80°C was 0.039%. Therefore, it was found that the developed

hydrogen sensor can detect hydrogen without the influence of the temperature.

IV. CONCLUSION

A hydrogen sensor of two serially connected Pt/Ti films having different hydrogen sensitivity was developed to measure the output voltage with self-temperature compensation. The developed sensor can detect hydrogen by utilizing the electrical resistance change of Pt thin films, and is operable at room temperature. It was found that the sensitivity of Pt/Ti film to hydrogen mainly depends on the film thickness, because the catalytic reaction occurs primarily on the surface. The temperature coefficient of resistance in Pt/Ti films was evaluated to reduce the temperature effect in the sensor. As a result, the temperature coefficient of Pt (5 nm thick)/Ti (3 nm thick) was found to be almost the same as that of Pt (10 nm thick)/Ti (20 nm thick). By using the combination of the optimized thickness, the new type of hydrogen gas sensor was able to measure the output voltage with stable operation against changes in temperature.

References

[1] K. Tsukada, H. Inoue, F. Katayama, K. Sakai, and T. Kiwa, "Changes in Work Function and Electrical Resistance of Pt Thin Films in the Presence of Hydrogen Gas," Jpn. J. Appl. Phys., no. 51, 2012, p. 015701.

[2] N. Yamazoe, J. Fuchigami, M. Kishikawa, and T. Seiyama, "Interactions of tin oxide surface with O_2, H_2O AND H_2," Surf. Sci., no. 86, 1979, pp. 335-344.

[3] A. Spetz, M. Armgarth, and I. Lundström, "Hydrogen and ammonia response of metalsilicon dioxidesilicon structures with thinplatinum gates," J. Appl. Phys., no. 64, 1988, pp. 1274-1283.

[4] K. Tsukada, T. Yamaguchi, and T. Kiwa, "A Proton Pumping Gate Field-Effect Transistor for Hydrogen Gas Sensor," IEEE Sens. J., no. 7, 2007, pp. 1268-1269.

[5] T. Ymaguchi, T. Kiwa, K. Tsukada, and K. Yokosawa, "Oxygen interference mechanism of platinum-FET hydrogen gas sensor," Sens. Actuators A, no. 136, 2007, pp. 244-248.

[6] K. Tsukada *et al.*, "Dual-Gate Field-Effect Transistor Hydrogen Gas Sensor with Thermal Compensation," Jpn. J. Appl. Phys., no. 49, 2010, p. 024206.

[7] A. S. Ryzhikov *et al.*, "Hydrogen sensitivity of SnO_2 thin films doped with Pt by laser ablation," Sens. Actuators B, no. 107, 2005, pp. 387-391.

[8] J. van Lith *et al.*, "A hydrogen sensor based on tunneling between palladium clusters," Appl. Phys. Lett., no. 91, 2007, p. 181910.

[9] E. Lee, J. M. Lee, J. H. Koo, W. Lee, and T. Lee, "Hysteresis behavior of electrical resistance in Pd thin films during the process of absorption and desorption of hydrogen gas," Int. J. Hydrogen Energy, no. 35, 2010, pp. 6984-6991.

[10] J. Yoon, B. Kim, and J. Kim, "Sensing properties for a microhydrogen sensor with modified palladium film," Sens. Actuators B, no. 187, 2013, pp. 540-545.

[11] K. Tsukada, T. Kiwa, T. Yamaguchi, and K. Yokosawa, "Hydrogen reaction characteristics of FET sensors with catalytic metal gate in high hydrogen concentration," in Proc. 11th Int. Meetiong Chem. Sensors, 2006.

[12] K. Tsukada, S. Takaichi, K. Sakai, and T. Kiwa, "Ultrathin-film hydrogen gas sensor with nanostructurally modified surface," Jpn. J. Appl. Phys., no. 53, 2014, p. 076701.

[13] T. Hübert, L. Boon-Brett, G. Black, and U. Banach, "Hydrogen sensors – A review," Sens. Actuators B, no. 157, 2011, pp. 329-352.

Noninvasive Monitoring of Temperature Distribution in Liquids with Ultrasound by Locally Resolved Measurement of Sound Velocity

M. Wolf, E. Kühnicke

Solid State electronics Laboratory
Technical University of Dresden
Dresden, Germany
Mario.Wolf@tu-dresden.de, Elfgard.Kuehnicke@tu-dresden.de

Abstract — **A new method to measure sound velocity and distance simultaneously and locally resolved is applied in media with continuously changing properties. Instead of using reflectors at known positions the echoes of moving scattering particles are analysed to determine the focus position of an annular array. Systematic deviation between measurements and sound field simulations show that sound propagation has to be described with a modified wave equation. A new approach determining Green's functions for a half space with continuously changing properties is presented. It combines the high frequency approximation with an integral transform method.**

Keywords - Ultrasound: measurement of sound velocity; locally resolved; annular arrays; high frequency approximation; integral transform method

I. INTRODUCTION

A locally resolved monitoring of sound velocity allows estimating locally physical quantities like concentration or temperature or material properties like density or elasticity. This facilitates investigating and optimising many industrial processes, like mixing or chemical reactions, as well as medical therapy like hyperthermia for cancer treatment.

In this contribution, a measurement technique is applied, which allows measuring sound velocity locally resolved using an ultrasound annular array with concentric rings. In contrast to conventional tomographic techniques, it works without any reflectors at known positions. Instead of evaluating different propagation paths, the focusing of the array is varied and the focus position and the sound velocity at the focus point are determined simultaneously by analysing the echoes of moving scattering particles. This is possible because the focus position depends on the sound velocity and the parameters of the used transducer. Therefore, the time of flight to the focus, which is equal to the maximum of the averaged amplitude of the echo signals, is used with calibration curves for the simultaneous determination of sound velocity and focus position.

The examined medium has to contain scattering particles, much smaller than wavelength and in a sufficient low concentration, so that the properties of the propagation medium are not influenced. The emitted wave is reflected at each particle in which the amplitude of the reflected signal is proportional to the amplitude of the incident wave. Therefore the echoes from particles within the focus area are strongest.

As particles are in movement it is possible to consider a uniform distribution of particles in average time. So the averaged echo signal amplitude becomes maximal for that time for flight to the focus and back. In preliminary work, media with constant sound velocity were investigated in-depth and sound velocity was determined with a deviance of less than 1‰ [1] [2]. This was possible because the sound field simulations based on GREEN's functions [3] represented the sound emission from the used array very well. To measure a sound velocity profile a static temperature gradient (heating at the top and cooling at the bottom) was generated in water because the dependence of temperature and sound velocity is well known [4] and can be generated in a stable state. To predict the focus position, the sound propagation was modelled with Fermat's principle calculating curved propagation paths by calculus of variation. But a significant deviation of measurements and simulation had been observed [2].

This contribution introduces a new method for modelling sound propagation in media with continuously changing material parameters. The modified wave equation caused by non-constant material parameters is solved for a point source with an integral transform method and a high frequency approximation. At the current state of this work the equation is solved for a point source in the transformed domain.

This paper is divided in 4 sections. The sound propagation in media with non-constant material properties is discussed theoretically in Section II. Section III shows some measurement results for a linear temperature gradient in water. Section IV gives a summary and perspectives.

II. SOUND PROPAGATION IN MEDIA WITH NON-CONSTANT PROPERTIES

A. Derivation of the wave equation

The sound propagation in liquids is based on two fundamental equations, the equations of motion and elasticity:

$$-\nabla p = \rho \dot{\vec{v}} \,, \qquad \chi \dot{p} = \nabla \vec{v} \,, \qquad (1)$$

with pressure p, particle velocity v, and the material parameters mass density ρ_0 and elasticity χ. If the material parameters are constant, differentiating these equations with respect to location and time leads to the well known wave equation. If these parameters are functions of location an

additional term appears in the derivative of (1) with respect to location. This additional term appears also in the wave equation:

$$\Delta p + \rho_0 \nabla\left(\frac{1}{\rho_0}\right) \cdot \nabla p - \rho_0 \chi \ddot{p} = 0 . \tag{2}$$

Also the definition of potential Φ has to be modified:

$$\vec{v} = \frac{1}{\rho} grad\,\Phi . \tag{3}$$

The following examination shall be done for a one-dimensional dependence of the material properties in direction z.

B. One-dimensional solution

Considering a plane wave propagating in the direction of the gradient of the material properties the wave equation for the potential is obtained

$$\frac{d^2}{dz^2}\Phi + \rho_0 \frac{d}{dz}\left(\frac{1}{\rho_0}\right)\frac{d}{dz}\Phi - \rho_0 \chi \frac{d^2}{dt^2}\Phi = 0 . \tag{4}$$

If the mass density depends linearly on z this equation has a solution in the form of a generalized power series [5]:

$$\Phi = \sum_{n=1}^{\infty} c_n (z - z_0)^{n+K} . \tag{5}$$

However, there are already numerical problems evaluating the coefficients and the solution with respect to the convergence for this one-dimensional case. So it seems not to be feasible finding an exact solution for a two- or three-dimensional problem.

C. High frequency approximation and integral transform

High frequency approximation had been developed in geophysics and is applied in techniques like ray tracing [6]. In this contribution, harmonic GREEN's functions shall be derived with this approach in combination with an integral transform method. This allows calculating a transfer function for a point source for a specific geometry. Just the axially symmetric problem is solved because it is much easier manageable than the general problem. The wave equation in cylindrical coordinates (r, φ, z) is used:

$$0 = \left[\frac{1}{r}\left(\frac{\partial}{\partial r}\left(r\frac{\partial}{\partial r}\right)\right) + \frac{\partial^2}{\partial z^2}\right]\Phi + \rho_0 \frac{\partial}{\partial z}\left(\frac{1}{\rho_0}\right)\frac{\partial}{\partial z}\Phi - \rho_0 \chi \frac{\partial^2}{\partial t^2}\Phi \tag{6}$$

The single derivative to r in the second term vanishes due to its scalar multiplication with the gradient of the mass density, having only a component in z direction. Applying a Hankel transform as described in [7] with respect to r

$$\Phi^{H0}(\xi, z, t) = \int_0^{\infty} \Phi(r, z, t) J_0(j\omega \xi r) r dr \tag{7}$$

leads to an one-dimensional wave equation in the transformed domain, which is denoted by the index $H0$:

$$0 = \frac{d^2}{dz^2}\Phi^{H0} + \rho_0 \frac{d}{dz}\left(\frac{1}{\rho_0}\right)\frac{d}{dz}\Phi^{H0} + \xi^2 \omega^2 \Phi^{H0} + \rho_0 \chi \frac{\partial^2}{\partial t^2}\Phi^{H0} \tag{8}$$

The high frequency approximation assumes that (8) can be solved with the following ansatz

$$\Phi = A(x, z) e^{j\omega(t - T(x,z))} . \tag{9}$$

Now, Φ is replaced with this ansatz and the terms are arranged according to its powers of ω.

$$0 = A\left[\omega^2\left[\rho_0\chi - \left[\frac{dT}{dz}\right]^2 - \xi^2\right]\right] - ...$$
$$j\omega\left[\frac{d^2T}{dz^2} + 2\frac{1}{A}\frac{dA}{dz}\frac{dT}{dz} + \rho_0\frac{d}{dz}\left(\frac{1}{\rho_0}\right)\frac{dT}{dz}\right] ... \tag{10}$$
$$... + \rho_0\frac{d}{dz}\left(\frac{1}{\rho_0}\right)\frac{dA}{dz} + \frac{d^2A}{dz^2}$$

Assuming that ω is very high the first two lines are equated to zero independently and the frequency-independent third line is neglected. So T can be determined directly from the first line and with this solution A is determined from the second line

$$T(\xi, z) = \pm \int_{z_0}^{z} \sqrt{\rho_0(z)\chi(z) + \xi^2}\, dz . \tag{11}$$

$$A(\xi, z) = A_0 \sqrt{\frac{(\rho_0(z_0)\chi(z_0) - \xi^2)\rho_0(z)}{(\rho_0(z)\chi(z) - \xi^2)\rho_0(z_0)}} . \tag{12}$$

with the solely free parameter A_0. Note that this leads to the solution for a homogeneous medium if ρ and χ are constants. All methods of generalized ray theory explained in [7] like the derivation of source functions for a point source acting on an interface considering the boundary conditions can be applied to this solution. Finally, the inverse transformation has to be done:

$$\Phi(r, z) = -\omega^2 \int_0^{\infty} A(\xi, z) e^{j\omega(t - T(\xi, z))} J_0(j\omega\xi r)\xi d\xi . \tag{13}$$

Current work is on an evaluation of this integral with a steepest descent approximation as it is described in [3]. The approximation facilitates the integral into a solvable form. This causes a neglect of surface waves being not of interest for the presented application. However, the method is complicated because of the integral expression of T in the exponent. Though, the integral can be evaluated by a finite series expansion resulting in additional terms containing higher powers of ξ.

III. MEASUREMENT RESULTS

An evident way to achieve a sound velocity gradient is to generate a temperature gradient with water, because the sound velocity as a function of temperature is well known for water [4] and it can be generated in a stable state. Figure 1

shows the general set-up. Water in a basin located at the bottom is kept at a temperature of 6°C. A second smaller basin is placed above. It contains a metal plate at its bottom for good thermal conduction and a heat source at its top. This generates a vertical layered arrangement of warm water above cooler water, whereby a fluid flow is avoided. The temperature is measured by an array of temperature sensors to determine the sound velocity profile in the experimental set-up. The sound field for this gradient and the time of flight to the focus point were calculated applying Fermat's Principle [2].
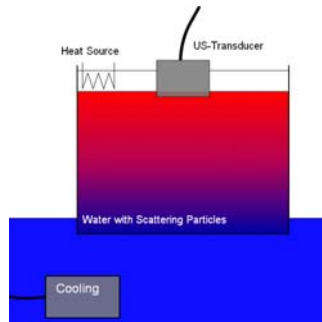
Figure 1: Experimental set-up for a sound velocity gradient

Figure 2 shows the comparison of calculated and measured times of flight to the focus as a function of used set of delay times, corresponding with a focus point (*Fok*) in the calibration medium water of 20 °C (Sound velocity gradient in water from 40 °C at the transducer to 6 °C at a distance of 50 mm).
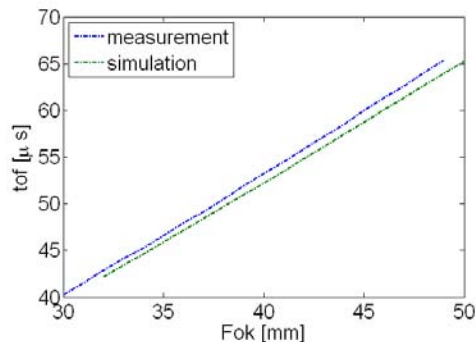
Figure 2: Comparison of measured and calculated times of flight as a function of used set of delay times

Although the notable difference is just in the range of one microsecond this would cause an error of more than 100 m/s determining the sound velocity.

For additional examinations, the sound velocity was measured conventionally via measuring the time of flight to a reflector at a known position. Moving the reflector along the acoustic axis allows a stepwise reconstruction of the sound velocity profile. Additionally sound velocity was determined from temperature sensors again. Figure 3 shows a comparison of two conventional methods to determine the mean sound velocity between the probe and a reflector at distance z. First the time of flight for different reflector distances is measured (blue line). Second the temperatures are measured at different locations and converted to a sound velocity according to [4] and averaged over the propagation path (green line). The systematic deviation can be seen here, too.
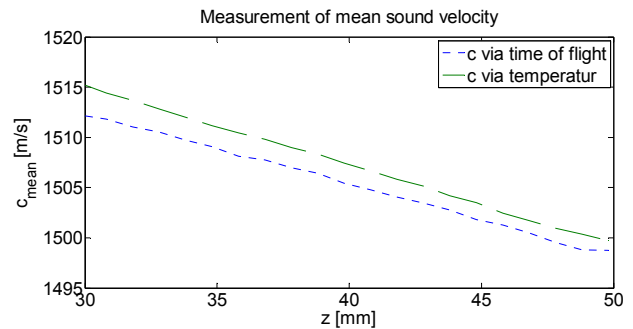
Figure 3: Comparison of two conventional methods to determine the mean sound velocity between the probe and a reflector at distance z

Both deviations (see Figures 2 and 3) result from the deficient assumption that wave propagation can be described with the wave equation for homogeneous media.

IV. SUMMARY AND PERSPECTIVE

This contribution discusses a method to measure the sound velocity along the acoustic axis of the used annular array. The three-dimensional distribution of sound velocity is obtained by scanning.

It has been shown that the continuous change of material properties has to be taken into account for the modelling of sound propagation. The potential of a point source has been calculated in the Hankel transformed domain. The inverse transform is actually realized and will allow calculating GREEN's functions for media with continuously changing properties.

Due to the assumed change of material properties in only one dimension a change of these properties in other dimensions would cause a lateral deviation of the focus position. This effect has to be examined in further works.

REFERENCES

[1] M. Lenz, M. Bock, E. Kühnicke, J. Pal, and A. Cramer, Measurement of the sound velocity in fluids using the echo signals from scattering particles, Ultrasonics, ULTRAS-D-11-00034.

[2] M. Wolf, E. Kühnicke, and M. Lenz, "Modelling of sound propagation in media with continuously changing properties towards a locally resolved measurement of sound velocity," Ultrasonics Symposium (IUS), IEEE International 21-25 July 2013, vol., no., pp.1045-1048.

[3] E. Kühnicke, "Plane arrays – Fundamental investigations for correct steering by means of sound

field calculations", Wave Motion, Volume 44, Issue 4,

[4] W. Marczak, "Water as a standard in the measurements of speed of sound in liquids." J. Acoust. Soc. Am. 102(5) 1997, pp. 2776–2779.

[5] L. Fuchs: "Zur Theorie der linearen Differentialgleichungen mit veränderlichen Coefficienten." In: Journal für die reine und angewandte

March 2007, pp. 248-261, ISSN 0165-2125. Mathematik 66 (1866), p. 121.

[6] V. Cerveny, Seismic Ray Theory, Cambridge University Press, 2005, p. 724.

[7] Y.H. Pao and R.R. Gajewski: The generalized ray theory and transient responses of layered elastic solids, Physical acoustics, 1977 - Academic, New York.

Numerical Model of Piezoelectric Lateral Electric Field Excited Resonator as Basic Element of Acoustic Sensors

Teplykh A. A, Zaitsev B. D.

Saratov Branch of Institute of Radio Engineering and
Electronics nm.V.A.Kotelnikov RAS
SB IRE nm.V.A.Kotelnikov RAS
Saratov, Russia
e-mail: teplykhaa@mail.ru

Kuznetsova I. E.

Institute of Radio Engineering and Electronics
nm.V.A.Kotelnikov RAS
IRE nm.V.A.Kotelnikov RAS
Moscow, Russia
e-mail: kuziren@yandex.ru

Abstract —Nowadays, piezoelectric lateral electric field excited resonators are frequently used for development of various acoustic sensors. But, the adequate theory of such resonators is absent. In this paper, the numerical method of calculation of characteristics of the acoustic oscillations in the piezoelectric lateral electric field excited resonators is developed. The developed method is based on the finite element analysis and allows computing the distribution of the components of the mechanical displacement in the piezoelectric plate and electric potential in the piezoelectric plate and surrounding vacuum at arbitrary frequency of the exciting field. This method allows setting various boundary conditions on various parts of a plate surface, including a condition of mechanical damping of oscillations. This allows calculating the frequency dependence of the real and imaginary parts of the electrical impedance/admittance of the resonator. We analyzed a piezoelectric lateral electric field excited resonator, which is based on a 0.5 mm-thick X-cut lithium niobate plate. Two infinitesimally thin metallic electrodes with width of 5 mm were deposited on top side of the plate. The electrodes were deposited in such a way that the lateral field was oriented along the crystallographic Y-axis. Calculations of electric impedance were carried out for various values of a gap in range 1 - 3 mm between electrodes. These results are in quantitative agreement with experimental data. A brief description of experimental set up is also presented.

Keywords - acoustic resonator; lateral exciting field; finite element analysis; lithium niobate;

I. INTRODUCTION

At present time researchers pay particular attention to the piezoelectric lateral electric field excited resonators because of development of various acoustoelectrical sensors. One of the main problems of the design of such devices is the suppression of undesirable acoustic oscillations and ensuring a high Q-factor of the resonator. Currently, this problem is solved experimentally [1][2] by selection the optimal shape of the electrodes and choosing the area of coverage of the damping coating. However, this process requires a creation of a large amount of experimental samples. Researchers can theoretically estimate the efficiency of such resonators using the Christoffel - Bechmann method, which allows computing the electromechanical coupling coefficient for bulk waves excited by a lateral electric field [3][4]. However, this method does not take into account the finite aperture of the excited waves. Therefore, the problem of more accurate

theoretical calculation of characteristics and efficiency of such resonators is considered as urgent.

In this paper, we developed a method for calculating the acoustic oscillations and the accompanying electric field in resonator representing a thin plate of a piezoelectric material with two rectangular electrodes on one side. The developed method is based on the finite element analysis and allows us to find the distribution of components of the mechanical displacement in the piezoelectric plate and electric potential in the piezoelectric plate and its surrounding vacuum at a certain oscillation frequency of the exciting field. This method takes into account the different boundary conditions on different areas of the resonator surface, and in particular, the mechanical damping of the parasitic oscillations, which was used in the [1][2].

In Section II, we give the description of the numerical model of resonator. In Section III, we describe the experimental set up. In Section IV, we make the comparison of theoretical and experimental frequency dependencies of real and imaginary parts of electrical impedance of lateral electric field excited resonator. Finally, Section V presents the conclusions and the future research.

II. THE DESCRIPTION OF NUMERICAL MODEL

In this paper, we consider a piezoelectric plate limited in x and y directions (Figure 1). There are different boundary conditions on different parts of plate surface. Value of time-varying electric potential is given on an infinitely thin electrodes *e1* and *e2*. The gap between electrodes is *G*. Special mechanical boundary conditions are specified on areas *d1* and *d2*. The rest of plate surface is assumed mechanically and electrically free. In the z direction, the plate and electrodes assumed to be unlimited.

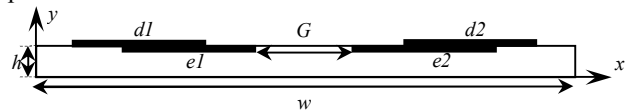Figure 1.   The geometry of the problem

So, we need to find a distribution of mechanical displacements within the plate, as well as the electric potential distribution inside the plate and in the surrounding vacuum. Exciting electric field varies according to harmonic law with a frequency of ω. Since there is no other sources of vibration excitation the solution must also be time-harmonic

with frequency ω. Thus, this problem may be represented as a system of differential equations [5]:

$$L(u_i, \varphi) - f = 0 \qquad (1)$$

where L is a differential operator, u_i is the mechanical displacement components, $i=1..3$ and φ is the electric potential. So, we need to find functions $u_i(x, y)$ and $\varphi(x, y)$, which satisfy (1). In this work this problem was solved by using the Galerkin's method [5]. For existence and uniqueness of the problem solution of (1), the boundary conditions must also be specified. As electrical boundary conditions, we used the given values of φ on the electrodes *e1* and *e2* and continuous of potential on the rest of boundary. The mechanical boundary conditions are more difficult to formulate properly. In our experiments with the resonator with a lateral field [1][2], the space around the electrodes and partly electrodes were covered with an absorbing varnish. This was done to suppress unwanted vibration modes of the plate and improve the quality of the resonator.

To take into account this fact in the theoretical model of the resonator, the mechanical boundary conditions were formulated as follows. On the surface of piezoelectric plates, except for regions *d1* and *d2*, the mechanical boundary condition is the absence of the normal components of the stress:

$$T_{ij} n_j = 0. \qquad (2)$$

In regions *d1* and *d2*, where the damping coating was applied, the boundary condition is written as:

$$T_{ij} n_j = i\omega Z_{ij} u_j. \qquad (3)$$

Here, T_{ij} is the tensor of mechanical displacement of piezoelectric plate, n_j is the surface normal, ω is the oscillation frequency, Z_{ij} is the acoustic impedance of damping coating, u_j is the mechanical displacement. This boundary condition is obtained as a generalization of the well known relationship [6] from fluids to anisotropic solids

$$p = Zv. \qquad (4)$$

Here, p is the acoustic pressure, v is the oscillation velocity. When $Z_{ij} \rightarrow 0$, this condition becomes the condition of the free surface $T_{ij} n_j = 0$, while $Z_{ij} \rightarrow \infty$ this condition becomes the condition of rigidly fixed surface $u_j = 0$. In the present case $Z_{ij} = Z\delta_{ij}$ where Z is the acoustic impedance of varnish.

III. THE DESCRIPTION OF EXPERIMENTAL SET UP

In order to compare the theoretical results with experimental data, the lateral electric field excited resonator on X-cut lithium niobate plate was made [2]. The scheme of this resonator is presented in Figure 2. The shear dimensions and thickness of plate were equal 18×18 mm^2 and 0.5 mm, respectively. Two 200 nm – thick aluminum rectangular electrodes with dimensions of 5×10 mm^2 were deposited on one side of the plate through a special mask in vacuum. The electrodes were deposited in such a way that the lateral field was oriented along the crystallographic Y-axis (Figure 2). This field component excited a longitudinal acoustic wave reflected between the plate sides with the largest electromechanical coupling coefficient [1]. The gap G between electrodes was equal to 1 mm. The area around the electrodes and part of electrodes with width of 3 mm were

coated with a damping layer of absorbing varnish with thickness of about 0.2 mm.
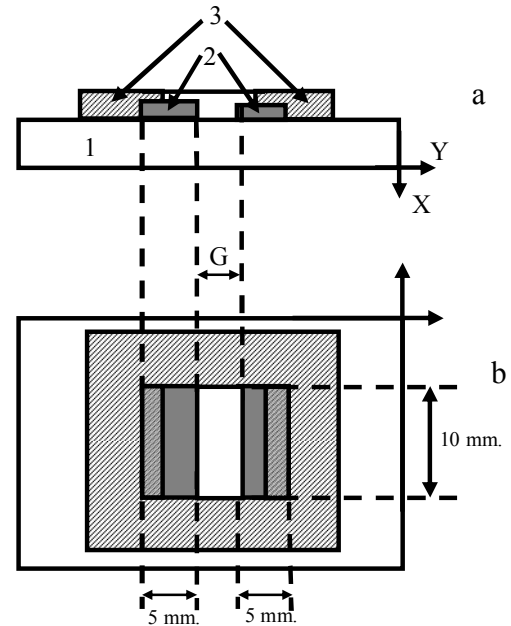
Figure 2. The side (a) and top (b) views of the resonator with the lateral exciting electric field: X – cut lithium niobate plate -1, electrodes -2, and absorbing coating - 3.

The frequency dependences of the real and imaginary parts of electric impedance of resonator were measured using the LCR meter (4285A, Agilent Technologies Inc.). These dependences for pointed above resonator are presented in Figure 4 by dashed lines.

IV. THE COMPARISON OF THE THEORETICAL AND EXPERIMENTAL RESULTS

In accordance with experiment, the calculation was performed for the case when the thickness h and width w of the plate were equal to 0.5 mm and 18 mm, respectively (Figure 1). On the upper surface of the plate, two electrodes *e1* and *e2* were deposited. The lateral electric field was oriented along the crystallographic Y-axis. The width of each electrode *e1* and *e2* was equal to 5mm with the gap G between them of 1 mm. The width of damping regions *d1* and *d2* was of 5 mm and the regions of overlap (*d1-e1*) and (*d2- e2*) were fixed to 3 mm.

Since the above-described method of calculation allows us to find the distribution of all variables and their derivatives for any given frequency, it was possible to build electrical impedance depending on the frequency of this resonator and compare them with experiment. So, we calculated the distribution of the acoustic field and the electric potential in the range f = 6-7 MHz. It is clearly seen in Figure 3 that the maximum amplitude of the acoustic vibrations are located in the gap between the electrodes. These oscillations correspond to the longitudinal bulk acoustic wave propagating in the vertical direction between the boundaries of the plate. This wave is the cause of deep

resonance on frequency dependence of the electrical impedance [1][2] shown on Figure 4.

The theoretical value of the impedance is calculated in accordance with the formula:

$$Z = (\varphi_2 - \varphi_1) / J , \qquad (5)$$

Here, $\varphi_2 - \varphi_1$ is the potential difference between electrodes, J is the displacement current:

$$J = \int_S \frac{\partial D}{\partial t} ds \qquad (6)$$

This integral is taken over the both top and bottom surfaces of the electrode. The calculated frequency dependencies of real and imaginary parts of electrical impedance are presented by solid lines in Figure 4. The material constants of lithium niobate were taken from [7].
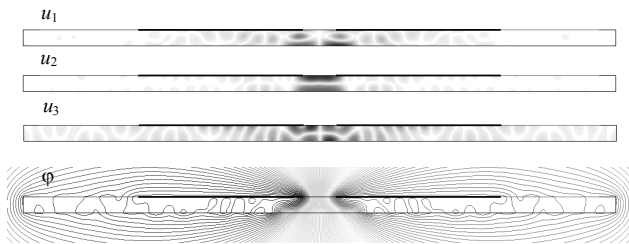
Figure 3. Distribution of the components of mechanical displacement and electric potential in resonator excited by electric field at frequency 6.55 MHz
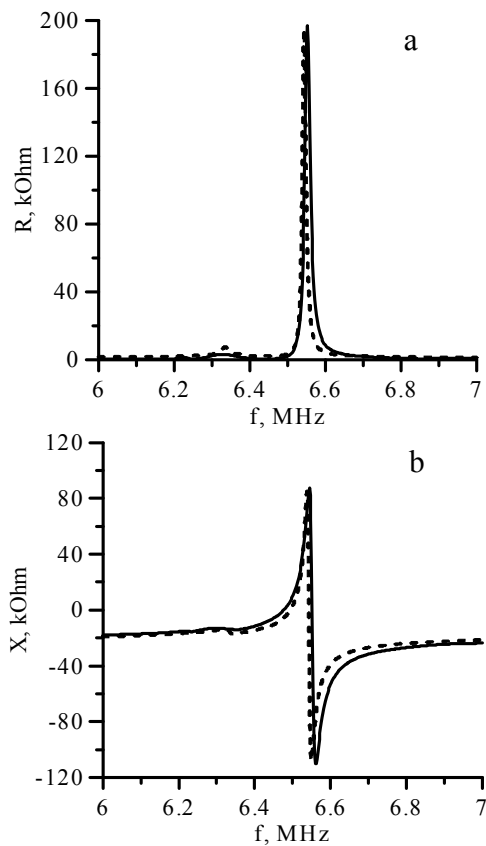
Figure 4. Theoretical and experimental value of the real (a) and imaginary (b) components of the electrical impedance of the resonator with a 1mm gap between the electrodes. Solid line is theory, dashed line is experiment.

One can see from Figure 4 that a good agreement exists between theoretical and experimental dependencies. Therefore, the difference between values of resonant frequency does not exceed 15 kHz. A slightly bigger distinction in absolute values of X is explained by the parasitic electric capacity of the device, which has not been considered in calculation. Moreover, the used material constants taken from [7] may differ from actual ones in the range ±5% (standard error for modern technology of crystal growing process).

V. CONCLUSION

The obtained results have shown the adequacy of the developed method for the characteristics calculation for resonators excited by a lateral electric field. These results will be used in future to develop sensors of fluid properties.

REFERENCES

[1] B. D. Zaitsev, I. E. Kuznetsova, A. M. Shikhabudinov, and A. A. Vasiliev, "The research of the piezoelectric crystal resonators with the lateral field excitation" in Proc. IEEE Int. Ultrasonics Symp., 2010, pp. 946–949.

[2] B. D. Zaitsev, I. E. Kuznetsova, A. M. Shikhabudinov, A. A. Teplykh, and I. A. Borodina, "The study of Piezoelectric Lateral-Electric-Field-Excited Resonator" in IEEE TUFFC, 2014, vol.61, no. 1, pp.166-172.

[3] D. F. McCann, J. M. McGann, J. M. Parks, D. J. Frankel, M. Pereira da Cunha, and J. F. Vetelino, "A Lateral-Field-Excited LiTaO$_3$ High Frequency Bulk Acoustic Wave Sensor" in IEEE TUFFC, 2009, vol. 56, no. 4, pp. 779–787.

[4] T. G. Leblois and C. R. Tellier, "Design of new Lateral Field Excitation Langasite Resonant Sensors" in Proc. IEEE Int. Ultrasonics Symp., 2009, pp. 2672–2675.

[5] L. Segerlind, Applied Finite Element Analysis. Second Edition. John Wiley & Sons, Inc. 1984.

[6] E. Skudrzyk, The Foundation of Acoustics. Basic Mathematics and Basic Acoustics. Springer-Verlag, 1971.

[7] G. Kovacs, M. Anhorn, H. E. Engan, G. Visintini, and C.C.W Ruppel, "Improved material constants for LiNbO3 and LiTaO3" in IEEE IUS Proceedings, 1990, vol.1, pp. 435-438.

Control of Ultrasonic Acoustic Fields by
Multiple Acoustic Waveguides and Piezoelectric Transducers

－ Simulation of 2D Acoustic Fields －

Shigeru Igarashi

Department of Electronic and Information
Polytechnic University
Kodaira-shi, Japan
E-mail: Igarashi.Shigeru@jeed.or.jp

Sinichi Takeuchi

Graduate School of Engineering
Toin University of Yokohama
Yokohama-shi, Japan
E-mail: shin1@toin.ac.jp

Abstract—**We propose a system for generating and controlling an ultrasonic acoustic field using multiple acoustic waveguides and piezoelectric transducers. This system can be used as a high-power ultrasonic source for nonlinear calibration of hydrophones. In the system, ultrasonic waves are emitted from multiple transducers with controlled transmission delays, and the acoustic power is increased through acoustic waveguides before being output, this allows synthesis and control of ultrasonic acoustic fields. We simulate the proposed system as a two-dimensional acoustic field in which the computed output sound pressure determines the basic shape of the acoustic waveguide. The proposed system of five transmitting transducers and five acoustic waveguides was compared with a single transmitting transducer, and the results showed a peak sound pressure of 1.5-fold increase value at the same beam width.**

Keywords-Acoustic waveguide; Piezoelectric transducer; Ultrasonic acoustic field; Nonlinear calibration; 2D acoustic field simulation.

I.   INTRODUCTION

In recent years in medicine, high-intensity focused ultrasonic fields have been used in many ways: for cancer treatment, including acoustic chemotherapy (sonodynamic therapy), for sonoporation to facilitate gene transfer, in ultrasonic elastography to image the hardness of soft tissues and organs by measuring acoustic radiation pressure, and in harmonic imaging methods that utilize harmonics for diagnosis. In industry, too, the use of high-intensity ultrasonic fields is increasing in applications such as ultrasonic cleaners and ultrasonic dispersers. In response to this growing use, the Consultative Committee for Acoustics, Ultrasonic, and Vibrations, was established in 1998 as part of the International Bureau of Weights and Measures. In addition to this, between 1999 and 2002 a pilot program of the Germany Engineering Physics Institute studied ultrasonic power, and hydrophone reception sensitivity was studied between 1999 and 2003 under a pilot program of the UK National Physical Laboratory [1]. Japan joined this effort in 2002, when the National Metrology Institute of Japan began development of measurement standards for ultrasonic.

Measurement standards for ultrasonic power of up to 15 W have been established using the acoustic balance method and standards for powers up to 100 W that use calorimetry are under development. Measurement standards for hydrophone reception sensitivity in the range 0.5–20 MHz are complete, and standards are under development for sensitivities outside of this range [1]. For ultrasonic power in particular, a source that can generate ultrasonic waves in the megahertz band at 100 W or more is needed. As ultrasonic of increasingly higher intensity is demanded in medicine, the desired acoustic fields exceed the region of linear increase, becoming nonlinear. For this reason, it is expected that nonlinear calibration and evaluation will be needed more often. Therefore, it is necessary to develop a robust hydrophone that can accommodate the spatial distribution of a powerful ultrasonic field [2], at the same time, it is necessary to develop a method to transmit high-intensity ultrasonic power.

Many previous studies have examined properties of acoustic waveguides: dispersion [3] and sound pressure profiles [4] in cylindrical waveguides, sharp bending of surface sound waves through photonic crystal waveguides [5][6], representations of acoustic waveguides with distributed transmission lines by scattering matrices [7], and ways to increase the sound pressure in a solid waveguide [8]. Additionally, one study details a patent for an ultrasonic source that can transmit ultrasonic waves along a fiber or rod [9]. Also recently, applications using acoustic waveguide are as follows: ultrasonic cleaning machine using the ultrasonic waveguide tube for reduce damage of the LSI pattern [10], structural health monitoring and nondestructive evaluation of inaccessible adhesively bonded joints using ultrasonic guided waves propagation across waveguide [11], the coiled stator ultrasound motor (CS-USM) using a closed-loop-type acoustic waveguide made from SUS304 [12], and microscopic images of tissue using a thin acoustic waveguide made from a fused quartz fiber [13].

Here, we propose a system for controlling an ultrasonic acoustic field by using multiple acoustic waveguides and piezoelectric transducers. We investigate the suitability of

the system for use as a high power ultrasonic source by numerical simulation of a two-dimensional acoustic field.

The paper is structured in 5 sections. In Section II, we describe an overview of our proposed system. In Section III, we describe the basic conditions of 2D acoustic field simulation. In Section IV, we describe the two-dimensional model, and the simulated spatial distribution, peak acoustic pressure for our proposed system using multiple acoustic waveguides. Section V presents the conclusions and future works.

II. OVERVIEW OF THE SYSTEM

To generate high-intensity ultrasonic waves with a single transducer, it is typical to increase the power of the ultrasonic wave by applying a higher voltage to the electrodes of the piezoelectric element, but this increases the risk of deterioration or destruction of the piezoelectric element by increased temperature, such as that due to high voltage. Also, although focusing the beam of the transducer may yield the desired ultrasonic power at the focus, quantitative evaluation becomes difficult because the produced wave is no longer a plane wave. Figure 1 shows the model of the system proposed for generating high-power ultrasonic by using acoustic waveguides.
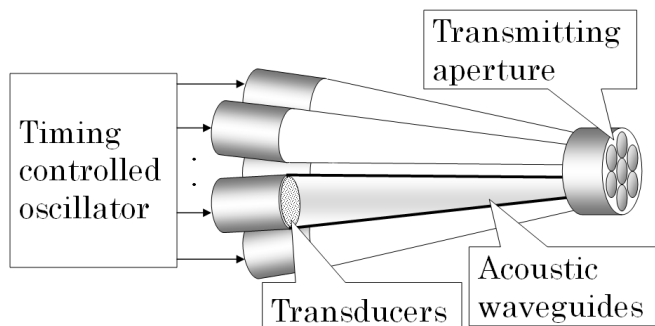
Figure 1.   Ultrasonic source system using multiple acoustic waveguides and piezoelectric transducers.

After ultrasonic waves are generated by some of the transducers and the sound pressure of each ultrasonic wave is increased by the acoustic waveguides, the outputs of the ultrasonic point sources on the transmit aperture surface are formed into a beam by Huygens' principle. In this way, a high-power sound source can be constructed without increasing the output from any single transducer. However, because the beam is formed from the point sources, it is important to control the amplitude, frequency, and phase of the ultrasonic waves that are generated by each of the transducers.

III. 2D ACOUSTIC FIELD SIMULATION

The Wave2000 (Cyberlogic Inc.) package was used for simulation. Wave2000 is a two-dimensional simulator that uses the finite difference method [14], a two-dimensional displacement distribution is produced in which the relative brightness represents the magnitude of the positive and negative displacements. Because of this, the data about displacement are all magnitudes. As the basic conditions of the simulation, a transmitting ultrasonic wave is assumed at a longitudinal wave continuous frequency of 1 MHz and amplitude of 1 [a.u.]. The acoustic medium is water (temperature: 25 °C, speed of sound: 1497 m/s, acoustic characteristic impedance: 1.497 MRayl), and the wavelength of ultrasonic wave to be transmitted is 1.5 mm. Acoustic waveguides are constructed from a boundary of air (temperature: 20 °C, speed of sound: 344.0 m/s, acoustic characteristic impedance: 0.427 kRayl) that is 0.2 mm thick. To investigate the sound pressure distribution of the acoustic field, a 0.3-mm wide receiving transducer was aligned along the central axis direction or the lateral direction, and the peak–peak amplitude of the sound pressure waveform was plotted as a relative sound pressure.

A. Sound pressure characteristics according to length of the acoustic waveguide

In this system, it is necessary to have transmitting aperture width of 1.5 ~ 3.0 mm for beam forming. After this, following the model of Figure 2, we simulate the sound pressure at x mm away point on the center axis from the transmitting aperture plane for both transmitter and waveguide widths of d = 1.5, 2.0, 2.4, and 3.0 mm and waveguide length L mm of the acoustic waveguide.
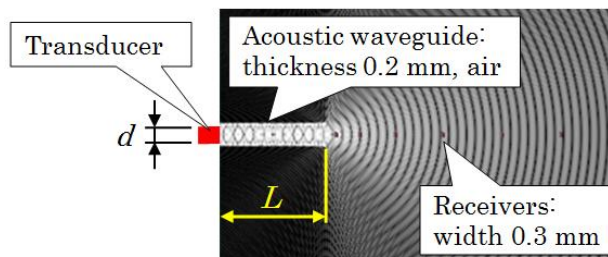
Figure 2.   Model for the sound pressure characteristic using an acoustic waveguide.
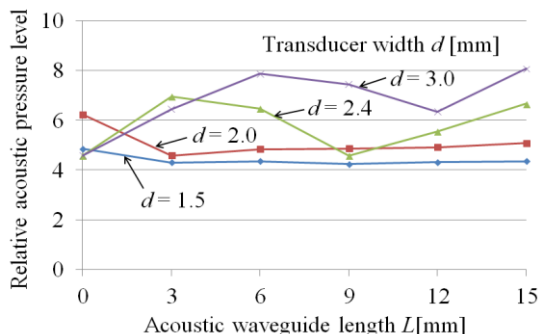
Figure 3.   Sound pressure characteristic due to acoustic waveguide (x = 30 mm).

The results at 30 mm away point are shown in Figure 3. At a transmitter width of 1.5 mm, the sound pressure becomes a constant that is independent of the length. At larger widths, it was found that the sound pressure is changed by the length.

B. Sound pressure characteristics due to bending of acoustic waveguide

To construct a system of transmitting transducers, it is necessary to bend the acoustic waveguide. As shown in Figure 4, two acoustic waveguides, each 6 mm in length, and the transmitting transducers moved from the center axis by offsets y_0 = 0.0, 0.5, 1.0, 1.5, 2.0, and 2.5 mm, simulate the sound pressure at x mm away point from the transmitting aperture plane for both transmitter and waveguide widths of d = 1.5, 2.0, and 2.4 mm.
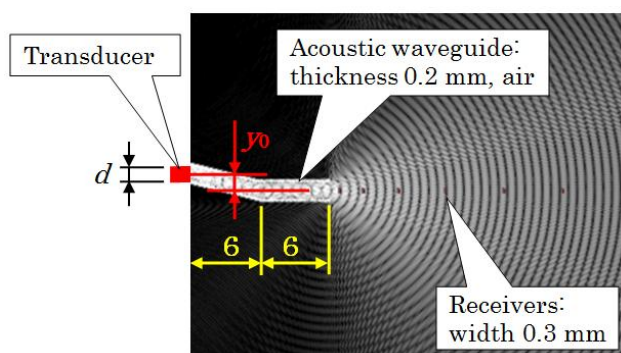
Figure 4.   Model for bending acoustic waveguide.
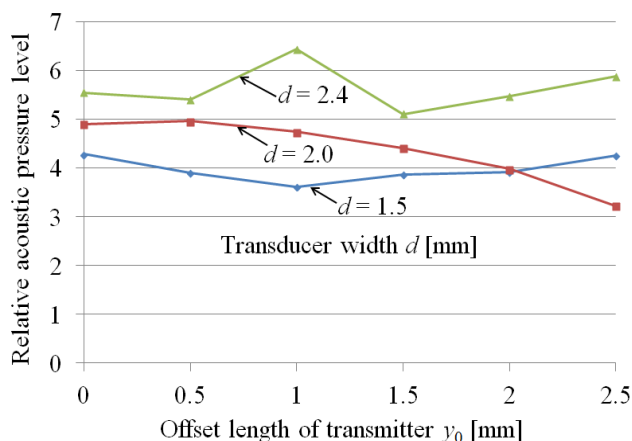
Figure 5.   Sound pressure characteristics due to bending of acoustic waveguide (x = 30 mm).

The results at 30 mm away point are shown in Figure 5. When the acoustic waveguide is focused on a 1.5 mm wavelength, it is seen that bending of the acoustic waveguide is possible.

C. Sound pressure characteristics due to focusing of acoustic waveguide

Next, waves are focused by an acoustic waveguide, as shown in Figure 6, where the acoustic waveguide runs straight from the transmitting transducer (12 mm in width). The end of waveguide is connected to an acoustic waveguide 1.5 mm in width and 6 mm in length. For lengths L of the focusing acoustic waveguide in the range 30–51 mm, the sound pressures at points along the center axis from the transmitting aperture plane of the acoustic waveguide are calculated.
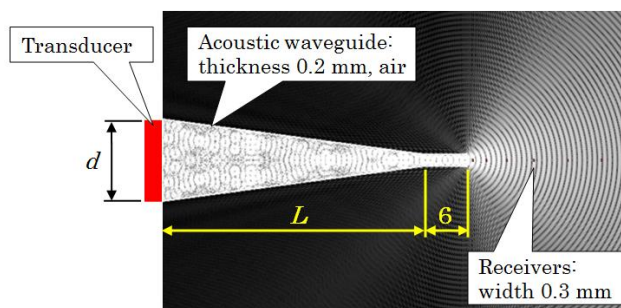
Figure 6.   Model for focusing acoustic waveguide.
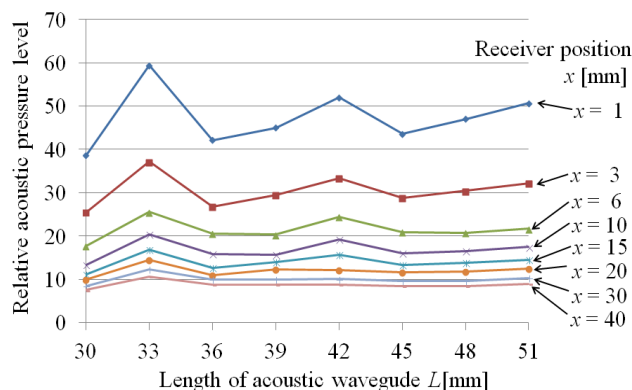
Figure 7.   Sound pressure characteristics due to focusing of acoustic waveguide.

The results are shown in Figure 7. The sound pressure level is increased at 33 mm and at 42 mm.

IV.   ULTRASONIC ACOUSTIC FIELDS USING MULTIPLE ACOUSTIC WAVEGUIDES

Figure 8 shows a two-dimensional simulation model of the proposed system by multiple acoustic waveguides and piezoelectric transducers. This system is composed of five transmitting transducers and five acoustic waveguides. The apertures of the acoustic waveguides vary from 12 mm to 1.5 mm along 42 mm of length to provide focus. For comparison, a single transducer must be 12 mm in width with a 2.4-mm aperture to obtain the equivalent of a 12-mm aperture arranged among the five acoustic waveguides. Because the inner and outer path lengths of each acoustic

waveguide are different, the beam is formed by delaying transmission from the transducers by 0.83, 0.27, 0.00, 0.23, and 0.90 μs, this delay happens in order from the top of the system. Distances to the transmitting aperture through each acoustic waveguide from each transducer are different. Therefore, for arrival of ultrasonic waves transmitted from each transducer at the transmitting aperture of the waveguide simultaneously, each transmission delay time was adjusted.
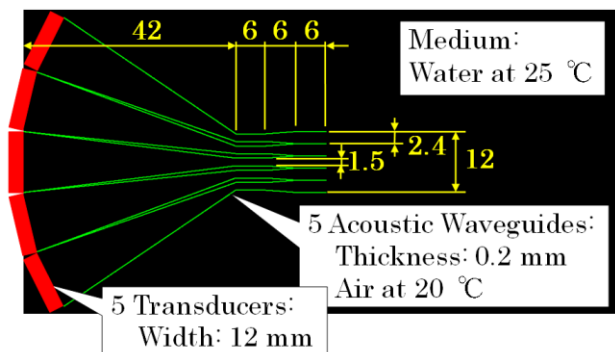
Figure 8. Two-dimensional simulation model of the proposed system.

Figure 9 shows the two-dimensional distribution of displacement by a single transducer. Figure 10 shows the same structure with the proposed system. These data show that the distribution of displacement by the single-transducer system and the proposed system are similar to each other at 60 mm away.
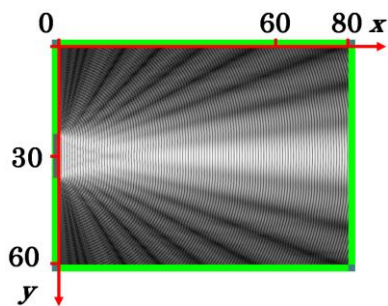
Figure 9. Spatial distribution of displacement with a single transducer (absolute value).
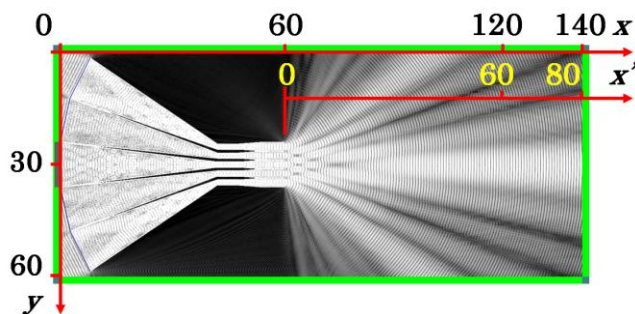
Figure 10. Spatial distribution of displacement with the proposed system (absolute value).

To quantitatively evaluate the results with the aim of determining the center pressure distributions, data from the proposed system at beyond 60 mm are overlaid with data from the single-transducer system. The results are shown in Figure 11.
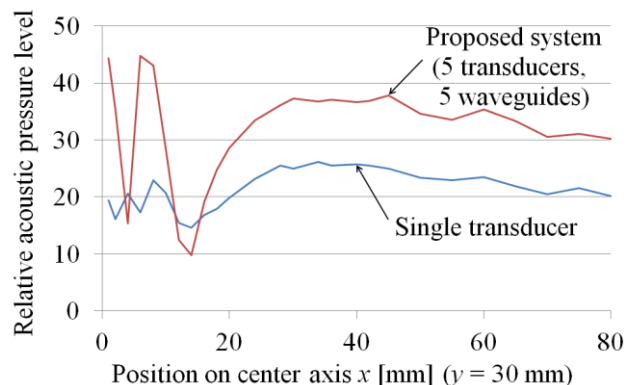
Figure 11. Comparison of the center sound pressure.
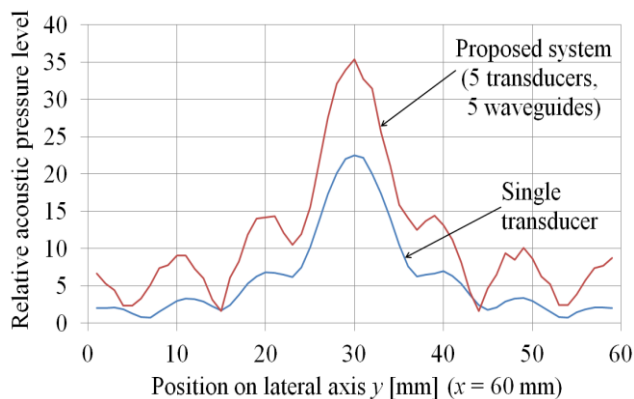
(a) Comparison of peak sound pressure.
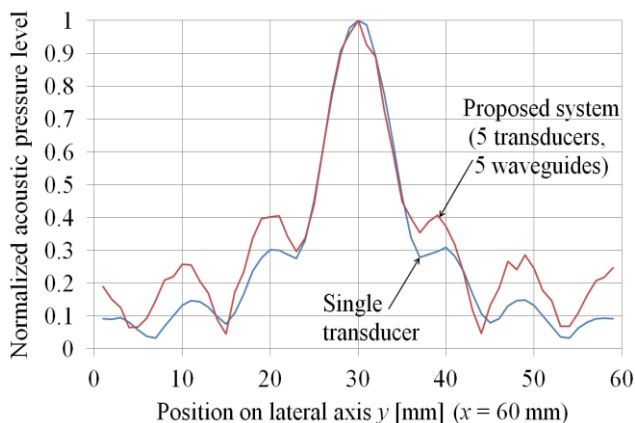
(b) Comparison of beam width of normalized sound pressure.

Figure 12. Lateral sound pressure distribution at 60 mm on the central axis.
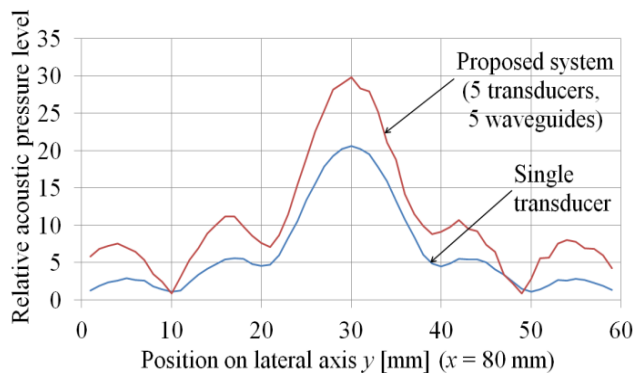
(a) Comparison of peak sound pressure.
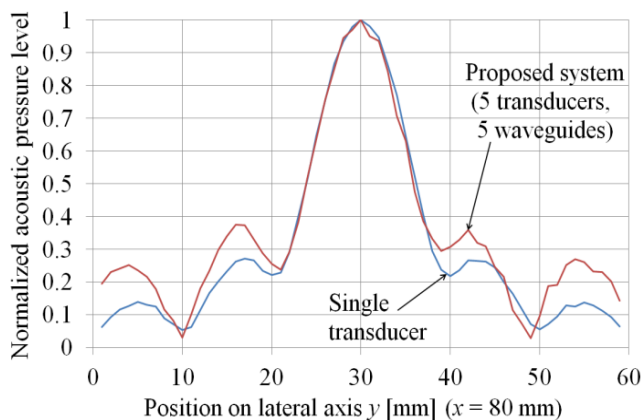
(b) Comparison of beam width of normalized sound pressure.

Figure 13. Lateral sound pressure distribution at 80 mm on the central axis.

Next, we simulated the sound pressure distribution in the lateral direction. Figure 12 shows the results of comparison between the proposed system and a single transducer at distance 60 mm from the transmitting aperture. Figure 12 (a) can compare the peak sound pressure levels each other. Figure 12 (b) can be comparison of beam width of normalized sound pressure.Figure13 shows the results of comparison of the same, at distance 80 mm from the transmitting aperture.

TABLE I. EVALUATION OF SOUND PRESSURE DISTRIBUTION IN THE LATERAL DIRECTION

Distance x [mm]	Relative peak acoustic pressure [a.u.]	Increase factor	-6 dB beam width [mm]
60	$P_{55} = 35.34$	$P_{55} / P_{10} = 1.57$	9.4
	$P_{10} = 22.46$		9.6
80	$P_{55} = 29.82$	$P_{55} / P_{10} = 1.44$	12.0
	$P_{10} = 20.64$		12.2

P_{55}: 5 transducers, 5 waveguides, P_{10}: 1 transducer, non-waveguide

The results at 60 and 80 mm from the transmitting surface are analyzed for a –6 dB beam width, and the rate of increase in peak–peak sound pressure is calculated. The results are shown in Table I. An 1.5-fold (resp., 1.4-fold) increase of peak sound pressure is seen at 60 mm (resp., 80 mm), and the –6 dB beam width is almost equal between systems. But it was found from the graph of the normalized acoustic pressure level in Figures 12 and 13, that the increase factors of peak side lobe pressure are about 1.3 to 1.4.
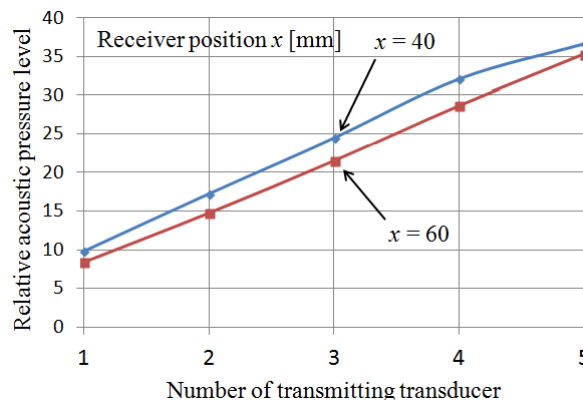
Figure 14. The relationships between maximum sound pressure levels and number of transmitting transducers.

In our proposed system, when changing the number of adjacent active transmitting transducer, we simulated the maximum sound pressure at the receiving position 40 mm and 60 mm from transmitting aperture. Results are shown in Figure 14.

V.   CONCLUSIONS

We used a two-dimensional acoustic field simulation to find the basic characteristics of a high-power ultrasonic system using acoustic waveguides. The proposed system uses five acoustic waveguides instead of a single transducer, and achieved a 1.4- to 1.5-fold increase in sound pressure at the same beam width.

In the future, we will consider the shape of the acoustic waveguides further and extend the model to a three-dimensional acoustic field simulation using finite element modeling. In addition, we hope to build the probe, acoustic waveguide, and pulse generator and test the system experimentally.

REFERENCES

[1] T. Kikuchi, "The situation of ultrasonic standards in Japan and the future development," Jpn J Med Ultrasonics, Vol.36, No.6, July 2009, pp.637-646.

[2] M. Shiiba, Y. Uemura, N. Okada, T. Uchida, T. Kikuchi, M. Kurosawa, and S. Takeuchi, "Performance improvement of

tough hydrophone using titanium front layer," IEIEC, 112(387), 2013, pp.87-92.

[3] J. B. Lastpvka and E. F. Carome, "Experimental Study of Dispersion in Ultarasonic Waveguide," JASA, Vol,35, No.8, Aug.1963, pp.1279-1284.

[4] E. F. Carome and J. B. Lastovka, "Theoretical and Experimental Studies of Pressure Profiles in Ultrasonic Waveguides," JASA, Vol.35, No.5, May 1963, pp.645-650.

[5] T. Miyashita, "A Study on Transient Behaviors of Wave Propagation in the Waveguides Made of Two-dimensional Artificial Crystals like Sonic Crystals and Photonic Crystals," IEICE, Vol.J85-A, No.10, Oct. 2002, pp.1138-1145.

[6] J. H. Sun and T. T. Wu, "Propagation of surface acoustic waves through sharply bent two-dimensional phononic crystal waveguides using a finite-difference time-domain method," APS, Physical Review B74, 2006, pp.174305-1-174305-7.

[7] J. Price, "Acoustic Waveguides" University of Colorado, Boulder, Jan. 2008, pp.14-31.

[8] G. Montaldo, P. Roux, A. Derode, C. Negreira, and M. Fink, "Generation on very high pressure pulses with 1-bit time reversal in a solid waveguide," JASA, Vol.110, No.6, Aug. 2001, pp.2849-2857.

[9] M. C. Bhardwaj, "High Intensity Guided Ultrasound Source," United States Patent No.5,371,483, Dec. 1994.

[10] Y. Koike, K. Suzuki, K. Suzuki, R. Machida, K. Han, S. Okano, and J. Soejima, "Sound Pressure Analysis of the Ultrasonic Cleaning Machine Using Waveguide mode," IEICE, US2009-44, Sep. 2009, pp.37-40.

[11] P. Puthillath, J. M. Galan, B. Ren, C. J. Lissenden, and J. L. Rose, "Ultrasonic guided wave propagation across waveguide transitions: Energy transfer and mode conversion," JASA, Vol.133, No.5, May 2013, pp.2624-2633.

[12] T. Abe, T. Moriya, T. Irie, N. Sato, and S. Takeuchi, "Experimental study of the Π-shaped coiled stator ultrasound motor," JJAP, Vol.53, June 2014, pp.07KE15-1-07KE15-5.

[13] T. Irie, N. Tagawa, M. Tanabe, T. Moriya, M. Yoshizawa, T. Iijima, K. Itoh, T. Yokoyama, H. Kumagai, and N. Taniguchi, "Transmission of 100-MHz-range ultrasound through a fused quartz fiber," Jpn J Med Ultrasonics Vol.41, No.4, 2014, pp.553-561.

[14] R. S. Schechter, H. H. Chaskelis, R. B. Mignogna, and P. P. Delsanto, "Real-Time Parallel Computation and Visualization of Ultrasonic Pulses in Solids," Science Vol.265, no.5176, Aug. 1994, pp.1188-1192.

Sensing of Essential Amino Acids Behaviour Under Fast Thermal Shocks in Liquid Water Environment

Michal Borecki, Jan Szmidt
Institute of Microelectronics and Optoelectronics
Warsaw University of Technology
Warsaw, Poland
borecki@imio.pw.edu.pl

Mariusz Duk, Andrzej Kociubiński
Lublin University of Technology
Department of Electronics
Lublin, Poland
akociub@semiconductor.pl

Michael L. Korwin-Pawlowski
Département d'informatique et d'ingénierie
Université du Québec en Outaouais
Gatineau, Québec, Canada
Michael.Korwin-Pawlowski@uqo.ca

Tomasz Niemiec, Maciej Szmidt, Kaja Urbańska
Warsaw University of Life Sciences
Warsaw, Poland
t_niemiec@tlen.pl

Przemysław Prus, Elżbieta Prus
Forcate
Wroclaw, Poland
przemyslaw.prus@forcate.pl

Abstract - **Essential amino acids exist normally in solid state, but in the environment they are often in contact with water or other liquids. The stability of solid state amino acids has been investigated under controlled atmosphere and pressure conditions. The amino acids stability in liquid water environment is important, especially for protein permanency and for human and animal food usage. In this work, the full set of essential amino acids are investigated in water environment at normal atmospheric pressure and under thermal shocks with slew rate as high as 4ºC/sec applied in a fiber optic capillary sensor set up. Reactions in some essential amino acids happen at temperatures lower than 80°C. The conclusion is that the stability of amino acids in water environment is different from their stability in solid state form.**

Keywords-essential amino acids; amino acids in water; L-lysine; capillary sensor

I.   INTRODUCTION

A.   Essential amino acids characteristics

Amino acids contain amine (NH_2) and carboxylic acid (COOH) functional groups, along with a side-chain specific to each amino acid, as shown in Figure 1. Amino acids are the basic bioelements of proteins, important macromolecules for the functions of humans and animals.

Amino acids are built of structural units called monomers that can join together to form short polymer chains called peptides or longer chains called either polypeptides or proteins. Amino acids that are precursors to proteins are called proteinogenic amino acids. There are 23 of proteinogenic amino acids, while 20 of them are directly encoded by the universal genetic code. Humans can synthesize 11 of these 20. The other 9 are called essential amino acids and must be consumed in the diet. The essential amino acids are histidine, isoleucine, leucine, lysine, methionine, phenylalanine, threonine, tryptophan, and valine. The essential amino acids in pure form exist in solid state. In the gas environment, the interactions of amino acids are enabled by Van der Waals forces, by electrostatic charge forces and, in some cases, by the single sigma bond that exists between the hydrogens. In the water environment, amino acids interactions are influenced by the electrostatic charge of the water particles and by the hydrogen bonds. The general properties of amino acids are presented in Table I.
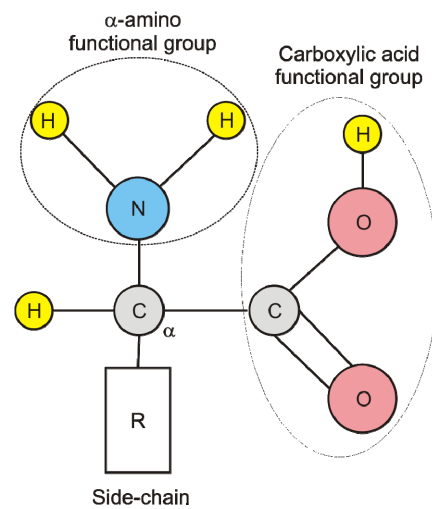

Figure 1.   Amino acids structure.

TABLE I.   GENERAL PROPERTIES OF AMINO ACID

Amino-acid	Molar mass [g mol^{-1}]	Approximate melting point [°C]	Solubility in H$_2$O at 25°C [g/100 mL]
leucine	131.17	286	2.43
lysine	146.19	220	150
valine	117.15	298	8.85
phenylalanine	165.2	275	2.96
isoleucine	131.17	288	4.12
threonine	119.12	270	9.0
methionine	149.21	258	3.38
histidine	155.16	284	4.19
tryptophan	204.24	282	1.14

TABLE II.   DIET REQUIREMENTS FOR ESSENTIAL AMINO ACIDS OF HUMANS

Essential amino acid	Requirement (mg/kg per day)	Amino acid composition of body protein (mg/g)
leucine	39	98
lysine	30	78
valine	26	56
phenylalanine	25	53
isoleucine	20	46
threonine	15	34
methionine	15	22
histydyne	10	32
tryptophan	4	0 (precursor of serotonin)

Amino acids are usually classified into groups according to the properties of their side-chains. Depending on the side-chain, an amino acid dissolved in liquid water environment could form a weakly acidic or a weakly basic solution. An amino acid is a hydrophilic substance when its side-chain is polar or carries a charge in liquid water environment. It would be a hydrophobic substance if the side-chain was nonpolar or neutral [1]. The effect of liquid water on the structure of amino acids is important because liquid water takes part in a wide range of reactions within a biological cell, and is an integral part of all proteins.

The amino acids side chains have a strong influence on how the protein behaves in liquid. For example, the structure of the lysine molecule in liquid differs for different charge states [2]. Below pH 9 both amino groups are protonated. Around pH 9, the α-amino group is protonated and the amino group of the side chain is not. Above pH 10.5 both amino groups are deprotonated. Therefore, lysine in drinking water is characterized by both amino groups protonated.

The requirements of essential amino acids of humans and the efficiency of amino acids in protein utilization at maintenance and sub-maintenance levels have been investigated [3]. Amino acids in the form of proteins are the second-largest component (water being the largest) of human muscles, cells and other tissues. Along with proteins, amino acids perform critical roles in the processes of neurotransmitter transport and of biosynthesis. The essential amino acids requirements in people's diet change significantly with their age [4].

The indicative values of amino acids diet requirement and amino acids composition of body protein are presented in Table II. Because it has to be present in food, lysine is one of the most interesting of essential amino acids. In many cases, lysine is supplemented into the animal and vegetarian feedstuffs [5].

Purified lysine is safe for human. Conventional dosages of lysine supplementation are of 3 to 6 grams daily [6]. One common use for lysine is the treatment of cold sores caused by herpes virus [7].

B. Essential amino acids examination in water enviroment

The thermal decomposition of amino acids depends on the environment [8]. The study of the thermal decomposition of amino acids in water environment is important, because it would allow refining the protein degradation model [9]. So far, the decomposition behavior of amino acids has been selectively investigated in water at high-temperature and high-pressure in a continuous-flow tubular reactor. The reactions were carried out in the temperature range of 200-340°C at a pressure of 20 MPa [10]. The mechanisms of heat damage in proteins when amino acids were in contact with water have been also examined. It was shown that lysine's disintegration may start when the temperature exceeded 37°C [11].

In this work, the possibilities of thermal decomposition of essential amino acids in water environment in conditions simulating those typical for some methods of thermal preparation of food were examined.

The paper consists of 5 sections. First section was the introduction where the amino acids properties were discussed and the aim of work is presented. Second section describes the proposed for this purpose experiment set-up. The examination results of essential amino acids are presented in section three. In the section four, the discussion of obtained results and their classification is proposed. The short conclusion of proposed examination is gathered in section five.

II.   EXPERIMENT SET-UP

To perform our experiments we used a photonic capillary sensor capable of producing a temperature ramp of over 4°C/sec in a liquid water environment. The sensor head schematic side cross-section is shown schematically in Figure 2. The light traces, from source to receiving fibers, for bubble presence, are shown schematically in Figure 3. In this situation, the received signals are minimal. When capillary is uniformly filled with liquid for the light travelling from source fiber the light refraction in liquid occurs, and reflected ray reaches received fiber.
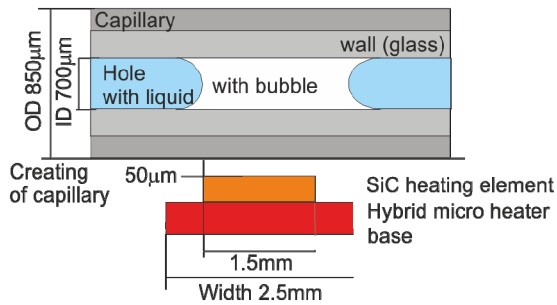
Figure 2.   Schematic side cross-section of the capillary head.
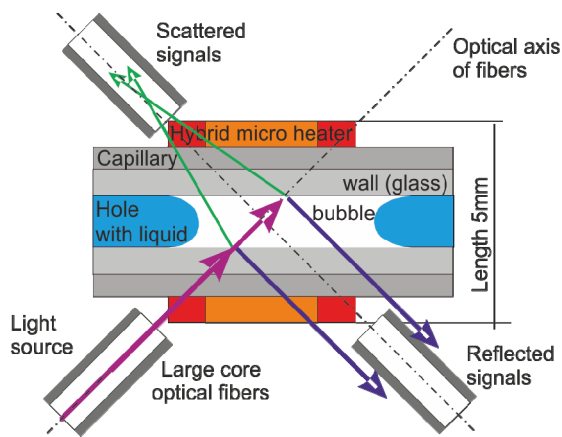
Figure 3.   Schematic top view of the capillary head.

Therefore, the sensor works on the principle of optical intensity changes taking place in dynamically forced measurement cycles. The sensor monitored simultaneously the thermodynamic and optical parameters of liquids [12]. It used an optical capillary in which the phase change from liquid to gas (a creation of a gas bubble in the liquid) was forced by local heating while the propagation of light across the capillary was monitored. After the bubble of gas was created, the local heating was switched off, but the bubble expansion still forced the flow of the liquid. The forced liquid flow in the capillary depended strongly on the vapor pressure and could be classified by a cavitating or non-cavitating type [13]. After the local heating, the gas phase could be absorbed in the liquid, or remain in the form of a small bubble. As a result of the decomposition of the components of the liquid, or alternatively, when the forced flown was turbulent or of the cavitating type, a series of air bubbles might exist in the liquid.

The capillary head used in this work was a modified version of one presented by Borecki et al [14]. The detection of the reflected signal was supplemented with the detection of scattered signal. The optical fibers were moved to the position in which their axes crossed in the central intersection point of the hybrid micro heater and the capillary. That enabled the monitoring of precipitation of the solution's components. Instead of the 2.5mm wide element using for the micro-heater [14], a new 1.5mm wide SiC heating element was developed. This way, the local heating area dimensions get closer to the dimensions of the optical

beams than in our previous investigations. The TSP 700-850 from Polymicro Inc. capillaries were cut into 10 cm sections. In experiments capillaries with both ends closed were used. On the measuring head large core optical fibers BFH 37-600 from Thorlabs were installed.

As light source, a fiber coupled laser device S1FC675 from Thorlabs was applied. The diode wavelength was 675nm. The source was electrically modulated with 1kHz frequency from a Rigol function generator DG2021. The optical power at the end of light source fiber was set to 0.1mW, by using the modulation signal amplitude, offset and knob of laser device.

The optoelectronic detection unit coupled to large core optical fibers was of our own developed construction. It is modified version presented in [14]. It is characterized by switchable from 10nW to 1mW detection optical range. Lower detection threshold, for output refresh rate less than 100Hz, is 50pW. The response time, for full scale signal change, is lower than 10ms. The optoelectronic unit was connected to a PC by an analog input of IOtech Personal daq 3000 data acquisition system. That system was also used to control the laboratory power supply HM8143 of the micro heater. The micro heater was powered with 5W in periods shorter than 30s. To operate the system, at a 0.1s sampling rate, script in DasyLab 10 was designed.

The initial experiments were made using capillaries filed with deionized water, as presented in Figures 4 and 5. As can be seen in Figure 4, the scattered signal was constant during the sample's local heating, meaning that precipitated components were not present in the water. The presence of a moving boundary between the gas and the liquid phases can be correlated with the peak in scattered signal. The deionized water boiled in the measurement cycle in the time range from 17.1 to 25 seconds, corresponding to a boiling temperature that could be explained by the superheating of water, when at atmospheric pressure it could reach 120°C. The conditions for superheating of water are fast heating of a not vibrating sample of clear water in a vessel with smooth walls. Those conditions were maintained in the analyzed measurement cycle.
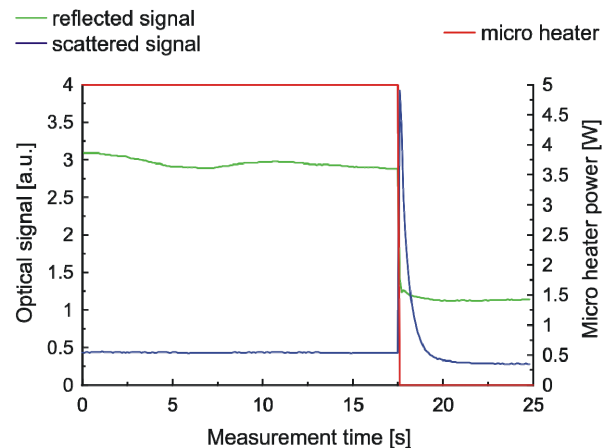
Figure 4.   Measurement cycle of deionized water showing the reflected and the scattered signal during heating.
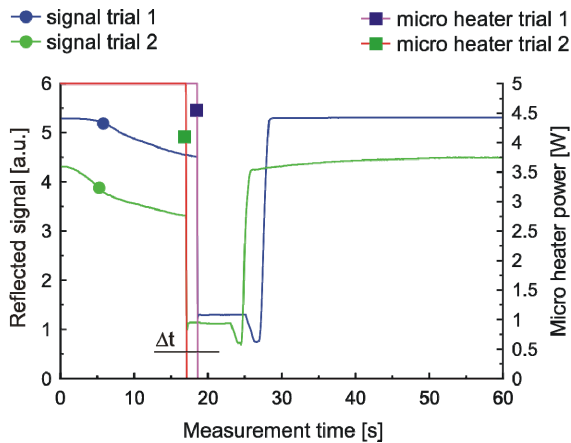
Figure 5. Measurement cycle of deionized water, two trials with characteristics repeatable shape of signal.
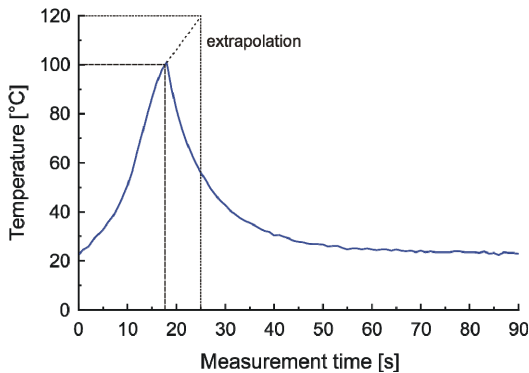
Figure 6. The maximum local temperature of deionized water in the capillary during a measurement cycle.

During the calibration of the sensor the temperature distribution in the capillary optrode was registered with the use of R300 NEC thermo-vision camera and the InfReC software. The measured and calculated water temperatures during the measurement cycles are presented in Figure 6. The obtained results confirm boiling at 100°C in 17.1 seconds of local heating. The extrapolation of the results showed that the temperature of superheating of water in the analyzed conditions did not exceed 120°C.

III. EXPERIMENTAL RESULTS

Deionized water was used for making solutions at 100mM/dm^3 concentrations containing amino acids of 99% Reagent Plus purity obtained from Sigma Inc [15]. Ten experiments series for each examined amino acid were performed. Scattered signals during local heating in all experiments were stable so solid state precipitates did not form. Therefore, these signals are not presented in following records. The random selected two characteristics of experiment series refracted and reflected signal, for each examined amino acid, are presented in subsequent figures.

The amino acid simplest in structure is glycine. It is not an essential amino acid. Its solubility in water is 24.99g/100 mL at 25°C and the decomposition temperature of glycine was about 230°C.
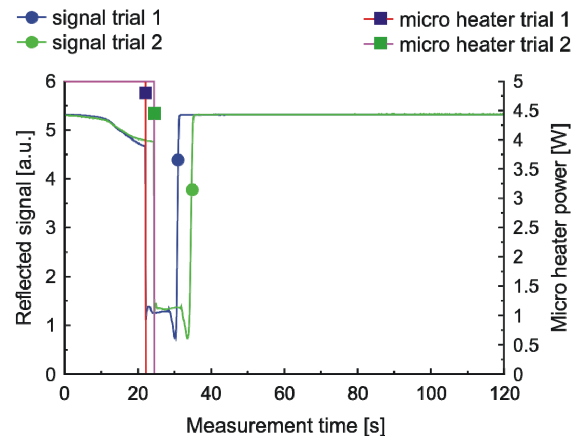
Figure 7. The measurement cycle of glycine

A solution of 100 mM/dm3 of glycine in water was used for the measurement cycles presented in Figure 7. The glicine measurement cycle was similar to that of water, as was expected, because the solution of glycine in water was uniform, its concentration did not approach the solubility limits.

A. Examination of essential amino acids

The measurement cycle of histidine is presented in Figure 8. The histidine solution starts boiling in 15.8-17.1 seconds of the measurement cycle, slightly before sample reached 100°C. In our opinion, the gas product of decomposition had a relatively higher pressure than that of water steam. This gas phase caused turbulent flow of liquid, as could be concluded from the highly non monotonic measurement cycle characteristic observed after the micro heater switch off.
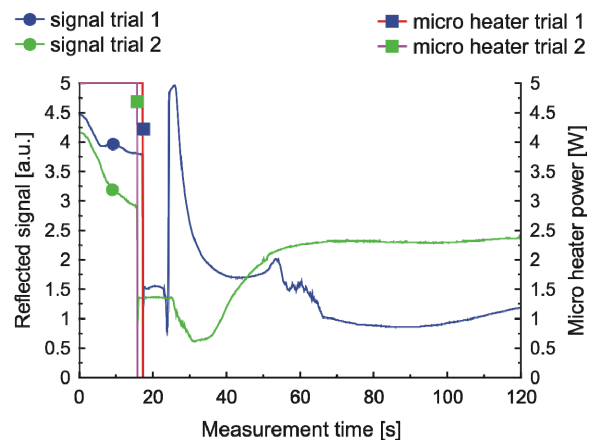
Figure 8. The measurement cycle of histidine

Isoleucine ($C_6H_{13}NO_2$) in water solution generated the gas phase in the range of 6.3-11.3 seconds of the measurement cycle, which was faster than water and histidine. The gas phase was next absorbed, as depicted in Figure 9. Leucine ($C_6H_{13}NO_2$) measurement cycle is shown in Figure 10.
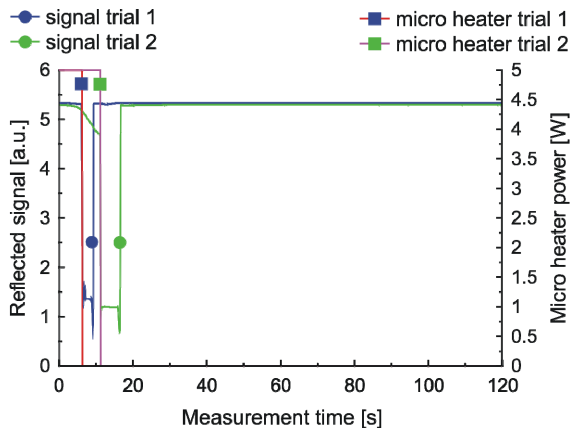
Figure 9. The measurement cycle of isoleucine
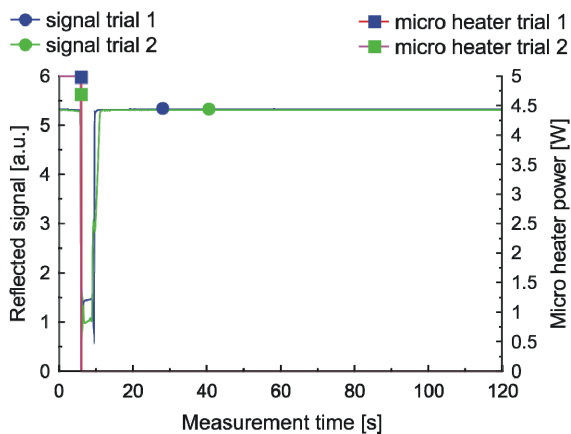
Figure 10. The measurement cycle of leucine

The measurement cycles of leucine had the same course as isoleucine, with the gas phase appearance in 6 seconds. The measurement cycles of isoleucine and leucine were similar, probably due to the small difference of their structures as their molecular formula is the same.

The measurement cycle of lysine is presented in Figure 11.
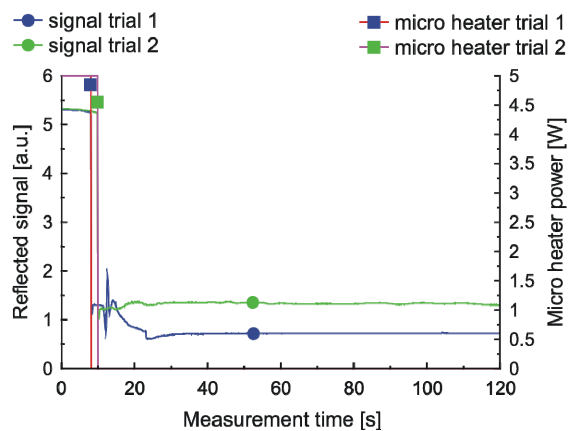
Figure 11. The measurement cycle of lysine

Lysine ($C_6H_{14}N_2O_2$) has the same carbon number as isoleucine and leucine, but measured characteristics differs significantly. The generation of the gas phase in the lysine solution was the most violent of the examined essential amino acids. It caused the cork of the capillary to shoot out in each measurement cycle. Therefore, the stable low level signal after the shut off of micro heater can be observed. The gas phase generation occurred in the range from 8.1 to 9.0 seconds of the cycle.

The methionine measurement cycle of Figure 12 shows similarity with the water cycle of Figure 5.
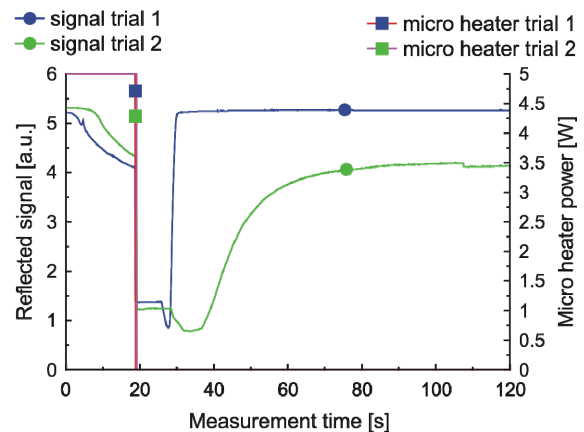
Figure 12. The measurement cycle of methionine

Phenylalanine was characterized in the measurement cycle by a rapid gas phase creation in 9.4-9.8 seconds, as shown in Figure 13.
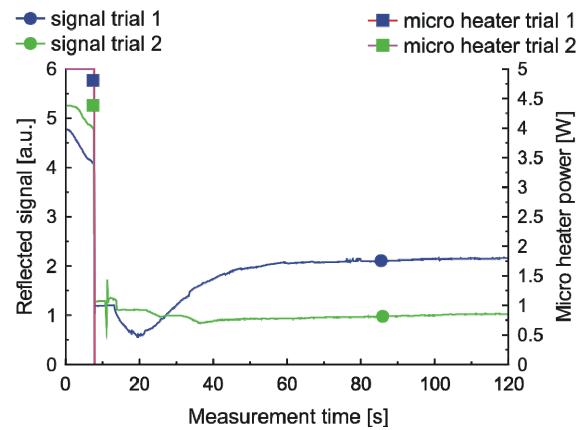
Figure 13. The measurement cycle of phenylalanine

Threonine decomposition occurred in 15.5-16.3 seconds of the measurement cycle, with a turbid flow of liquid, as presented in Figure 14.

The measurement cycle of tryptophan of Figure 15 is similar to the cycle of water.

Valine has the measurement cycle similar to water and tryptophan, as depicted in Figure 16.
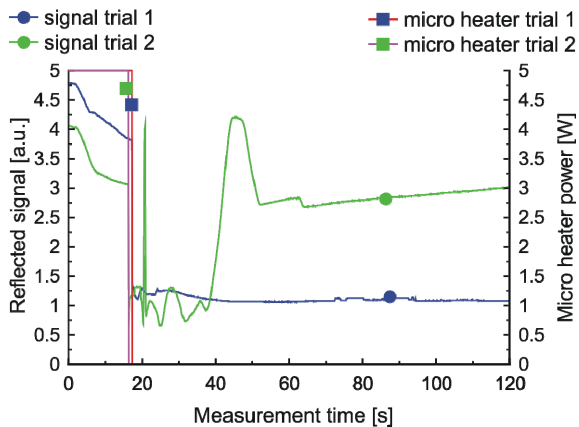
Figure 14. Measurement cycle of threonine
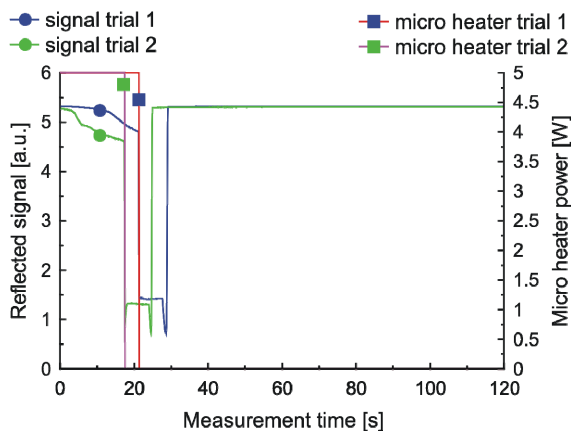
Figure 15. The measurement cycle of tryptophan
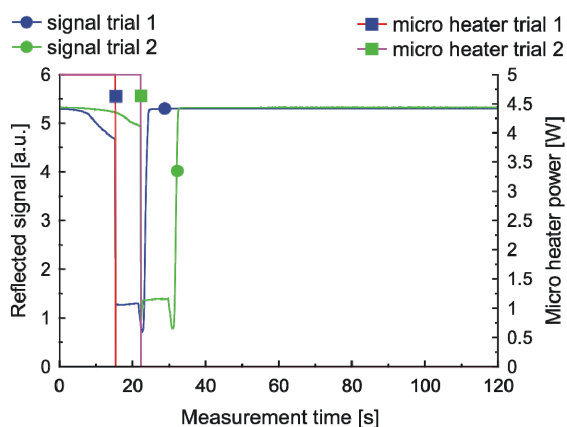
Figure 16. The measurement cycle of valine

IV. DISCUSSION OF RESULTS

Sensing of essential amino acids under fast thermal shocks in water environment shows that the amino acids solutions behavior can be described according to the form of gas phase creation as 1) similar to water (H_2O-like); 2) early;

and 3) impetuous and early, as listed in Table III. The water-like behavior can be described as one with the bubble appearance later than 16 seconds of the measurement cycle. The early gas phase creation can be described as when the gas phase creation happens before 16 seconds of local heating - below 80ºC. Impetuous and early gas phase creation occurs when, additionally, the gas phase forces rapid or turbid solution flow.

TABLE III.   SUMMARY OF RESULTS OF ESSENTIAL AMINO ACIDS EXAMINATION

Amino acid	Type of amino acid in water	Relation to water	Avg. time of rapid thermal reaction [s]	Type gas phase creation
leucine	neutral	hydrophobic	6.0	early
lysine	charged	hydrophilic	8.5	impetuous and early
valine	neutral	hydrophobic	18.8	H_2O like
phenyl-alanine	neutral	hydrophobic	9.6	impetuous and early
isoleucine	neutral	hydrophobic	8.8	early
threonine	polar	hydrophilic	16.0	H_2O like
methionine	neutral	hydrophobic	19.0	H_2O like
histidine	charged	hydrophobic	16.4	H_2O like
tryptophan	neutral	hydrophobic	19.4	H_2O like

Four distinct cases are of interest. The early gas phase creation of leucine and isoleucine happens because they have similar structures and parameters. The impetuous and early gas phase creation happens for lysine and phenylalanine.

On the other hand, the degradation of amino acids in water environment for situations involving enzymatic oxidation or hydrolytic deamination is well-known [16].

V. CONCLUSION

Developed capillary sensor set-up enables sensing of essential amino acids behavior under fast thermal shocks in liquid water environment. Experiment show that, a fast temperature increase may act as a reaction catalyst for the disintegration of some amino acids, particularly lysine. This can be used for explaining, efficiency of herpes virus curing with lysine supplementation in some group of peoples. This can also clarify traditional medicine recommendations of raw parsley and chives consumption, which can be compiled with highest in vegetables lysine concentration [17]. Therefore, food preparation processes with fast ramp ups of temperature, are not ideal when the food is to be a source of amino acids. Consequently, we intend to examine amino acids stability in oil environment as some oriental kitchen methods base on putting shredded food into boiling oil or heated clarified butter which may lead to proven lysine deficit of India people [18].

The phenomena of lysine disintegration may be used in new nanotechnology medical or diagnostic particles carriers using graphene oxide [19]. That effect will be the subject of

our further studies. We will concentrate on examining the presence of products while heating graphene oxide - amino acids solutions in liquid water environment.

References

[1] T. H. Creighton, "Proteins: structures and molecular properties," W. H. Freeman, San Francisco, second ed., 1993, pp. 1-507.

[2] D. Nolting , E. F. Aziz , N. Ottosson , M. Faubel , I. V. Hertel, and B. Winter "pH-Induced Protonation of Lysine in Aqueous Solution Causes Chemical Shifts in X-ray Photoelectron Spectroscopy," J. Am. Chem. Soc., vol. 129 (45), 2007, pp. 14068-14073.

[3] J. C. Waterlow, "The requirements of adult man for indispensable amino acids," European Journal of Clinical Nutrition, vol. 50, 1996, pp. 151-171.

[4] M. F. Fuller and P. J. Garlick, „Human amino acids requirements; can the controversy be resolved?," Annual Review of Nutrition, vol. 14, 1994, pp. 217-241.

[5] W. Pfefferle, B. Möckel, B. Bathe, and A. Marx, "Biotechnological Manufacture of Lysine," in Microbial Production of l-Amino Acids, R. Faurie and J. Thommel Eds, Springer, Berlin, Heidelberg, vol. 79/2003, 2003, pp. 59-112.

[6] N. W. Flondin, "The metabolic roles, pharmacology, and toxicology of lysine," J. Am. Coll. Nutr. vol. 16, 1997, pp. 7-21.

[7] F. A. Tomblin and Jr., K. H. Lucas, "Lysine for management of herpes labialis," Am J Health Syst Pharm. vol. 58(4), 2001, pp. 298-300.

[8] J. R. Banga, A. A. Alonso, J. M. Gallardo, and R. I. Perez-Martin, "Degradation kinetics of protein digestibility and available lysine during thermal processing of tuna," Journal of Food Science, vol. 57(4), 1992, pp. 913-915.

[9] B. Fackovec and J. Vondrasek, "Decomposition of intramolecular interactions between amino-acids in globular proteins - A consequence for structural classes of proteins and methods of their classification," in Ed. Ning-Sun Yang, Systems and Computational Biology – Molecular and Cellular Experimental Systems, InTech, Rijeka, 2011, pp. 69-82.

[10] N. Sato, A. T. Quitain, K. Kang, H. Daimon, and K. Fujie, "Reaction kinetics of amino acid decomposition in high-temperature and high-pressure water," Industrial & Engineering Chemistry Research, vol. 43(13), 2004. pp. 3217-3222.

[11] R. F. Hurrell and K. J. Carpenter, "Mechanisms of heat damage in proteins," Br. J. Nutr. vol. 32, 1974, pp. 589-604.

[12] M. Borecki and M. L. Korwin-Pawlowski, "Optical capillary sensors for intelligent microfluidic sample classification" in: Nanosensors: Theory and Applications in Industry, Healthcare and Defence, Lim T.-C. Ed., CRC Press, Boca Raton, FL, USA, 2011, pp. 215- 245.

[13] X. Wang and W. H. Su, "A numerical study of cavitating flows in high-pressure diesel injection nozzle holes using a two-fluid model", Chinese Sci Bull, vol. 54, 2009, pp. 1655-1662.

[14] M. Borecki, et al. " Sensing of the Functional State of Fertility of Cows," IARIA, Sensordevices, 2012, pp. 14-20.

[15] http:/sigmaaldrich.com/technical-service-home/product-portfolio.html, accessed 29.09.2014.

[16] M. Sohn and C. T. Ho, "Ammonia generation during thermal degradation of amino acids," Journal of Agricultural and Food Chemistry, vol. 43, 1995, pp. 3001-3003.

[17] http://www.dietandfitnesstoday.com/vegetables-high-in-lysine.php, accessed 22.09.2014.

[18] S. M. Rutherfurd, K. Bains, and P. J. Moughan, "Available lysine and digestible amino acid contents of proteinaceous foods of India," Br. J. Nutr. vol. 108, 2012, pp. S59-68.

[19] M. Chhowalla, M. Vittadello, and K. Woronowicz, "Chemically modified graphene," Patent, PCT/US2012/038626, 2012, http://www.google.com/patents/WO2012159051A2?cl=en, accessed 22.09.2014.

Redox Sensors for the Control of Process and Waste Waters

Winfried Vonau, Frank Gerlach, Kristina Ahlborn, Sandra Sachse

Kurt-Schwabe-Institut für Mess- und Sensortechnik
Waldheim, Germany
vonau@ksi-meinsberg.de

Abstract—**The state of waste and process water depending on the particular application can be characterised by quantitative analysis of its composition (e.g., heavy metal ions, nitrate or phosphate) but often, at least in a complementary manner, by determinating of non-specific parameters like electrolytic conductivity or redox potential. The latter is usually measured potentiometrically using indicator electrodes of precious metals. However, their application is connected with measurement errors caused by interactions between the media and the noble metal surfaces. Specifically this problem occurs in real media that can be found in process chemistry and in waste water sector, for example. Using electron conducting glass instead of noble metal membranes in potentiometric redox electrodes solves this problem. We present possibilities for their fabrication and results from their use.**

Keywords-redox potential; sensor; glass membrane; thick film; thin film; potentiometry

I. INTRODUCTION

The redox potential, also denoted as oxidation reduction potential (ORP), is a measure for the ability of an aqueous system to take up electrons from a chemical reaction or to give up electrons. The ORP of a system can be changed by the addition of substances unless they are oxidative or reductive. Determination of redox potential is very important in nature and technology as it characterises the present state of a system. Additionally, ORP can be used as controlled process variable for the performance of technical reactions.

As control variable it is essential, e.g., for the water treatment as in many cases it is comparable to the pH value. Temperature, ionic strength and pH value are all important contributing factors. Studies have shown that the lifetimes of bacteria and other microorganisms are also strongly dependent on the ORP of the media.

Currently, noble metal based electrodes (mostly in compact embodiment according to standards) [1, 2] are predominantly used for the determination of redox potentials, while occasionally, electrodes based on film technology or electroplating [2] are used. Independent of the shape of the noble metal indicator electrode, potentiometry is used for the redox potential determination. The material of the measuring electrode is critical for the results. Typically, gold, platinum or palladium are used in their construction.

Gold electrodes react to chlorides and cyanides present, while platinum electrodes do not. Instead, in reducing solutions together with palladium they form hydrides. This impacts the electrode properties, particularly the absolute position of the potentials measured in analyte solutions with the redox electrodes, as well as the adjustment behaviour of the potentials in case of composition changes in the measured media. In addition to the poor reproducibility of noble metals electrodes, successive measurements are subject to an additional measurement uncertainty of ± 25 mV.

The electrodes become unusable when catalytic poisons such as SO_2 or other sulfur compounds reach their surface. Proteins also cause an inactivation of noble metal surfaces and the presence of gaseous oxygen or hydrogen in the test medium influences the half cell potential. Precious metals can act as an undesired catalyst, e.g., they promote the decomposition of hydrogen peroxide. Precious metals are expensive meaning and a substitute is highly desirable. Investigations of cheaper carbon electrodes (e.g., graphite electrodes) have shown that a high reproducibility of the electrode potentials is very difficult to achieve; therefore, they are not an adequate alternative.

The problems of precious metal electrodes can be circumvented by using glasses with very high electron conductivity. Such glasses were first investigated at the end of the 1970s [3]. These electrodes operate based on the presence of iron and titanium oxides in the glass, whereby in the case of Ti the metal coexists in the oxidation states +3 and +4 in a predefined proportion. Currently, redox glass electrodes are based on platinum wires covered with redox glass [3] or prepared analogously to conventional pH glass electrodes [4]. However, it is rarely possible to handle the special glasses which readily crystallise by the glass blower. The thermal coefficients of expansion are incompatible, in general, with those of usual electrode shaft glasses, inevitably leading to high wastage rates. For some niche uses it is reported about results of their application [5]. Recently published works deal with the use of thick film [6] and thin film technology [7] as new manufacturing technologies for redox glass based indicator electrodes.

Previous solutions for the measurement of redox potentials in this and other process waters in circulation were based on the use of noble metal indicator electrodes, solely.

The above mentioned drawbacks were accepted. Alternatively, a bioactivity sensor (BAS) [8, 9] was developed, based on the principle of a biofuel cell. The electron transfer from the biological component to the anode of the sensor

was used for analytical applications. An application in the practise is not given currently.

In this paper a new glass based system for the determination of the redox potential is introduced. The paper is organised as follows. The motivation for the development of new a redox sensor system and its use in paper industry processes is outlined in Section II. Section III describes manufacturing of the planar redox glass electrodes in thick film technology. First results of measurements with this multisensordevice as a part of a process water analyser are demonstrated in section IV. Additionally, we introduce a procedure to extend the lifetime of the measurement system. The conclusions and acknowledgement close this article.

II. PROBLEM

In the production of paper, water is required for auxiliary and cleaning purposes and it is often used several times. Beside the raw materials, the production details are critical to the quantity and composition of the sewage. In general, ecological and economic considerations lead the paper industry to reduce the sewage it produces. In reducing the volume of waste water the proportion of soluble substances increases, creating an undesirable nutrient-rich habitat for micro-organisms. This leads to an increase of slime and biofilm growth in the system. The problem is treated effectively by an optimised application of biocide active substances. In any case, an efficient sewage treatment with biological stage of degradation is necessary. Further reduction of sewage volume necessitates an enlargement of the biological sewage treatment arrangement with biofilters. For the controlled addition of peroxide based biocides to suppress the slime growth in the process water, redox potential determination can make an essential contribution, whereby the complicated composition of the medium does not require the use of precious metal electrodes.

For the assessment of the determined redox potentials it has to be taken in account that beside the concentration of the biocides the position-dependent amount of oxygen and/or the pH values have a significant influence on the sensor signal. These parameters should additionally be determined and considered for the evaluation of the redox potentials.

III. SOLUTION

First a glass mixture consisting of SiO_2, Na_2O, CaO, Li_2O, Fe_2O_3, and Fe_3O_4 was prepared according to [10], homogenised, melted in a high temperature chamber furnace at 1400 ^{o}C and processed into rods. These were milled in a planetary ball mill. Afterwards, the resulting powder was sieved through a mesh, weighed, blended with the identical amount of a terpineol containing binder and mixed again in the planetary ball mill. To fabricate planar thick-film sensors, a circular electrode structure of platinum with a thickness of 8 μm was screenprinted on an alumina substrate, dried and fired. For the redox-sensor fabrication by thick-

film technology the sensitive pastes and covered substrates were heated to decrease the paste-viscosity and to simplify the application of the pastes onto the substrates. Then, the glass paste was carefully applied to the substrate. After drying at 150 ^{o}C in an oven with recirculating air the sintering process was executed. The resulting redox glass membrane had a thickness of 40 … 100 μm.

For the application of the electrodes in process water, the glass coated substrates were assembled in a high-grade steel case and equipped with a protective hood. As reference electrode for the measurements, a solid state electrode with an epoxy-membrane filled with KCl according to [11] was used. Figure 1 shows both electrodes separately assembled.
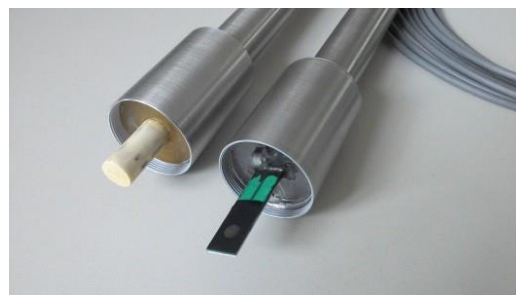
Figure 1. Glass based redox potential probe (right) and polymer based reference electrode (left) for the industrial application

They were placed in measuring lances, where additional electrochemical sensors (T, pH, pO$_2$) also were installed. Data collection is possible at different places within the water cycle and as can be seen in Figure 2, it can also be measured beyond this circulation system after sample collection by means of pumps.

Figure 2. Measuring system for the monitoring of process water, consisting of control box (a), Measuring lance (b) and measuring barrel (c)

The cleaning of contaminated sensors occurs in the measuring tube under the following conditions:

The measuring tube represents a current-optimised flow measuring cell with minimised volume and ¾" hose connection delivering a high-enough current. This minimises the slime and biofilm growth in the sensors and inner surfaces of the measuring cell. Without measuring tube, the measuring lance can be used as a multi-parameter insertion probe in large containers. The compressed air is provided by an autonomous small compressor. A compressed air nozzle was placed for every sensor to clean the sensitive surfaces. The number and the duration of the cleaning impulses can be adapted for every sensor of the respective load of the measuring solution. The cleaning cycles should be chosen so that biofilm formation is avoided. The inflow can be interrupted by an added electromagnetic valve to detect the biological load of the process water by the oxygen reduction per unit time and the change of the redox potential. The efficiency of the cleaning procedure is demonstrated in Figure 3.

Figure 3. Multi sensor system to control process water of the paper industry left contaminated; right after cleaning with compressed air

The results obtained by means of the continous use of multisensors during the paper manufacturing process at different places of the water cycle system enable the plant operators to judge the state of the system and its biological contamination (slime growth). The focus lies on the measurement of redox potentials by means of glass-based electrode.

IV. RESULTS

We present results of the multisensor-equipped measuring lances in model waters and in process water of the paper industry with particular focus on the innovative new redox glass electrodes. As a paper mill typical model medium, a solution of $CaCl_2 * 6 H_2O$, $Na_2SO_4 * 10 H_2O$, starch and NaCl was prepared. The influence different biocides have

on the electrochemical measurements if no micro-organisms exist in the solution was examined. The biocide Wofasteril E 400 was used and Figure 4 shows it has a clear effect. For the investigations, different electrode types were used. In addition to the glass-based redox electrodes, conventionally made pH glass electrodes and a platinum sheet for referencing redox measurements were taken. The pH electrode exhibits a decrease of the pH value with the addition of the peracetic acid based biocides, as is expected. The redox glass electrode records the change of the redox potential as a result of the biocide addition. The fact that the potential change with the platinum sheet also acting as a redox electrode does not precipitate so high, can be traced back on its known pH dependence. Figure 5 shows the results of own investigations into the pH dependence of the measurements.
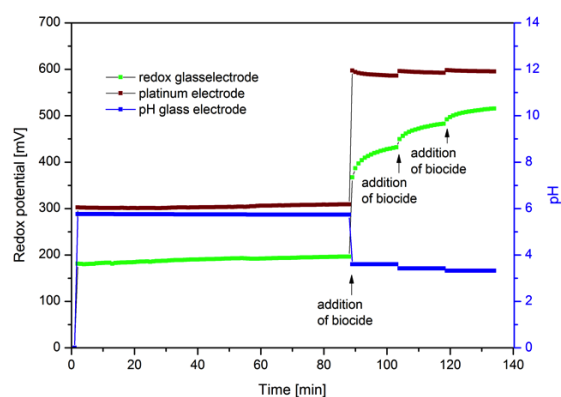
Figure 4. Changes of potential and pH value when biocide is added to a paper mill typical model solution
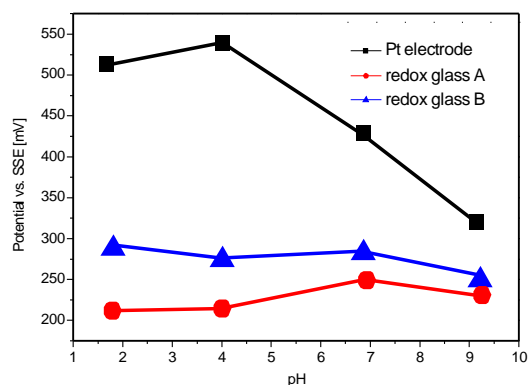
Figure 5. pH dependence of ORP for different redox electrodes

Figure 6 displays an exemplary measurement of process water in a paper factory. Besides the redox potential which was measured using both a platinum and a glass electrode, the oxygen content as well as the temperature are shown. The sensors were installed in the measuring lances shown in Figure 3. The electrodes were automatically cleaned by means of compressed air every 12 hours, corresponding to 4, 16, 28, 40 and 52 hours in Figure 6.
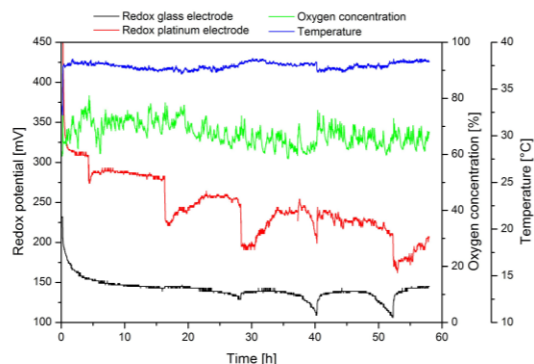
Figure 6. Course of redox potential, oxygen content and temperature in the process water of a paper mill (automatic cleaning cycle: 12 h)

The oxygen concentration as well as the temperature are nearly constant in Figure 6. The redox potential curves partially deviate by more than ~100 mV from each other due to the cross sensitivity of the platinum electrode to components in the process water. By means of the redox potential, determined with the redox glass electrode, contamination caused by the microbial load of the process water can be determined. At the beginning of the measurement the redox potential appears to a roughly steady level of about 150 mV. Over longer timespans, the influence of the automatic cleaning by means of compressed air becomes more pronounced. The cause is the biofilm that forms on the electrodes as a result of the microbial contamination, which lowers the redox potential. The cleaning removes this and the original potential can be reached again. The platinum electrode is influenced immediately by the cleaning with compressed air, because this reacts to the aerial oxygen. This precious metal-based electrode is therefore completely unsuitable for measurements in process waters of paper mills.

CONCLUSION

Target of the development was the realisation of redox glass electrodes to overcome some problems of noble metal electrodes like inhibition and catalytic side reactions. Results of the application of thick film redox glasses based on Ti- and Fe-oxides are presented in this paper. They are suitable for the requirement of process water in paper industry. As a part of multisensor devices the planar electrodes have successfully been used for the controlling of biocide input in industrial paper processing. This sensor system enables the save prevention of unwanted slime and biofilm growth in paper production processes without biocide overdosage.

ACKNOWLEDGMENT

REFERENCES

[1] German standard methods for the examination of water, waste water and sludge, DIN 38404-6, German standard methods for the examination of water, waste water and sludge, Physical and physical-chemical parameters (group C), determination of the redox potential (C 6).

[2] M. Reinecke, J. Spindler, W. Vonau, F. Berthold, "Sensors by chemical metallisation", in Mittweida Scientific Reports, J. Univ. of Appl. Sci. Mittweida Part I, Modern processes in surface engineering, Vol.13 , pp17-24, 2000.

[3] B.P. Nikolsky, M.M. Shults, A.M.Pisarevsky, A.A. Beljustin, S.K. Bolkhontseva, V.A. Dolidze, V.M. Terasova, J.M. Karachentseva, L.I. Dolmazova, "Electron-conductive glass", United States Patent 3 773 642.

[4] M.M Schults, A.A. Beljustin, A.M. Pisarevsky, L.V. Avramenko, S.J. Volkov, V.N. Lachtikova, V.A. Dolidze, V.M. Tarasova, "Glass electrode", German Patent DE 2645623.

[5] M. Miloshova, E. Bychkov, A. Pradel, M. Ribes, "New redox sensors for environmental monitoring, biotechnology and medical applications" in meeting abstracts of the 1997 joint International meeting: Electrochemical Society 192nd meeting and International Society of Electrochemistry 48th annual meeting: Paris, August 31-September 5,1997. Electrochemical Society, Philadelphia , vol 97-2, p. 940-941, 1997.

[6] W. Vonau, F. Gerlach, K. Ahlborn, "Glass-based redox sensor" J. Solid State Electrochem. Vol.17, pp.969-976, April. 2013.

[7] W. Vonau, F. Gerlach, K. Ahlborn, M.J. Schöning, H. Iken, "Miniaturised potentiometric indicator electrode and processes for the production thereof", German Patent DE 10 2012 014 861.

[8] D. Holtmann, D. Sell, Sensor Systems for Monitoring Microbial Activity in Industrial Water Circuits. Eng. Life Sci. (1) 6: 233-236

[9] D. Sell, Ways for an online determination of microbial metabolic activity by a newly bioactivity sensor. University Department, University Hannover, Habilitation, 2004

[10] W. Vonau, K. Ahlborn F. Gerlach, B. Hahnebach, E. Pöhler, "Electrochemical electrode and process for their preparation", German Patent DE 10 2011 118 409.

[11] W. Vonau, F. Gerlach, R. Sauer, S. Ruder, "Reference electrode", German Patent DE 10 2010 050 481.

Sensitivity of Photo-Elastic Nd-YAG Laser for Small Force Sensing

Naceur-Eddine Khelifa

Laboratoire Commun de Métrologie: LNE-CNAM
1, rue Gaston Boissier, Paris, France
naceur.khelifa@cnam.fr

Marc Himbert

Laboratoire Commun de Métrologie: LNE-CNAM
61, rue du Landy, La Plaine Saint-Denis, France
marc.himbert@cnam.fr

Abstract— **The sensitivity of a force sensor based on photo-elastic effect in a monolithic Nd-YAG laser depends strongly on the geometrical shape and dimensions of the laser medium. The theoretical predictions of sensitivity are in good agreement with first results obtained with a cylindrical crystal of (4x4) mm and some values reported by other groups. However, for small size of the laser sensor, the developed model predicts sensitivity, about 30 % higher than the values given by available experiments. In this paper, we present experimental results obtained with a force sensor using a monolithic cylindrical Nd-YAG laser of dimensions (2x3) mm with suitable optical coatings on its plane end faces. The new measure of sensitivity has allowed us to refine the theoretical model to treat photo-elastic sensors with small dimensions.**

Keywords- solid-state laser; photo-elastic effect; force sensor; beat frequency; sensitivity.

I. INTRODUCTION

The metrological characterization of scientific and industrial instrumentation employing small forces remains an intermediate target to ensure that measurements of forces lower than 1 N are traceable to the S.I. system of units [1][2]. Recently, a number of laboratories have shown a particular resurgence and interest to connect results of small forces measurements obtained with various devices [3][4]. Indeed, development of micro-robots for microsurgery for the retina or colonoscopy, measurement of stiffness of atomic force microscope cantilevers and handling fragile objects all require one to know the forces exerted on the manipulated objects [5]. In these areas of activity, the implementation of forces in the range of 1N to 0.1 mN by instruments has led to the necessity to develop ways to measure and control the forces generated. In fact, measurements based on different physical principles can be compared, at least in the range of their overlap. Systems of different configurations, based on the exploitation of the photo-elastic effect in a crystal, have been developed and used to measure small forces. The results obtained are encouraging despite the difficulties raised for the generation and application of small forces with good reproducibility [6][7].

Here, a focus on photo-elastic force sensors with high sensitivity is made. The reason for this approach lies in the fact that in previous work we observed significant discrepancy between available experimental values of sensitivity and those predicted by the theoretical model based on some assumptions that are discussed in Section II. To improve the theory we started to make a photo-elastic force sensor whose dimensions lie in a range for which there is no experimental data, i.e. length $\times$ diameter is in between 3 and 12 mm^2. To realize a monolithic solid-state laser, we chose a cylindrical Nd-YAG (neodymium-yttrium aluminum garnet) rod of 2 mm in length and 3 mm in diameter having plane end-faces.

In the next Section, a brief reminder on the theoretical photo-elastic effect in a laser will be done. Section III will describe the new laser, Nd-YAG playing the role of sensitive element of the force sensor, as well as the experimental set-up. The results will be presented and discussed in connection with theoretical predictions in Section IV.

II. MECHANICAL-STRESS INDUCED BIREFRINGENCE

The birefringence is induced in an Nd-YAG laser rod under mechanical stress generated by external force applied on the crystal, as illustrated in Figure 1.

In order to link the force intensity to the induced birefringence (based on photo-elastic effect), we assume the stress distribution over the length of the laser rod is uniform. The stress components σ_y and σ_x along the principal directions of the rod, induced by the applied force F, are represented by [8]:

$$\begin{cases} \sigma_x = \dfrac{\alpha}{\pi \ell d} \times F \\ \sigma_y = -\dfrac{\beta}{\pi \ell d} \times F \end{cases} \qquad (1)$$

where ℓ and d are respectively length and diameter of the cylindrical crystal while the parameters α and β depend on the nature of the contact between the laser crystal and its support and on the orientation of the pumping beam at 808 nm relative to the principal axis of the Nd-YAG crystal.

The relative stress, along the orthogonal directions x and y, induced in the center of the rod is then given by relation:

$$\sigma_x - \sigma_y = \frac{(\alpha + \beta)}{\pi \ell d} \times F \qquad (2)$$

The induced frequency shift between the frequencies of the orthogonal polarizations $E^{//}$ and $E^{\perp}$ of the oscillating laser mode is expressed as a function of external force by:

$$\Delta \nu = \nu_q^{\perp} - \nu_q^{//} = \frac{(\alpha + \beta)\, C_{PE}^{\lambda_q}}{\pi\, n} \times \frac{\nu_q}{\ell\, d} \times F \qquad (3)$$
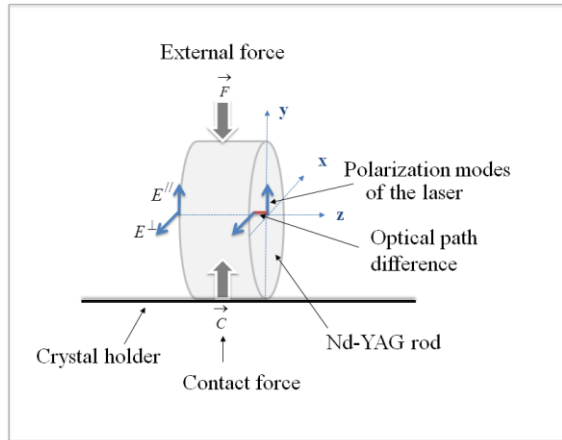
Figure 1. Orientation of the photo-elastic rod relative to the direction of the applied force.

where $C_{PE}^{(\lambda_q)}$ is the photo-elastic constant of the Nd-YAG crystal. For laser light of wavelength $\lambda_q = 1064$ nm or frequency $\nu_q \cong 281,76$ THz, the theoretical value of $C_{PE}^{(\lambda_q)}$ is 1.25×10^{-12} m²/N.

The sensitivity of the force sensor is approximated by the relation:

$$S(\ell, d) \cong \frac{(\alpha + \beta)\, C_{PE}^{\lambda_q}}{\pi\, n} \times \frac{\nu_q}{\ell\, d} \qquad (4)$$

In an ideal configuration, one edge of the cylindrical rod is in contact with a flat surface and the rod is illuminated by the laser beam along its axis of revolution. In this case α and β are related via [9]:

$$(\alpha + \beta) \cong 8/\pi \qquad (5)$$

These conditions are not easy to implement in the case of a monolithic laser of small diameter. To interpret the observed differences between measurements and theoretical predictions already used before [7], we sought to correctly model value of the form factor $(\alpha + \beta)$.

For value of $(\alpha + \beta)$ given by (5), the sensitivity is reduced to:

$$S(\ell, d) \cong 492,8 \times \frac{1}{\ell\, d} \qquad (6)$$

In (6), the sensitivity is in $\mathrm{MHz\, N^{-1}}$ if ℓ and d are in mm.

Precisely, the results of this approach have been confronted to experiments. As we will show in Section IV, the model used is not suitable especially for laser sensors using a small crystal. To improve this model, experimental values of sensitivity for different sizes $(\ell \times d)$ of the laser

transducer are of great interest and particularly for crystal size $(\ell \times d)$ where no data are available.

III. EXPERIMENT

The laser sensor is a cylindrical Nd-YAG crystal of parallel end faces (Figure 2). The pumping face is coated to have HR@1064 nm and HT@808 nm and the second one is coated with HT@808 nm and HR (99 %) @1064 nm. The laser is bonded to its holder formed by a rectangular channel having a width of 3.5 mm and a depth of 3 mm, machined in an aluminum part. The temperature of the rod and the holder assembly is stabilized to better than ± 0.02 °C by using a proportional-integral-derivative (P.I.D) controller.

In this experiment a new procedure is employed for loading the laser rod by a standard mass. In fact, a rectangular (3x2) mm flexible blade made from a sheet of HAVAR (a non-magnetic alloy, Co/Cr/Ni/Fe/W/..., of high strength) with a thickness of 10µm is bonded to the upper portion of the laser and plays the role of a pan as in an electromagnetic compensation balance. The photography of Figure 3 gives an overview of the experimental set-up. One can find more details on the experimental design in [7].

The various components as indicated in this Figure 3 are:
(1)- laser diode system @ 808 nm; (2)- lens; (3)- Nd-YAG rod; (4)- bandpass filter; (5)- $\pi/4$ polarizer; (6)- adjustable pinhole; (7)- lens; (8)- nanosecond photo-detector; (9)- spectrum analyzer.

IV. RESULTS

The response and the sensitivity of this photo-elastic sensor were analyzed by measuring the deviation of the beat note frequency when applying on the top of the laser deadweight linked to a mass standard, m_e.

A. Response of the sensor
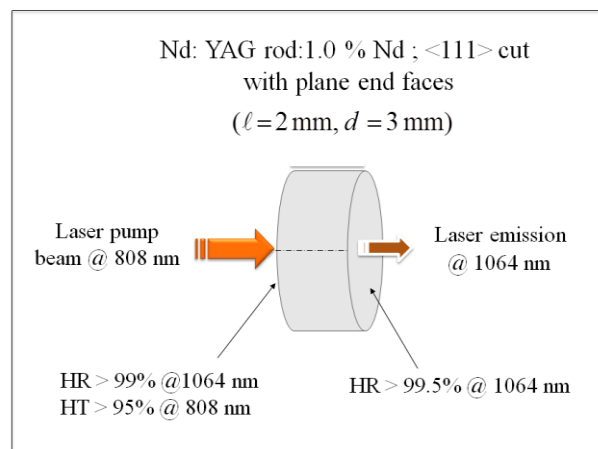
Figure 2. Monolithic configuration of the Nd-YAG laser force sensor.
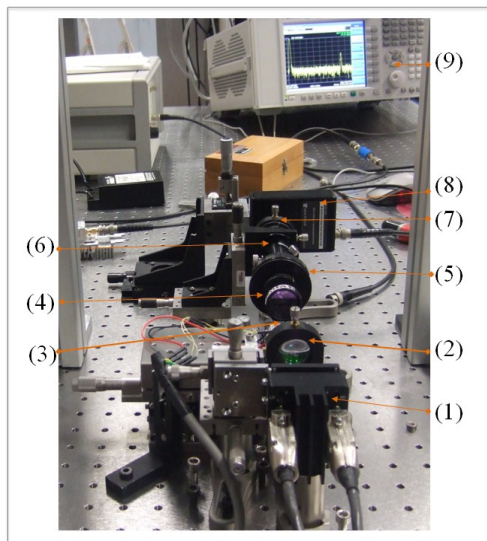
Figure 3.   View of the photo-elastic force sensor.

Figure 4.   Response of the sensor under the action of deadweight.

Mass standard of 0.1 g to 20 g were used to study the response of the photo-elastic sensor. As shown in Figure 4, the response is almost linear over the range studied and is checked on a wider range. In fact, same results were reported before for other size of photo-elastic Nd-YAG force sensor [6][7].

Using the least squares method, we deduce, from results reported in Figure 4, the mean value of the sensitivity and its uncertainty to:

$$S_{\mathrm{exp}} \cong 0.5947 \ (0.0034) \ \mathrm{MHz\,g}^{-1}.$$

In terms of force this value of sensitivity is equivalent to: $60.63\,(0.35) \ \mathrm{MHz\,N}^{-1}$

To study the reproducibility of measurements of frequencies we made several series of measurements using a calibrated mass of 5 g by measuring the frequency of the beat signal when the laser crystal was free and when it was subjected to the action of the net weight of the mass standard, m_e placed and staying on the top of the crystal in a perfect balance in the local gravitational field.

The condition to take correctly a frequency measurement is that mass standard placed on the crystal must remain truly balanced on the rod so that the load is distributed equally in each cycle of mass insertion and removal. This phase of measurement is the most critical because it affects the reproducibility of the stress exerted by the dead weight on the crystal.

Despite the fact that the procedure of insertion and removal of the mass standard is performed manually, the measurements turn out to be reproducible. The results of the beat frequency measurement are given in Table I.

TABLE I.   MEAN VALUES OF OBSERVED BEAT FREQUENCY WHEN THE LASER CRYSTAL IS UNLOADED THEN LOADED WITH A DEADWEIGHT OF 5 g.

State of the laser crystal	Observed beat frequency	
	Mean value (MHz)	Repeatability/ Reproducibility (MHz)
Unloadded	20.55	0.04/ 0.08
Loaded by mass $m_e = 5$ g.	23.51	0.05/ 0.1

The mean value and the associated uncertainty of repeatability are derived from the average of an actual range of ten values of measured frequencies for each state of the laser crystal.

The uncertainty of reproducibility is evaluated from the measurement of several repeated cycles of applying and removing the mass standard of 5 g. During successive cycles of loading and withdrawal of the force transducer, the mean frequency of the beat signal changes from 20.55 to 23.51 MHz. These values are obtained by averaging the observed frequencies measured alternately when the mass standard is inserted then removed. For a given situation of the the sensitive element of the transducer, the frequency of the beat note is measured with a repeatabilty better than 50 kHz. However, the reproducibility of the frequencies observed during a series of about fifteen successive loadings and removals is of the order of 100 kHz. This large scatter is mainly generated by the reproducibilty of internal stress distribution, induced in the center of the laser sensor, after each cycle of measurement when the sensing element is loaded by mass standard. A priori, one could reduce this limitation by improving the system of loading and unloading the sensitive element of the transducer.

Experimental sensitivity of the transducer, determined here by using only one mass standard, is given by:

$$S_{\text{exp}}^* = \frac{\Delta \nu^{(load)} - \Delta \nu^{(free)}}{m_e} \cong 0.592 \,\text{MHz g}^{-1} \qquad (8)$$

Or, $S_{\text{exp}}^* \cong 60.35 \,\text{MHz N}^{-1}$; this value is very close to $S_{\text{exp}} = 60.63 \,\text{MHz N}^{-1}$, deduced from linear fit of results reported in Figure 4.

The associated uncertainty of repeatability is:

$$u_{repeat}(S_{\text{exp}}) \cong 1.30 \,\text{MHz N}^{-1}$$

If one considers the most pessimistic situation related to the reproducibility of frequencies measurement in a series of mass standard insertions and removals, one obtains:

$$u_{reprod}(S_{\text{exp}}) \cong 2.61 \,\text{MHz N}^{-1}$$

This last uncertainty is the main limitation in terms of measurement for this kind of force sensor.

B. Sensitivity and size of the sensing element of the force sensor

The new values of sensitivity and his uncertainty are reported in Figure 5 and compared to the experimental measurements available for different force transducer reported before by others authors [9][10]. In this figure, only results obtained with a photo-elastic force sensor using monolithic Nd-YAG laser are considered for comparison. It can be seen, from this figure, that the predicted sensitivities by (6) corresponding to the ideal situation, discussed in Section II, are clearly superior to experimental values when the dimensions ($\ell \times d$) of the laser sensor are small. As one can see from Figure 5, this is the case of the two available experimental values of sensitivity, corresponding to $(\ell \times d) = 3$ and $6 \,\text{mm}^2$.

In Figure 5, the solid line is given by $S_1 = 492,8/(\ell d)$ and corresponds to a simple theoretical model (Section II) while the dot one, $S_2 = 310/(\ell d) + 3\ell d/4$, is an empirical relation which provides sensitivity values close enough to experimental results. Thus, the new results show that, when the sizes of the sensor are small, the sensitivity of the photo-elastic force sensor depends, in a relatively complex way, on the nature of the contact and on the localization of the applied force associated with the calibrated weight. Therefore, for the small size of the sensitive element, it is difficult to obtain high sensitivity with good reproducibility required for the measurement of small forces at the micronewton level with acceptable accuracy.

However, this type of sensor should prove useful for force measurement over a range of five orders of magnitude, namely from 0.1 mN to more than $10 \,\text{N}$. This wide range is very useful when trying to make comparisons with results obtained with other devices used in small force measurement.
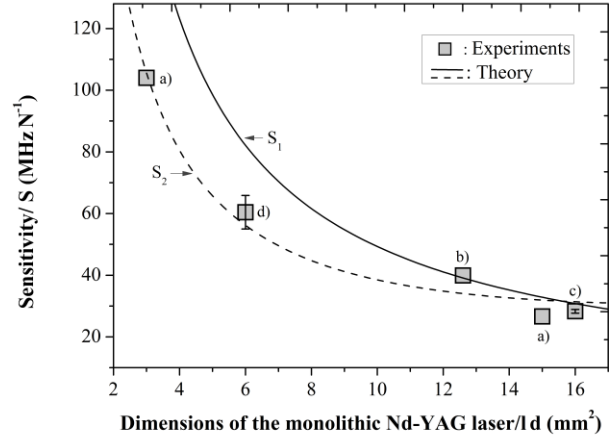
Figure 5. Sensitivity of the photo-elastic force sensor versus dimensions of the Nd-YAG rod. a)- [9]; b)- [10]; c)- [11]; d)- This work.

TABLE II. VALUES OF PHYSICAL QUANTITIES USED FOR THE DETERMINATION OF DEADWEIGHT F_{dw}.

Quantity	Value	Uncertainty
local gravity (ms^{-2})	$g_l = 9{,}8093810$	3×10^{-7}
Mass standard (g)	$m_e = 0.1$	5×10^{-6}
Mass density (kg m^{-3})	$\rho_e = 7850$	4×10^{-3}
Air density (kg m^{-3})	$\rho_a = 1.1950$	2×10^{-4}

C. Force measurement

The force acting on the laser sensor when a mass standard m_e is balanced on the rod, corresponds to the dead weight in the local gravity g_{loc}. It is given by:

$$F_{dw} = m_e g_{loc}(1 - \rho_a/\rho_e) \qquad (9)$$

i.e. the weight in vacuum minus the buoyancy correction. ρ_a and ρ_e are respectively the air density and the density of mass standard.

Using the values measured in the laboratory, as given in table II, the force exerted on the laser by the action of $m_e = 0.1$ g is theoretically: $F_{dw} = 9.808 \times 10^{-4} \,\text{N}$.

The dominant component of the overall uncertainty associated with this value of force comes from that of the standard mass, m_e.

$$u(F_{dw}) \cong (\partial F_{dw}/\partial m_e) u(m_e) \cong 10^{-8} \,\text{N}.$$

When this force acts on the sensing element, the shift induced on the frequency of the beat note is about 60 kHz, i.e., at the level of the reproducibility of frequency measurement. The measured force is determined from the experimental sensitivity of the force sensor and measurement of the frequency shift $\Delta \nu^{load} - \Delta \nu^{unload}$, induced by the action of an unknown force.

The intensity of this force is then calculated from:

$$F_{\exp} = (\Delta v^{load} - \Delta v^{unload})/S_{\exp} \qquad (10)$$

In the case of deadweight associated to $m_e = 0.1\,\text{g}$, the values of force determined from (10) and respectively $S_{\exp}$ and $S_{\exp}^*$ are:

$$\begin{cases} F_{\exp} = 9.90 \times 10^{-4}\ \text{N} \\ F_{\exp}^* = 9.94 \times 10^{-4}\ \text{N} \end{cases}$$

These experimental values differ by about 1 % from that calculated using (9). Considering the uncertainty of repeatability in the determination of the experimental sensitivity, the uncertainties associated with these values of force are at the same order, or:

$$u_{repeat}(F) \cong 1 \times 10^{-3}\ \text{N}.$$

Note that this uncertainty is at the level of the measured value for the applied force. On the other hand, the uncertainty of reproducibility is twice as important.

Since the sensor output is governed by the stress developed in the photo-elastic material, reading could be erroneous if the contact is located at one end of the crystal and not along one of its edges. The range of the applied force, at the micronewton level, can be improved by increasing the contact area of the sensor or by using photo-elastic material with higher constant of optical stress.

V. CONCLUSION

In this report, we have presented the photo-elastic force sensor used to characterize the response, in terms of sensitivity and its uncertainty, especially when the dimensions of the sensing element are small. The new determination of sensitivity was used to obtain the best fit between theoretical predictions and experimental values of sensitivity for the photo-elastic force sensors. Hence, the result is novel in the sense that it provides new information on the behavior of the sensitivity for a given sensor size, which showed the overall effect of the nature of the contact, represented by the geometrical factor, on the sensitivity of the sensor. To adjust the theoretical model so it agrees with the results of a set of measurements, we have reconsidered the contribution of the shape factor to the value of the sensitivity. Thus, fitting this parameter, we have reduced the observed differences between experimental values of sensitivities, based on photo-elastic effect in a monolithic Nd-YAG laser, and theoretical predictions.

Finally, we can conclude that this type of force sensor can provide high sensitivity, when using small size for sensitive element but we observe a slight deterioration in the reproducibility of the measurements. To avoid aging of the sensing element, the force range should be adjusted to avoid causing any distortion of the crystal as a result of lateral forces or torques. We plan to study these aspects in order to characterize the two sensors we have used for potential applications in industry. However, we believe that it can be quite suitable for the detection and measurement of force in the range of 1N- 0.1 mN. Also, it can be used and integrated to other systems in the view of traceable small force measurements to the International System of Units.

REFERENCES

[1] M.-S. Kim and J.R. Pratt, "SI traceability: Current status and future trends for forces below 10 microNewtons" Measurement 43, pp.169-182, 2010 . http://dx.doi.org/doi:10.1016/j.measurement.2009.09.005.

[2] C. Diethold and F. Hilbrunner, "Force measurement of low forces in combination with high dead loads by the use of electromagnetic force compensation" Meas. Sci. Technol. 23 pp. 1-7, 2012. http://iopscience.iop.org/0957-0233/23/7/074017.

[3] G. Xiao, X. Long, B. Zhang and G. Li, "Precise force measurement method by Y-shaped cavity dual-frequency laser", Chinesse Optics Letters 9(10), 101201, pp.1-4, 2011. http://dx.doi.org/10.3788/COL201109.101201.

[4] C.-F. Tuan, F.-L. Pan, Y.-C. Lin, S.-S. Pan and C.-L. Wu, "Sub-milligram weight subdivision and application in force calibration of nanoindenter", XIX IMEKO World Congress, Fundamental and Applied Metrology, Lisbon, september 6-11, 2009, pp. 393- 396.

[5] M. Appleyard, C. mosse, T. Mills, G. Ducan, D. Castillo and C. Swain, "The measurement of forces exerted during colonoscopy", Gastrointestinal endoscopy 52, pp. 237-240, 2000. http://dx.doi.org/10.1067/mge.2000.107218.

[6] W. Holzapfel and M. Finnemann, "High-resolution force sensing by a diode-pumped Nd-YAG laser"Optics Lett.18, n°13, pp.2062-2064, 1993. http://dx.doi.org/10.1016/S0263-2241(00)00042-7.

[7] N. Khelifa, "Small-Force Measurement by Photo-Elastic Transducer" Optics and Photonics Journal 4, n° 1, pp. 14-20, 2014. http://dx.doi.org/10.4236/opj.2014.41003.

[8] M. M. Frocht, " Photoelasticity" 1, Willey 1948, pp.144-149.

[9] Holzapfel, S. Neuschaefer-Rube and M. Kobusch, "High-resolution, very broadband force measurement by solid-state laser transducers", Measurement 28, pp. 277-291, 2000, http://dx.doi.org/10.1016/S0263-2241(00)00042-7.

[10] J. Ding, L.Zhang, Z. Zhang and S. Zhang, "Frequency splitting phenomenon of dual transverse modes in Nd:YAG laser", Opt. & Laser Technol. 42, pp. 341-346, 2010. http://dx.doi.org/10.1016/j.optlastec.2009.08.002

[11] N-E Khelifa and M. Himbert, "Induced birefringence in a solid-state laser: Towards a photo-elastic Nd:YAG transducer for small force measurement", Proceedings of the 3rd International Conference on Optics Photonics and their Applications ICOPA'2013, Algiers, december 9-11, 2013, paper n° 60, pp. 1-15.

Optical Processor Based on a-SiC Technology for Error Detection on a Spectral Data

Manuel Augusto Vieira[1,2]
[1]DEETC/ ISEL
Lisbon, Portugal
[2]CTS/UNINOVA
Monte de Caparica, Portugal
e-mail: mv@isel.pt

Paula Louro[1,2]
[1]DEETC/ ISEL
Lisbon, Portugal
[2]CTS/UNINOVA
Monte de Caparica, Portugal
e-mail: plouro@deetc.isel.ipl.pt

Manuela Vieira[1,2]
[1]DEETC/ ISEL
Lisbon, Portugal
[2]CTS/UNINOVA
Monte de Caparica, Portugal
e-mail: mv@isel.ipl.pt

Vitor Silva[1,2]
[1]DEETC/ ISEL
Lisbon, Portugal
[2]CTS/UNINOVA
Monte de Caparica, Portugal
e-mail: vsilva@deetc.isel.ipl.pt

Abstract— **In this paper, we exploit the nonlinear property of the SiC multilayer devices to design an optical processor for error detection that enables reliable delivery of spectral data of four-wave mixing over unreliable communication channels. The SiC optical processor is realized by using double pi'n/pin a-SiC:H photodetector with front and back biased optical gating elements. Visible pulsed signals are transmitted together at different bit sequences. The combined optical signal is analyzed. Data show that the background act as selector that pick one or more states by splitting portions of the input multi optical signals across the front and back photodiodes. Boolean operations such as EXOR and three bit addition are demonstrated optically, showing that when one or all of the inputs are present, the system will behave as an XOR gate representing the SUM. When two or three inputs are on, the system acts as AND gate indicating the present of the CARRY bit. Additional parity logic operations are performed using four incoming pulsed communication channels that are transmitted and checked for errors together. As a simple example of this approach, we describe an all-optical processor for error detection and then provide an experimental demonstration of this idea.**

Keywords- Optical processor, Integrated optical filter, Boolean operations, Coder/decoder device

I.   INTRODUCTION

Using visible light for data transmission, which is referred to as Visible Light Communication (VLC), opens a broad spectrum of applications, such as photonic circuits for the purpose of chip-level communications and location estimation. Increases in power efficiency per bit of data are projected to be achieved by replacing electrical interconnects with their optical counterparts in the near future. Digital optical systems and optical processors demand an all-optical arithmetic unit to perform different optical arithmetic operations. Various architectures, logical and/or arithmetic operations have been proposed in optical/optoelectronic computing [1][2][3][4]. Effort has been made for the development of all-optical logical functions [5] by using different schemes like optoelectronic devices based on optical nonlinear micro-ring resonators [6][7].

Multilayered Si/C structures based on amorphous silicon technology are reconfigurable to perform WDM optoelectronic logic functions [8][9]. They have a nonlinear magnitude-dependent response to each incident light wave. In this paper we exploit the nonlinear property of the SiC multilayer devices under steady state backgrounds to design an all-optical adder unit.

The SiC optical processor for error detection and correction is realized by using double pin/pin a-SiC:H photodetector with front and back biased optical gating elements. Red, green, blue and violet pulsed signals are transmitted together at different bit sequences. The combined optical signal is analyzed by reading out the photocurrent, under low wavelength background (350 nm) and different intensities. The operational principle of SiC based switches is discussed and the theoretical design of all-optical adder operation is reported. Experimental results confirming the described method are also presented.

After a short introduction, in Section II the design, characterization and operation of the device are presented. In Section III, the spectral sensitivity of the device is analyzed and, in Section IV, the nonlinear spectral gain is presented. Section V, refers the coder/decoder optical processor and in Section VI, the full-adder design is shown.

Error control methodology based on SiC technology is explained, in Section VII, and the conclusions appear, in Section VIII.

II. DEVICE DESIGN, CHARACTERIZATION AND OPERATION

The full-adder device is realized by using a double pi'n/pin a-SiC:H photodetector with TCO front and back biased optical gating elements as depicted in Figure 1. The active device consists of a p-i'(a-SiC:H)-n/p-i(a-Si:H)-n heterostructure. The thicknesses and optical gap of the front i'- (200 nm; 2.1 eV) and back i- (1000 nm; 1.8 eV) layers are optimized for light absorption in the blue and red ranges, respectively [10].

Optoelectronic characterization was performed through spectral response measurements without and with steady state applied optical bias.

Monochromatic (red, green, blue and violet; $\lambda_{R,G,B,V;}$) pulsed communication channels (input channels) are combined together, each one with a specific bit sequence and absorbed accordingly their wavelengths (see arrow magnitudes in Figure 1). The combined optical signal (multiplexed signal; MUX) is analyzed by reading out the generated photocurrent under negative applied voltage (-8V), without and with 390 nm background lighting at different intensities, applied either from front or back sides. The device operates within the visible range using as input colour channels the square wave modulated low power light supplied by red (R: 626nm), green (G: 524 nm), blue (B: 470 nm) and violet (V: 400 nm) LEDs.
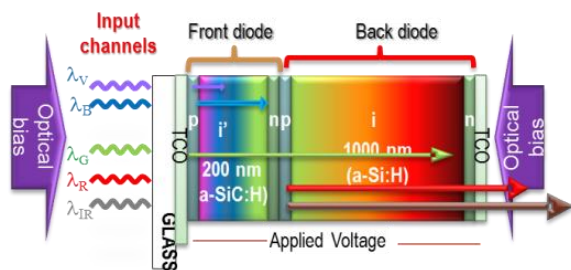
Figure 1.   Device configuration and operation.

III. SPECTRAL SENSITIVITY

The spectral sensitivity was tested through spectral response measurements [11] without and under 350 nm front and back violet backgrounds using different intensities. In Figure 2, the spectral gain (α), defined as the ratio between the spectral photocurrent with and without applied optical bias, is displayed under near-UV (λ=350 nm) illuminations. In Figure 2a, the light was applied from the front (λ_F) and in Figure 2b, the irradiation occurs from

the back side (λ_B). The background intensity (ϕ) was changed between 5µWcm^{-2} and 3800 µWcm^{-2}.

Results show that the optical gains have opposite behaviours under front and back irradiations. Under 350 nm front irradiation (Figure 2a) and low flux, the gain is high in the infrared region, presents a well-defined peak at 750 nm and strongly quenches in the visible range. As the power intensity increases the peak shifts to the visible range and can be deconvoluted into two peaks, one in the red range that slightly increases with the power density of the background and another in the green range that strongly increases with the intensity of the UV radiation. In the blue range, the gain is much lower.

This shows the controlled high-pass filtering properties of the device under different background intensities. Under back bias (Figure 2b) the gain in the blue/violet range has a maximum near 420 nm that quickly increases with the intensity. Besides it strongly lowers for wavelengths higher than 450 nm, acting as a short-pass filter. Thus, back irradiation, tunes the violet/blue region of the visible spectrum whatever the flux intensity, while front irradiation, depending on the background intensity, selects the infrared or the visible spectral ranges..

a)

b)
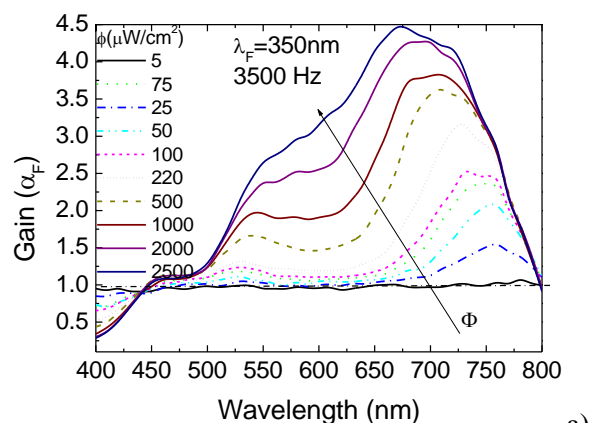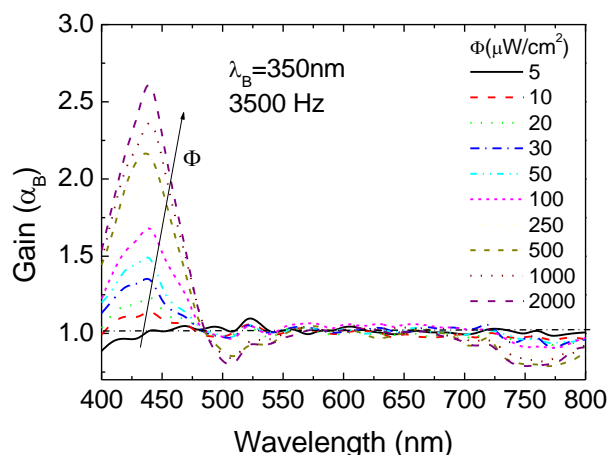
Figure 2.   a) Front (λ_F) and b) back (λ_B) spectral gains ($\alpha_{F,B}$) under λ=350 nm irradiation.

The results show that, low fluxes select the near infrared region and cuts the visible one, the reddish part of the spectrum is selected at medium fluxes, and high fluxes tune the red/green ranges with different gains

IV. NONLINEAR SPECTRAL GAIN

Several monochromatic pulsed lights separately (697 nm, 626 nm, 524 nm, 470 nm, 400nm input channels; transmitted data) or combined (MUX signal) illuminated the device at 12000 bps. Steady state 390 nm bias at different intensities due to different LED input currents ($0 < I_{LED} < 30$ mA) were superimposed separately from both sides and the photocurrent was measured. For each individual channel the photocurrent was normalized to its value without irradiation (dark) and the photocurrent gain ($\alpha^V_{R,G,B,V}$) determined. Figure 3, displays the different gain as a function of the drive currents of the lighting LED under front (a) and back (b) irradiation.

a)

b)
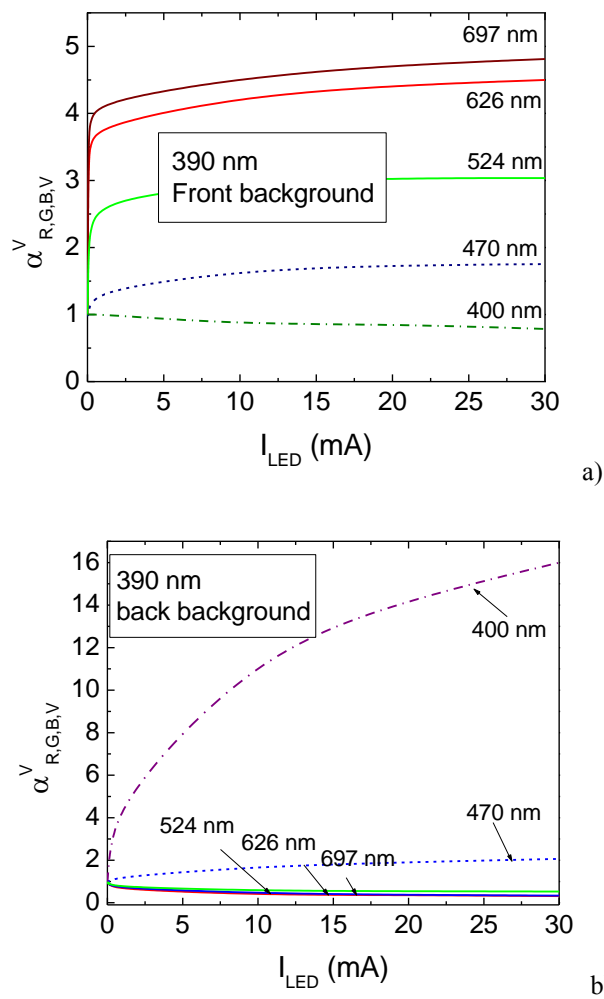
Figure 3. a) Front and b) back optical gain at λ=390 nm irradiation and different input wavelengths.

Results show that the gain depends mainly on the channel wavelength and slightly on the lighting intensity, for high fluxes. Even across narrow bandwidths, the gains are quite different. Under front irradiation (Figure 3a) the magnitude of the short wavelengths signals is quenched and enlarged in the long wavelengths range. The opposite happens when the background lighting is at the back side (Figure 3b). Here, the short wavelengths gain increases while the long wavelengths gain decreases. This behavior can be used to build selective filters, where the gain of the short and long pass filters is controlled by optical bias either at the front or back sides.

This nonlinearity allows identifying the different input channels in the visible range. Due to its low wavelength, the background light is absorbed at the top of the front diode and, due to the self-bias effect [6], increases the electric field at the back diode where the red incoming photons are absorbed accordingly their wavelengths (see Figure 1) resulting in an increased collection. Under back irradiation the electric field decreases mainly at the i-n back interface quenching the red/green input signals.

V. CODER/DECODER DEVICE

In Figure 4, the normalized MUX signal due to the combination of the red, green, blue and violet input channels (received data) is displayed under front and back irradiations (I_{LED}=30 mA). On the top, the input channels (transmitted data) are displayed. In the right side of the figure all the possible sixteen RGBV sublevels and their 4-bit binary code are inserted.

The results show that to each of all the possible 2^4 *on/off* states it correspond a well-defined level. Under front or back irradiation, each of those four channels, in turn, is enhanced or quenched (Figure 2 and Figure 3) accordingly its wavelength. So, 2^4 ordered levels (d_0-d_{15}) are detected (horizontal dot lines) and grouped into two main classes due to the high amplification of the red channel (α^V_{626}=4.5). The upper eight (2^3) levels are ascribed to the presence of the red channel (R=1), and the lower eight to its absence (R=0), allowing the red channel recognition. Since under front irradiation the green channel is also amplified (α^V_{524}=3) the four (2^2) highest levels, in both classes, are ascribed to the presence of the green channel (G=1) and the four lower ones to its lack (G=0). The blue channel is slightly amplified (α^V_{470}=1.75), so, in each group of 4 entries, two subclasses (2^1) can be found: the two higher levels correspond to the presence of the blue channel (B=1) and the two lowers to its absence (B=0). Finally, each group of 2 entries have two near sublevels (α^V_{400}=0.78), the higher level where the violet channels is ON (V=1) and the lower level where it is missing (V=0).

Figure 4.   MUX/DEMUX signals under 390 nm front and back UV irradiation and decoded RGBV binary bit sequences. On the top of the figure the transmitted channels are displayed.

Under back irradiation, the violet channel is strongly enhanced (α^V_{400}=16), the blue channel moderately (α^V_{470}=2) and the green and red strongly reduced ($\alpha^V_{524,626}$=0.3) allowing to confirm the presence of violet channel. In Figure 4, under front irradiation, $d_1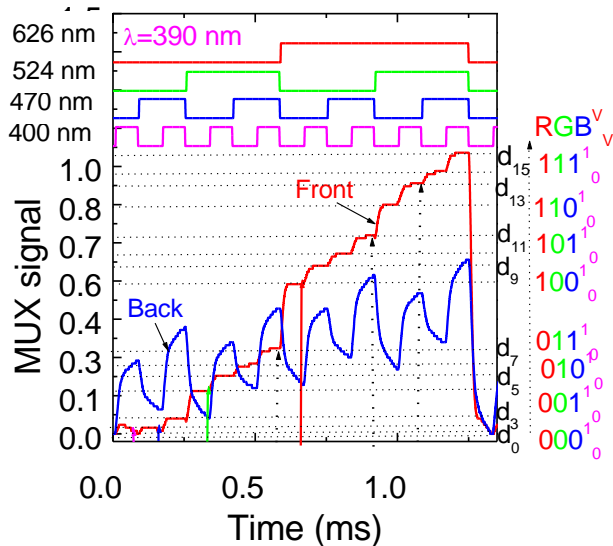$ and d_2 have similar values making difficult the decoding; however under back irradiation their recognition is obvious. So, from the front and back information the different bit sequences were decoded and the signal demultiplexed [9].

VI.   DESIGN OF FULL-ADDER BASED ON A-SIC TECHNOLOGY

A full adder circuit adds three single bit binary numbers (X, Y, Z) and gives result in two single bit binary outputs, called Sum (S) and Carry (C) that is a three-bit modulo-2 addition [12].
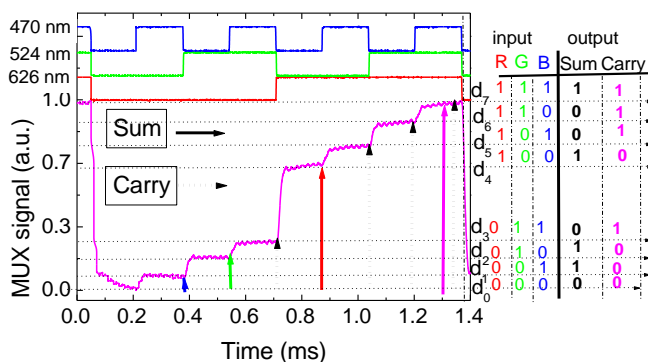
Figure 5.   MUX signal, output levels and truth table of a SiC full adder.

A full-adder circuit based on a-SiC technology uses the same principle; it adds three color single bit binary numbers (R,G,B) and gives result in two single bit binary outputs, (Sum, Carry). The design of full adder circuit is illustrated in Figure 5. Depending upon the state of the variables (R, G, B) the output is obtained from one of the eight output levels (d_0 to d_7).

Figure 5 displays the normalized MUX signals (received data) due to the combination of the red (R), green (G) and blue (B) input channels (transmitted data), under front irradiation. On the top the signals used to drive the input channels are displayed showing the presence of all the possible 2^3 on/off states ascribed to 8 separate current levels (d_0-d_7). All eight conditions presented above are listed in Table 1.

The corresponding truth table of full adder for three input binary (RGB) variables is shown in the right side of the figure. As expected from Figure 3 and Figure 4, the levels magnitude depends on the inputs wavelength amplification factors under irradiation.

So, a 3-binary code is associated to each level allowing signal decoding. Data shows that when one or all of the inputs are present the output will be weighted by their gains ($\alpha^V_{R,G,B}$), which corresponds to four different levels (d_1, d_2, d_4, d_7; solid arrows in Figure 5), the system behaves as a XOR gate, i.e., S =1 [13].

TABLE I   STATE OF DIFFERENT OUTPUT LEVELS

Inputs			Output of the different terminals							
R	G	B	d_0	d_1	d_2	d_3	d_4	d_5	d_6	d_7
0	0	0	1	0	0	0	0	0	0	0
0	0	1	0	1	0	0	0	0	0	0
0	1	0	0	0	1	0	0	0	0	0
0	1	1	0	0	0	1	0	0	0	0
1	0	0	0	0	0	0	1	0	0	0
1	0	1	0	0	0	0	0	1	0	0
1	1	0	0	0	0	0	0	0	1	0
1	1	1	0	0	0	0	0	0	0	1

If two or three input channels are simultaneously on, the output level will be weighted by each of the individual gains, therefore the system acts as AND gate. This corresponds to four separate levels (d_3, d_5, d_6, d_7; dot arrows) and indicates the presence of CARRY bit (C=1).

TABLE II   THE TRUTH TABLE OF THE FULL-ADDER

Inputs			Output	
R	G	B	Sum	Carry
0	0	0	0	0
0	0	1	1	0
0	1	0	1	0
0	1	1	0	1
1	0	0	1	0
1	0	1	0	1
1	1	0	0	1
1	1	1	1	1

Figure 6.   Schematic of the coding when the three parity bits are generated simultaneously in a SiC WDM circuit.

The truth table of the full-adder shown in the right side of the Figure 5 is displayed in Table 2.

VII.   ERROR CONTROL BASED ON A-SIC TECHNOLOGY

Fault tolerance can be achieved in many systems by using parity bits. SiC optical processor for error control is realized by using the same double pin/pin a-SiC:H photodetector.

Taking into account Figure 4, the encoder for code takes four input data bits [R, G, B,V; d_8, d_4, d_2, d_1] and creates three additional parity bits,

$$[P\text{-}(VRG), P\text{-}(VRB), P\text{-}(VGB); d_{13}, d_{11}, d_7] \qquad (1)$$

given by:

$$P\text{-}(VRG) = V \oplus R \oplus G \qquad (2)$$

$$P\text{-}(VRB) = V \oplus R \oplus B \qquad (3)$$

$$P\text{-}(VGB) = V \oplus G \oplus B \qquad (4)$$

i.e., the parity bits are SUM bits of the three-bit additions of violet pulsed signal with two additional bits of RGB. So, the seven-bit word at the output of the encoder will be in a bytewide format, with the data and the parity bits separated as decoded in Figure 4.

Here, the solid arrows shows the different signals that arise from to the presence of one of the four wavelength channels [R, G, B, V] and the doted arrows marks the generate parity bits. Thus, three independent logic functions can be implemented in a SiC WDM circuit. In this case the three-bit adder circuit described above can be used as an encoder for the code, which simultaneously generates the three parity bits. This is schematically shown in Figure 6.

To make a distinction between transmitted and received data, the transmitted bits are denoted by upper case and the received bits are by lower case. Thus, the transmitted word is:

$$[R, G, B,V, P\text{-}(VRG), P\text{-}(VRB), P\text{-}(VGB)] \qquad (5)$$

whereas the received word is:

$$[r, g, b,v, p\text{-}(vrg), p\text{-}(vrb), p\text{-}(vgb)] \qquad (6)$$

or else:

$$[d_8, d_4, d_2, d_1, d_{13}, d_{11}, d_7]. \qquad (7)$$

Since d_1 is present in all three parity bits, it is the first bit that is checked for errors. The following additions are performed on the received bits:

$$v\text{-}(rg) = SUM[p\text{-}(vrg), r,g] \qquad (8)$$

$$v\text{-}(gb) = SUM[p\text{-}(vgb),g,b] \qquad (9)$$

$$v\text{-}(rb) = SUM[p\text{-}(vrb), r,b] \qquad (10)$$

Taking into account Figure 3b and Figure 4 under back irradiation, the signal is strongly enhanced if the violet bit is on it *on* state, allowing confirming it presence if generated. Combining the two pieces of information (generated parity bits and back signal levels) either the absence, or the presence of one or double errors, even for similar values of, for instance, d_1 and d_2, will be easily checked.

In the absence of any errors, received bit equals transmitted bit. Each of the above additions would equal d_1. If v-(rg) is computed in the absence of any errors, it equals d_1.

$$v\text{-}(rg) = SUM[p\text{-}(vrg), r,g] = SUM[d_{13}, d_8 , d_4] =$$

$$= d_{13} \oplus d_8 \oplus d_4 = d_1 \oplus d_8 \oplus d_4 \oplus d_8 \oplus d_4 = d_1 \qquad (11)$$

In the presence of one error, for example, if the error is on d_2, (see Figure 4), i.e:

$$\overline{d}_2 = d_2 \oplus 1 \qquad (12)$$

and making the same operation:

$$v\text{-}(gb) = SUM[p\text{-}(vgb),\ g,\ b),\ d_4,\ \overline{d}_2\ ] \qquad (13)$$

$$= d_7 \oplus d_4 \oplus \overline{d}_2\ = d_1 \oplus d_2 \oplus 1 \oplus d_4 \oplus d_2 \oplus d_4 = \overline{d}_1$$

obviously, the results for the two other operation are:

$$v\text{-}(rg) = d_1 \qquad (14)$$

and

$$v\text{-}(rb) = \overline{d}_1 \qquad (15)$$

However, any double error will not violate the parity check of *P*

$$P = r \oplus g \oplus b \oplus v \oplus p\text{-}(vrg) \oplus p\text{-}(vrb) \oplus p\text{-}(vgb) \qquad (16)$$

but will violate some of the p-(vrg), p-(vrb), p-(vgb) parity checks, thus providing an indication of the double error.

Thus, parity preserving reversible circuit design can be implemented optically being very useful in the development of fault tolerant reversible systems in emerging nanotechnology.

VIII. Conclusions

The nonlinear property of the SiC multilayer devices under front and back lighting backgrounds were exploited to design an optical processor for error detection and correction that enables reliable delivery of spectral data of four-wave mixing over unreliable communication channels.

The design of an optical full-adder was presented. Additional parity logic operations were performed using four incoming pulsed communication channels that are transmitted and checked for errors together. As a simple example of this approach, we described an all optical processor for error detection and then provided an experimental demonstration of this idea.

Acknowledgment

References

[1] S.Lin, Y.Ishikawa, and K.Wada, ''Demonstration of optical computing logics based on binary decision diagram'', Optics Express, 20 (2), 2012, pp. 1378-1384..

[2] Jin Y, Shen, et al. "Principles and construction of MSD adder in ternary optical computer." Sci China Inf Sci, 53: 2010, pp.2159–2168.

[3] R. W. Hamming, ''Error detecting and error correcting codes'' Bell Syst. Tech. J. 29, 1960 pp. 147–160.

[4] A. J. Poustie, K. J. Blow, A. E. Kelly, and R. J. Manning, ''All-optical binary half-adder,'' Opt. Commun. 156, 1998 pp. 22–26.

[5] K.E. Zoiros, G. Papadopoulos, T. Houbavlis, and G.T. Kanellos, ''Theoretical analysis and performance investigation of ultrafast all-optical Boolean XOR gate with semiconductor optical amplifier-assisted Sagnac interferometer'', Opt. Commun. 258 (2) 2006, pp.114–134.

[6] T.A.Ibrahim, et al. ''All optical nonlinear switching in GaAs-AlGaAsmicroring resonators'', IEEE Photonics Technology Letters, 14 (1), 2002, pp.74-76.

[7] J.N. Roy and D.K. Gayen, ''Integrated all-optical logic and arithmetic operations with the help of TOAD based interferometer device – alternative approach'', Appl.Opt. 46 (22), 2007, pp.5304–5310.

[8] M. Vieira, P. Louro, M. Fernandes, M. A. Vieira, A. Fantoni, and J. Costa, ''Three Transducers Embedded into One Single SiC Photodetector: LSP Direct Image Sensor, Optical Amplifier and Demux Device'', Advances in Photodiodes, InTech, Chap.19, 2011, pp. 403-425.

[9] M. A. Vieira, M. Vieira, J. Costa, P. Louro, M. Fernandes, and A. Fantoni, "Double pin Photodiodes with two Optical Gate Connections for Light Triggering: A capacitive two-phototransistor model" Sensors & Transducers Journal, 9, Special Issue, December 2010, pp.96-120,.

[10] M.A. Vieira, P. Louro, M. Vieira, A. Fantoni, and A. Steiger-Garção, "Light-activated amplification in Si-C tandem devices": A capacitive active filter model 2012 IEEE sensor jornal, 12, NO. 6, 2012, pp. 1755-1762.

[11] M. A. Vieira, M. Vieira, P. Louro, V. Silva, and A. S. Garção, "Photodetector with integrated optical thin film filters" 2013 Journal of Physics: Conference Series 421 012011 (March 2013) doi:10.1088/1742-6596/421/1/012011.

[12] J. H. Kim, Y. T. Byun, Y. M. Jhon, S. Lee, D. H. Woo, and S. H. Kim, "All-optical half adder using semiconductor optical amplifier based devices," Optics Communications, 218, 2003, pp. 345–349.

[13] T. Houbavlis and K.E. Zoiros, "Ultrafast pattern-operated all-optical Boolean XOR with semiconductor optical amplifier-assisted Sagnac switch", Opt. Eng. 42 (12), 2003, pp. 3415–3416.

Near-UV Background in Photonic Based pi'n/pin Amorphous SiC Sensors

Manuela Vieira, Manuel AugustoVieira, Vitor Silva,
Paula Louro,
CTS/UNINOVA
Monte de Caparica, Portugal
e-mail: mv@isel.ipl.pt

Manuela Vieira, Manuel Augusto Vieira, Isabel
Rodrigues, Vitor Silva, Paula Louro,
DEETC/ISEL
Lisbon, Portugal
e-mail: mv@isel.ipl.pt

Abstract— **In this paper, we present a wavelength selector based on a monolithic multilayer pi'n/pin a-SiC:H optical filter that requires appropriate near-ultraviolet steady states optical switches to select the desired wavelengths in the visible-near infrared (VIS-NIR) ranges. Results show that the background intensity works as a selector in the infrared/visible regions, shifting the sensor sensitivity. Low intensities select the NIR range while high intensities select the visible part. Here, the optical gain is very high in the red range, decreases in the green range, and stays near one in the blue region decreasing strongly in the near-ultraviolet range. The transfer characteristics effects due to changes in steady state light intensity and wavelength backgrounds are presented. The relationship between the optical inputs and the output signal is established when a multiplexed signal is analysed. An optoelectronic model gives insight into the physics of the selector.**

Keywords- Integrated optical filter, VIS-NIR communications, Photonics-based sensors, Optoelectronics

I. INTRODUCTION

Newly developed technologies for infrared telecommunication systems allowed the increase of capacity, distance and functionality, switching and control with the design of new reconfigurable logic active filter gates by "bridging the gaps" and combining the optical filters properties. Expanding far beyond traditional applications in optical interconnects at telecommunication wavelengths [1] [2], the SiC nanophotonic integrated circuit platform has recently proven its merits for working with visible range optical signals. To enhance the transmission capacity and the application flexibility of optical communication efforts have to be considered, namely the Wavelength Division Multiplexing based on tandem a-SiC:H light controlled filters, when different visible signals are encoded in the same optical transmission path [3] [4]. In this paper, the shift of the visible range to telecom band can be accomplished using the same wavelength selector but under near-ultraviolet optical bias, acting as reconfigurable active filters in the visible and near infrared ranges. These active filters act as interface devices that establish the bridge between the infrared and red spectral range playing a key role to bridging the infrared and the visible optical communication technology. They can be used to perform different filtering processes, such as: amplification, switching, and wavelength conversion.

After a short introduction, in Section II, the design, characterization, and operation of the device is described. In Section III, the light filtering properties are analyzed and in Section IV, the methodology that supports the visible/infrared tuning is presented. In Section V, an optoelectronic model gives insight into the physics of the device and, finally in Section VI the main conclusions are presented.

II. DEVICE DESIGN, CHARACTERIZATION AND OPERATION

The selector is realized by using a double pi'n/pin a-SiC:H photodetector with TCO front and back biased optical gating elements as depicted in Figure 1. The active device consists of a p-i'(a-SiC:H)-n/p-i(a-Si:H)-n heterostructure. The thicknesses and optical gap of the front i'- (200 nm; 2.1 eV) and back i- (1000 nm; 1.8 eV) layers are optimized for light absorption in the blue and red ranges, respectively [5].

Optoelectronic characterization was performed through spectral response and transmittance measurements without and with steady state applied optical bias. The optical bias (ϕ; background) was superimposed using near-ultraviolet Light Emitting Diodes (LEDs) (390 nm). Currents between 0.005 mA and 30 mA were used to drive the LEDs in order to change the light flux background.
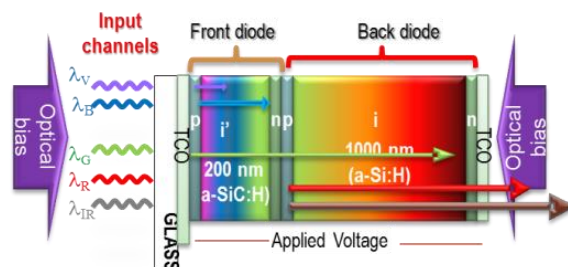

Figure 1. Device configuration and operation.

Monochromatic (infrared, red, green, blue and violet; $\lambda_{IR,R,G,B,V;}$) pulsed communication channels (input channels) are combined together, each one with a specific bit sequence and absorbed accordingly their wavelengths (see arrow magnitudes in Figure 1). The combined optical signal (multiplexed signal; MUX) is analyzed by reading out the generated photocurrent under negative applied voltage (-8V), without and with near-ultraviolet background (390nm) and different intensities, applied either from front (λ_F) or back (λ_B) sides. The device operates within the visible/NIR range using as input color channels the square wave modulated low power light supplied by near-infrared/red (NIR/ R: 880 nm-626nm), green (G: 524 nm), blue (B: 470 nm) and violet (V: 400 nm) LEDs.

In Figure 2a, the transmittances from the front and back diodes are plotted as well as the transmittance of the complete device without any background light. In Figure 2b, the transmittance is displayed under different 390 nm background intensities.
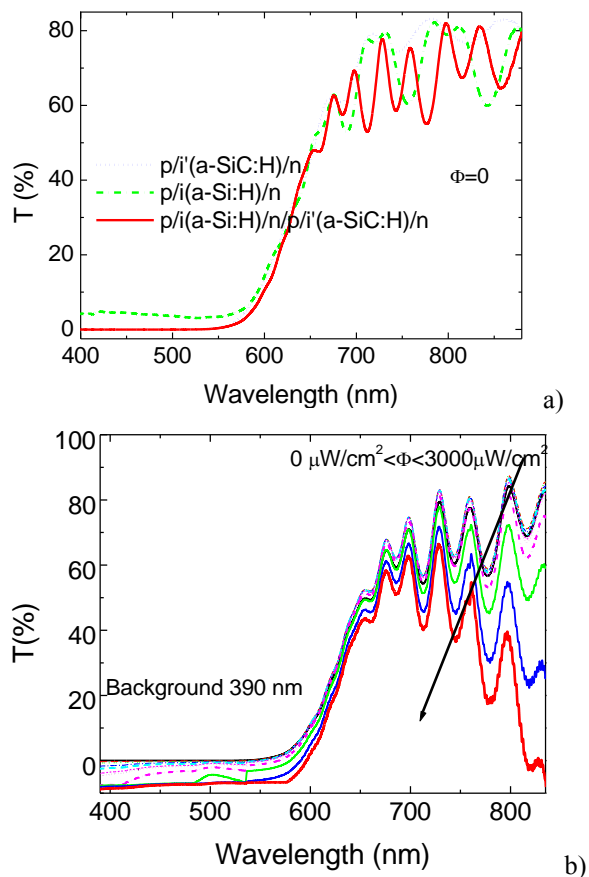
Figure 2.   Transmittances from: a) front, back and whole device; b) the pi'npin structure under front irradiation, with 390 nm irradiation and different intensities.

Results confirm the influence of the thickness of each front and back diode on the transmittance of the whole device. It is interesting to notice that under front light

irradiation, the transmittance decreases in the infrared range as the background intensity increases leading to an infrared absorption window.

III.   LIGHT FILTERING PROPERTIES

The spectral sensitivity was tested through spectral response measurements [6] [7] without applied optical bias and under 390 nm front and back backgrounds of variable intensities. In Figure 3 the spectral gain (α), defined as the ratio between the spectral photocurrent with and without applied optical bias, is displayed under near-UV (λ=390 nm; Figures 3a and 3b) illuminations. In Figure 3a, the light was applied from the front (λ_F) and in Figure 3b, the irradiation occurs from the back side (λ_B). The background intensity (ϕ) was changed between $5\mu Wcm^{-2}$ and 3800 μWcm^{-2}.
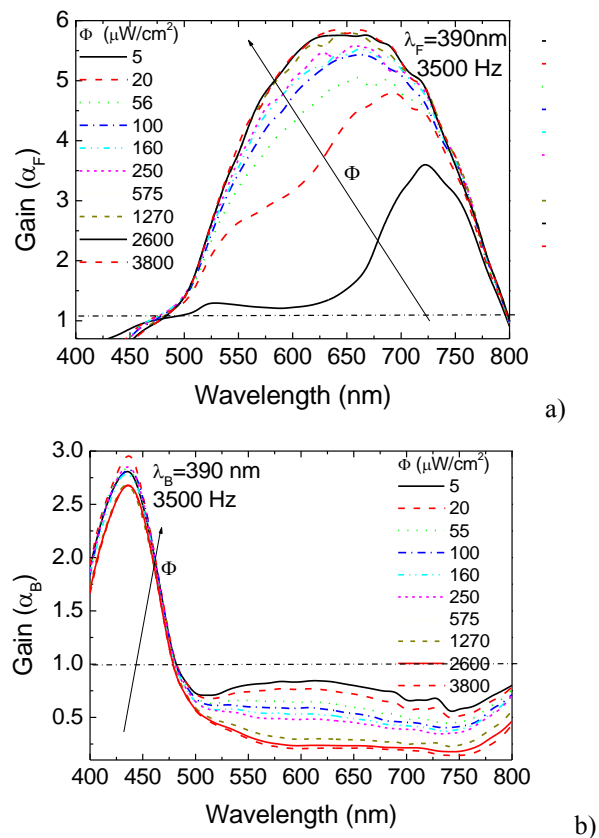
Figure 3.   Front (a) and back (b) spectral gains ($\alpha_{F,B}$) under λ=390 nm irradiation.

Results show that the optical gains have opposite behaviors, under front and back irradiations. Under 390 nm front irradiation (Figure 3a) and low flux, the gain is high in the infrared region, presents a well-defined peak at 750 nm and strongly quenches in the visible range. As the power intensity increases, the peak shifts to the visible range and can be deconvoluted into two peaks, one in the red range that slightly increases with the power density of the background and another in the green range that strongly

increases with the intensity of the ultra-violet radiation. In the blue range, the gain is much lower. This shows the controlled high-pass filtering properties of the device under different background intensities. Under back bias (Figure 3b) the gain in the blue/violet range has a maximum near 420 nm that quickly increases with the intensity. Besides it strongly lowers for wavelengths higher than 450 nm, acting as a short-pass filter. Thus, back irradiation, tunes the violet/blue region of the visible spectrum whatever the flux intensity, while front irradiation, depending on the background intensity, selects the infrared or the visible spectral ranges. Here, low fluxes select the near infrared region and cut the visible one, the reddish part of the spectrum is selected at medium fluxes, and high fluxes tune the red/green ranges with different gains.

IV. VISIBLE AND INFRA-RED TUNING

Four monochromatic pulsed lights separately (645nm, 697 nm, 850 nm and 880 nm input channels) or combined (MUX signal; Figure 5) illuminated the device at 12000 bps.

Steady state 390 nm bias at different intensities ($1\mu Wcm^{-2} < \phi_{F,B} < 3000\mu Wcm^{-2}$) were superimposed separately from the front and the back device side and the photocurrent was measured. The ratio between the photocurrent with and without applied optical bias was inferred and the gain for each wavelength channel determined. In Figure 4a, 880 nm transient signals at different flux irradiation are presented under front irradiations and back irradiations and in Figure 4b for the 645 nm channel the diverse gain are also displayed. In Figure 4c the gains for the four analyzed channels are shown as a function of the background intensity.

As expected from Figure 3, in the red/infrared spectral ranges, the optical gain depends on optical bias intensity and on the wavelength of the input channels. Results show that, even under transient conditions and using commercial visible and NIR LEDs, the background side and intensity alters the signal magnitude of the input channels. Under front irradiation, as the light flux increases, the magnitudes of all the input channels increases being higher at 645 nm then at 697 nm, 850 nm or 880 nm. Under back irradiation, as the flux intensity increases the magnitude of the channels decreases, quickly in the visible range and stays almost constant in the infrared range. Even across narrow bandwidths, the photocurrent gains are quite different (Figure 4c). This nonlinearity provides the possibility for selective tuning of the visible and IR wavelengths allowing their recognition.

In Figure 5, the MUX signals due to the combination of the four wavelength channels is displayed, under front and back irradiation. The signals were normalized to their values at the maximum flux.

Results confirm that the magnitude of the combined signal depends mainly on the channel wavelength through its own gain.
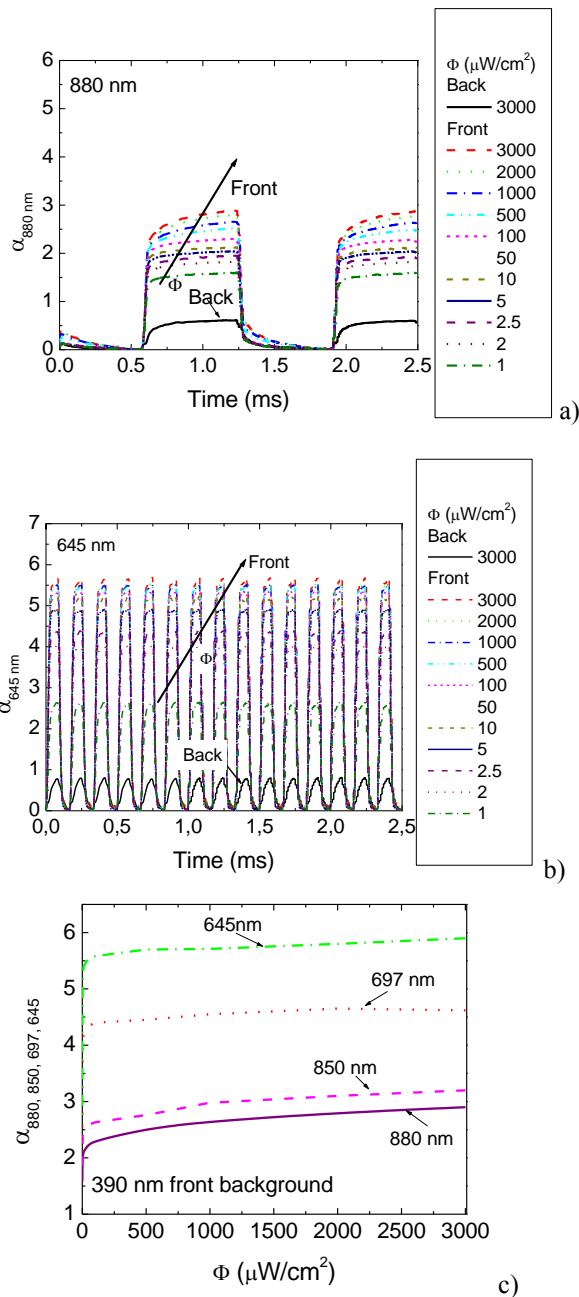
Figure 4. Front (a) and back (b) gains using λ=390 nm irradiation at different intensities. (c) Optical gains as a function of the background intensity.

Under front and back irradiation, the gains are different, front irradiation enhances the red/infrared channels (Figure 4c) while back light quench them. The gains inferred under 3000 µW/cm² back irradiation were respectively $\alpha_{880}=0.61$, $\alpha_{850}=1.03$, $\alpha_{697}=0.92$, $\alpha_{645}=0.85$.
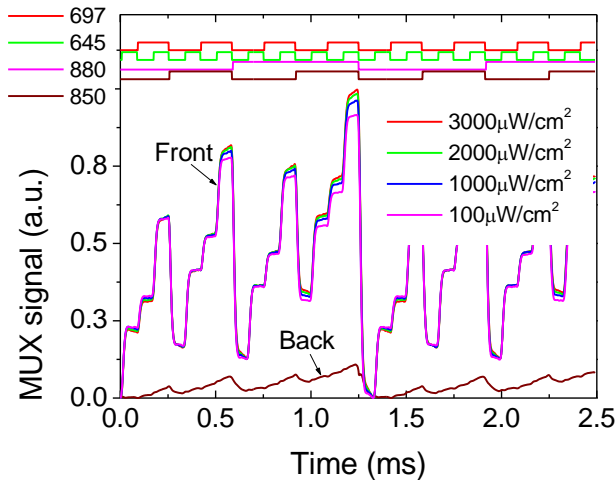
Figure 5.   Front and back MUX signals under front and back λ=390 nm irradiation and different background intensities.

This nonlinearity allows identifying the different input channels in a narrow red/infrared range. The 390 nm radiation is absorbed at the beginning of the front diode and, due to the self-bias effect, increases the electric field at the back diode where the red/infrared incoming photons (see Figure 2) are absorbed accordingly to their wavelengths (see Figure 3) resulting in an increased collection. Under back irradiation, the electric field decreases mainly at the i-n back interface quenching the red/NIR input signals in different ways. This effect may be due to the increased absorption under back irradiation (Figure 2) that increases the number of carriers generated by the infra-red photons. So, by switching between front and back irradiation the photonic function is modified from a long- to a band-pass filter allowing, alternately selecting the red or the infrared channels, making the bridge between the visible and the infrared regions.

V.   OPTOELECTRONIC MODEL

Based on the experimental results and device configuration a two connected phototransistors model (Figure 6a), made out of a short- and a long-pass filter was developed [5] and upgraded to include several input channels.

In Figure 6b, the block diagram of the optoelectronic state model is displayed. The resistors (R_1, R_2) and capacitors (C_1, C_2) synthesize the desired filter characteristics. The input signals, $\lambda_{IR,Rn,G,B,V}$ model the input channels and $i(t)$ the output signal. The amplifying elements, α_1 and α_2 are linear combinations of the optical gains of each impinging channel, respectively into the front and back phototransistors and take into account the enhancement or quenching of the channels (Figure 4) due to the steady state irradiation. Under front irradiation: $\alpha_2 \gg \alpha_1$ and under back irradiation $\alpha_1 \gg \alpha_2$. This affects the reverse

photo capacitances, ($\alpha_{1,2} / C_{1,2}$) that determine the influence of the system input on the state change.
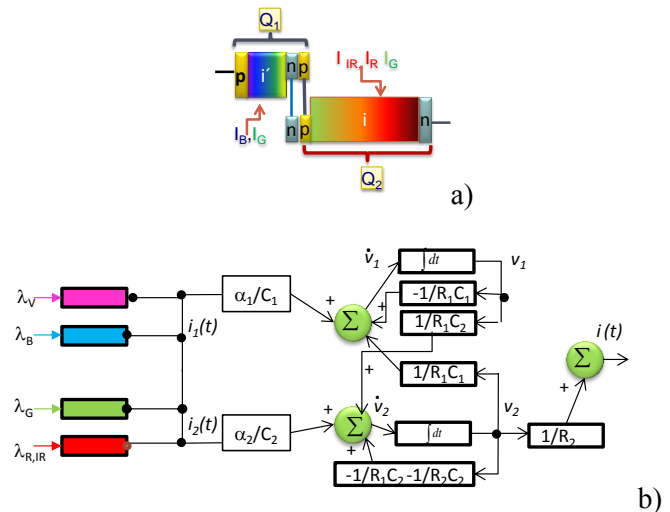
Figure 6.   a) Two connected transistor model, b) block diagram of the optoelectronic state model.

A graphics user interface computer program was designed and programmed within the MATLAB® programming language, to ease the task of numerical simulation. This interface allows selecting model parameters, along with the plotting of both bit signal and simulated and experimental photocurrent results. To simulate the input channels we have used the individual magnitude of each input channel without background lighting, and the corresponding gain at the simulated background intensity (see Figures 4). Figure 7, presents results of a numerical simulation with 3000 µW/cm² front and back λ=390 nm irradiation, using in Figure 7a the MUX signal of Figure 5 and in Figure 7b a VIS/NIR combination of λ_V=400 nm, λ_G=524 nm, λ_R=697 nm, λ_{IR}=850 nm input channels. Here, the front gains were α_V=0.82, α_G=2.85, α_R=4.35, α_{IR}=3.27 and the back ones, respectively: 11.5, 0.68, 0.92 and 0.5. Values of R_1=10 KΩ, R_2=1 KΩ, C_1=1000 pF, C_2=20000 pF were used during the simulation process (Figure 6b). On top of both figures the drive input LED signals guide the eyes into the different *on/off* states and correspondent wavelengths.

A good fitting between experimental and simulated results was achieved. The plots show the ability of the presented model to simulate the sensitivity behaviour of the proposed system in the visible/infrared spectral ranges. The optoelectronic model with light biasing control has proven to be a good tool to design optical filters. Furthermore, this model allows for extracting theoretical parameters by fitting the model to the measured data (internal resistors and capacitors).
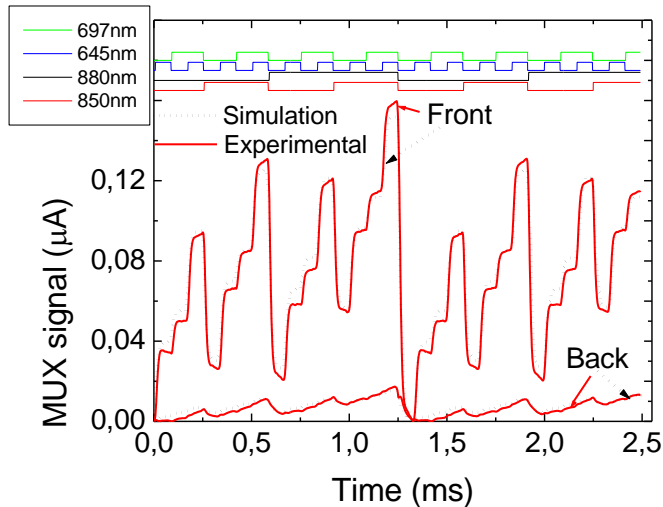
a)
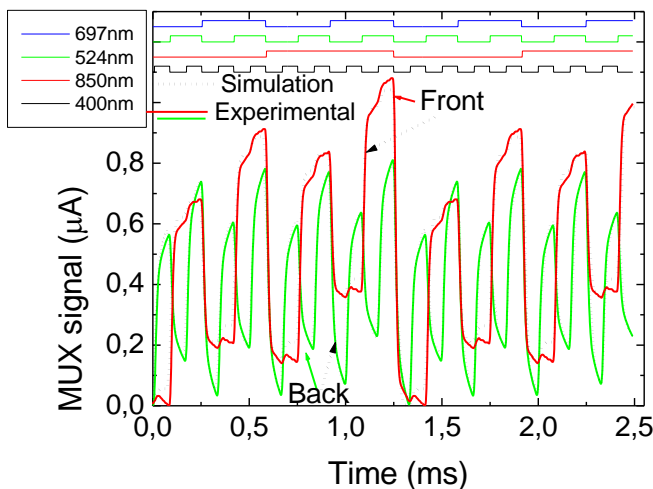
b)

Figure 7. Numerical simulation with front and back λ=390 nm irradiation, and different channel wavelength combinations

Under back irradiation higher values C_2 were obtained confirming the capacitive effect of the near-UV radiation on the device that increases the charge stored in the space charge layers of the back optical gate of Q_2 modelled by C_2.

VI. CONCLUSIONS

An optoelectronic device based on a-SiC:H technology is analyzed. Tailoring the filter wavelength in the NIR/VIS was achieved by using near-ultraviolet backgrounds and changing the irradiation side and intensity. Results show that the pi´n/pin multilayered structure functions and parameters are reconfigurable under front and back irradiation, acting as data selector in the VIS/NIR ranges. The device performs wavelength division multiplexing (WDM) optoelectronic logic functions providing photonic functions such as signal amplification, filtering and switching. The opto-electrical model with light biasing control has proven to be a good tool to design optical filters in the VIS/NIR. An optoelectronic model was presented and proven to be a good tool to design optical filters in the VIS/NIR range.

REFERENCES

[1] P. P. Yupapin and P. Chunpang, "An Experimental Investigation of the Optical Switching Characteristics Using Optical Sagnac Interferometer Incorporating One and Two Resonators," Optics & Laser Technology, Vol. 40, No. 2, 2008, pp. 273-277.

[2] S. S. Djordjevic et al. "Fully Reconfigurable Silicon Photonic Lattice Filters With Four Cascaded Unit Cells" IEEE photonics Technology Letters, 23, NO. 1, january 1, 2011, pp.41-44.

[3] M. Vieira, P. Louro, M. Fernandes, M. A. Vieira, A. Fantoni and J. Costa, "Three Transducers Embedded into One Single SiC Photodetector: LSP Direct Image Sensor, Optical Amplifier and Demux Device", Advances in Photodiodes", InTech, Chap.19, 2011, pp. 403-425.

[4] M. A. Vieira, M. Vieira, J. Costa, P. Louro, M. Fernandes, and A. Fantoni, "Double pin Photodiodes with two Optical Gate Connections for Light Triggering: A capacitive two-phototransistor model", Sensors & Transducers Journal, 9, Special Issue, December 2010 , pp.96-120.

[5] M.A. Vieira, P. Louro, M. Vieira, A. Fantoni, and A. Steiger-Garção, "Light-activated amplification in Si-C tandem devices: A capacitive active filter model" IEEE sensor jornal, 12, NO. 6, 2012, pp. 1755-1762.

[6] M. A. Vieira, M. Vieira, P. Louro, V. Silva, and A. S. Garção, "Photodetector with integrated optical thin film filters" Journal of Physics: Conference Series, 421, 012011 March 2013.

[7] M. Vieira, M. A. Vieira, I. Rodrigues, V. Silva, and P. Louro,"Tuning optical a-SiC/a-Si active filters by UV bias light in the visible and infrared spectral ranges", Phys. Status Solidi, C, 2014, pp. 1-4 .Article first published online: 25 JUL 2014. DOI: 10.1002/pssc.201400020

Remote Health Monitoring Device for the Elderly

Development of an Affordable and Easy-to-use Breathing Monitoring Device

Matthew Clark, Jaerock Kwon, Girma Tewolde

Electrical and Computer Engineering
Kettering University
Flint, MI, USA
{clar8299, jkwon, gtewolde}@kettering.edu

Abstract— **In the USA, the oldest of the baby-boomer generation just started to reach retirement age a few years ago. In the years to come, a much larger percentage of the population will be dependent on others for their daily care. There are not many low-cost monitoring devices available on the market to help caregivers keep dependent elderly people comfortable and healthy in a home setting without a monthly service charge. The device presented in this paper addresses this challenge to provide caregivers an emergency alert system for the elderly based on monitoring of their breathing activities and room temperature measurements. The device also allows the dependents to make on demand request for assistance. The remote communication is enabled through the cellular telephone services; so there is no special or additional subscription services needed. This is essential to make the device more affordable for the elderly.**

Keywords-health monitoring; remote elderly monitoring; breathing monitoring; emergency alert.

I.   INTRODUCTION

The oldest of the baby-boomer generation just started to reach retirement age a few years ago. In the years to come a much larger percentage of the population will be dependent on others for their daily care. In fact, the ratio of caregivers to boomers needing care in 2010 was 7.2 to 1 and is expected to decrease to 2.9 to 1 by 2050 [1].

Being a caregiver for an elderly relative can be a very demanding experience. Therefore, there will be higher demand on devices that help caregivers to remotely monitor the elderly. Unlike the devices in the market that are available for newborn care, there are not many products for home use intended for elderly monitoring applications. Such devices would be of critical value for caregivers to help keep elderly dependents comfortable and healthy in a home setting without a monthly service charge.

There are only a handful of elderly monitoring devices on the market that offer features such as help at the push of a button and fall detection. Not only are these devices lacking potential life-saving features such as movement detection and room temperature monitoring, they also require a monthly service fee in addition to an existing telephone line. For example, Philips Lifeline, a popular elderly monitoring device, requires a subscription with plans starting at $29.95 per month [2].

In the research community, there are a few systems that have been developed for breathing monitoring of the elderly.

For example, Fook et al. [3] present non-intrusive respiratory monitoring system for detection of life threatening systems in bed ridden patients. The system uses Fiber Bragg Grating pressure sensors mounted on beds for continuous monitoring of the respiratory rate of patients without requiring them to wear any device.

In the wearable bio sensors category, there are a number of devices available for many different monitoring applications. As an example, Chan et al. [4] present wireless patch sensor for remote monitoring of heart rate, respiration, activity, and falls.

The goal of our project is to monitor breathing movement of elderly dependents and provide the capability to send automatic alerts to health care professionals in case of abnormalities. Data analysis is conducted to study the nature of the data and minimize false alarms, so users do not lose confidence in the device and stop using it. Additional feature of temperature monitoring is also incorporated to ensure that the dependent stays in a comfortable environment. If the room temperature exceeds a pre-set limit, an automatic alert is sent to the care giver. The device also allows the dependent to request assistance on demand, by pressing a help button.

Here is a list of criteria that our monitoring device will meet in order to benefit both the caregivers and the dependent elderly.

- The device must alert the caregiver if no breathing movement is detected. This will allow the caregiver to get emergency help right away.

- The device must not produce false breathing movement alarms. False alarms would dramatically decrease the usefulness of the motion detection feature and could frustrate users to the point of not using the feature.

- The device must be able to monitor room temperature and alert the caregiver if the temperature is outside of the preset range. This will help ensure the dependent elderly is comfortable.

- The device must allow the dependent elderly to request assistance. This request could be for anything from needing a drink to needing help getting to the bathroom.

The rest of this paper is organized as follows. The next section details the hardware design of the monitoring device.

Section III presents the software design, which is made up of the software running on the embedded microcontroller and the software for the Smartphone app. Finally, the project results are discussed and concluding remarks as well as future recommendations provided.

II. MONITORING HARDWARE DESIGN

The critical component of this project is the breathing detection sensor. The sensor pad shown in Figure 1 is created for breathing movement detection. This unit is made up of one pressure sensor and three piezo vibration sensors. It is built by placing the sensors between two clear plastic folder dividers. The folders are held together using both extra strength double sided tape as well as epoxy. Electrical tape is also used to hold the wires together where they exit the sensor pad. The sensors were positioned in a way to help minimize the risk of false alarms. The vibration sensors are spread out to detect movement in different areas of the sensor pad and the pressure sensor is located near the vibration sensors to make sure the dependent is on the sensor pad correctly before enabling breathing alerts. Lastly, there are four pieces of Velcro on the back of the sensor pad. These were used to help the sensor pad stay in position when using it in a recliner. A rectangular piece of cotton fabric is purchased and Velcro sewn to it. This fabric could then be draped over the back of the recliner and the sensor pad could be securely placed on it.

Figure 1.   Sensor pad. (a) Vibration sensor; (b) Pressure sensor; (c) Velcro that is used to help the sensor pad stay in position.

The data collection and processing of the breathing sensor device is handled by the Arduino Uno microcontroller, which offers 6 analog inputs and 14 digital I/O pins. This is a commonly available and inexpensive microcontroller that is excellent for quick proof-of-concept and prototyping.

Wireless communication between the Arduino microcontroller and Android devices is done using a Bluetooth interface module. For this project, the Bluetooth Mate Silver [5] is used, which gave reliable connection and reasonably good range.

A temperature sensor is used for monitoring the room temperature. For this purpose, the Maxim Integrated temperature sensor DS18B20 [6], shown in Figure 2, is chosen due to its low cost and adjustable precision temperature sensing.

Figure 2.   Maxim Integrated DS18B20 temperature sensor

Inside of the breathing sensor pad there is one FlexiForce Pressure Sensor for the sole purpose of enabling motion detection when pressure is applied. There are also three piezo vibration sensors spread out inside the sensor pad to detect breathing movement.

An LCD screen is used for the primary purpose of displaying the current room temperature. A basic 16x2 character LCD is sufficient for the task, since the information to be displayed is simple alphanumeric characters. The LCD is equipped with a backlight to improve its readability in a dark room. A toggle switch is connected to the backlight control pins to allow the user control the backlight on or off.

A large red pushbutton switch is used to allow the dependents to press it when they require assistance. The choice or the large size is to make it easier for an elderly person to find it when looking to press the pushbutton.

Two LEDs are mounted on the front panel of the device for use as indicator lights. A green LED is used to indicate that the dependent is on the sensor pad and the breathing monitoring is active. A red LED is used as a warning indicator. It would blink for a short duration if the help button is pressed or if no breathing motion is detected while a dependent elderly is on the sensor.

An actual prototype of the circuitry for the control system is shown in Figure 3 below. In the final implementation the microcontroller and all the other components will be assembled on a printed circuit board, to make a clean and robust device.
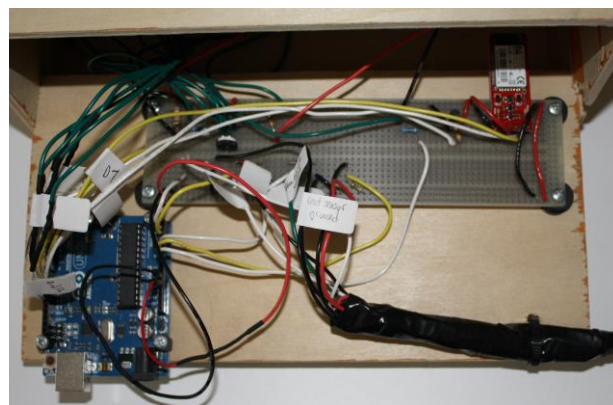

Figure 3.   Initial prototype of the control system

The wiring diagrams that describe the circuit design are shown in Figures 4 and 5. To reduce complexity of the diagrams the LCD diagram is shown in a separate figure.
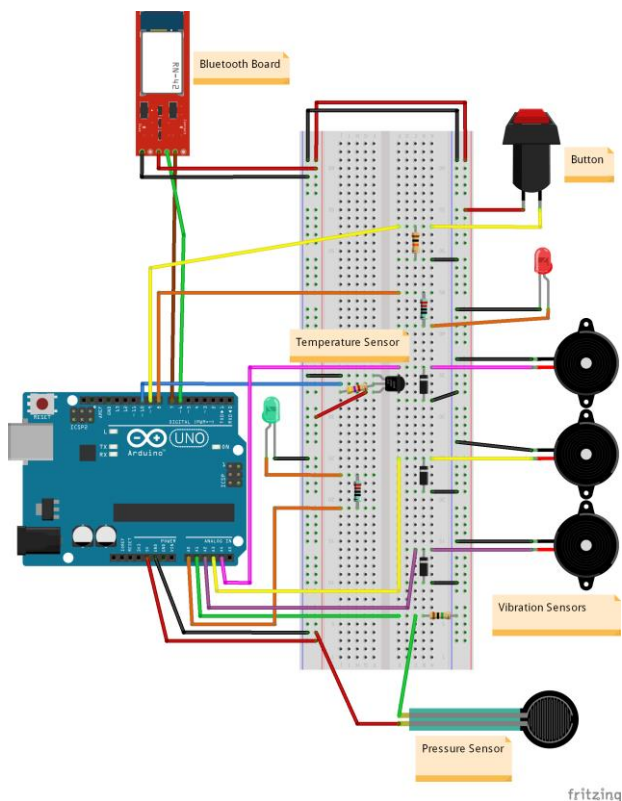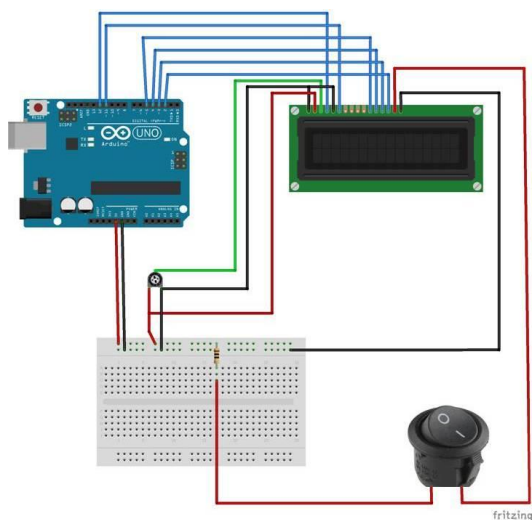
Figure 4.   Wiring diagram excluding LCD

Figure 5.   Wiring diagram for an LCD and a switch

All of the user interface elements that the dependent elderly needs to interact with are conveniently mounted on the device enclosure. As seen in Figure 6 below, the LCD screen and LEDs are mounted on the front of the box for easy viewing whereas the toggle switch and help button are mounted on top for easy pressing.
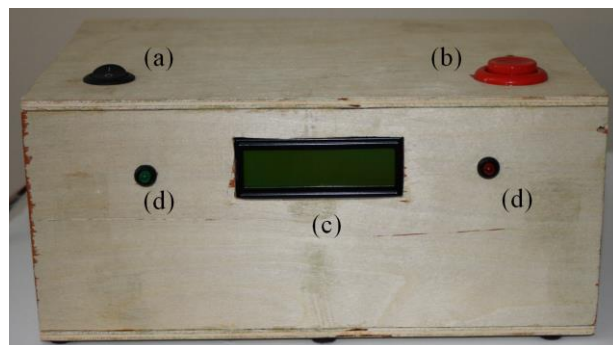

Figure 6.   Monitor front view. (a) LCD backlight toggle switch; (b) Pushbutton; (c) LCD screen; (d) Green and Red LEDs

This prototype system is powered by a 9V battery. The design is verified to meet its functional requirements through basic testing by the authors and a few random subjects.

III.   MONITORING SOFTWARE DESIGN

There are two software programs developed for the monitoring system. The Arduino software dealt with data from the various hardware and sensors whereas the primary purpose of the Android software is to get data from the monitoring device and send text message alerts to healthcare providers when needed.

The Arduino application starts by initializing all of the variables and hardware components. It then constantly loops through the various functions which include checking for a pushed button, updating the room temperature, sending data to the Android device, checking for breathing movement, and toggling the LEDs if necessary. Software timers are used to limit how often the room temperature is checked and how often information is sent to the Android device. These timers are also used to create breathing movement detection time frames which will be further discussed later.

When the Android application starts, it loads previously saved data such as the contact phone number and the desired room temperature range. If this data has not been updated it will load the default room temperature range of 70-80°F and notify the user that they need to enter a phone number so that alerts can be sent. At start-up the application also automatically connects to the Arduino Bluetooth board. A new thread is created that waits to receive data from the Arduino. Each time data is received, the user interface elements such as the current temperature are updated. The data is also evaluated to determine if a text message needs to be sent. Further details about this are discussed later.

A simple data structure is created for the communication between the Arduino and Android devices. During every communication, the Arduino device sends data made up of two integers separated by a colon. The first number is the current temperature (in Fahrenheit) and the second is an alert code (Table I). For example, "77:0" would mean the current room temperature is 77°F and there are no alerts.

TABLE I. ALERT CODES

Alert Code	Alert Type
0	No alert
1	Help button was pressed
2	Movement not detected

Alert codes are used to inform the care provider if they need to give attention to the user. They could be triggered by the user pressing the help button, or automatically by the sensor when it determines that the breathing state of the person is below a specified threshold value.

A. Breathing Movement Detection

Breathing movement detection is a bit complex. To be enabled, the reading from the pressure sensor pin has to be at least 0.3 volts. When enabled, there are motion detection time windows. Each window is 25 seconds long. During these windows the software keeps track of the minimum and maximum readings for each of the three vibration sensors. At the end of the window, it takes the difference for each of the sensor's minimum and maximum values and compares the difference with set threshold values. This method was found to work well experimentally for detecting the difference between a breathing person (Figure 7) and a non-breathing object (Figure 8). If all three differences are below the set threshold values, the emergency alert is set and sent to the Android device. This also enables fast toggling of the red LED for 8 seconds. After each detection window ends, all of the variables are reset to prepare for the next window.
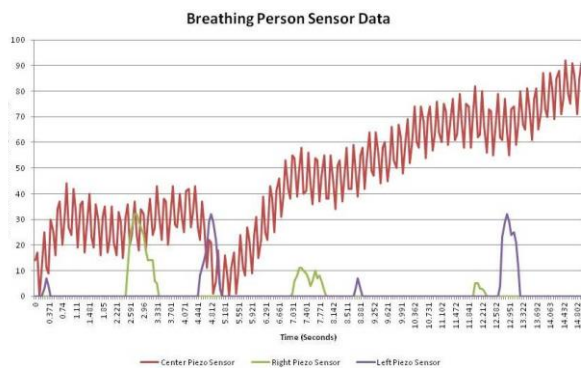
Figure 7. Sensor data for a breathing person

B. Android Application – Caregiver Assistant

The Android application, titled Caregiver Assistant, has been designed and tested to operate on any Android device with OS 2.3 or newer. The application allows the user to change settings such as the desired room temperature range and the phone number where text alerts are sent. It also acts as a second room temperature display. Figure 9 shows what the application looks like with each section labeled.

The first thing the Android application does after it establishes a Bluetooth connection with the Arduino device is to send it a short message. This is how the Arduino device

is notified that the Android device has been connected. Following this the Arduino immediately sends temperature data that is displayed on the Android device right away.
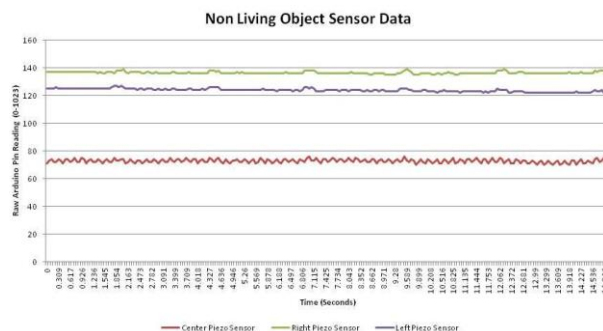
Figure 8. Sensor data for a non-breathing object
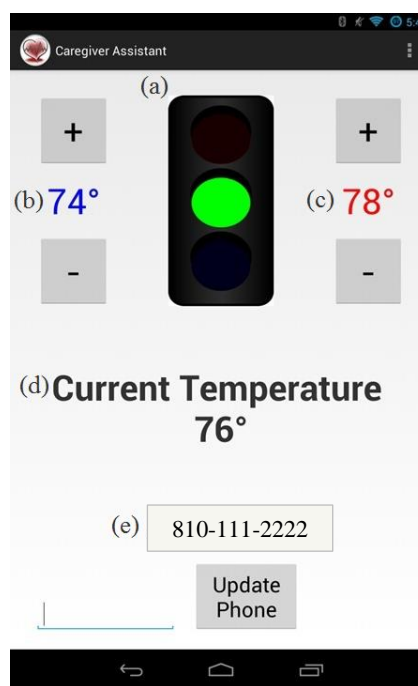
Figure 9. Android application user interface. (a) Temperature status indicator; (b) Minimum room temperature setting; (c) Maximum room temperature setting; (d) Current room temperature display; (e) Alert phone number display and update field

In the Android application, there is a thread that waits to receive data from the Arduino device. Once data is received a few things occur. First the information needs to be split to separate the temperature from the alert code. Next, the temperature on the display is updated. It also checks this updated temperature value to see if it is outside of the range in the current settings. If it is outside of the range, then a text message alert is sent indicating that the room temperature is either too warm or too cold. It then looks at the alert code. As stated earlier, if the alert code is 0 then nothing needs to

be done. If the code is not 0 then it would send the text message alert for either a button press or no breathing detected. Sample text messages for all of these instances can be seen in Table II.

TABLE II.   PREDEFINED TEXT MESSAGES

Alert Type	Text Message
Temperature Alert	Temperature Warning - Current room temperature is 62 which is outside of the current desired range
Alert Code = 1 (Button Press)	I need assistance (Button pressed)
Alert Code = 2 (Emergency)	EMERGENCY - Help ASAP

IV. DISCUSSION

In this section the analysis of the device's operation is presented. After initial testing of the breathing monitoring device that was presented in this paper the following observations are made from evaluations on how well the system meets its initial requirements.

- The device must alert the caregiver if no breathing motion is detected
  - An emergency text message is sent to the caregiver if not enough movement is detected.

- The device must not produce false breathing movement alarms
  - A pressure sensor is included in the sensor pad to disable motion sensing when the user is not on the sensor pad. This eliminates false alarms caused by the user not sitting on the sensor pad.
  - Data was collected both with people and with non-breathing objects on the sensor pad. Using the data, thresholds for each vibration sensor were set accordingly. This eliminates false alarms when the user is on the sensor pad.

- The device must be able to monitor room temperature and alert the caregiver if the temperature is outside of the entered range.
  - The caregiver can use the Android application to set a desired room temperature range.
  - A text message alert is sent to the caregiver if the temperature goes outside of the range indicated in the Android application.

- The device must allow the dependent to request assistance.
  - The dependent can press a large red button if they need the caregiver for any reason.
  - The device will send a text message to the caregiver, indicating that the button was pressed and the dependent needs help.

V. CONCLUSION AND FUTURE WORK

A prototype of a fully-functional elderly monitoring device was developed that is able to monitor breathing movement and room temperature, and alert the caregiver whenever assistance is needed. Overall, the proposed system was successful as each of the system criteria was met, as demonstrated in the previous section. Similar to competing devices, the alerts require a phone service that supports text messages and a smartphone that can run Android App. However, by sending the alerts to a caregiver or family member directly, the proposed system eliminates the additional service fee that the competition requires to operate their call centers.

Although the presented elderly monitoring device was successful, the following improvements could be considered to make the device even better.

- Implement a wireless version of the sensor pad for easier device placement

- Add an option to allow fall risk alerts. An alert can be sent to the caregiver if the elderly dependent gets up.

- Add the ability to add multiple contact phone numbers within the Android application, allowing more than one person to be contacted in emergency situations.

- Add a momentary toggle switch to allow the user to cycle through various predefined text messages instead of only being able to use the general "I need help" message.

REFERENCES

[1] W. Hamilton, Baby boomers may have no one to care for them in old age. Los Angeles Times. [Online]. Available from: http://www.latimes.com/business/money/la-fi-mo-baby-boomers-may-have-no-one-to-care-for-them-in-old-age-20130826,0,2883385.story#axzz2v7YvAMTE   [Retreived: September 15, 2014]

[2] Philips, What Lifeline Costs. [Online]. Available from: http://www.lifelinesys.com/content/lifeline-products/what-lifeline-costs, 2014 [Retreived: September 15, 2014]

[3] V. F. S. Fook, et al., "Non-intrusive respiratory monitoring system using Fiber Bragg Grating sensor," 10th International Conference on e-Health Networking, Applications, and Services, July 2008, pp. 160-164, doi: 10.1109/HEALTH.2008.4600128.

[4] A. M. Chan, N. Selvaraj, N. Ferdosi, and R. Narasimhan, "Wireless patch sensor for remote monitoring of heart rate, respiration, activity, and falls," 35th Annual International conference of the IEEE EMBS. July 2013, pp. 6115-6118, doi: 10.1109/EMBC.2013.6610948.

[5] Bluetooth Mate Silver. [Online]. Available from: https://www.sparkfun.com/products/12576   [Retreived: September 15, 2014]

[6] Maxim Integrated DS18B20 Prgrammable resolution 1-wire digital thermometer. [Online]. Available from: http://www.maximintegrated.com/en/products/analog/sensors-and-sensor-interface/DS18B20.html [Retreived: September 15, 2014]

Benthic Fish Behavior Characterization
with a Mechanically Scanned Imaging Sonar

Wen-Miin Tian

Department of Marine Environment and Engineering
National Sun Yet-sen University
Kaohsiung City, Taiwan
tiwemi@mail.nsysu.edu.tw

Abstract—**A point stationary, acoustic-based surveying system was proposed to fulfill the necessities of benthic fish behavior assessment. The surveying system can be split into two major and inter-dependent techniques, i.e., acoustic image acquisition and image processing. The first part comprises a high-frequency, mechanically scanned imaging sonar (MSIS) with bottom-fixed, side-looking working configuration. Major modules of the proposed image processing procedure include: stationary objects subtraction, region and textural feature extraction, unsupervised classification, fish target identification and quantification. For the specific case study conducted in a deep water fishpond, it is evident that both individual and school fish could be discriminated by image frames collected at a randomly selected point with scanning range setting at 5 m and frame rate at 75 second. Based on spatial and temporal analyses on position and area of the discriminated fish targets, it was concluded that fish movement pattern in the scanned area followed two distinctive corridors with significant different passage rate, i.e., a discrete, periodic and high passage rate mode in Corridor#1 and a continuous, steady and low passage rate mode in Corridor#2. Environmental features, such as bank slope, substrate mound and float raft represented specific meeting points for dynamic aggregations and schooling. Fish tended to converge into prominent schools subsequent to interactions with these features. The proposed system represented a practical and cost effective tool in acquiring image frames with sufficient spatial and temporal resolution for the characterization of fish behavior.**

Keywords-image sonar; mobile target; image processing; unsupervised classification; fish behavior.

I. INTRODUCTION

Artificial benthic habitats are known to be effective in promoting coastal fishery resources and coastal fisheries management. A large number of artificial reef programs have been conducted world wide, basically in Japan, France, the United States of America and Spain among others [1][2]. In Taiwan, a long-term, government sponsored project for the construction and deployment of artificial reefs to enhance commercial fisheries was initiated in 1973. For the last forty years, over 220,000 units of various types of artificial reefs were deployed in 88 promulgated sites [3]. For the purpose

to promote an efficient administrative and management system, these artificial reef sites were systematically surveyed especially by side-scan sonar [4]. Information regarding geographic position and engineering characteristics of these artificial reefs as well as substrate composition were collected, evaluated and documented. However, due to a shortage of professionals devoted to conduct in-situ biological assessment investigation and the limitations of some traditional sampling techniques employed, the biological effectiveness of the most of these artificial reef sites was assessed in a very primitive way.

From a physics point of view, benthic fish which aggregated around artificial reefs is a type of underwater mobile object which distributed on or near to the artificial reefs and sea bottom. The dimensions of a typical reef fish could be varied from as small as several centimeters (e.g., juvenile fish) to over 50 cm. The swimming speed and behavior of the fish added complexity to an assessment system. Nondestructive underwater surveying techniques which can offer adequate information for the effective detection and evaluation of this type of mobile object to fine spatial and temporal scales should therefore include the following fundamental requirements, i.e., effective in dark and turbid water environment, capable of cover sufficient water volume and feasible for extended working time (24 hours or even over a week). In addition, the quality and resolution of the information collected should comply with the criteria to the detection, classification or even identification of each object individually.

Underwater acoustic systems are standard tools for monitoring fish and other objects in marine and freshwater environments [4]-[8]. Advances in acoustic technology and analysis software have made this survey method more powerful in recent years. Based on deployment configurations, these systems can be classified into two categories of operation modes, i.e., mobile survey mode (e.g., echo sounder and side-scan sonar) and point stationary survey mode (e.g., split-beam sonar, sector scanning sonar, multi-beam sonar and 3D-sonar). Among them, systems operated in mobile survey mode with a vertically oriented, hull-mounted transducer are a standard tool for assessment of mid-water fish stocks. A significant benefit of this survey mode is that large areas can be sampled continuously in a

short amount of time [5]. Systems operated in point stationary survey mode with fixed-location and side-looking sonar techniques are capable of detection, quantification and even identification of demersal and benthic fish. They are mostly used for anadromous fish abundance estimation, fish behavior observation around fixed facilities and may be helpful in validation of fish species [7][8].

To fulfill the necessities of underwater mobile object detection and benthic fishery abundance assessment in a cost effective way, a comprehensive research project sponsored by National Science Council and National Chung-Shan Institute of Science and Technology was conducted. Based on theoretical evaluations, a point stationary, acoustic-based surveying system was proposed and implemented. The system can be split into two major and inter-dependent components, i.e., image acquisition and image processing. The first part comprises a high-frequency, mechanically scanned imaging sonar (MSIS) with bottom-fixed, side-looking working configuration. The second part incorporates an unsupervised Bayesian classification procedure for fish target detection and quantification. The objective of this paper was dedicated in evaluating the practicality and characteristics of the proposed surveying system.

Performance of the proposed sonar equipment in detecting mobile objects is discussed in Section 2. Image processing procedures and techniques are described in Section 3. A comprehensive evaluation of the entire surveying system for the purpose of fish target detection, relative abundance quantification and behavior investigation is illustrated in Section 4. Finally, results and conclusion remarks are shown in Section 5.

II. Equipment and Acoustic Principles

MSISs perform scans in a 3D volume by rotating a sonar beam through a series of small angle steps. The side-looking acoustic pulse is projected perpendicular to the sonar head. For each emitted beam, distance vs. echo-amplitude data is returned. Thus, accumulating this information along a complete 360° sector, a composite acoustic image of the surroundings can be obtained [9]. Commonly, the waiting time between each beam is directly proportional to the selected range setting and a total of 1,200 pings are needed to complete a 360° sector with stepping speed of 0.3°. Therefore, these devices have a slow scanning rate of at least several seconds per image frame.

The quality or naturalness of the acoustic images, i.e., identifiability of image content, can be degraded by distortion due to an unstable transducer. MSISs with bottom-fixed and completely stationary configuration for image acquisition provide a stable mount and there will be no effects of yaw or roll-induced movement when the sonar is suspended from a cable [10]. This working configuration is, therefore, ideal for operations to obtain the highest quality or undistorted images.

The basic principles behind the detection of an object in the water with an acoustic system are described by the "sonar equation" [11]:

$$V = SL + G - 40logR - 2\alpha R + TS + 2B(\theta, \phi) \qquad (1)$$

where,

V	=	the received intensity of the echo
SL	=	the transmitted source level
G	=	the receiving gain of the system
40logR	=	the two-way spreading loss, R is the range
α	=	the sound attenuation coefficient
TS	=	the acoustic target strength
$B(\theta,\phi)$	=	the transducer directivity pattern function

If the value of V is sufficiently greater than background noise, the object will be detected. For any given noise level, the potential to detect a target is improved with greater source level, less propagation loss, greater target size, and proximity of the target to the center of the beam. As a result, the received echo intensity of an individual target is primarily dependent on the sonar equipment (e.g., frequency and electronic characteristics), physical properties of seawater as well as the physical and behavior properties of the target. The importance of these factors is discussed in the following sections.

A. Sonar equipment

The primary component of the acoustic equipment in this investigation is a digital, multi-frequency imaging sonar (model 881A, Imagenex), capable of operating at frequencies of 1 MHz, 675 kHz and 310 kHz with fan shaped beams of 0.9°x10°, 1.8°x20° and 4°x40°, respectively. The stepping speeds of the sonar are from 0.3°/step to 2.4°/step with range scales from 1 m to 200 m. Because the sonar is limited to 512 by 512 pixels for displaying each frame, the size of the frame determines the display resolution and images with smaller range length are better resolved. The mid-range area insonified by a single ping of the sonar at range setting of 5 m, frequency of 1 MHz and fan shaped beam of 0.9°x10° is 3.9 cm (width) by 44 cm (height). The area insonified will increase dramatically with increased range length setting due to the inherent adjustment of frequency and beam pattern settings. The frame update rate of the sonar is controlled by the combination of range and stepping speed settings. At range scale of 5 m and stepping speed of 0.3°/step, the minimum theoretical scanning time for each frame needs 42 seconds. At the same range scale but faster stepping speed (e.g., 0.9°/step), the time could be reduced to 14 seconds.

B. Environmental and target properties

Physical properties of seawater, physical and behavior properties of the target, as well as the influence of noise to the detection of mobile object were discussed in this section.

As the sound wave passes through the water column, transmission loss due to absorption and spreading occurs, which reduces the energy strike on the target. In general, sound absorption is greater with higher sound frequencies and more saline water [11].

The two key measurement issues in the acoustic quantification of fish are target strength and fish behavior [5]. Target strength of a single fish is dependent upon its species, length, shape, body structure, orientation relative to the transducer, condition of maturity and sonar frequency. Fish

behavior, or how the fish is moving and orienting itself, includes swimming speed and direction of individual fish.

The ultimate limit to the detection of a specific target is noise. Noise is the background against which sonars must detect signals from targets. For the active sonar, noise is augmented by reverberations from unwanted sources and the signal is an echo from the target. Major sources on noise include: thermal noise, noise from the sea, vessel noise and biological noise. Reverberation may be classified into surface, volume and seabed reverberation. Among them, volume reverberation plays an important role in fish detection and arises from small organisms, bubbles, suspended sediment particles, turbulence and other inhomogeneities in the volume of water being insonified.

C. Survey design

Imaging sonar systems have two main functions to perform: the detection of objects and the identification of such objects [5]. An effective and optimized imaging sonar survey in the quantification of fish target should incorporate the considerations of the following two aspects, i.e., the detectability of the fish (i.e., target strength and fish behavior) and the resolution of the sonar image. Theoretically, it is capable of detecting any target that produces an echo above the background noise level. From a practical point of view, to achieve the task of object detection by the application of an active imaging sonar system, the minimum requirement is that the object must receive five consecutive sonar insonifications. On the other hand, for the purpose of identification a specific object, a conservative plan should include one which chooses scanning speeds and ranges that will allow for at least 12 consecutive insonifications in a scanning distance equal to the object's dimension [11][12]. It is evident that with range setting of 5 m and stepping speed of 0.3^o/step, the smallest detectable objects at mid-range of the image frame should have a scanning length of 6.5 cm. In addition, for an object with scanning length of over 15.6 cm, outline and shape of this object might be delineated or defined which would improve its characteristics recognition or even identification.

For bottom-fixed, side-looking MSISs, the system parameters affecting the number of insonifications an object receives are: sonar range scale (which sets pulse repetition rate), stepping speed and horizontal beam directivity (i.e., horizontal aperture). Among these parameters where the operator has control over are range scale and stepping speed. Adjustment of system parameters illustrates how acoustic surveys can be fine tuned to match the purpose of a specific investigation.

III. PROCEDURE FOR IMAGE PROCESSING

Acoustic data are generally voluminous. Processing such data can be overwhelming without the aid of image processing software. In fact, the successfulness of image processing is highly dependent on quality, resolution and signal-to-noise ratio (SNR) of the image acquired, i.e., the existence of acoustic diversity is a pre-requisite for the detection of fish target [11]. The overall goal of the imaging processing software was to aid the operators in detection and

evaluation of fish target in the MSIS imagery collected in the field. Major modules of the proposed image processing procedure included: stationary objects subtraction, region extraction, textural feature extraction for fixed-sized regions, unsupervised classification based on texture features, hierarchical cluster analysis and principle feature threshold evaluation for fish target detection, and target quantification and visualization of the results (see Figure 1).
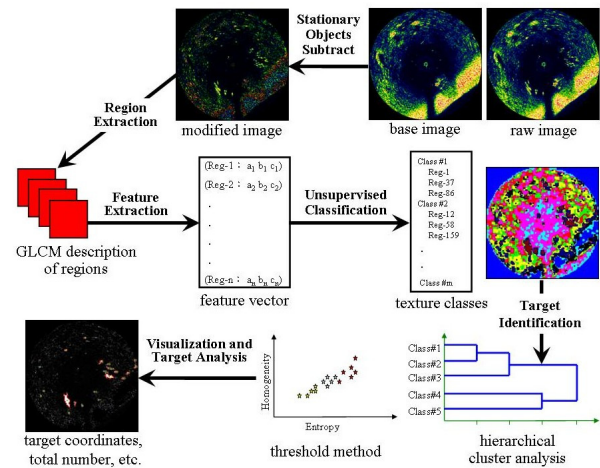

Figure 1. Image processing procedure for fish target detection and quantification.

A. Stationary objects subtraction

The existence of various stationary objects (e.g., seabed and anthropogenic structures) in acoustic image frames collected by bottom-fixed and side-looking sonar techniques is an unexceptional reality. In fact, seabed echoes have levels that are 20 to 40 dB higher than fish and their existence in the image frames tends to obscure the detection and evaluation of fish target [6]. However, due to their stationary status in the image frames, these objects could be removed straightforward from the image frame by using a pixel-based image superposition and subtraction algorithm [13]. The result was a modified image frame showing the changes in the image area due to fish movement.

B. Textural feature extraction for fixed-sized regions

Image texture is an attribute of groups of adjacent pixels, therefore, it is useful to group pixels into regions and to extract features that describe the texture of the region. A square sliding region was used for region extraction in this investigation [14]. Region size and sliding distance are, therefore, the two major parameters for the algorithm.

Measurements of texture in images can be one dimensional (e.g., run-length and fixed-size pixel neighborhoods) or two dimensional (e.g., grey level co-occurrence matrices, fractal dimension and wavelet transform) [14]. In this investigation, three textural features (mean, entropy and homogeneity) were proposed and incorporated into the classification system [15][16]. Among them the mean pixel intensity is one dimensional feature and the other two are two dimensional features. For a specific

region, the mean is the average of the intensity value of the unquantized pixel values for this region. The entropy and homogeneity are computed based on the grey level co-occurrence matrix (GLCM) for this region [15].

C. Feature classification

The goal of classification is to assign the regions of an image to an 'appropriate' class in such a way that some error measure is minimized. An unsupervised Bayesian classification system, i.e., AutoClass, was used to cluster regions from acoustic images [16]. Three texture features with equivalent weight were used in this process.

D. Target identification

Like any unsupervised classification routine, it cannot give these classified classes descriptive names or assign target to a specific class. To fulfill the necessity of target class identification among classified classes, two independent approaches were proposed in this investigation, i.e., a hierarchical cluster analysis and principal feature threshold evaluation. The hierarchical cluster analysis of the classified classes was based on the posterior probabilities and the algorithm of between-groups linkage with Euclidean distances. The results of the analysis are illustrated in a dendrogram and the similarity among classes can be evaluated based on the sure group clicking value. Target cluster detection through principal feature threshold method was conducted by visual inspection of scatter plots of cluster averaged textural features. Under this circumstance, a single textural feature threshold or a combination of multiple thresholds among textural features might suffice for the discrimination of the fish target class among classified classes.

E. Target quantification and visualization of the results

Region growing technique was employed to isolate contiguous target blocks to a single detected target. Visualization of the results was accomplished by mapping the representative pixels of the specific region classified as fish target cluster and those of non-fish target clusters into a distinctive binary plot. Physical properties of each fish target were therefore quantized which includes center coordinates, perimeter, area and shape factor as well as averaged value of textural features (i.e., mean, entropy and homogeneity).

IV. CASE STUDY AND RESULTS

A comprehensive evaluation of the entire surveying system with consecutive image acquisition and image processing for the purpose of fish target detection, relative abundance quantification and behavior investigation was performed in a deep water aquaculture pond in 2010. The pond covers an area with dimensions of 70 by 90 m (6,300 m^2) and an averaged depth of 3 m was reported. Due to the existence of suspended particulate matters, water clarity of this pond is quite poor which makes video observations completely obscured. Approximately 20,000 milk fish (*Chanos chanos*), each about 40 cm in length, were cultured in the pond. The MSIS was deployed at a randomly selected point near to the southern dike and 4 m off the pond bank

where a small plastic pipe raft was deployed previously for the purpose of a surface working platform. Acoustic image frames collected with range setting at 5 m, stepping speed at 0.3^o/step and gain setting at 20 dB were selected for detailed analyses. Under these specific settings, each frame provided a viewing area of 78.5 m^2 (1.2% to the pond area) with spatial resolution of 2 x 2 cm per pixel, temporal resolution or scanning rate of 75 seconds per frame and maximum scanning speed of 42 cm/sec. A total of 46 consecutive image frames was acquired in this case study which lasted for an hour at around noon time (i.e., 12:54 to 13:54 local time).

A. Image processing program verification and calibration

Image processing computer program developed for fish target detection and relative abundance estimation was verified and optimal system parameters were determined with the modified image frames (i.e., stationary objects subtracted) of two typical examples (i.e., EX#1 and EX#2 in Figure 2). In this case, the entire image frames were used to generate the synthetic background frame for the purpose of stationary objects subtraction process.

(a) Ex#1, raw image frame.   (b) Ex#1, modified image frame.

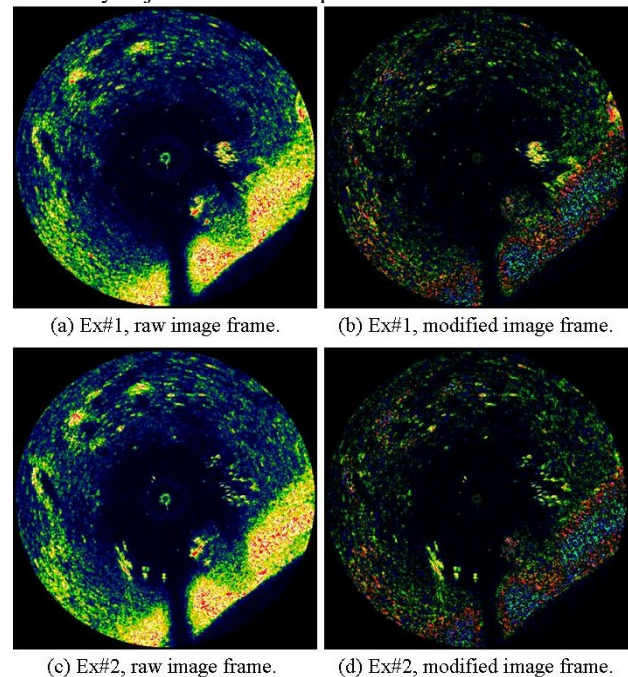(c) Ex#2, raw image frame.   (d) Ex#2, modified image frame.

Figure 2.   Two typical examples illustrated bottom features (raw image frame) and the readily discriminated fish targets (modified image frame).

Feature extraction is a dominant issue in target detection from images. Values for a number of different parameters related to feature extraction and classification need to be determined, which include: region size, region sliding distance, number of grey levels and number of clustered classes. An evaluation process based on producer's and consumer's accuracy was adopted in this investigation [14].

Optimal region size and region sliding distance for this specific type of image frames were evaluated and determined empirically. Initial investigation illustrated that a region

sliding distance of 4 pixels and 16 grey levels are acceptable selections in this case. Based on these sliding distance and grey levels, ten sets of square region sizes from 6x6 to 24x24 were systematically evaluated. For these experiments, AutoClass was set to execute for 4 attempts as suggested by the computer program, all regions were used for classification, and AutoClass was allowed to determine the optimum number of classes. In most cases, AutoClass would cluster the features into 9 classes. Performance evaluation was conducted by comparing manually depicted target pixels and computer classified target pixels of the two examples where manual detections were assumed without error. Results of the evaluation indicated that the 8x8 region size, with maximum value of producer's accuracy (85% and 78%, with respect to EX#1 and EX#2), was the optimal region size for the detection of fish target in this case. The relatively low producer's accuracy in EX#2 was correlated with a relatively high amount of fish target off the acoustic beam axis which was omitted by the manual detections and therefore caused the difference between manually depicted target pixels and computer classified target pixels.

Binary visualization and characteristic properties quantification of the detected fish targets of EX#1 were illustrated in Table 1. Basic fish target information extracted in this case included positional parameters (Cartesian and Polar Coordination), morphological descriptors (e.g., area, perimeter, shape factor and/or length) and energetic characteristics (e.g., acoustic energy reflected and indices of internal variation). In addition, information regarding size of detected fish target (in 'block' of 4x4 pixels), abundance variations and cumulative area of fish target by frame, which are associated with fish abundance and behavior patterns in the insonified volume, were estimated and enumerated for further investigation.

As criteria for fish target class identification is concerned, both hierarchical cluster analysis and principal feature threshold criterion were systematically tested and evaluated. It is evident that both procedures are effective in discriminating fish target class among classified classes. However, for principal feature threshold method, a combination of two thresholds among textural features (i.e., mean and homogeneity) is more efficient than a single textural feature threshold. An automatic image processing computer procedure with limited human intervention is therefore developed and verified.

B. Results and discussion

Both surficial and bottom stationary environmental and anthropogenic features within the scanned volume of this randomly selected test point were imaged and recognized. At the water surface, a meter-sized floating object (i.e., the plastic pipe raft) is located at a location closed to the bank slope. On the bottom, among a relatively flat, muddy and stiff substrate, two types of explicit features are identified which include a continuous and moderately steeped bank slope at the pond bank area and several prominent mud mounds at the off bank area (see Figure 2). These features offered strong reflecting surfaces and therefore stronger echo intensities were generated at these areas in the image frames.

Quantitative information of fish targets discriminated from the consecutive 46 image frames was generated and exported to text formats for evaluating the characteristics of the proposed surveying system especially in the quantification of fish behavior related issues. A total of 2,928 individual and school fish targets were tabulated and based on the basic target area counting unit adopted in this investigation (i.e., "block" of 4x4 pixel), target area size or type of target varied from 1 block (#b-1) to as large as 171 blocks (#b-171). Among them, #b-1 and #b-2 are strictly linked to individual fish, whereas #b-5 can be considered as a minimum threshold for a fish school or closely spaced individuals. By the relationship of abundance of detection at each type of target in a semi-logarithmic plot (see Figure 3), two distinct categories, which are strictly related to fish behavior, were observed. The first category (i.e., Cat#1: Individual-School Mixture) followed an approximately linearly and continuously declined trend from #b-1 to #b-16 where number of target abundance varied by nearly two logarithmic cycles from 1,160 to 13. The second category (Cat#2: Prominent Schools) exhibited a level off trend from #b-17 up to #b-171. Based on a mutual consideration of target area size (type of target), number of abundance and continuity of distribution, the contents of the second category were further classified into two sub-categories by #B-40, i.e., Cat-2(A): Large School Set (#B-17 to #B-39) and Cat-2(B): Giant School Set (#B-40 and above).

TABLE 1. BASIC FISH TARGET INFORMATION EXTRACTED IN EX#1 INCLUDED POSITIONAL, MORPHOLOGICAL AND ENERGETIC PARAMETERS.

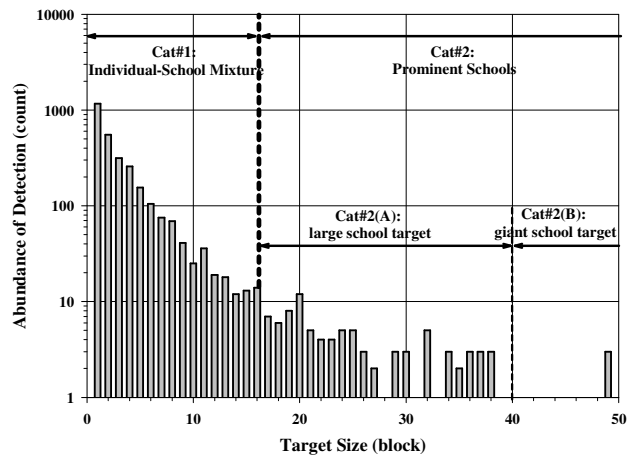| Target number	Center of Target (x , y)	Target Area	Target Perimeter	Shape Factor	Entropy	Average Homogeneity	Mean	Polar Coordination (Distance , Bearing)
#1	(−170.8 , −111.8)	48	32	1.5	1.497	0.375	63.7	(204.2, −123.2)
#2	(−121.5 , −166.5)	16	12	1.3	1.521	0.374	52.9	(206.1, −143.9)
#3	(−74.8 , 114.8)	48	32	1.5	1.515	0.390	63.2	(137.1, −33.1)
#4	(99.8 , 5.7)	832	156	5.3	1.555	0.473	97.3	(100.0, 86.8)
#5	(118.5 , −46.5)	16	12	1.3	1.487	0.420	55.8	(127.3, 111.4)
#6	(141.2 , −38.1)	144	60	2.4	1.555	0.465	64.5	(146.2, 105.1)
#7	(157.8 , −7.2)	96	40	2.4	1.554	0.465	60.9	(158.0, 92.6)
#8	(160.5 , −32.5)	64	32	2.0	1.560	0.419	61.6	(163.8, 101.4)
#9	(168.9 , −17.7)	80	40	2.0	1.557	0.444	63.7	(169.8, 96.0)
#10	(222.5 , 99.5)	32	24	1.3	1.564	0.443	73.7	(243.7, 65.9)
#11	(227.7 , 68.7)	384	80	4.8	1.492	0.371	93.2	(237.8, 73.2)

Figure 3. Number of detected target in logarithmic scale vs. target size (in the unit of 'block' of 4x4 pixels) collected in 46 image frames.

Quantitative evaluation of fish behavior from a spatial point of view was conducted by two measures, i.e., target area distribution by polar angle sectors (see Figure 4) and the relationship between fish target and environmental features (see Figure 5). Fish targets and environmental features, when presented and analyzed together, can provide valuable information about population dynamics and aggregation location with respect to these environmental features and surrounding environment. Two fish movement corridors in parallel with the pond bank were concluded (i.e., Corridor#1 and Corridor#2), which guided the mass movement and direction of travel of both individual and school fish (see Figure 5). Among them, Corridor#1, which is bordered by the pond bank, extends off bank to a distance of 5m in wideness and includes the floating raft within its coverage. A proportion of 73% detected targets by area were located in Corridor#1 and only 27% were located in Corridor#2. Nearly all of the targets which fit in Cat#2 (i.e., Prominent Schools Category) were located in Corridor#1 at specific locations such as bank slope area, substrate mound area and the area around the floating raft. In addition, all of the targets in Cat-2(B) (i.e., Giant School Set) were located at only two restricted areas in the vicinity of the floating raft. Alternatively, in Corridor#2, only six targets which fit in Cat-2(A) (i.e., Large School Set in the Prominent Schools Category) were located specifically on the substrate mound.
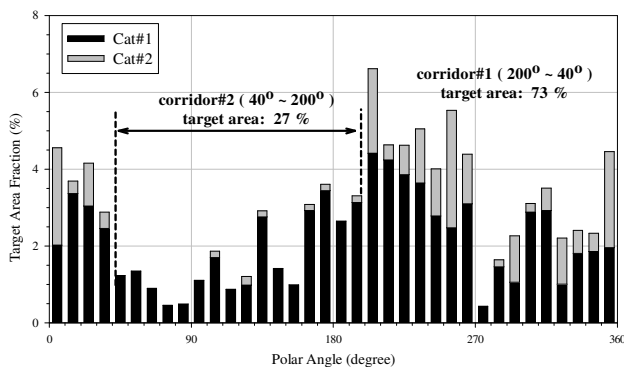

Figure 4. Target area distribution by polar angle sectors. Two fish movement corridors were concluded (i.e., Corridor#1 and Corridor#2).

Time-dependent variations of target area in each frame were evaluated by means of total integrated area and area by the Prominent Schools Category (see Figure 6). Values of the total integrated area varied significantly by a factor of 11 times from a maximum value of 10,224 pixels to a minimum of 896 pixels with average and standard deviation of 3893±2081 pixels. Periodic fluctuations in target areas through time were observed evidently, which included five key epochs with total integrated area over 6,000 pixels. Combined with time-dependent variations of target area through fish movement corridors illustrated that major fish movement patterns in the scanned area followed a continuous, steady and low passage rate mode (Corridor#2) (see Figure 7) superimposed a discrete, periodic and high passage rate mode (Corridor#1). A total of eight discrete and high passage rate events were discriminated and an averaged

period of about seven minutes in time was concluded for each discrete and high passage rate event. During each event, the fish converged into large and giant schools subsequent to interactions with environmental features such as bank slope, substrate mound and the float raft.
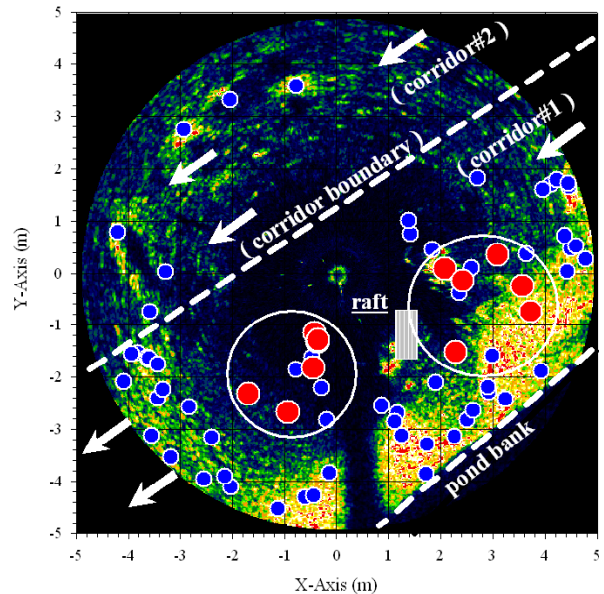

Figure 5. Relationship between fish target and environmental features. Two fish movement corridors were recognized. Arrows outline a general travel direction of the fish target. Blue and red circle represent large and giant school fish respectively.
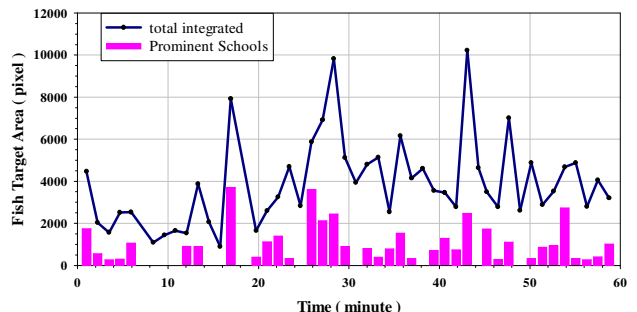

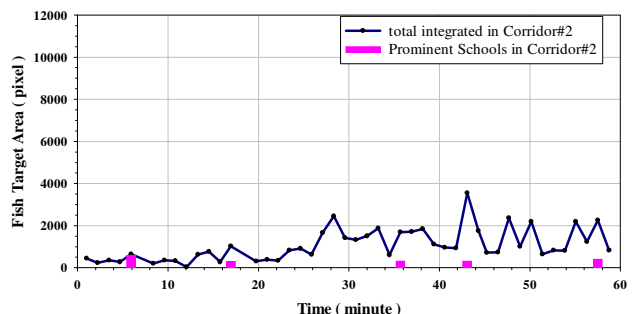Figure 6. Time-dependent variations of fish target area.

Figure 7. Time-dependent variations of target area in Corridor#2 followed a continuous, steady and low passage rate mode.

Based on spatial and temporal analyses on position and area of discriminated fish targets, it was concluded that fish movement behavior in the scanned area followed two distinct patterns in two separate corridors with significant different passage rate, i.e., a discrete, periodic and high passage rate (73%) mode in Corridor#1 and a continuous, steady and low passage rate (27%) mode in Corridor#2. Environmental features, such as bank slope, substrate mound and the float raft represented specific meeting points for dynamic aggregations and schooling. Fish tended to converge into large and even giant schools subsequent to interactions with these features. The fish converging effects of these environmental features varied in proportion with fish passage rate. In addition, behavior characteristics suggested by the first category (i.e., Cat#1: Individual-School Mixture), defined in the abundance and target size relationship, could be correlated with schooling and erratic behavior as well as swift swimming activity and chasing, occasional leaping and water-slapping activities of milk fish [17]. Behavior characteristics represented by the second category (Cat#2: Prominent Schools) were correlated with the existence of principal environmental features which acted as meeting points for swimming fish to converge into prominent schools.

V. Conclusions

A point stationary, acoustic-based surveying system, which incorporated acoustic image acquisition and image processing techniques, was developed and evaluated for its applicability in fulfilling the necessities of time-dependent benthic fish behavior investigation.

For the specific case study conducted in a deep water fishpond, it is evident that both individual and school fish could be discriminated by image frames collected at a randomly selected point with range setting at 5 m and frame rate at 75 second. Based on this investigation, fish movement behavior in the scanned area followed two distinct patterns, i.e., a discrete, periodic and high passage rate mode in Corridor#1 and a continuous, steady and low passage rate mode in Corridor#2. Environmental features, such as bank slope, substrate mound and float raft represented specific meeting points for dynamic aggregations and schooling. Fish tended to converge into large and even giant schools subsequent to interactions with these features.

The proposed system, which is an effective sampling tool due to its large sampling volume and the target-identification power, represented a practical and cost effective tool for the characterization of fish behavior. Other related issues such as the determination of fish swimming speed and length by the proposed system will be discussed in additional publications.

References

[1] S. F. Vik, Japanese Artificial Reef Technology, Maryland, USA: Aquabio, Inc. 1982.

[2] W. Jr. Seaman and L. M. Sprague, "Artificial habitat practices in aquatic system," in Artificial habitats for marine and freshwater fisheries, W. Jr. Seaman and L. M. Sprague, Eds. New York, USA: Academic, 1991, pp. 1-16.

[3] Fishery Administration Taiwan, *Coastal Fishery Resources*, Available from: ftttp://www.fa.gov.tw [retrieved: July 2014].

[4] W. M. Tian, "Side-scan sonar techniques for the characterization of physical properties of artificial benthic habitats," Brazilian Journal of Oceanography, vol. 59 (special issue CARAH), April 2011, pp. 77-90, doi: 10.1590/S1679-87592011000500010.

[5] D. N. MacLennan and E. J. Simmonds, Fisheries Acoustics, London, England: Chapman & Hall, 1992.

[6] W. M. Tian, "Integrated method for the detection and location of underwater pipelines", Applied Acoustics, vol. 69, April 2008, pp. 387-398, doi:10.1016/j.apacoust.2007.05.001.

[7] R. A. Moursund, T. J. Carlson, and R. D. Peters, "A fisheries application of a dual-frequency identification sonar acoustic camera," ICES Journal of Marine Science, vol. 60, March 2003, pp. 678–683, doi:10.1016/S1054–3139(03)00036-5.

[8] J. A. Holmes, G. M. W. Cronkite, H. J. Enzenhofer, and T. J. Mulligan, "Accuracy and precision of fish-count data from a 'dual frequency identification sonar' (DIDSON) imaging system," ICES Journal of Marine Science, vol. 63, April 2006, pp. 543–555, doi:10.1016/j.icesjms.2005.08.015.

[9] Imagenex Technology Corp, Imagenex model 881A Digital Multi-Frequency Imaging Sonar, Port Coquitlam, Canada: Imagenex Technology Corp, 2007.

[10] Konsberg Mesotech, Use of Scanning and Side-scan Sonar for Body Recovery, Port Coquitlam, Canada: Konsgerg Mesotech, 2002.

[11] X. Lurton, An Introduction to Underwater Acoustics: Principles and Applications, Chichester, UK: Praxis Publishing, 2002.

[12] J. P. Fish and H. A. Carr, Sound Underwater Images—A guide to the generation and interpretation of side scan sonar data, Orleans, MA: Lower Cape Publishing, 1990.

[13] N. O. Handegard and K. Williams, "Automated tracking of fish in trawls using the DIDSON (Dual frequency IDentification SONar)," ICES Journal of Marine Science, vol. 65, March 2008, pp. 636–644, doi:10.1093/icesjms/fsn029.

[14] J. B. Campbell, Introduction to Remote Sensing, 3rd ed., NewYork, USA: The Guilford Press, 2002.

[15] Ph. Blondel, "Automatic Mine Detection by Textural Analysis of COTS Sidescan Sonar Imagery," International Journal of Remote Sensing, vol. 21, Dec. 2000, pp. 3115-3128, doi:10.1080/01431160050144983.

[16] S. Bridges, J. Hodges, B. Wooley, D. Karpovich, and G. B. Smith, "Knowledge Discovery in an Oceanographic Database," Applied Intelligence, vol. 11, Sep. 1999, pp. 135-148, doi: 10.1023/A:1008395129406.

[17] I. C. Liau and E. M. Leano, Milkfish Aquaculture in Asia, Keelung, Taiwan: National Taiwan Ocean University, 2010.

Comparison of Dry and Wet Electrode Systems for Spontaneous and Event Related Electroencephalograms

M. Fatoorechi, R.J. Prance, H. Prance

Department of Engineering and Design
University of Sussex
Brighton, UK
e-mail: M.Fatoorechi@sussex.ac.uk
R.J.Prance@sussex.ac.uk; H.Prance@sussex.ac.uk

D. Schwartzman, J. Parkinson, A. Seth

Department of Informatics
University of Sussex
Brighton, UK
e-mail: D.Schwartzman@sussex.ac.uk;
J.M.Parkinson@sussex.ac.uk; A.K.Seth@sussex.ac.uk

Abstract— **Low frequency noise performance is the key indicator in determining the signal to noise ratio of a capacitively coupled sensor when used to acquire electroencephalogram (EEG) signals. For this reason, a prototype Electric Potential Sensor (EPS) device based on an auto-zero operational amplifier has been developed and evaluated. The absence of 1/f noise in these devices makes them ideal for use with signal frequencies ~10 Hz or less. The active electrodes are designed to be physically and electrically robust and chemically and biochemically inert. They are electrically insulated (anodized) and have diameters of 12 mm or 18 mm. In both cases, the sensors are housed in inert stainless steel machined housings with the electronics fabricated in surface mount components on a printed circuit board (PCB) compatible with epoxy potting compounds. Potted sensors are designed to be immersed in alcohol for sterilization purposes. A comparative study was conducted with a commercial wet gel electrode system. These studies comprised measurements of both free running EEG and Event Related Potentials (ERP). A strictly comparable signal to noise ratio was observed and the overall conclusion from these comparative studies is that the noise performance of the new sensor is appropriate.**

Keywords-Sensors; EEG; Biosensors; Assistive technology.

I. INTRODUCTION

The traditional methods employed for the acquisition of EEG signals rely on the use of wet silver/silver chloride (Ag/AgCl) transducing electrodes. These convert ionic current on the surface of the body to electronic current for amplification and subsequent signal processing. Such electrodes are cheap and disposable but require the use of a conducting gel between the electrode and the skin, since they rely on maintaining a low electrical resistance contact [1]. Operationally significant care is required in the preparation of the skin, usually involving abraision, by skilled personnel. In addition, the gel may cause skin irritation and discomfort as well as drying out after a period of time, meaning that wet electrodes are unsuited to long term monitoring applications [2]. The gel may also be responsible for cross coupling or shorting between electrodes in an array if great care is not taken during placement. Dry conducting electrodes provide a more user

friendly approach with electrodes making resistive contact with the skin [3]. This overcomes the problems caused by the wet electrode gel, but introduces an additional variable, the variation in contact resistance due to perspiration or skin creams. For these reasons, they tend to be noisier than wet electrodes and can suffer from movement artefacts if they are not securely fastened.

An alternative approach is to dispense with the resistive contact and couple capacitively through an insulating layer [4]. With this method the signal fidelity no longer relies on skin resistance, however they can also suffer from movement artefacts and charge sensitivity. In most embodiments of dry and insulated electrodes an active electrode structure is used with high impedance amplification [4][5]. This minimizes the noise due to cabling and transmission of the signal. EPS is a high performance version of the insulated active sensor.

With specific reference to EEG signal acquisition, evidence exists that smaller, lighter sensors with a higher array density are required in order to reduce movement artefacts and to allow for redundancy [6]. A comprehensive review of wet, dry and insulating electrode technologies concludes that insulated active electrodes offer the most promising solution for future healthcare applications [1]. More recent work on dry electrodes has included a trial of a 6 sensor EEG system [7] and concludes that this could offer a cost effective solution for brain-computer interfacing. A clinical comparison of concurrent measurements with wet and dry EEG electrodes concludes that a high degree of correlation is seen and that dry electrodes offer better long term performance [8]. New work on motion artefact reduction relies on the simultaneous measurement of the contact impedance of each sensor [9] using a small a.c. current (20 nA @ 1 kHz) and multiple dry spring loaded contacts in each sensor to introduce redundancy. Other workers have designed quasi-dry polymer electrodes which use a small quantity of moisturizing agent to address these problems [10].

In summary, EPS technology has already demonstrated that these problems can be addressed for electrocardiogram (ECG) data acquisition where the inherent DC stability and short settling time of the sensors

differentiate them from other insulated electrode implementations [11]. However, the low frequency noise performance required for accurate EEG data acquisition is considerably more stringent and it is this important parameter which will be addressed in this paper. A review of sensor developments for healthcare [11] discusses the low frequency noise performance of a number of active sensors and characterizes them in terms of the noise spectral density at 1 Hz. This is a useful indicator of the performance for EEG use and gives values ranging from 2 µV/√Hz to 10 µV/√Hz, however these values will increase at lower frequencies due to 1/f noise. The aim of this work is to produce a high impedance capacitively coupled sensor with noise that is comparable or lower than conventional electrode systems in a 0.1-10 Hz bandwidth.

The design and specifications of the EPS sensor used in these experiments are described in section II, along with details of the commercial system used for comparing EPS with gel electrodes. In section III the results for free running EEG is demonstrated followed by data for two ERP studies in section IV. The second ERP experiment outlines the comparative study conducted between the two systems.

II. PROTOTYPE SENSOR AND SYSTEM

The prototype Sussex EPS device for this project is based on an auto-zero operational amplifier, chosen to give the lowest possible low frequency noise [12]. The absence of 1/f noise in these devices makes them ideal for use with signal frequencies ~10 Hz or less, with a quoted noise performance of 22 nV/√Hz and 5 fA/√Hz. The input capacitance is ~8 pF with an associated voltage noise between 0.1-10 Hz of 0.5 µVp-p. After consideration of the expected signal amplitudes and frequency the sensor was configured to have an operational bandwidth of 0.1 Hz to 78 Hz and a voltage gain of x50. The voltage gain was distributed between two stages with x5 and x10 respectively for the first and second stages. The operation and circuit details of EPS devices have been published previously by the authors [13]. Here, the sensors are operated from split symmetric power supply rails of ±2.5V. Two versions were produced with different electrode sizes to enable reliable contact to be made to different parts of the body. The electrodes are electrically insulated through an anodized electrode with diameters of either 12 mm or 18 mm. In both cases the sensors were housed in inert stainless steel machined housings with the electronics fabricated in surface mount on a PCB compatible with epoxy potting compounds. Potted sensors are designed to be immersed in alcohol for sterilization purposes.

The gain and operational bandwidth of the sensors was confirmed using a standard spectrum analyzer to be as specified. The most significant parameter for the specification of the sensor in this particular application is the voltage noise referred to the input. This was measured by placing the sensor in a screened environment and recording the spectral noise density over a 1 kHz bandwidth. From this

data, shown in Figure 1, two numbers are produced to characterize the noise performance these are the spot noise figure at 1 Hz and the integrated noise from 0.1 Hz to 10 Hz. The results obtained for the voltage noise measurements are: 30 nV/√Hz at 1 Hz and 0.2 µVp-p from 0.1 to 10 Hz; consistent with the data provided by the manufacturer. The absence of 1/f noise in this data confirms that the auto-zero amplifier used in this design is performing as expected.
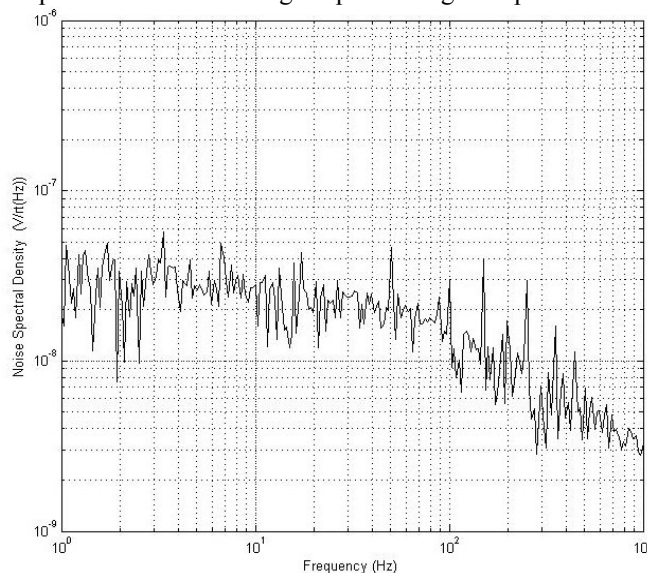

Figure 1. Noise spectral density plot for prototype auto-zero sensor.

In order to confirm, at an early stage in the design process, that the sensor design was both suitable for high quality EEG signal acquisition and that it was compatible with commercial systems and practice we interfaced the sensors to a TMS International system currently in use in the School of Psychology at Sussex. This also enabled us to do direct comparisons with wet gel electrode measurements. The prototype sensors were interfaced to a Refa8 amplifier produced by TMS International [14] with 64 EEG channels at 24 bit resolution with an input noise of $1 \mu V_{rms}$. All electrode cables have active shielding to reduce 50 Hz mains interference and cable movement artefacts. In the comparative data presented here the TMS International acquisition system and data processing were applied to both sets of data.

In order to provide a comprehensive comparison between the Sussex EPS prototype and the commercial system two different types of EEG data were measured. The spontaneous, or free running, EEG as shown by recording the alpha signal and in particular by observing the, well known, alpha blocking signal. The second type is the ERP, here an oddball paradigm was chosen to record ERP signals [15]. In both cases the International standard 10-20 system was employed to record EEG [16]. In our case all signals were recorded against a reference, this may be the signal from any electrode on the head or an average of all

electrodes. Usually a linked mastoid reference is used and we followed this practice with the signals from the O2 and O1 positions and the reference sensor on M1 (left mastoid).

III. FREE RUNNING EEG

Initial measurements were carried out on the free running EEG to verify that the prototype sensor had an appropriate noise performance to allow EEG data to be seen. The alpha
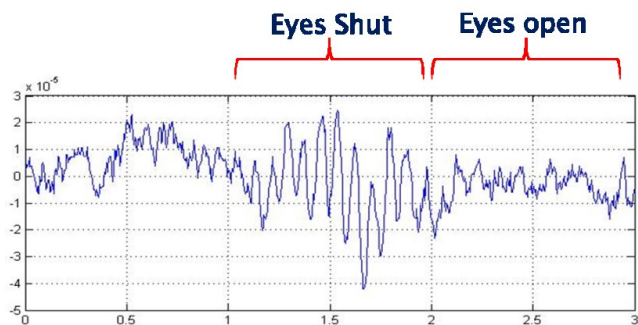

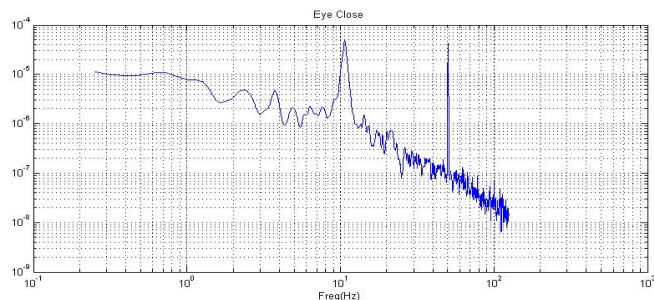Figure 2. Time domain data showing the alpha blocking phenomena measured using the prototype sensor.

Figure 3. Fourier transform of 40 s of time domain data showing a broad alpha signal peak at ~10 Hz.

signal is observed when the eyes are closed and is characterized by an increase in amplitude of the 8-13 Hz EEG signal. Alpha activity can be recorded from 95% of people [15] and is blocked when the eyes are open. The signal may be seen in real time in the time domain, as shown in Figure 2, where the alpha blocking caused by opening the eyes may be seen clearly. Alternatively, if the time series data is Fourier transformed we see a broad peak in the frequency domain data. This is illustrated in Figure 3 where a 40 s section of time series alpha data has been Fourier transformed to show a clear ~10 Hz peak. A residual 50 Hz mains interference signal may also be seen, however the common mode rejection ratio (CMRR) is sufficient to reduce this amplitude to be comparable to the measured signal.

IV. EVENT RELATED POTENTIAL

The oddball effect is a measure of the response of the brain to the frequency of occurrence of differing events on a screen. The ERP resulting from this shows a time shift which

arises from this difference. Two different events are presented on a screen with one event randomly chosen to occur more often than the other. A volunteer is asked to press the space bar only when they are presented with one of the two events. Typically, signals are averaged and band-pass filtered at 0.1 to 30 Hz, again we have followed this standard practice. A typical setup is where the letters X and O are displayed on a monitor with 80% and 20% relative frequency respectively. The letters are displayed for 100 ms with a blank screen presented for 1.4 s space between each letter.
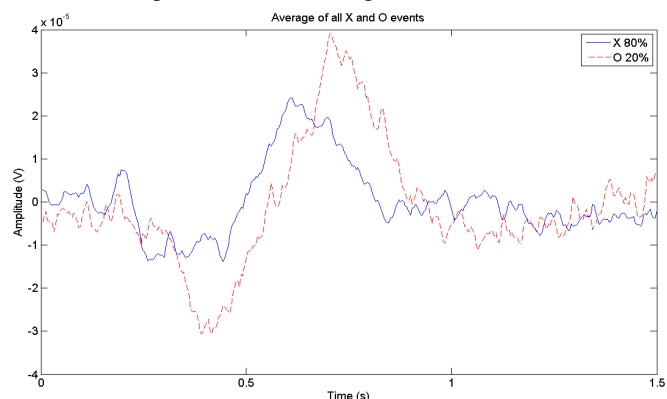

Figure 4. Averaged prototype sensor ERP data showing the expected time delay associated with the oddball effect.

Little or no useful information may be gained from real time data and averaging over a number of events is usual. The data is usually recorded using the Pz position and a reference electrode. Figure 4 shows the results for 67 averages, 53 for the 'X' and 14 for the 'O'. There is a clear time difference between the 'X' and 'O' data as expected. This is a relatively low number of averages for this type of measurement and indicates that the EPS prototype sensor is very capable in this challenging mode of operation. For ERP measurements direct comparisons between the wet gel and EPS systems are shown in Figures 5 and 6 with measurement electrodes located at the P7 and P8 positions. In order to improve the quality of the data and to allow a more accurate comparison to be conducted a grand average was produced over 4 subjects.
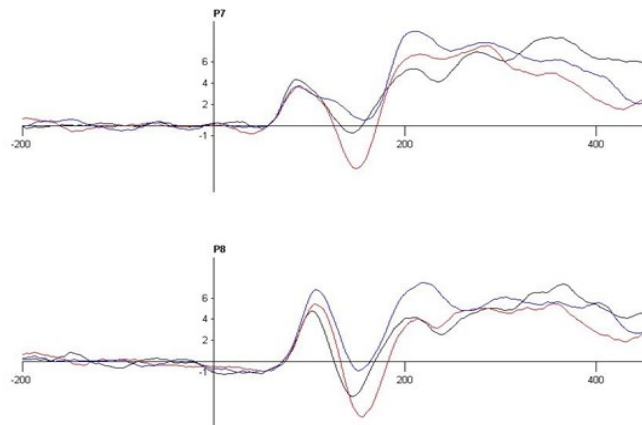

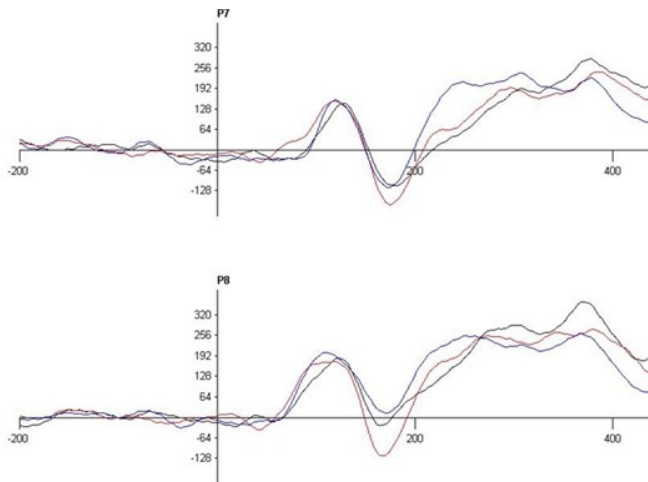Figure 5. Grand average of ERP data from TMS system.

Figure 6. Grand average of ERP data from prototype EPS.

Three different images were presented to the subjects; faces (black line); inverted faces (red line) and scrambled faces (blue line). The overall conclusion from these ERP measurements is that the grand average data sets show a high degree of correlation between the two systems with the apparent signal to noise ratio looking strictly comparable. From these initial results we therefore conclude that the current prototype EPS device has an adequate level of noise performance for all the EEG signals observed during these tests.

V. CONCLUSIONS

The Sussex EPS prototype has been verified as suitable for the acquisition of both free running EEG and ERPs. The prototype performance has also been verified by interfacing with a commercial system and comparing results with those from wet gel electrodes. All results obtained indicate that the Sussex EPS prototype produces strictly comparable signal to noise ratios to conventional wet gel electrode devices for both free running and ERP measurements. The low frequency noise has been identified as the key performance indicator for capacitively coupled active sensors. In particular, the frequency range of typical EEG signals lies within the 1/f noise region of most active devices. The use of an auto-zero operational amplifier within the prototype sensor has been demonstrated to eliminate this problem and yield results which are strictly comparable to wet gel electrodes.

ACKNOWLEDGMENT

REFERENCES

[1] A. Searle and L. Kirkup, "A direct comparison of wet, dry and insulating bioelectric recording electrodes," Physiological Measurement, vol. 21, 2000, pp. 271-283, ISSN 0967-3334J.

[2] D. Prutchi and M. Norris, Design and Development of Medical Electronic Instrumentation, John Wiley and Sons New Jersey, 2005, ISBN 0-471-67623-3.

[3] Y.M. Chi, T-P Jung and G. Cauwenberghs, "Dry-Contact and Noncontact Biopotential Electrodes: Methodological Review," IEEE Reviews in Biomedical Engineering, vol. 3, 2010, pp. 106-119, ISSN 1937-3333.

[4] A.J. Clippingdale, R.J. Prance, T.D. Clark, H. Prance, and T. Spiller, "Ultra-high impedance voltage probes and non-contact electrocardiography," In: Sensors VI: Technology, Systems and Applications, K.T.V. Grattan (Ed.), IOP publishing, 1991, pp.469-472, ISBN 0-7503-0316-0.

[5] E. Spinelli and M. Haberman, "Insulating electrodes: a review on biopotential front ends for dielectric skin-electrode interfaces," Physiological Measurement, vol. 31, 2010, pp. S183-S198, ISSN 0967-3334.

[6] B.A. Tahari, R.T. Knight, and R.L. Smith, "A dry electrode for EEG recording," Electroencephalography and clinical Neurophysiology, vol. 90, 1994, pp. 376-383.

[7] F. Popescu, S. Fazli, Y. Badower, B. Blankertz, and K.R. Muller "Single Trial Classification of Motor Imagination Using 6 Dry EEG Electrodes," PLos ONE, Issue 7, e637, July 2007.

[8] G. Gargiulo et al. "A new EEG recording system for passive dry electrodes," Clinical Neurophysiology, vol. 121, 2010, pp. 686-693.

[9] A. Bertrand, V. Mihajlovic, B. Grundlehner, C. van Hoof, and M. Moonen, "Motion artifact reduction in EEG recordings using multi-channel contact impedance measurements," Biomedical Circuits and Systems Conference (BioCAS), IEEE, Oct. 2013, pp. 258-261,

doi:10.1109/BioCAS.2013.6679688

[10] A.R. Mota et al. "Development of a quasi-dry electrode for EEG recording," Sensors and Actuators A, vol. 199, 2013, pp. 310-317.

[11] H. Prance, "Sensor Developments for Electrophysiological Monitoring in Healthcare," Applied Biomedical Engineering, Dr. Gaetano Gargiulo (Ed.), InTech, 2011, ISBN: 978-953-307-256-2, Available from:

http://www.intechopen.com/books/applied-biomedical-engineering/sensor-developments-for-electrophysiological-monitoring-in-healthcare, [retrieved: June, 2014]

[12] AD8628 datasheet, Analog Devices, Inc., One Technology Way, P.O. Box 9106, Norwood, MA 02062-9106, U.S.A., Available from: http://www.analog.com/static/imported-files/data_sheets/AD8628_8629_8630.pdf, [retrieved: June, 2014]

[13] C.J. Harland, T.D. Clark, and R.J. Prance, "Electric potential probes - new directions in the remote sensing of the human body," Meas. Sci. and Tech., vol. 13, 2002, pp. 163-169.

[14] Refa8 amplifier datasheet, TMS International, Zutphenstraat 57, 7575 EJ Oldenzaal, The Netherlands, Available at: http://www.tmsi.com/products/systems/item/refa, [retrieved: June, 2014]

[15] P. L. Nunez and R. Srinivasen, Electric Fields of the Brain: The Neurophysics of EEG, 2nd Edition, Oxford University Press, 2005, ISBN-13: 978-0195050387

J. Malmivuo and R. Plonsey, Bioelectromagnetism: Principles and Applications of Bioelectric and Biomagnetic Fields, Oxford University Press, 1995, ISBN-13: 978-0195058239

A Disc-shaped Power Supply Line-free Mass Sensor for Measuring Biomarker

Masaki Yamaguchi, DongSu You, Yuki Nakayama

Biomedical Engineering & Robotics Laboratory
Graduate School of Engineering, Iwate University
e-mail: masakiy@iwate-u.ac.jp

Abstract—The purpose of this research is to demonstrate a new design for a mass sensor with a disc-shaped resonator that is free of power supply lines. The line-free mass sensor comprises a resonator and a piezoelectric element for vibrating it. Since electrical power is used to actuate the piezoelectric element, the resonator is free from power lines. Target molecules become attached to the resonator, changing its resonant frequency. The geometric shape and dimensions of the resonator were designed using the finite element method (FEM). The resonator was fabricated in the shape of a circular plate of diameter 4 mm by photolithography, so that the radial oscillation primary mode of vibration would be 3.68 MHz. The concentrations of glucose solutions were measured using the line-free mass sensor. The sensitivity of the line-free mass sensor was estimated to be 0.06 fg when a frequency resolution of 1 mHz was used.

Keywords-mass sensor; resonator; power supply line; resonant frequency; photolithography.

I. INTRODUCTION

Micro-cantilever transducers have certain advantages in terms of detecting and identifying chemical and biological elements in air or liquid environments with high sensitivity [1][2]. The sensitivity of micro-cantilever transducers is superior to those of traditional quartz crystal microbalances (QCM) [3] and surface acoustic wave (SAW) [4] transducers. It has been reported in one theoretical study that the potential measurement sensitivity of micro-cantilever transducers is 2.34×10^{-19} g [5].

Crystal oscillators and piezoelectric elements can be used to excite vibrations in micro-cantilever transducers. When the excitation source is directly fixed to the micro-cantilever, the electrical power required to feed it seriously degrades the vibrations. Moreover, capacitive coupling of the vibrator influences the frequency and decreases the quality factor (Q-factor) of the micro-cantilever transducers. We have already proposed a power supply line-free mass sensor for measuring biomarkers [6]. Our study indicates that, if an optical displacement sensor with a frequency resolution of 1 mHz is used, a sensitivity of 76.2 ng/ml can be achieved with a line-free mass sensor.

The purpose of this research is to improve the sensitivity of a line-free mass sensor to as high as the tens of fg/Hz range. The geometric shape and dimensions of a disc-shaped resonator were designed using FEM and the resonator was fabricated by photolithography. The measured results of glucose concentrations using the fabricated line-free mass sensor were discussed.

II. MATERIALS AND METHODS

A. Structure and Principle

The line-free mass sensor consists of a resonator, a piezoelectric element (20 mm diameter and 0.5 mm thickness, NEC Tokin Corporation, Japan) to excite the resonator as the vibrator, an alternating current power source, and an optical non-contact displacement sensor. Since the power source is used to actuate the vibrator, the sensing element, i.e. the resonator, is free from power lines (Figure 1(a)). A microscope-type Laser Doppler vibrometer (KV-100, Denshigiken Corporation, Japan) and a spectrum analyzer (frequency resolution: 1 mHz, Advantest Corporation, Japan) were used for measuring the resonant frequency of the resonator (Figure 1(b)).

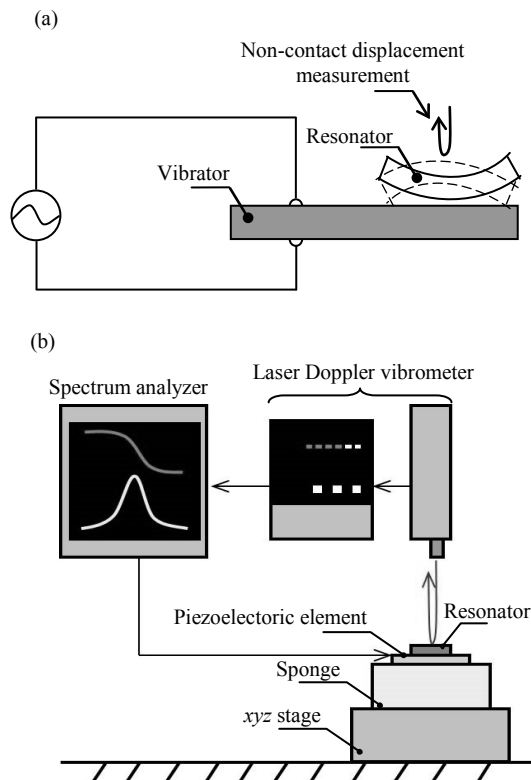Firstly, the target material adheres to the resonator

(a)

(b)

Figure 1. Principle of a line-free mass sensor ((a): Schematic of mass sensor, (b): Block diagram of resonant frequency measuring system).

without chemical bonding. Then the resonator is placed on the piezoelectric element. When the piezoelectric element is excited at an arbitrary frequency, the vibration is transmitted to the resonator mounted on it, which then vibrates at its resonant frequency. The resonator will never fall from the piezoelectric element because the amplitude of vibration is smaller than a nanometer scales. The change in resonant frequency is proportional to the mass of target material adhering to it.

B. Design of Disc Resonator

A disc-shaped resonator was designed to have a resonant frequency of several MHz (Fig.2). The outer diameter and thickness were 4.0 and 0.5 mm, respectively. The detecting area, d, was used as a parameter to design the resonator, then two types of resonator were fabricated (type A and B). Using an eigenvalue-eigenvector analysis employing a FEM was calculated to compare the resonance frequency of the two types of the resonator. The boundary conditions at the outer peripheral edge of the resonator were set to free edge. The density, longitudinal modulus of elasticity, and Poisson's ratio were set to 2,329 kg/m^3, 185 GPa, and 0.28, respectively

C. Fabrication of Disc-shaped Resonator

A photolithography technique such as deep-reactive-ion etching (DRIE) was used to fabricate the disc-shaped resonators with several diameters of detecting area from a 4-inch sized silicon wafer. The entire photolithography process was carried out in three steps; 1st wet etching, 2nd wet etching, and DRIE process (Fig.3).

1st wet etching process: A wafer was coated with a positive-type photoresist (OFPR-800, Tokyo Ohka Kogyo Co., Ltd, Japan) using a spin coater (ASC-4000, Actes Inc., Japan). The photoresist exposed to the UV light using a photomask α and a mask aligner (MA6, Suss MicroTec, Japan). After the developing, the silicon was liquid (wet)-etched to remove the unprotected oxide. The SiO$_2$ was removed using hydrogen fluoride. Finally, the photoresist was removed from the substrate using heating sulfuric acid treatment.
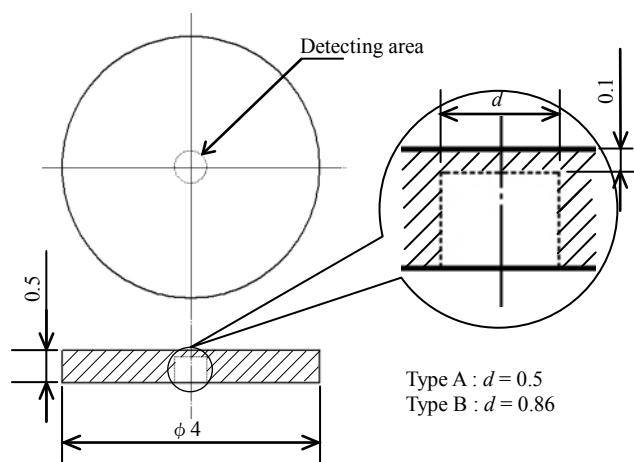
2nd wet etching process: The wafer was coated with a positive-photoresist (PMER P-LA900, Tokyo Ohka Kogyo Co., Ltd, Japan) using the spin coater. The photoresist was exposed using a photomask β and the mask aligner. After that, the developing and the wet etching were processed.

DRIE process: The 1st DRIE was performed for 23 min using a DRIE system (MUC-21, Sumitomo Precision Co. Ltd., Japan). After the photoresist was removed, a supporting substrate was adhered using the positive-type photoresist. The 2nd DRIE was performed for 90 min using the DRIE system. Finally, the supporting substrate was peeled using a stripping solution (Microposit Remover 1165, Shipley Co., Inc., US).
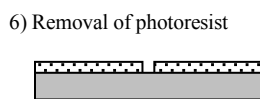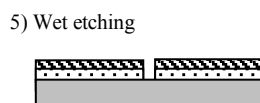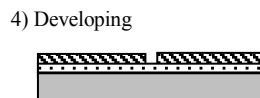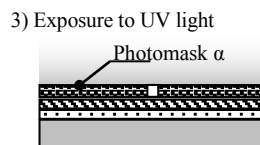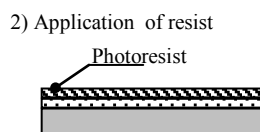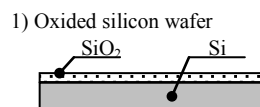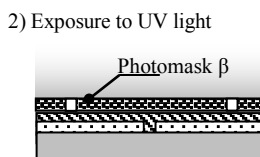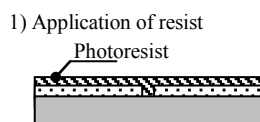

Figure 2. Cross sectional view of a disc-shaped resonator used for the line-free mass sensor (Units in mm).
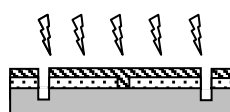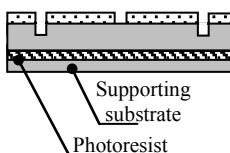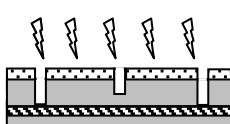
Figure 3. Photolithography of a disc-shaped resonator for deep etching including a two-step exposure process.

D. Measurement of Resonant Frequency

The resonant frequencies of each mode of vibration of the disc-shaped resonators were measured using a microscope-type Laser Doppler vibrometer, a spectrum analyzer, and a *xyz* stage.

E. Measurement of Glucose Concentration

As a typical human blood biomarker, glucose was selected as a sample material to evaluate the sensitivity of the line-free mass sensors. A set of D(+)-glucose (180.16, CAS No. 50-99-7, Wako Pure Chemical Industries, Ltd., Japan) solutions with concentrations between 250 ng/mL and 100 mg/mL was used.

A 0.1 μL sample of each solution was dropped on the detecting area of the disc-shaped resonator by a precision dispenser (SMP-3, Musashi Engineering, Inc., Japan). After that, the disc-shaped resonator was dried at room temperature for 10 min. The change in resonant frequencies compared to those without the sample solutions was then measured for each glucose concentration.

The disc-shaped resonator was cleaned using an ultrasonic washing machine (2210DTH, Emerson Japan Ltd., Japan) for 5 min. and dried for 30 min. in order to refresh and reuse it.

III. RESULTS AND DISCUSSION

### A. Design and Fabrication of Disc Resonator

The calculated results of the resonant frequencies for types A and B at 1st mode were 3.919 and 1.934 MHz, respectively (Table I). The surface areas of types A and B were 0.2 and 0.6 mm^2, respectively. The type A condition was selected to fabricate the disc-shaped resonator.

A disc-shaped resonator was fabricated from a silicon wafer.

B. Measurement of Resonant Frequency

The measured results of the resonant frequency of type A was 3.682 MHz, which agreed well with the theoretical

results obtained using FEM (Fig.4). The Q-factor was calculated to be 10,000, which was particularly high compared with those given in previous reports [1] [3]. It was considered that the noise of frequency was reduced enough to synchronize with the exciting frequency by use of the spectrum analyzer.
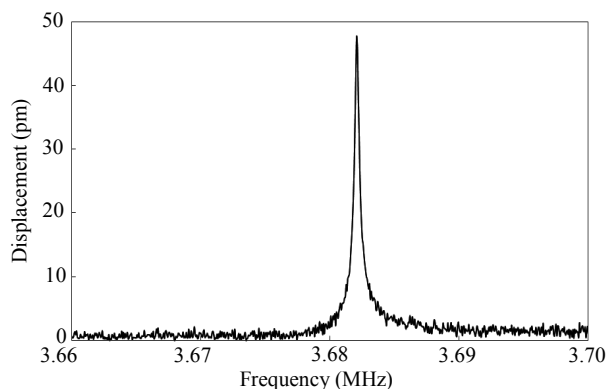
Figure 4. Measured results of the resonant frequency using a disc-shaped resonator at the primary mode.
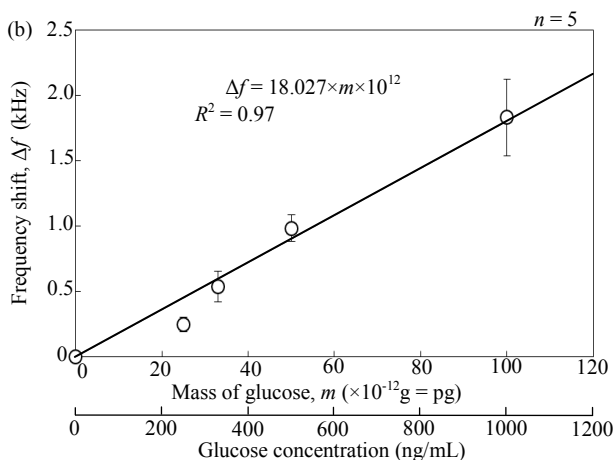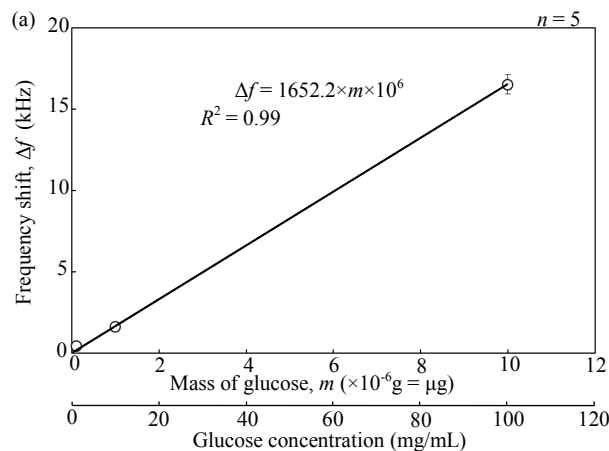
Figure 5. Relationship between the frequency shift and the mass of glucose for the line-free mass sensor ((a): 100 ng – 10 μg of mass of glucose, (b): 25 – 100 pg of mass of glucose).

TABLE I. CALCULATED RESULTS OF THE RESONANT FREQUENCY FOR EACH VIBRATION MODE.

		Circumferential oscillation mode of vibration	
		1st	2nd
Radial oscillation mode of vibration	1st	Type A	
		3.919 MHz	6.473 MHz
		Type B	
		1.934 MHz	3.707 MHz
	2nd	Type A	
		12.162 MHz	14.087 MHz
		Type B	
		5.612 MHz	7.216 MHz

C. Measurement of Glucose Concentration

The glucose concentrations were converted into a mass of glucose per 0.1μL of sample volume (Fig.5). The frequency shifts for the 0.1, 1 and 10 μg masses of glucose were 0.45, 1.64, and 16.52 kHz, respectively (Fig.5 (a)). The frequency shifts for the 0, 25, 33, 50 and 100 pg of glucose samples were 0, 0.24, 0.54, 0.98, and 1.83 kHz, respectively (Fig.5 (b)). The results of a linear regression analysis between 0 – 100 pg for the line-free mass sensor showed the R^2 value to be 0.97. The calibration curve between the frequency shift, Δf, and the mass of glucose, m, is given by $\Delta f = 18.027 \times m \times 10^{12}$ (Hz), showing that the frequency shift is proportional to the concentration of m in the sample solution. Since the frequency shifts by 18.03 Hz per 1 pg mass of glucose, the sensitivity is calculated as being 55 fg/Hz. Finally, the sensitivity of the line-free mass sensor was estimated to be 0.06 fg because the optical displacement sensor has a frequency resolution of 1 mHz.

IV. CONCLUSION

We designed and analyzed the performance of a line-free mass sensor, comprising a disc-shaped resonator and a separate excitation source. Our study indicates that, if an optical displacement sensor with a frequency resolution of 1 mHz is used, a sensitivity of 0.06 fg can be achieved with this line-free mass sensor. This sensitivity is adequate for the required level in order to carry out salivary hormone analysis.

REFERENCES

[1] M. Sepaniak, P. Datskos, N. Lavrik, and C. Tipple, "Peer Reviewed: Microcantilever Transducers: A new Approach in Sensor Technology", Anal Chem, Vol.74, pp. 568A-575A, 2002.

[2] E. A. Wachte and T. Thundat, "Micromechanical sensors for chemical and physical measurements", Review of Scientific Instruments. Vol.66, pp. 3662-3667, 1995.

[3] A. Janshoff, H. J. Galla, and C. Steinem, "Piezoelectric Mass-Sensing Devices as Biosensors – An Alternative to Optical Biosensors?", Angewandte Chemie - International Edition Vol.39, pp. 4004-4032, 2000.

[4] E. Benes, M. Gröschl, W. Burger, and M. Schmid, "Sensors based on piezoelectric resonators", Sensors and Actuators: A. Physical Vol.48, pp. 1-21, 1995.

[5] N. V. Lavrik, M. J. Sepaniak, and P. G. Datskos, "Cantilever transducers as a platform for chemical and biological sensors", Rev. Sci. Instrum. Vol.75, pp. 2229-2253, 2004.

[6] M. Yamaguchi and Y. Kimura "Proposal for a Power Supply Line-free Mass Sensor for Measuring Total Protein in Human Saliva", Sensor Letters, Vol.12. 2014 in press.

Comparison of PS25015A Dry Electrodes and Two Different Ag/AgCl Wet Electrodes for ECG Applications

Nika Zolfaghari, Mohsen Shafeie, Shahini Sirikantharajah, and Kristiina M. Valter McConville

Electrical and Computer Engineering
Ryerson University
Toronto, Canada
kmcconvi@ee.ryerson.ca

Abstract— The electrocardiogram (ECG) is one of the most important signals acquired from the body, as it serves as the immediate source of information relating to heart performance. Hence, a lot of research has gone into various types of ECG acquisition methods and systems. With the numerous methods and systems available at hand, it is important to compare, contrast, and evaluate the existing techniques. Not only does this help distinguish between the different techniques, it also helps build on the existing methods to create successful acquisition systems that can surpass the effect of unwanted factors, such as movement and other noise artifacts. This paper compares two different ECG acquisition systems, one of which uses PS25015A dry electrodes and the other, which uses two different silver/silver chloride (Ag/AgCl) wet electrodes. ECG signals were acquired from three healthy individuals, in the sitting position, using both systems simultaneously. Signals were first filtered to diminish noise then the R-wave peaks were detected. The voltage values of these peaks were compared between the devices and electrodes via statistical analysis. The signal-to-noise ratio (SNR) values of the signals were obtained as well and finally, the correlation coefficient of the signals were obtained. Overall, the dry electrodes may have a better SNR. However, the dry electrodes provided a lower wave amplitude, compared to the wet electrodes.

Keywords-Electrocardiogram (ECG), wet electrode, dry electrode, cross correlation, peak detection

I. INTRODUCTION

The electrocardiogram (ECG) has arguably become one of the most recognized and used biomedical signals. ECG is the electrical interpretation of the activity of the heart, and can easily be recorded with the use of surface electrodes either on the chest or limbs [1]. As the heart is one of the most important organs in the body, its contraction activity and performance is vital to monitoring health. The most important attribute of the ECG is that its shape is altered by abnormalities and cardiovascular diseases, such as arrhythmia, myocardial ischemia, premature ventricular contraction (PVC), infarction, and many more [1].

In terms of its signal acquisition, there are various methods of electrode placement. ECG is traditionally recorded using 12-channels for clinical use. In this 12 lead configuration, electrodes are placed on the right leg, and both wrists. The three augmented leads are (aVR, aVL, aVF) and six leads are placed on the chest [1]. Additionally, the left and right arm, and the left leg are used for leads I, II, and III,

which together form Wilson's central terminal (reference for chest leads) [1]. However, ECG can also be recorded using 6, 5, or 3 leads [1]. Recently, the advancement in technology has made it possible to record ECG from only 1 lead, either on the chest or on a limb. Furthermore, various reputable sources, such as the American Heart Association (AHA), recommend that a minimum sampling rate of 500 Hz be used for ECG data acquisition, but that a sampling rate twice that of the theoretical minimum would be ideal, i.e., 1000 Hz [1][2][3].

ECG is traditionally used in clinical settings, such as in the operating room, to monitor the heart rate of the patient, or to analyze a patient for various cardiovascular diseases or abnormalities. However, as technology progresses and as we become more and more aware of our health and the proper functioning of our body, this important biomedical signal is being slowly introduced in our daily life as a way of continuously monitoring one of our most important organs. New electronics and hardware, with their high efficiency and small size, have created an opportunity for the design of wearable and wireless ECG recording devices and real-time monitoring systems.

Like other biomedical signals, raw ECG signals contain various sources of interference. These noise interferences are comprised of high and low frequencies from the power line, muscle movement, breathing, and other near-by electromagnetic sources and/or cables [4]. Since in many cases real-time monitoring of ECG is important, the ECG needs to be filtered and processed in such a way that there is nearly no delay between the acquisition and representation of the signal. Different processing techniques and algorithms have been suggested by researchers and used by manufacturers, however, when we look into implementing such processing techniques in a wearable wireless ECG device, extra caution needs to be employed with the algorithm design due to processing times and data transfer speeds.

Another way in which ECG data acquisition differs is in the choice of electrode. The two most common categories of surface electrodes are wet and dry electrodes. Wet electrodes, specifically Ag/AgCl, are among the most commonly used electrodes for bioelectric applications. They certainly have their advantages, such as their simplicity, ease of use, low weight, and that they are disposable [5]. However, they are not without their disadvantages. Electrolytic gel should be applied between the skin and the

electrode in order to improve conductivity. This gel could cause allergic reactions or skin irritation [5]. These electrodes also have a limited shelf life due to dehydration, which affects impedance, generating noise [6]. The dehydration issues make these electrodes unsuitable for long-term continuous measurement [7]. Finally, the spacing between electrodes may be so small that the gel may smear and lead to short circuiting [8]. On the contrary, dry electrodes, generally metal plates, do not encounter any of these problems, and are easier to set up, however, they have their own drawbacks as well. Since there is no secure adhesion between the electrode and the skin, they can shift during motion [6]. Furthermore, these electrodes have relatively large contact impedance with the skin [6][9].

For the purpose of this pilot study, two wet Ag/AgCl electrodes (3MTM Red DotTM Monitoring Electrodes, and Bio-Protech Telectrodes) and a PS25015A dry electrode will be used to simultaneously record ECG signals from the chest using one lead for 60 seconds while the subjects are seated. The resulting signals will then be analyzed and compared in order to draw conclusions based on their performance.

This paper will proceed by looking at previous studies which have been done in relation to the comparison of dry and wet electrodes, in section II. Section III will move on to outlining the proposed procedure. The results will be presented in section IV, and finally section V will wrap up with the concluding remarks.

II. PREVIOUS STUDIES

A paper by Chi M.Y., et al. [10] compared dry electrodes by analyzing the data acquired, as well as their performance limits. As mentioned in this paper, the circuit designs of electrodes seem to be described well in literature; however a detailed comparison between electrodes are yet to be found. A standard testing procedure that compares noise and errors between the electrodes does not exist.

Furthermore, Gandhi N., et al. [11] compared Ag/AgCl wet electrodes to dry and non-contact electrodes. The comparisons were made by analyzing noise processes, as well as the physiological measurements. The non-contact electrodes had a higher resistance compared to the conductive electrodes. ECG data acquired from various materials were all compared to data acquired Ag/AgCl electrodes. Simple comparisons were made between the graphs, by analyzed different amplitudes, noise artifacts and frequency drifts. Results showed that the best dry electrodes that can potentially replace wet electrode are ones with a PCB finish. Many dry non-contact electrodes were found to have low frequency noise, which restricts their use for clinical purposes.

Additionally, another study performed by Chi M. Y. et al. [12] compared wet and dry electrodes for EEG purposes. The electrodes were compared using EEG data acquired from 10 subjects as they gazed at a target simulus, and amplitude sizes and steady state visual evoked potential (SSVEP) were used to compare the signals. The signals were compared using PSD values, signal-to-noise ratios,

and cross correlation. The correlation between the wet and dry electrodes was nearly perfect. However, the correlation between the wet and non-contact were lower. However, a lot of the comparisons made between electrodes seem to be based on just the graphs or a few parameters, such as amplitude, SNR, and correlation. Table I compares the existing techniques used to compare electrodes, and shows how this paper further builds on these techniques to compare wet and dry electrodes.

TABLE I. Comparison of Existing Techniques

Comparison of Existing Techniques	
Chi M.Y., et al.	✓ Circuit designs ✓ Performance limits
Gandhi N., et al.	✓ Amplitudes ✓ Noise artifacts ✓ Frequency drifts
Chi M. Y. et al.	✓ Amplitudes ✓ SNR
Currently Presented Method	In-depth Statistical Analysis: ✓ Amplitudes ✓ Noise artifacts ✓ SNR ✓ Cross correlation ✓ DC off-set ✓ Mean ✓ Variance ✓ Std deviation ✓ Std error

Moreover, the previous studies have been limited in the parameters used for comparison. This paper proposes an in-depth statistical analysis method with numerous parameters to compare wet and dry electrode systems.

III. METHODS

A. Subjects

This comparison method was tested on data acquired from the first three authors of this paper, which included one 32 year old male, and two females, 23 and 22 years old. The subjects were healthy and had no history of heart conditions.

B. Experimental Setup

Testing was performed on two ECG acquisition systems. The systems as well as different electrode types were compared by acquiring ECG signals from the chest at 1000 Hz. The Plessey ECG system was used to acquire dry electrode data, while the wet electrode system used was the CleveMed BioCapture. The skin was cleaned with alcohol wipes before positioning the wet electrodes.

The dry and wet electrodes can be seen in Figure 1 and 2 respectively. As prescribed in the user manuals of the systems, the PS25015A dry electrodes, 3M Red Dot Ag/AgCl electrodes, and the Bio-Protech Ag/AgCl Telectrodes were placed near the subclavius muscles (3cm beneath the left and right clavicles), as seen in Figure 3 [13].
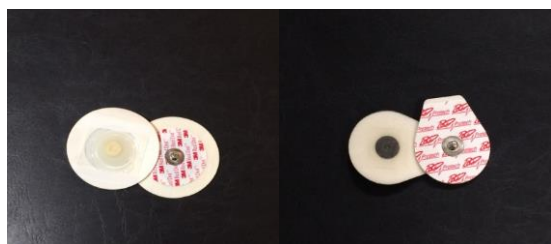
Figure 1: PS25015A Dry Electrodes

Figure 2: Wet Ag/AgCl Electrodes: 3M™ Red Dot™ Monitoring Electrodes (left) and Bio-Protech Telectrodes (right)
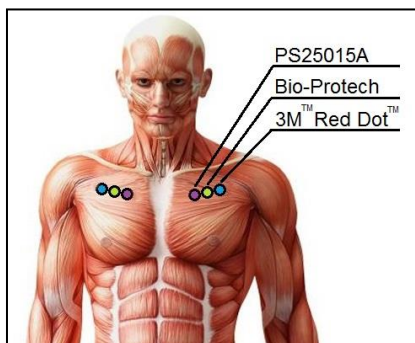

Figure 3: Electrode Placement on the Chest [adapted from 15]

Standard chest electrode positions can also be referred to in a paper authored by P.M. Rautaharju et al [14]. Both elbows were used as ground (not shown in Figure 3).

Once the electrodes were placed on the body, the dry electrodes were fed into the Plessey system, which was connected to a computer, and an offset of 0.1V was implemented. Snap leads were attached to each of the wet electrodes. The snap leads were fed into the input channels 1 and 2 and ground on the CleveMed Bioradio 150 system. The Bioradio was then connected to another computer via a wireless receiver. Moreover, data was acquired from both systems simultaneously; providing the same input to both systems, allowed for the quality and variations in the ECG signals to be analyzed.

The ECG was measured from each subject for 60 seconds, in the sitting position, and three trials were performed on each subject. The data files were converted into CSV files, in order to perform signal processing in MATLAB.

C. Signal Processing

The ECG signals acquired from both systems were sampled at 1000 Hz. Furthermore, the raw ECG data was filtered using low-pass, high-pass, and notch filters.

First, an 8th order low-pass Butterworth filter was used with a cutoff frequency of 180 Hz. The filter was designed based on (1) [1].

$$|H(\Omega)|^2 = \frac{1}{1+(\frac{\Omega}{\Omega_c})^{2N}} = \frac{1}{1+\varepsilon^2(\frac{\Omega}{\Omega_p})^{2N}} \qquad (1)$$

Where N is the order of the filter, Ω_c is the corner frequency, Ω_p is the pass-band edge frequency, and $1/(1+\varepsilon^2)$ is the band edge value.

Next a stop-band filter was used for a notch filter at 55-65 Hz, followed by a high-pass FIR filter with a cutoff frequency of 0.002 Hz. In order to detect heart rate, the R waves were made prominent by squaring the entire ECG signal. Peak detection was performed using the thresholding technique, similar to the R-wave detection performed by H. Kew and D. Jeong [16]. A threshold value was used to detect the R-wave peak, as seen in a study by P. Verdecchia et al. [17].

Statistical analysis was performed on the R-wave peak values detected in order to compare the ECG signals obtained through the wet and dry electrode systems. The parameters computed include mean (2), standard deviation (3), variance (4), and standard error (5). The signals were also compared by computing the signal-to-noise ratios (SNR) and the cross-correlation. Cross-correlation (6) was performed on the outputs from each electrode to evaluate the similarity between the signals by obtaining the correlation coefficient [1][18][19].

$$\bar{x} = \frac{\sum x}{n} \qquad (2)$$

Where $\bar{x}$ is the mean, n is the number of samples, and x are the data values.

$$\sigma = \sqrt{\frac{\sum_{i=1}^{n}(x_i-\bar{x})^2}{n-1}} \qquad (3)$$

Where σ is the standard deviation x_i are the data values, and $\bar{x}$ is the mean of x_i.

$$\sigma^2 = \frac{\sum(x_i-\bar{x})^2}{n-1} \qquad (4)$$

Where σ^2 is the variance.

$$SE = \frac{\sigma}{\sqrt{n}} \qquad (5)$$

Where SE is the standard error.

$$r = \frac{\sum_i[(x(i)-mx)\times(y(i-d)-my)]}{\sqrt{\sum_i(x(i)-mx)^2}\sqrt{\sum_i(y(i)-my)^2}} \qquad (6)$$

Where *r* is the correlation coefficient, *x(i)* and *y(i)* are the two signals, *mx* and *my* are their means respectively, and *d* is the delay.

IV. RESULTS

Figure 4 shows a sample plot illustrating the three ECG signals obtained from the three electrodes, PS25015A dry electrodes, Bio-Protech Ag/AgCl wet electrodes, and 3M Red Dot Ag/AgCl wet electrodes respectively. It is evident from Figure 4 that the dry electrode system shows a lower amplitude, compared to the wet electrode systems. Both of the wet electrode systems show amplitudes of approximately 1 mV.

Thresholding was used to perform R-wave detection in order to detect the heart rate, similar to the techniques used by H. Kew and D. Jeong [16]. The average instant heart rate can be seen in Figure 5.

Table II compares the processed data acquired from the three electrodes. As expected, the two wet electrodes showed higher correlation with each other than with the dry electrodes. The dry electrodes were found to have a negative DC-offset, compared to the wet electrodes, and provided the best SNR. Statistical analysis was performed on the R-wave peak values for each of the three electrodes, similar to analysis performed by G. Crifaci et al [20]. The 3M Red Dot electrodes showed higher mean R-wave peak voltages. For example, subject A had a mean R-wave peak of about 0.99 mV when measured through the 3M Red Dot electrodes and a mean of only 0.39 mV when measured through the dry electrodes.

When comparing the standard errors across the three electrodes for the different subjects, the results seem to vary. Subject A had an error of 0.0011 mV for the dry electrode, and errors of 0.003 mV and 0.0054 mV for the wet electrodes, giving a slight difference of 0.0043 mV between the dry and wet electrodes, with the dry electrode having the lowest error. On the other hand, Subject B had an error of 0.0045 mV for the dry electrode, and errors of 0.0019 mV and 0.0017 mV for the wet electrodes, resulting in a difference of 0.0028 mV, with the dry electrode having the highest error. Similarly, for Subject C, there was an error of 0.01 mV for the dry electrode, and errors of 0.0072 mV and 0.0055 mV for the wet electrodes, resulting in a difference of 0.0045 mV with the dry electrode once again having the highest standard error. In summary, there is no suggestion of consistent differences in the standard errors between electrodes.

It is important to note that there were a few factors which may have affected the results. Although the data was acquired simultaneously from the three electrodes, there was an inter-electrode distance of 3.0 cm. This may have affected the results, as the electrodes were each acquiring ECG data from slightly different positions on the chest. The skin was wiped with alcohol before the electrodes were positioned; however, there may not have been 100% electrode-to-skin contact.

TABLE II. Numerical Analysis

|	PS25015A	3M Red Dot	Bio-Protech
DC-Offset (mV)	-0.2099	0.0205	0.0239
Corr Coef (%)	PS25015A & 3M Red Dot = 5.05		
	3M Red Dot & Bio-Protech = 87.6		
	PS25015A & Bio-Protech = 5.71		
SNR (db)	28.9	19.5	19.3
Subject A			
Mean (mV)	0.3897	0.9940	0.7050
Variance (mV)	0.0013	0.0094	0.0364
Std Dev (mV)	0.0355	0.0925	0.1669
Std Error (mV)	0.0011	0.0030	0.0054
Subject B			
Mean (mV)	0.172	0.7952	0.6320
Variance (mV)	0.0056	0.0066	0.0027
Std Dev (mV)	0.0697	0.0572	0.0510
Std Error (mV)	0.0045	0.0019	0.0017
Subject C			
Mean (mV)	0.0708	0.2490	0.4420
Variance (mV)	0.0010	0.0124	0.0295
Std Dev (mV)	0.0322	0.1110	0.1711
Std Error (mV)	0.0100	0.0072	0.0055
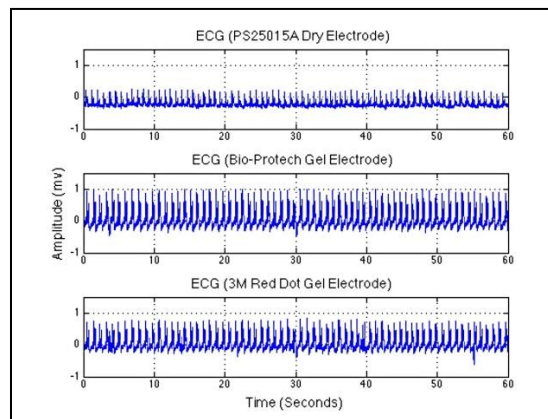
Figure 4: ECG signals acquired from the three electrodes
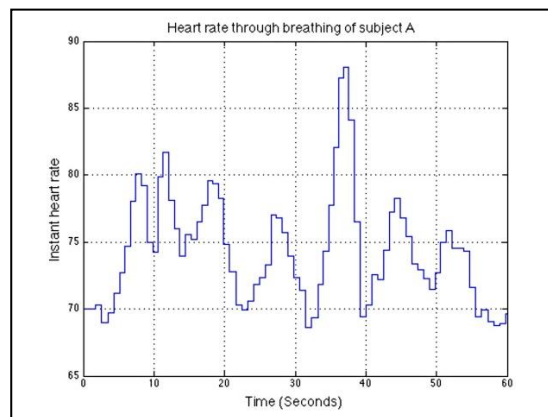

Figure 5: Heart Rate while Breathing

Furthermore, the dry electrodes were attached firmly onto the subject, but the pressure on the electrodes may not have been uniform for the entire duration of the experiment because of the elasticity of the fastening band. Moreover, two individuals were running the two systems on two different computers to start data acquisition. Hence, there may have been a slight delay in start/stop times during acquisition, but this was adjusted in the data analysis by aligning the R-waves.

For future work, the results may be more definitive if more subjects are used.

V. CONCLUSION

The results showed fairly high signal-to-noise ratios and varying mean and variance ranges for each electrode type. However, there were suggestions of differences between the electrodes, such as the SNR, where the dry electrodes seemed to have a better SNR in our subjects, compared to the wet electrodes even though they recorded at lower amplitude. Although both types of electrodes have their own advantages and disadvantages, the determination of the most advantageous option is dependent on the individual user's applications and needs. For example, if the user desires a higher SNR value, dry electrodes should be used. However, if a lower standard error is desired, then wet electrodes should be used. The advantage of this approach consists of clearly defined pros and cons for each system so that the user can make a more informed decision. For future work, these values can be compared to a wider range of dry and wet electrodes and ECG acquisition systems, and can be tested on a larger population for more accurate results. Most importantly, the methods discussed in this paper can be used as a platform for the comparison of electrodes in order to help evaluate different systems and their accuracies.

ACKNOWLEDGMENT

REFERENCES

[1] R.M. Rangayyan, "The electrocardiogram (ECG)," Biomedical Signal Analysis. IEEE Press, pp. 14-28, 2002.

[2] G.P. Pizzuti, S. Cifaldi, and G. Nolfe, "Digital Sampling Rate and ECG Analysis," Journal of Biomedical Engineering, vol. 7, Aug. 1985, pp. 247-250, doi: 0.1016/0141-5425(85)90027-5.

[3] P.R. Rijnbeek, J.A. Kors, and M. Witsenburg, "Minimum Bandwidth Requirements for Recording of Pediatric Electrocardiograms," Circulation: Journal of the American Heart Association, vol. 104, Dec. 2001, pp. 3087-3090, doi: 10.1161/hc5001.101063.

[4] A. Gacek and W. Pedrycz, "The Main Properties of ECG Signals," ECG Signal Processing, Classification, and Interpretation, 2012, pp. 25-26.

[5] Y. Wang et al., "Dry Electrode for the Measurement of Biopotential Signals," Science China, vol. 54, Nov. 2011, pp. 2435-2442, doi: 10.1007/s11432-011-4354-0.

[6] A. Gruetzmann, S. Hansen, and J. Muller, "Novel Dry Electrodes for ECG Monitoring," IOP Publishing, Oct. 2007, pp. 1375-1390, doi:10.1088/0967-3334/28/11/005.

[7] E. Nemati, J. Deen, and T. Mondal, "A Wireless Wearable ECG Sensor for Long-Term Applications," IEEE Communication Magazine, Jan. 2012, pp. 36-43, doi: 10.1109/MCOM.2012.6122530.

[8] A. Searle and L. Kirkup, "A Direct Comparison of Wet, Dry, and Insulating Bioelectric Recording Electrodes," Physiological Measurement, vol. 21, May 2000, pp. 271-283, doi: 0.1088/0967-3334/21/2/307.

[9] X. Pu et al., "A Wireless 8-Channel ECG Biopotential Acquisition System for Dry Electrodes," IEEE International Symposium on Radio-Frequency Integration Technology, Nov. 2012, pp. 140-142, doi: 10.1109/RFIT.2012.6401640.

[10] Y. M. Chi, T. Jung, and G. Cauwenberghs "Dry-Contact and Noncontact Biopotential Electrodes: Methodological Review," IEEE Reviews in Biomedical Engineering, vol. 3, Dec. 2010, pp. 106-119, doi: 10.1109/RBME.2010.2084078.

[11] N. Gandhi, C. Khe, D. Chung, Y. M. Chi, and G. Cauwenberghs, "Properties of Dry and Non-contact Electrodes for Wearble Physiological Sensor," International Conference on Body Sensor Netowrks, May 2011, pp. 107, doi: 10.1109/BSN.2011.39 -112.

[12] Y. M. Chi, Y. Wang, C. Maier, T. Jung, and G. Cauwenberghs, "Dry and Noncontact EEG Sensors for Mobile Brain-Computer Interfaces," IEEE Transactions on Neural Systems and Rehabilitation Engineering, vol. 20, May 2012, pp. 228-235, doi: 10.1109/TNSRE.2011.2174652.

[13] CleveLabs, "Electrocardiography I Laboratory," Cleveland Medical Devices, 2006, pp. 1-14.

[14] P.M. Rautaharju, L. Park, F.S. Rautaharju, and R. Crow. "A Standardized Procedure for Locating and Documenting ECG Chest Electrode Positions," Journal of Electrocardiology, vol. 3, Jan. 1998, pp. 17-29, doi: 016/S0022-0736(98)90003-6.

[15] Cypher Avenue, "Human Muscle Anatomy," 2013, Retrieved March 10, 2014 from < http://cypheravenue.com/wp-content/uploads/2013/01/human-muscle-anatomy.jpg>

[16] H. Kew and D. Jeong, "Variable Threshold Method for ECG R-peak Detection," Journal of Medical System, vol.35, Jun. 2011, pp 1085-1094, doi: 0.1007/s10916-011-9745-7.

[17] P. Verdecchia et al., "The Voltage of R Wave in Lead aVL Improves Risk Stratification in Hypertensive Patients without ECG Left Ventricular Hypertrophy," Us National Library of Medicine National Institutes of Health, vol. 8, Aug. 2009, pp. 1697-704, doi: 10.1097/HJH.0b013e32832c0031.

[18] W. Thalheimer and S. Cook, "How to Calculate Effect Sizes from Published Research Articles: A Simple Mythology," 2002, pp. 1-9.

[19] L. Welch, "Information Theory," IEEE Transactions on Information Theory, vol. 30, 1974, pp 397-399.

[20] G. Crifaci et al., "ECG and GSR measure and analysis using wearable systems: Application in anorexia nervosa adolescents," Image and Signal Processing and Analysis (ISPA), 2013 8th International Symposium on, Sept. 2013, pp. 499-504, doi: 10.1109/ISPA.2013.6703792.

A Miniature Multisensor Biosignal Data Recorder and its Evaluation for Unsupervised Parkinson's Disease Data Collection

Chris Bailey, Garry Hollier,
Anthony Moulds, Michael Freeman
Department of Computer Science
University of York, UK
chrisb@cs.york.ac.uk
anthony.moulds@york.ac.uk
garry.hollier@york.ac.uk
mike.freeman@york.ac.uk

Jim Austin,
Alex Fargus, Thomas Lampert
Cybula Ltd,
York, UK
austin@cybula.com
alex.fargus@york.ac.uk
tom.lampert@hotmail.com

Abstract—**An improved miniature biosignal data sensor and recorder device is described, (NAT-1-4G) with 3-axis accelerometer, and a 2K Sa/sec all-channel recording capacity of 24 hours or more with a single zinc-air battery cell. Like the previous NAT-1 prototype device, this measures less than 18x22x10mm and weighs less than 2.3 grams, including the battery. In this paper we describe the device in detail, and introduce the presentation of tremor data measurement captured in the context of Parkinson's disease fore-arm monitoring. The NAT-1-4G device has already achieved translation to commercialization and we expect it to become commercially available in the near future.**

Keywords- Neurophysiology; Bio-signal sensors; Medical sensors, Parkinson's Disease.

I. INTRODUCTION

It is well understood that use of biosignal data acquisition is increasingly important in many application scenarios, not the least of which are biomedical applications. Often, such measurements are taken in wired or wireless umbilical modes, in other words, within a clinical evaluation setting, with data captured and analyzed over relatively short time windows, and in unnatural settings.

However, the ability to perform ambulatory monitoring of patients provides the possibility of long-duration data capture of bio-parameters in a normal living situation or work-place. This has been an aim for many decades, and has developed from early magnetic tape based data capture [1], to digital systems [2], custom integrated circuits [3][4] and more advanced medical data recorders [5][6]. Such capabilities are identified by many clinical researchers as being desirable. The opportunity to learn more about medical conditions as well as the condition of individual patients themselves is seen as a major motivator for developing suitable devices. This is very true of application in the domain of Parkinson's Disease and similar tremor-related medical conditions, where often the primary mode of data capture is limited to a supervised scenario [7][8][9]. The importance of gathering continuous data for drug management, establishing and gauging long-term prognosis, and the personal reassurance for patients afforded by suitably presented feedback from monitoring systems, cannot be underestimated.

The "NAT" (Neural Activity Tracker) project aims to produce a multi-purpose data sensing and recording solution that is extremely small, lightweight and having a recording capacity of days to weeks, dependent upon the selection of parameters such as sample frequency. The NAT-1 device [10] introduced our first solution to this problem in 2013. Since then we have enhanced and improved our design, resulting in NAT version 1-4G. This newer device includes multiple improvements, including the ability to alter the signal sensitivity of individual recording channels to adapt to a given bio-signal type, including ECG/EEG/EMG/EOG (Electro-encephalography (Electro-myography, Electro-cardiography, Electro-oculography), and also auxiliary sensor modules (such as temperature for instance). The NAT-1-4G also retains its capability for tri-axial accelerometer data capture, and in an accelerometer-only recording mode allows 500 samples per second across three simultaneous axes, with recording times up to 3 days in current prototypes.

This paper presents the NAT-1-4G in technical detail in Sections II and III, whilst Section IV documents some initial experimental applications of the device with a Parkinson's Disease tremor collection scenario. Note that the intention of this paper is not clinical, we do not make any clinically definitive claims about the data collected, but will observe and determine the suitability of the device for capturing such data, and for showing characteristics typically symptomatic of a Parkinson's Disease subject.

Section V highlights the additional resources developed alongside NAT, including docking station, wrist-mount, and the infra-red data signature time-stamp daughterboard. A brief state-of-the-art is given in Section VI, and conclusions are presented in Section VII.

II. A SMALL FORM-FACTOR DATA-RECORDER

The NAT is a device family of only 18x22mm in size, less than 10mm in height (when using a zinc-air disposable power cell). It weighs less than 2.3 grams, which means it is attractive in applications where regulatory constraints apply

(e.g., use with small animals). It is so light in weight that it quite unobtrusive as a human-subject wearable body-sensor. This low-weight attribute also means that multiple devices can be worn individually or in small groups where appropriate, without causing encumbrance of the subject's normal movements and behavior. We have verified this in a fashion, with team members wearing the device continuously for up to three days (using a 3D-printed wrist-capsule) with no issues.

A NAT device is shown in the image of Figure 1, with a ball-point pen of normal size for scale. In the photograph provided in Figure 1, we can see some interesting features. The major part of the device has a profile of less than 4 mm. Also visible in Figure 1 is a specially designed battery clip for housing a zinc-air cell (as used in hearing aids). This is the gold-plated metal structure. The use of flatter button cells can be envisaged to make a smaller profile possible, though this has weight implications. We also note the potential for ultra-thin flexible lithium polymer rechargeable batteries, which have a similar footprint and only 2mm height profile,
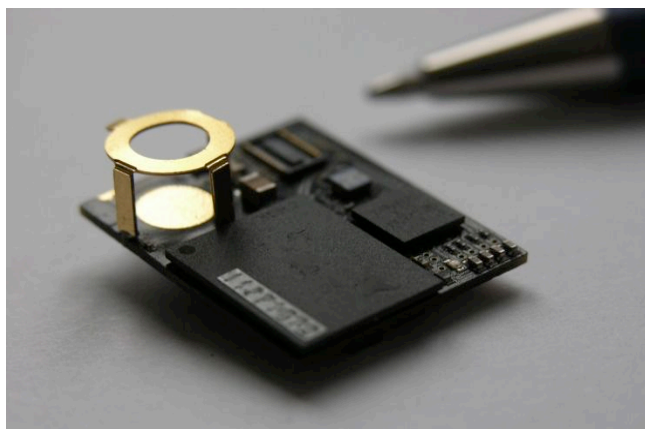
that would align well with the NAT PCB module in situ.
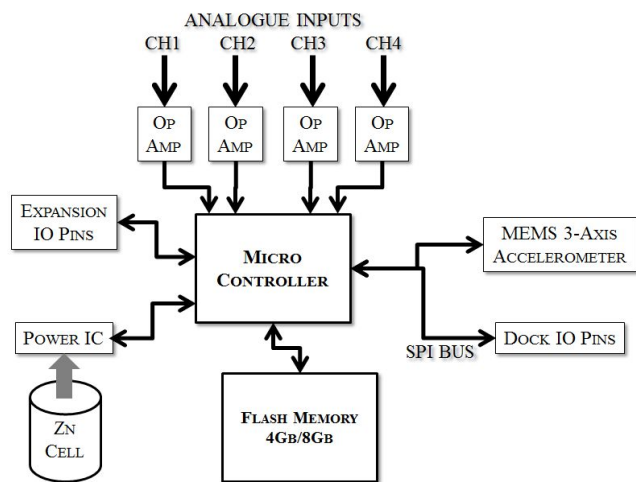
Figure 1. Top View of NAT Device

Figure 2. NAT Device – Sub-component Block Diagram.

Near the tip of the ball-point pen, one can see a small low-profile connector socket, which is actually a mezzanine daughterboard connector port. This permits a range of possible extension modules. Figure 2 shows the system level block diagram. As for our previous NAT-1 device [10], this device comprises of three key components – a flash memory chip (largest chip in Figure 1), a proprietary CPU (mid-sized chip of Figure 1), and a proprietary MEMS (Micro-Electro-Mechanical System) device for accelerometer (smallest chip of Figure 1). Additional analogue front-end components provide appropriate signal conditioning for the signal ranges typically encountered in a range of biosensor and biomedical applications. This is augmented by the introduction of programmable gain on a per-channel basis, with signal range up to +/-8mV, and ability to scale to signals in the sub-1mV range without appreciable noise.

III. NAT-1-4G DEVICE SPECIFICATIONS

The NAT-1-4G has the specifications as outlined in Table I. The device has a wide range of possible sample rates, ranging from 100 Sa/sec to 2 KSa/sec via the user interface software application. At 2 KSa/sec, the device consumes 4.8mA of current from a single 1.4-volt cell, and can record for up to 12 hours. An 8-GBit flash option is possible (NAT-1-8G) and would have up to 24 Hours of recording capacity at maximum rates. At lower sample rates, the capacity of the flash is extended to many days, for example 6 days at 100 Sa/sec for accelerometer only. This compares well with reported state of the art examples [3,4], given that the system is comprised of readily available commodity integrated circuits. The device has three important connection mechanisms, these being the analog input connector (angled connector block to left of device in Figure 3a), the daughterboard extension socket (Figure3b) and the docking-shoe connectors (seen in Figure 3a)

A particular feature of NAT-1 was the use of a single zinc-air power cell. Such cells are widely used in hearing aids, and have an active power-delivery life-span of around two weeks, after which the cell begins to lose effectiveness. We have retained this mode of power provision in NAT-1-4G. However the possibility of using alternative power cells is being actively investigated at present. To date, the Zinc-Air modules appear to give the best power density for size and weight with considerable record times up to 2 weeks.

IV. EVALUATION METHODOLOGY

Previously, most of the testing of the prototype device has been limited to test scenarios including (a) EEG and Accelerometer data collection from mice in live test scenarios undertaken by researchers at the University of Aberdeen, (b) a preliminary EMG capture evaluation at the University of York, and a (c) high-G test setting using a golf-club attachment to capture golf swing behaviors in terms of club rotation, side-movement and swing-path motion [10]. In all cases, the device was used untethered and powered exclusively with a single zinc-air cell. This

work was aimed at gaining an initial scope of capabilities of the device. In this paper, with the newer NAT-1-4G, we describe the use of the device in capturing tremor motion in a Parkinson's disease subject, and we compare this to data captured in the same way for healthy control subjects. This is a limited test-scenario owing more to engineering evaluation than clinical study, and should not be considered as a practical clinical evaluation study.

The experimental method consisted of a wrist-mounted device (see later section VI for details and photographs) which in most cases is worn continuously for several days, and only being removed where not appropriate for the device operation (e.g. whilst showering). All three accelerometer channels were sampled at 500 Sa/Sec with a resolution of 8 bits per channel for a full-scale range of +/- 2000 milli-G. An important aspect of the data collection is that there is no knowledge of activities during data collection (it is unsupervised).

Unlike short laboratory assessed (supervised) tremor measurements, where a series of directed or constrained actions are monitored for a period of perhaps 1 hour, here the data was collected blindly for up to 72 hours. This presents particular issues for data interpretation which we discuss further in later sections. The purpose of the evaluation was to make a straightforward determination that the NAT-1-4G device is (or is not) capable of gathering potentially clinically-useful tremor data during long unsupervised periods of use.
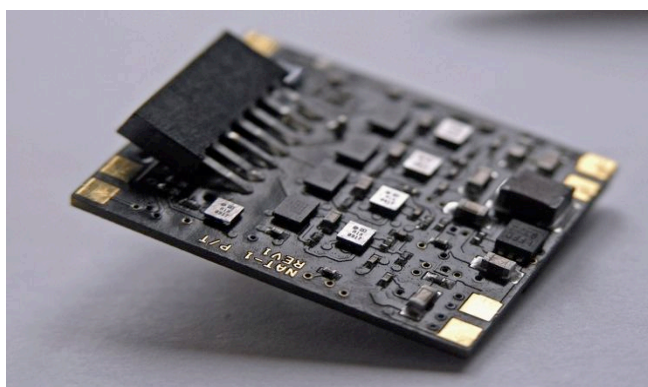
(a)
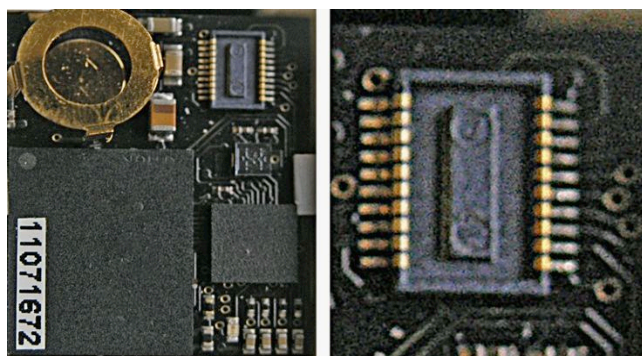
(b)

Figure 3. (a) Overhead View of NAT and Daughterboard Connector, and (b) Analogue Connector Port on NAT Device Underside

In order to understand our evaluation, it is useful to first of all exemplify the typical data characteristics likely to be observed in such an experimental study. A common aspect of Parkinson's tremor is the presentation of an excess of frequency components in the 5 to 7 Hz range as compared to typical healthy subjects.

The example of Figure 4, reproduced from a recent publication [11], illustrates this quite well. It is seen that a control subject has a relatively broad range of frequency components in movement measurements, whilst a Parkinson's patient exhibits a classical dominant frequency peak centered around the 5-6 Hz frequency, (often described as the unilateral or bilateral resting tremor) which is attributed to motor-neuron induced involuntary movements in the instrumented limb. These components usually have noticeably larger magnitudes than typical average motions generated by intended limb motion.

TABLE I. NAT-1-4G SPECIFICATIONS

Parameter	Limits	Units
Analogue inputs	4	channels
Bits per analogue channel recorded	11	bits
Mems Accelerometer	3	Axis
Bits per Accel. Axis	8	bits
Sample rate (max)	2000	x 4 ch
Max Current 2KSa/s 500Sa/s	4.8 2.4	mA mA
Data Capacity	4 or 8	Gbits
All-Channel Recording Time at 2K Sa/Sec	12 or 24 [a]	Hours
Analogue Range (previous NAT)	± 500 min ± 8000 max ± 1000 [b]	uV
Accelerometer range	Selectable 2 / 8	G (G-force)
Accelerometer sensitivity	18 / 72	mG (G-force)

[a]   Recording time for all channels. Revised device has accellerometer-only option with 6 day record time at 100 Sa/Sec.

[b]   Original NAT had fixed +/-1mv voltage range. Revised NAT range is channel programmable up to +/- 8mv.
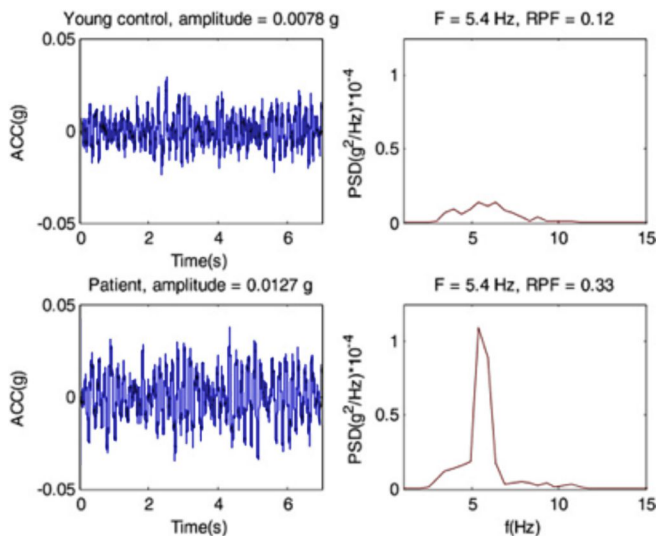
Figure 4, Example of Parkinson's Tremor components centered around 5 to 6 Hz for control (top) and affected patient (bottom). Reproduced from Meigal et al [11]

It is important perhaps to note that there is a significant difference between a resting limb exhibiting tremor (as might be observed under a controlled measurement scenario) and a limb measured over a significant timescale with unsupervised 'every-day' behaviors. The challenge for long-term unsupervised monitoring is to distill reliable indicators from inherently component-rich data sets. NAT-1-4G can of course be used for both a controlled resting limb study and an unsupervised data recording scenario.

In terms of existing devices, of which there are too many to present a comprehensive survey here, we have surveyed a subset of current devices that have succeeded in achieving commercial translation into common use, as tabulated in Table II, for comparative purposes. Several of these are wirelessly tethered devices, and several are non-wireless devices, including NAT-1-4G itself.

The Neurologger-2A device has some similar sets of capabilities to the NAT-1-4G, as might be expected as it is a similar onboard storage recorder, whereas the wireless devices have significant demands for power, requiring larger batteries and more circuitry. It can be seen that NAT-1-4G provides the smallest, lightest, and longest recording lengths for a device integrating both accelerometer and analogue sensor (e.g. EEG) channel recording as standard. Neurologger-2 with add-on accelerometer board has comparable weight and size to NAT-1-4G. The NAT device has a large signal range and is programmable to accept analogue signal inputs up to +/-8mV and can be reduced to < +/- 500uV for high-sensitivity .

Ambulatory monitoring has importance for the role of extended out-patient monitoring of EEG as a diagnostic aid and guide to treatment [12][13]. Recent work in this field includes many wireless approaches to ambulatory monitoring, but these are effectively 'tethered' via a secondary monitoring or recording station [14][15]. Recent literature reports an 8-channel EEG sensor node which "measures 35mm x 30mm x 5mm excluding Li-ion battery" [14], and power consumption in the range of 27-42mW., equivalent to around 3 to 5 mW per channel.

TABLE II.   COMPARISON WITH SOME RECENTLY REPORTED DEVICES

Device & Type	SIZE & WEIGHT	Battery Type & Record Time	Sensors and Inputs	Sample Rates	Data Storage	Refs if any
MCROBERTS HYBRID Bluetooth Tethered	87x45x17 mm 74 grams	Lithium Polymer 60 hrs at 100 Hz	2G tri-axial accelerometer triaxial Gyroscope	100 Sa/sec	SD card	[16]
Neurologger 2A Untethered EEG logger	22x15x5 mm 1.7 grams with battery and 3-axis accelerometer	2x ZN10 battery 124 hrs at 100 Hz 32 hrs at 400 Hz	4 channel analog input extra board provides triaxial accelerometer with additional weight (about 0.4 gram).	100 Sa/sec up to 19 kSa/sec for one channel 1000 Hz for accelerometer	On board flash Up to 1GBit	[17]
G-Link Wireless tethered	58x43x21 mm 40 grams	Lithium polymer Record time not stated	2 G/10 G Triaxial accelerometer, temperature sensor	2 channel (accel/temp) 4 kSa/sec 4 channel 2 kSa/Sec	Onboard 2Mbyte	[18]
NAT-1-4G Untethered EEG/EMG/ECG and Accel Logger	22 x18x10 mm < 2.3 grams with battery	Zinc-Air hearing aid battery 9 hours at 2000 Sa/Sec 72 hours at 250 Sa/sec >1 week at 100 Hz	2 G/8 G triaxial Accelerometer 4 channel +/-8 mV analog in	Up to 2000 Sa/sec	Built in Flash 4 or 8 Gbit.	This paper

V.   EVALUATION RESULTS

After gathering data from a total of four subjects, various data processing approaches were explored to derive useful data. The initial raw data sets contain a number of artifacts that need to be managed. Inevitably the accelerometer range encounters clipping (saturation) , since the sensitivity of the accelerometer scale needs to be fine enough to detect tremor motions, even though other motions in unsupervised data collection can be more dynamic. A second issue is that of constant-G offsets caused by orientations of the limb (in this case the wrist) in different postures for instance. Both of these aspects may be observed in Figure 5a, which shows the raw data collected over a 48-hour period, and clearly exhibits variable constant-G offsets as well as saturation.

Figure 5a highlights a further aspect of interest, colorized in red on the trace. In the data survey we have conducted we have observed that it is possible to automate identification of 'quiet periods' where activity is relatively low. These are analogous to a resting limb, though in fact these so-called quiet periods contain non-resting activity, but less so than other segments of the data.

By applying very-low-frequency component extraction and adjustments to the raw data, it is possible to remove the constant-G offsets from the data, whereupon it is possible to plot the magnitude of acceleration of the data on each channel without bias due to such offsets. This is illustrated by Figure 5b, which shows the normalized magnitude in red against the whole data set in pink. Figure 5c shows a small segment of the data with the raw data magnitude plot versus the offset adjusted case.

Once these treatments are applied to the gathered data, it becomes possible to generate power-spectra plots of magnitude versus frequency components using FFT analysis. We may then plot each accelerometer axis as well as a combined power spectra plot, which combines motion from all three axes. Figure 6a shows such a collection of plots for a healthy subject, whilst Figure 6b shows the same for a known Parkinson's disease volunteer. It is already noticeable that the Parkinson's disease plots show the classical excess of activity in the 5 to 6 Hz region.

Figures 7a and 7b show the combined data sets for four human volunteers for comparison. The subjects included three healthy individuals and one Parkinson's disease diagnosed subject. Data was collected for each wrist (left/right) on separate occasions. When only the quiet periods of the data sets are analyzed, the components of the data become less 'cluttered'. That is not to say there is not much to be discovered by analyzing a more complex data context – but rather that there is much to be done to develop useful analytical models from such data sets.

Figures 8a and 8b show examples of non-selective data analysis (i.e. all data from a multi-day data capture run) and using the so-called 'quiet periods' only.

In the healthy subjects the plots have a clearly defined roll-off toward 20 Hz and if the slope of the characteristic was subtracted from these plots there would be a fairly uniform response. In the case of the Parkinson's subject however , one can observe an obvious excess of frequency activity in the 5 to 7 Hz range and this correlates well with our expectation if the device were capable of effective collection of tremor data. We note that the left and right hand characteristics of the Parkinson's disease volunteer are different. This may reflect the fact that the dominant limb and non-dominant limb have different use in every-day activity and/or a function of the tremor being non-symmetrically presented.

All of the subjects exhibited a strong signal in the area of 1 to 2 Hz, which we attribute to normal behavior – most likely arm swing due to walking and gait behavior. This will be subject to further investigation in future work planned by the group. As noted earlier this is not intended to be a clinical study – rather an observation of the suitability of our device for long term signal capture in this domain – can we capture data that is useful in differentiating tremor related micro-movements? The data captured seems to confirm the value of the device for such work.

VI.   DOCKING STATION, ANALYSIS TOOLS, AND EXTENSION DAUGHTER BOARDS

The NAT device has the advantage of being provided with a bespoke docking station, for download of data from flash via USB. This is illustrated in Figure 9. Once downloaded, the data can be processed using Cybula Ltd Signal Data Explorer software suite, which can be trained to perform auto detection and classification of signal behaviors and events [10]. A final notable aspect of the current NAT-1-4G system suite is the infra-red time-code recording daughterboard. This extremely small add-on allows recording of an infrared pulse code stream along-side the analogue channels and accelerometer (see Figure 10 for photograph of IR device fitted on NAT main unit).

Figure 11 shows the wrist-mount prototype capsule in various views when worn. The wrist module is quite compact but could be further reduced in size. With certain power cells the format and size of the capsule could certainly be reduced considerably. These early prototypes were developed using 3D rapid prototyping (close up view shown n Figure 12). We are currently working on more sophisticated one-piece wrist-mount modules with integral strap, and using more flexible plastics.

Future developments for the daughterboard connector socket could include RF telemetry functions. It is also possible to use the daughterboard connector to act as a micro-backplane to permit multiple NAT devices to be ganged and synchronized to perform something like 16 or 32 channel acquisition, thus linking multiple NATs in a synchronized data capture mode. This is particularly interesting for multi-limb monitoring where relationships between respective limb data-sets might be of interest.
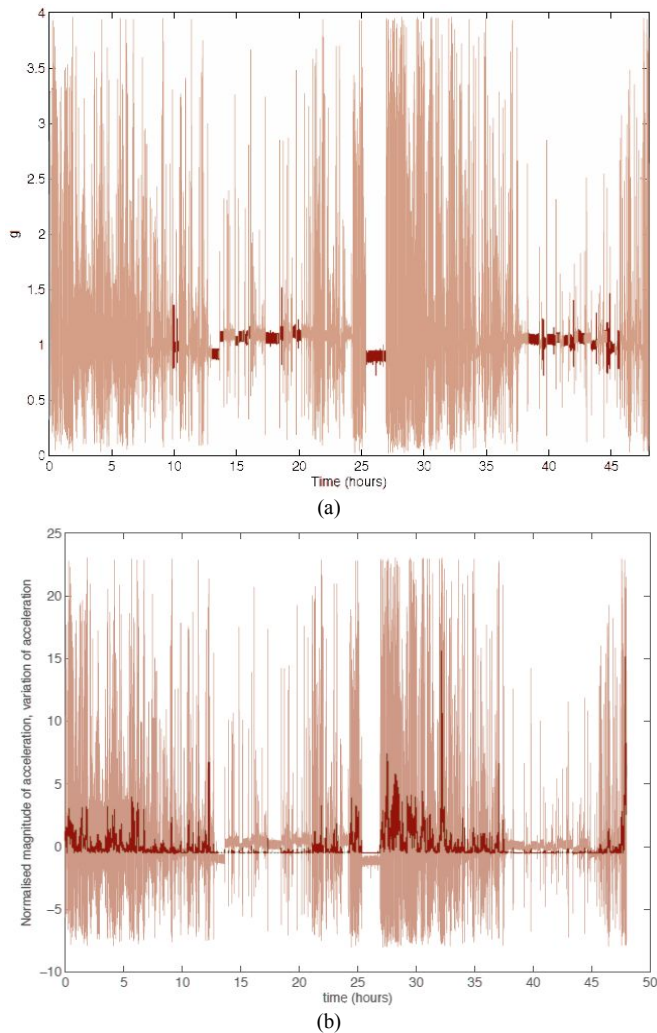
(a)

(b)

Figure 5. (a) Raw Data Collection over 48 hours.
(where red sections represent 'quiet' periods).
(b), Raw data and Magnitude after Constant-G Correction
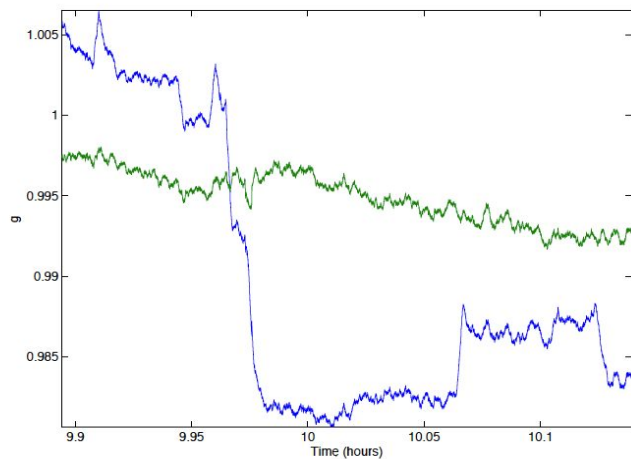*(where red represents adjusted data).*

Figure 5c, Magnitude of Acceleration with Correction
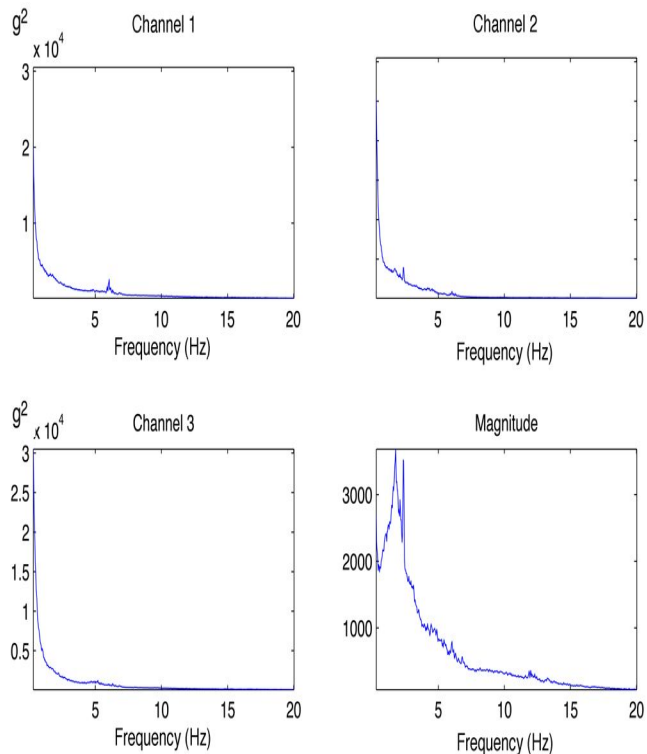*(blue - original data, green – offsets removed)*

Figure 6a, Three-Axis Power Spectra (Non-Parkinson)
*(right - dominant – hand), showing channels 1,2, and 3, plus
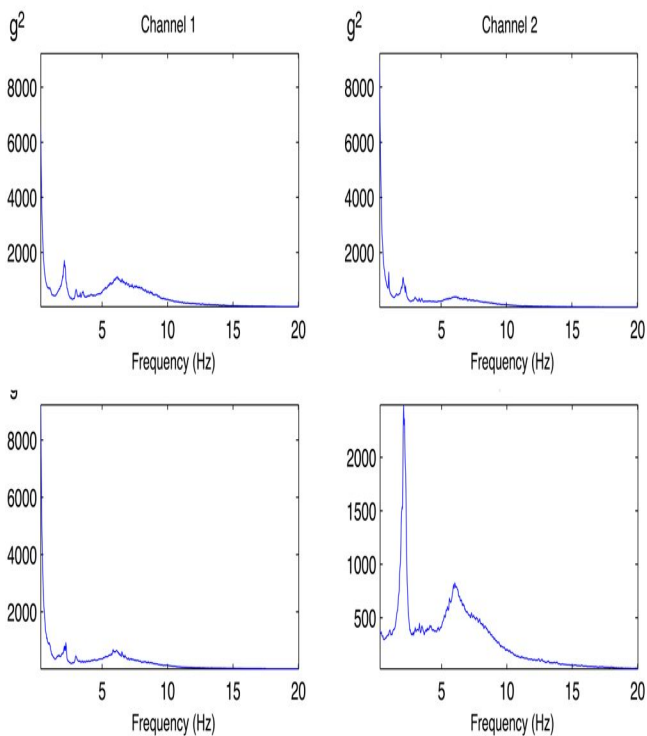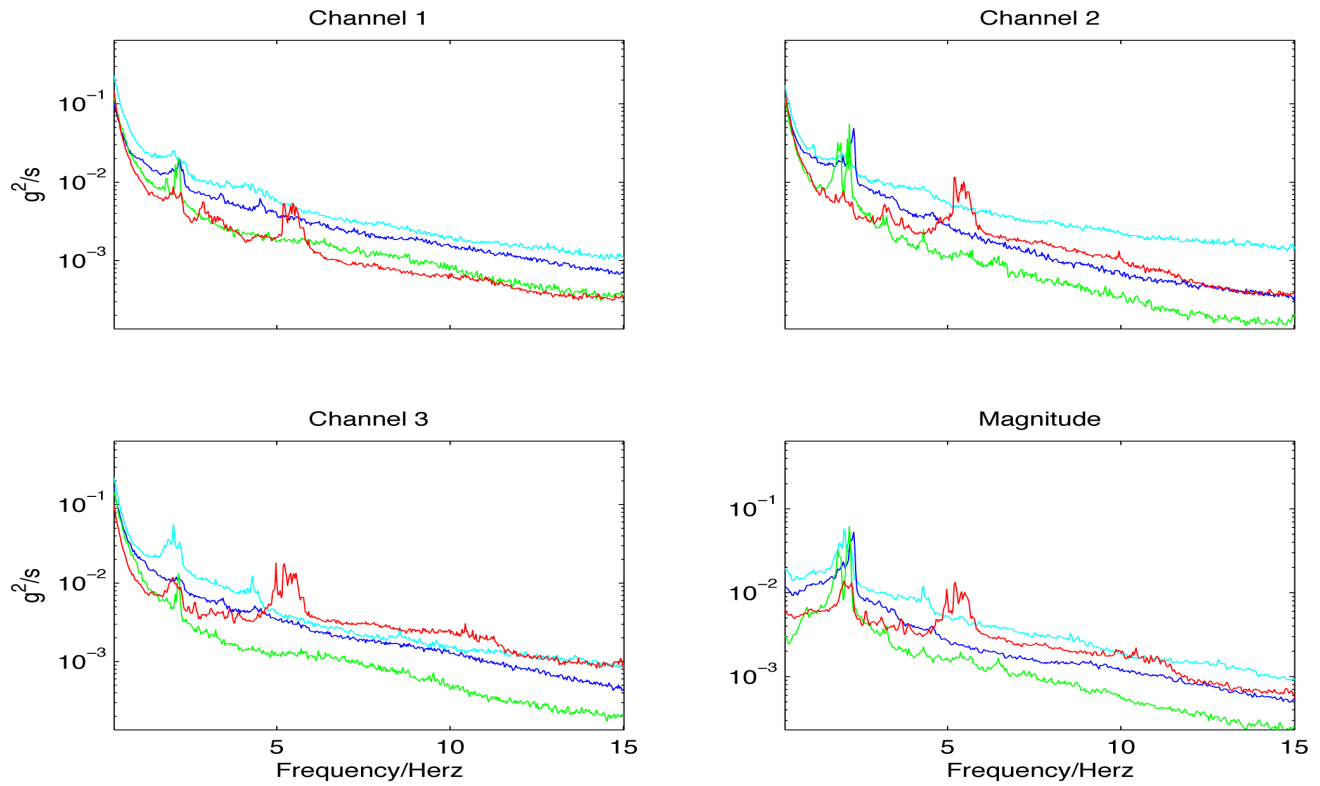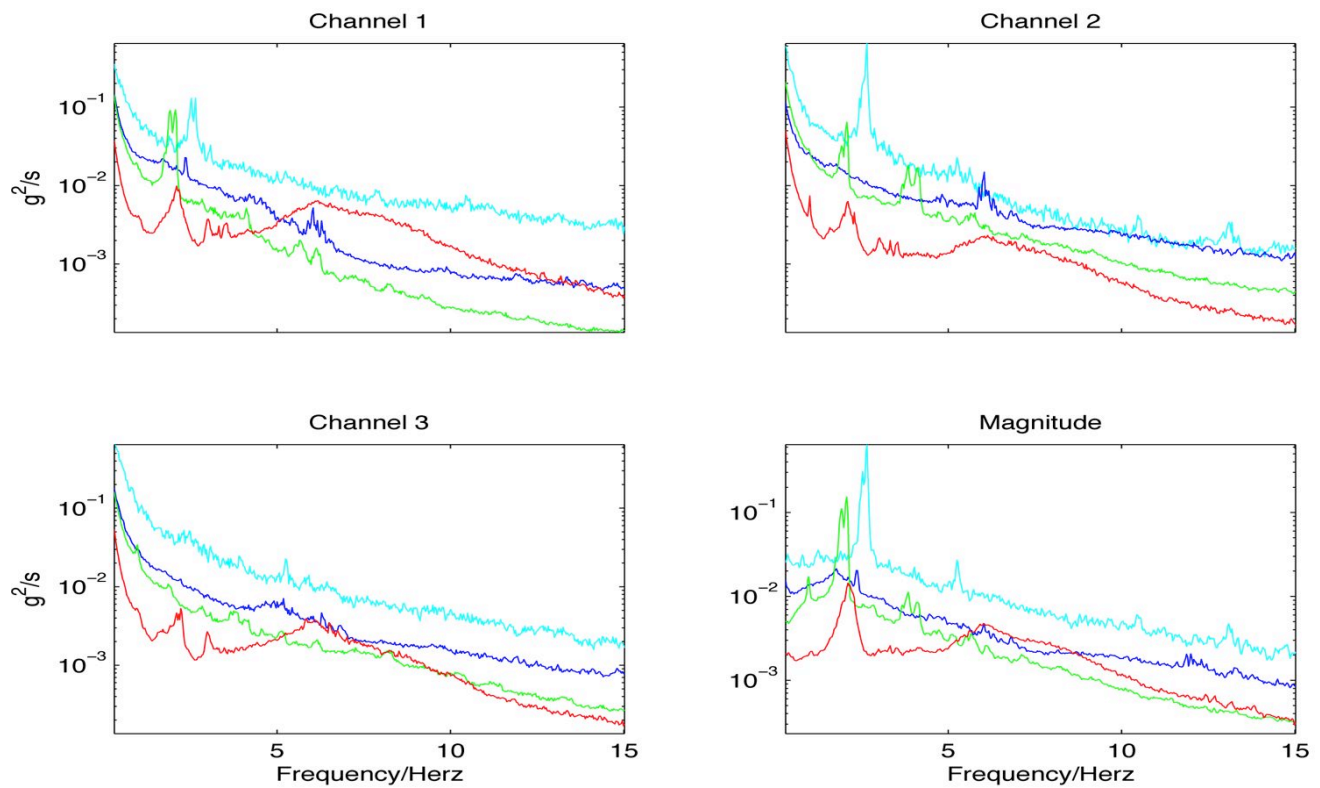combined magnitude, linear vertical scale.*

Figure 6b, Three-Axis Power Spectra (Parkinson)
*(right - dominant - hand, showing channels 1,2, and 3, plus
combined magnitude, linear vertical scale)*

Figure 7b, Power Spectra for Parkinson's Case and Controls: (a) Left Wrist, (b) Right Wrist.
(Parkinson's subject red, blue and green are controls, right wrist Data Collection, log vertical scale)
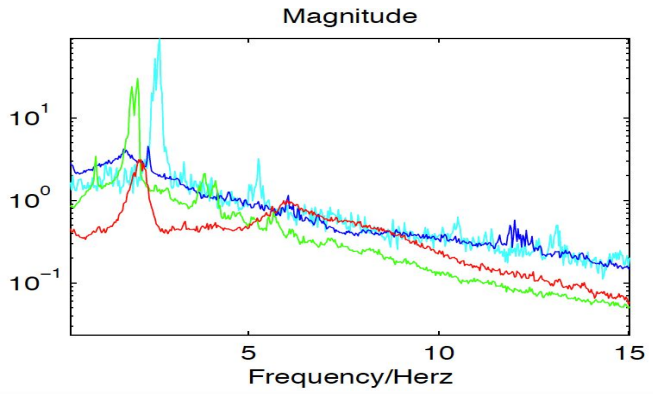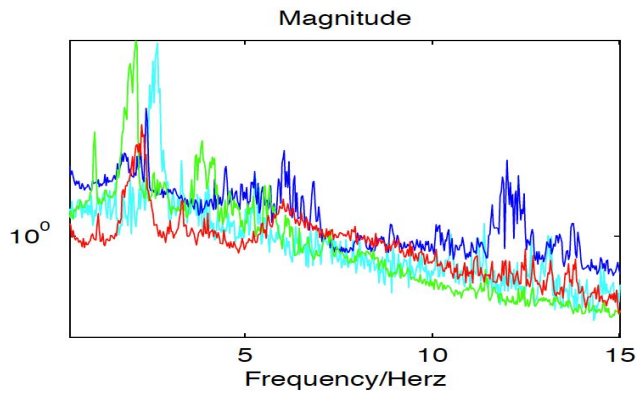
Figure 8, Frequency vs. Magnitude for All , (a) without selectivity, and (b) with 'quiet period' selectivity
(right wrist, trace colours as noted in Figure 7.)

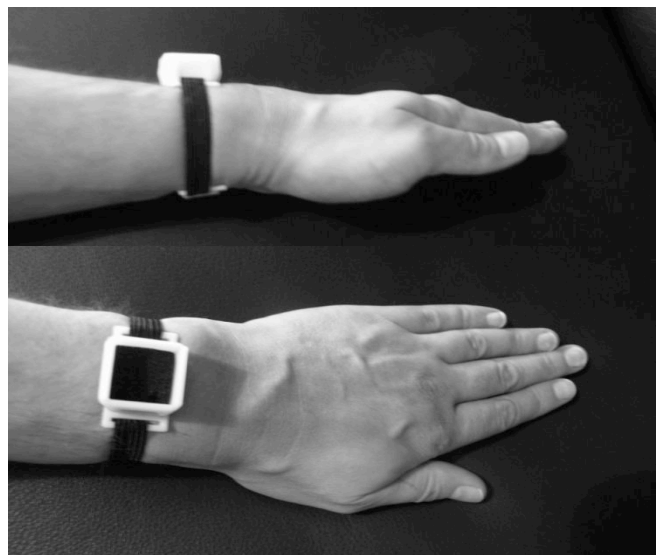Figure 9. NAT USB docking station

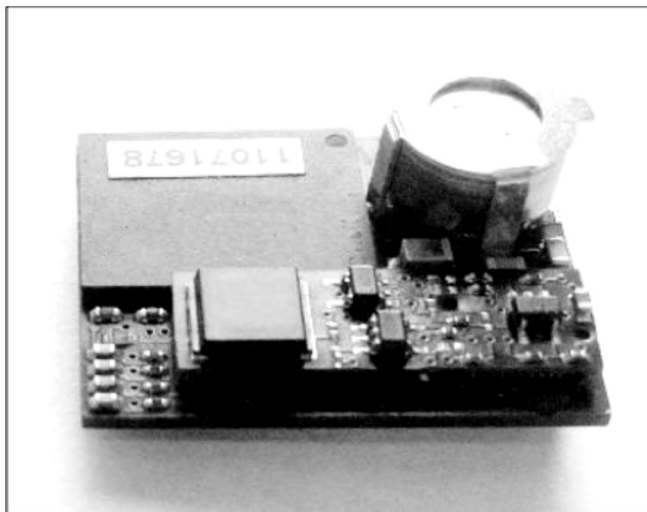Figure 11 NAT Wrist-Mounted Early Prototype Capsule

Figure 10 NAT1-IRDB Infra-red Receiver
Daughter-Board, Shown mounted on NAT device

Figure 12, Close-up of NAT Capsule Prototype.

VII. CONCLUSIONS AND ONGOING WORK

The improvements made to the NAT-1-4G device are undoubtedly beneficial for its wider use in application areas such as EEG, EMG and in more complex mixed monitoring scenarios. This includes combined tremor-motion and EMG capture in patients with conditions such as Parkinson's disease: a key area of interest at the present time. Research continues within our group on more sophisticated data analysis and algorithmic treatment of gathered data in long-duration unsupervised contexts. The use of low sample rates for accelerometer data recording of the order of 7 days is possible with the newer device, and we hope in future to evaluate the tradeoff between data quality and sample rates to establish a clinically useful long-duration recording configuration. The York team [19] and partners CYBULA Ltd. [20] are very interested in developing collaborative partnerships and would welcome enquiries from prospective evaluators and end-users in the clinical domain at the present time.

This work, forms the first phase of a longer-term research project in which we expect to continue to collect data in increasingly sophisticated scenarios with continuous data capture over months and possible years. The particular aim is to achieve clinically useful continuous unsupervised and untethered monitoring in every-day environments. The availability of rich data sets in this area from a single device will be extremely valuable and lwill also guide development of the next generation NAT devices.

REFERENCES

[1] J. R. Ives, and J. F. Woods. "4-channel 24 hour cassette recorder for long-term EEG monitoring of ambulatory patients." Electroencephalography and clinical Neurophysiology 39, no. 1 (1975): pp. 88-92.

[2] A. L. Vyssotski et al. "Miniature neurologgers for flying pigeons: multichannel EEG and action and field potentials in combination with GPS recording." Journal of neurophysiology 95, no. 2 (2006): 1263-1273.

[3] R. F. Yazicioglu, P. Merken, R. Puers, and C. Van Hoof, "A 200μW eight-channel acquisition ASIC for ambulatory EEG systems". Solid-State Circuits Conference, 2008. ISSCC 2008, San Francisco. IEEE International Digest of Technical Papers, Feb 2008, pp. 164,603.

[4] N. Verma, A. Shoeb, J. V. Guttag, and A. P. Chandrakasan. "A micro-power EEG acquisition SoC with integrated seizure detection processor for continuous patient monitoring." In 2009 Symposium on VLSI Circuits, 2009, pp. 62-63.

[5] E. Waterhouse. "New horizons in ambulatory electroencephalography." Engineering in Medicine and Biology Magazine, IEEE 22, no. 3 (2003): pp. 74-80.

[6] F. S. Jaw, Y. L. Tseng, and J. K. Jang. "Modular design of a long-term portable recorder for physiological signals." Measurement 43, no. 10 (2010): pp. 1363-1368.

[7] W. Maetzler, J. Domingos, K. Srulijes, J.J. Ferreira, and B.R. Bloem. "Quantitative wearable sensors for objective assessment of Parkinson's disease." Movement Disorders 28, no. 12 (2013): pp. 1628-1637.

[8] M. A. Hobert, W. Maetzler, K. Aminian and L. Chiari. "Technical and clinical view on ambulatory assessment in Parkinson's disease." Acta Neurologica Scandinavica (2014), Volume 130, Issue 3, pp. 139–147.

[9] R. LeMoyne, T. Mastroianni, and W. Grundfest. "Wireless accelerometer configuration for monitoring Parkinson's disease hand tremor." Advances in Parkinson's Disease 2 (2013): pp. 62-67.

[10] C. Bailey et al. "A Miniaturized 4-Channel, 2KSa/sec Biosignal Data Recorder With 3-Axis Accelerometer and Infra-red Timestamp Function." In SENSORCOMM 2013, The Seventh International Conference on Sensor Technologies and Applications, 2013, pp. 213-219.

[11] A. Meigal et al. "Linear and nonlinear tremor acceleration characteristics in patients with Parkinson's disease." Physiological measurement 33, no. 3 (2012): pp. 395-412.

[12] S. A. Rizvi, J. F. Téllez-Zenteno, S. L. Crawford, and A. Wu. "Outpatient ambulatory EEG as an option for epilepsy surgery evaluation instead of inpatient EEG telemetry." Epilepsy & Behavior Case Reports 1 (2013): pp. 39-41.

[13] H. J. Faulkner, H. Arima, and A. Mohamed. "The utility of prolonged outpatient ambulatory EEG." Seizure 21, no. 7 (2012): pp. 491-495.

[14] S. Patki et al. "Wireless EEG system with real time impedance monitoring and active electrodes." In IEEE Biomedical Circuits and Systems Conference (BioCAS), 2012, pp. 108-111.

[15] S. Mitra, J. Xu, A. Matsumoto, K. A. A. Makinwa, Chris Van Hoof, and R. F. Yazicioglu. "A 700μW 8-channel EEG/contact-impedance acquisition system for dry-electrodes." In 2012 Symposium on VLSI Circuits (VLSIC),,. IEEE, 2012. pp. 68-69.

[16] McRoberts Hybrid, commercial product data-sheet, https://www.mcroberts.nl/files/Flyer%20Hybrid%20En2.pdf, url checked 21st July 2014.

[17] Neurologger 2A Product Data Sheet, http://www.evolocus.com/Products/Neurologger2A.pdf url checked 21st July 2014.

[18] G-Link–LXRS datasheet, Lord Corporation MicroStrain© SensingSystems (USA), www.microstrain.com url last checked 21st July 2014.

[19] Advanced Computer Architectures Group (ACAG). www.cs.york.ac.uk/arch , last accessed 01/10/2014.

[20] Cybula Limited. UK Limited Company. www.cybula.com , last accessed 01/10/2014.

Π-shaped Coiled Stator Ultrasound Motor for Rotating Ultrasound Sensor in Intravascular Ultrasound Imaging

Toshinobu Abe, Shinichi Takeuchi
Graduate School of Engineering
Toin University of Yokohama
Yokohama-shi, Japan
b22c003n@ust.toin.ac.jp

Tadashi Moriya
Professor Emeritus
Tokyo Metropolitan University
Hino-shi, Japan

Takasuke Irie, Masakazu Satou
Microsonic Co., Ltd.
Kokubunji-shi, Japan

Abstract—**The primary focus of this paper is the development of an ultra-miniature ultrasound motor for rotating the ultrasound sensor in an intravascular ultrasonography (IVUS) system for use in the human blood vessel. Recently, intravascular diagnosis by IVUS has become widely used in medicine. IVUS is minimally invasive and can reduce pain felt by the patient, and is mainly used for examination of coronary artery disease. Since the size of the drive source for rotating the ultrasound sensor is large in the IVUS systems currently in practical use, it is installed outside the body, and the rotational power for the ultrasound sensor is transmitted through the long tortuous blood vessel. Such systems suffer from the problem that the rotation becomes non-uniform due to overloading of the wire transmitting the rotational power, and the problem that the available time is limited in order to prevent the wire from being damaged by overloading. We have therefore developed a Π-shaped coiled stator ultrasound motor (CS-USM) as a miniature ultrasound motor for rotating the ultrasound sensor for use in blood vessels in order to solve these problems. The CS-USM will achieve stable rotation of the ultrasound sensor in the blood vessel, since there is no need to transfer the rotational power though the long tortuous blood vessel. Furthermore, damage to the wire due to overloading is expected to be prevented. In this paper, we describe measurement of the torque, revolution speed, output power, and efficiency of the Π-shaped CS-USM.**

Keywords-CS-USM; Coiled stator; Ultrasound; Motor; Closed-loop waveguide; Revolution speed; Torque

I. INTRODUCTION

Recently, intravascular surgery and diagnosis have been used in medicine, for example, in atherectomy and IVUS. Intravascular surgery is a minimally invasive surgical method. Atherectomy is a method for removing atherosclerosis from blood vessels [1]. IVUS is mainly used to observe the luminal area and to confirm coronary stent expansion. IVUS visualizes the tissue beneath the surface, which is not possible by optical angiography [2] [3]. These devices need to perform rotational movement within the vessel.

The device that drives the revolution, such as a motor, is located outside the body in the IVUS systems currently in practical use. Non-uniform rotation and breakage of the shaft that transmits the rotational motion can occur due to undesired mechanical loading in long tortuous blood vessels. A small motor that can be used within the blood vessels is therefore needed in order to overcome these problems. A small motor can be installed as the driving source inside the blood vessel, removing the need to transmit rotational motion through a long tortuous blood vessel. This would improve the rotational stability and prevent the shaft of the rotating device from breaking.

Various types of ultrasound motors, including ring motors, linear motors, levitated-rotor motors, and coiled-stator motors have been actively investigated [4] [5] [6] [7]. We have been developing a CS-USM to construct a micromotor [8] [9] [10]. Since the CS-USM has a simple structure compared to other types of ultrasound motors, it is suitable for miniaturization. Ultrasound micromotors with outer circumferences of less than 1 mm have been fabricated using the coiled-stator structure by some groups [8] [11]. The main problem in terms of practical use is its low efficiency. A quadratic driving method using a closed-loop waveguide has been proposed for improving the efficiency [12]. However, the piezoelectric transducers need to be attached to the waveguide, and the acoustic impedances of a closed-loop waveguide are non-uniform at the attachment points. We thus think that these attachment points may cause the low efficiency. Further improvement may therefore be required. We previously proposed a new CS-USM structure that had an ultrasound power circulation-type acoustic waveguide and employed the quadratic excitation method [10]. Furthermore, a connection method between the piezoelectric transducer and acoustic waveguide was proposed to minimize the effect of acoustic propagation characteristics on the acoustic waveguide. in the previous paper [10]. Also, we previously reported a method for measuring the torque of the micromotor and the torque-revolution speed characteristics of the CS-USM [9]. These papers did not deal with the relationship between torque and revolution speed

characteristics and the relationships among torque, output power, and efficiency of a Π-shaped CS-USM. These relationships are described in the present paper.

The remainder of this paper is organized into the following five sections. Section II presents the concept of the CS-USM for IVUS. Section III describes the driving principle of our CS-USM. Section IV shows the fabrication of the Π-shaped CS-USM. Section V describes the measurements of the characteristics of the Π-shaped CS-USM. Finally, Section VI gives our conclusions.

II. CONCEPT OF CS-USM FOR IVUS

Recently, intravascular diagnosis by using IVUS has become widely used in medicine [1]. IVUS is minimally invasive and can reduce pain felt by the patient, and is mainly used for examination of coronary artery disease. Since the size of the drive source for rotating the ultrasound sensor is large in the IVUS systems currently in practical use, it is installed outside the body, and the rotational power for the ultrasound sensor is transmitted through the long tortuous blood vessel. Such systems suffer from the problem that the rotation becomes non-uniform due to overloading of the wire transmitting the rotational power, and the problem that the available time is limited in order to prevent the wire from being damaged due to overload. We thus developed the CS-USM as a miniature ultrasound motor that can be used inside the blood vessels in order to solve these problems. Figure 1 shows a conceptual diagram of the structure of an IVUS system using a small CS-USM for rotating the ultrasound sensor.
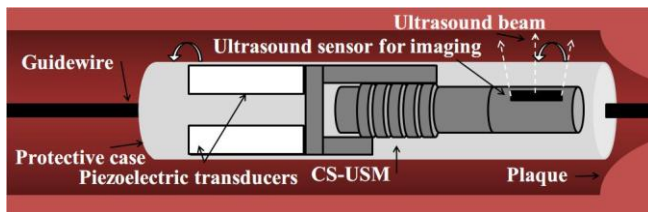

Figure 1. Conceptual diagram showing the structure of an IVUS system using a CS-USM small motor for rotating the ultrasound sensor.

If an ultra-miniature CS-USM can be developed for use inside blood vessels, it is expected that the CS-USM will be able to rotate stably in the blood vessel since there is no need to transfer the rotational power though the long tortuous blood vessel. Furthermore, damage to the wire due to overloading is expected to be prevented.

III. DRIVING PRINCIPLE

In this section, we describe the driving principle of the CS-USM and Π-shaped CS-USM. The driving principle of the CS-USM is described in Subsection A. The driving principle of the Π-shaped CS-USM is detailed in Subsection B.

A. Driving Principle of CS-USM

The CS-USM is a traveling-wave ultrasound motor that uses a coiled stator. When a flexural wave propagates along the coiled stator, particles on the surface of the coiled stator are displaced along an elliptical locus due to the coupling of longitudinal and transverse waves. A rotor arranged inside of the coiled stator is driven in the opposite direction to the particle movement by the frictional force as shown in Figure 2.
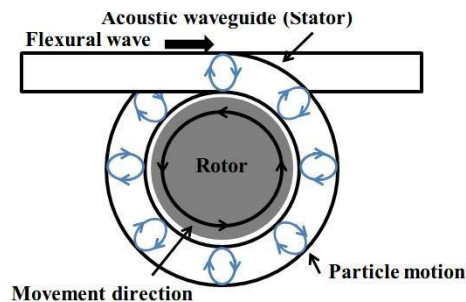

Figure 2. Rotor rotating in the opposite direction to the propagation of the flexural wave in the coiled stator [10].

The CS-USM consists of piezoelectric transducers, an acoustic waveguide, and a rotor. Since it has such a simple structure, it is expected to be able to be miniaturized as an ultrasound motor. Since a coiled acoustic waveguide is used as the stator, driving force is imparted to the rotor along a large part of the interface between the rotor and the stator. That is, even if the stator has a small driving force per unit length, a large drive force can be imparted to the rotor by using a coiled stator [13].

B. Driving Principle of Π-shaped CS-USM

Figure 3 shows the structure of the Π-shaped CS-USM. The motor consists of a rotor, a coiled stator, and two lead zirconate titanate ceramic (PZT)-based piezoelectric transducers. The stator forms a closed acoustic waveguide loop with the coiled waveguide and straight waveguide connected at connection points A and B. The length of the closed-loop waveguide is an integer multiple of the wavelength of the ultrasound wave.
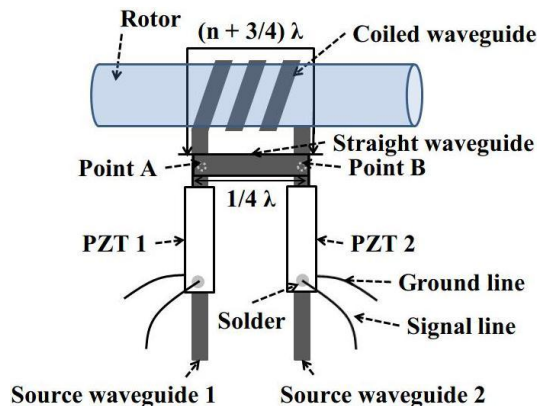

Figure 3. Configuration of our Π-shaped CS-USM [10].

The traveling wave for rotating the rotor can be generated by superposing two standing waves of phases that differ by 90 degrees with respect to both position and time [14]. In the following equations, standing wave (1) is induced at point A by PZT 1, standing wave (2) is induced at point A by PZT 2, and traveling wave (3) is then generated from the two standing waves.

$$u_1 (x, t) = A \sin kx \sin \omega t, \tag{1}$$

$$u_2 (x, t) = A \cos kx \cos \omega t, \tag{2}$$

$$u_t (x, t) = u_1 (x, t) + u_2 (x, t)$$

$$= A \sin kx \sin \omega t + A \cos kx \cos \omega t$$

$$= A \cos (kx - \omega t), \tag{3}$$

where, A, k, x, ω, and t are the flexural wave amplitude, wavenumber, position, angular frequency, and time, respectively. It is easy to change the rotation direction by switching the phase difference from 90° to -90°.

IV. FABRICATION OF Π-SHAPED CS-USM

The fabrication of the CS-USM is described in this section. The structure and design of the Π-shaped CS-USM are described in Subsections A and B, respectively.

A. Structure of Π-shaped CS-USM

As shown in Figure 3, the length of the straight section from point A to point B is $\lambda/4$. The length of the closed-loop waveguide including coiled stator from point B to point A in a counterclockwise direction is $(n + 3/4)\lambda$, where n is an arbitrary integer. Source waveguides 1 and 2 are connected to the closed-loop waveguide at connecting points A and B by electric spot welds. The two PZT transducers are attached by soldering to source waveguides 1 and 2, respectively.

B. Design of Π-shaped CS-USM

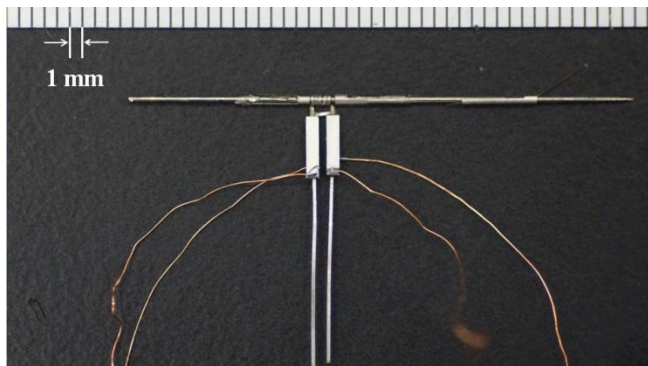Figure 4 shows a photograph of the fabricated Π-shaped CS-USM.

Figure 4. Fabricated Π-shaped CS-USM [9].

The thickness and width of the acoustic waveguides are 0.1 and 0.3 mm, respectively. The material of the acoustic waveguide is SUS 304. The coiled stator is wound 5 turns around the rotor. The thickness, width, and length of the PZT transducer (C-213, Fuji Ceramics) are 0.25, 1.0, and 5 mm, respectively. The rotor is a steel wire with a diameter of 0.56 mm. The inner diameter of the coiled stator is 0.6 mm. The length of the straight waveguide from point A to point B is 1.5 mm. The length of the closed waveguide from point B to point A in a counterclockwise direction is 10.5 mm.

V. MEASUREMENT OF CHARACTERISTICS OF Π-SHAPED CS-USM

We measured the characteristics of the Π-shaped CS-USM. Subsections A, B, and C, respectively, describe the following relationships for the Π-shaped CS-USM: the relationship between applied voltage and revolution speed; the relationship between torque and revolution speed; and the relationships among torque, output power, and efficiency.

A. Measurement of Revolution Speed

We measured the revolution speed of the Π-shaped CS-USM by using a laser Doppler velocimeter. The laser beam is reflected by reflective tape attached to the rotor, and the revolution speed is determined from the reflected beam. The Π-shaped CS-USM is held in a CS-USM holder for characteristics measurement as shown in Figure 5. The CS-USM holder is able to hold the rotor, keeping constant contact between the rotor and the coiled stator.
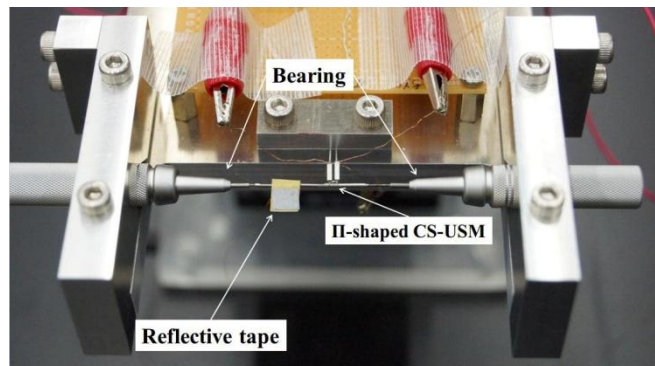

Figure 5. CS-USM holder for measuring characteristics [9].

First, the resonance frequency of the piezoelectric transducers was measured with a fixed voltage applied to the piezoelectric transducers. The resonance frequency of the Π-shaped CS-USM was estimated to be 311 kHz from the results. Next, the revolution speed was measured by sweeping the applied voltage from 2 to 32 V_{pp} at the resonance frequency. Furthermore, the revolution speed and direction of revolution were measured at the resonance frequency after switching the phase difference of the driving signal from 90° to -90°. A continuous sinusoidal wave was used for the driving signal in this experiment.

Figure 6 shows revolution speed as a function of applied voltage. We repeated the measurement of rotational speed 10 times. Mean values with error bars indicating the standard deviation are plotted in Fig. 6.
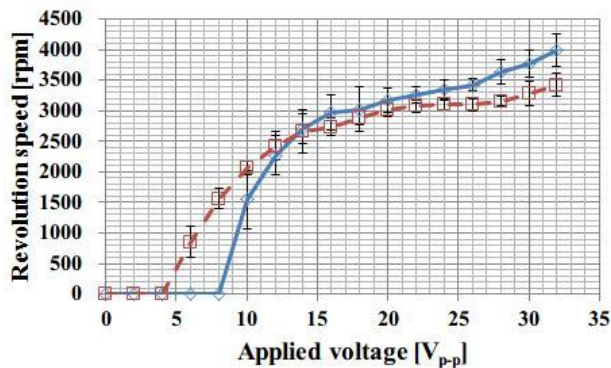
Figure 6.   Revolution speed as a function of applied voltage.

It was found that the revolution speed was about 3500 rpm, but it differed between the forward and reverse directions. The forward direction is defined as the direction in which the traveling wave propagates along the coiled stator.

B. Measurement of Torque-Revolution Speed

We next measured the relationship between torque and revolution speed. Figure 7 shows a schematic diagram of the measurement of the torque-revolution speed characteristics, where R, T, W_{tr}, W_{ap}, M_{tr}, M_{ap}, and g are the radius of the rotor, tensile force, true weight, apparent weight, true mass, apparent mass, and gravitational acceleration, respectively. A weight was suspended from the Z stage using a string, and was wound once around the rotor.
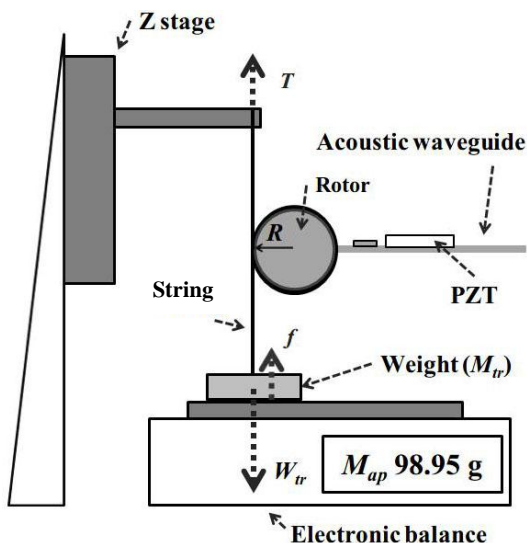

Figure 7.   Schematic diagram of measuring torque-revolution speed characteristics [9].

This structure provides a load on the rotor by the movement of the Z stage. At the same time, the revolution speed of the motor was measured using a laser Doppler velocimeter. As in the measurement of the revolution speed, the Π-shaped CS-USM was held by the CS-USM holder while measuring the characteristics as shown in Figure 5. Torque τ is given by (4) as follows:

$$\tau = R \times T. \qquad (4)$$

In addition, A and B can be obtained by (5) and (6) as follows:

$$T = W_{tr} - W_{ap}, \qquad (5)$$

$$W_{ap} = M_{ap} \times g. \qquad (6)$$

The drive conditions were the same as those in the revolution speed measurement. Drive frequency, applied voltage, and drive signal were 311 kHz, 30 V, and continuous wave, respectively. We measured the torque while changing the load on the rotor by moving the Z stage. Figure 8 shows the system for measuring the torque-revolution speed characteristics. Figure 9 shows the revolution speed as a function of torque.
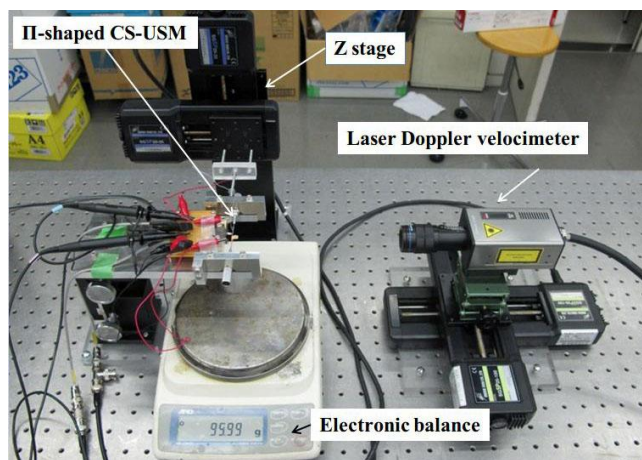

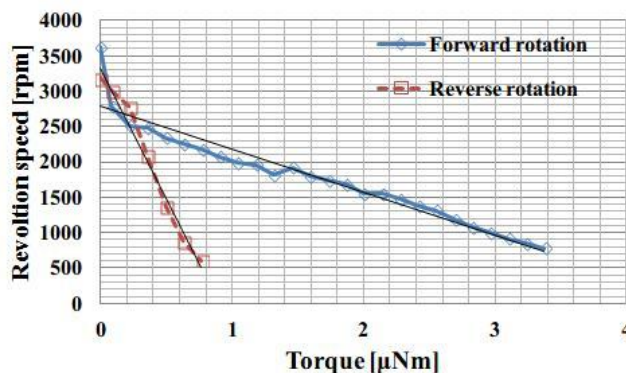Figure 8.   System for measuring torque-revolution speed characteristics [9].

Figure 9.   Torque-revolution speed characteristics [9].

It was confirmed that the torque of the Π-shaped CS-USM was about 3.4 µNm and 0.9 µNm in the forward and reverse rotation directions, respectively. The revolution speed decreased with increasing torque. The torque in the forward direction was different from that in the reverse direction.

C. Estimation of Output Power and Efficiency of Π-shaped CS-USM

We calculated the output power of the Π-shaped CS-USM from the torque and rotational speed. We also calculated the efficiency from the torque and rotational speed. In addition, we calculated the efficiency from the output power of the Π-shaped CS-USM and the input power of the PZT transducers. The input power to the PZT transducers taking into account the power factor was 21.6 mW at 30 V_{pp}. The input power required to drive the motor was 43.2 mW. Figure 10 shows the output power and efficiency as a function of torque for forward rotation. Figure 11 shows the output power and efficiency as a function of torque for reverse rotation.
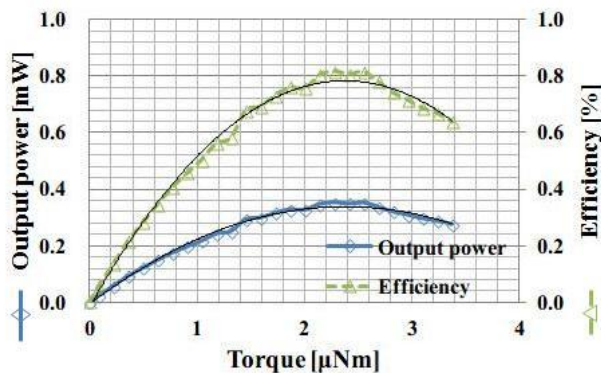

Figure 10. Output power and efficiency as a function of torque for forward rotation
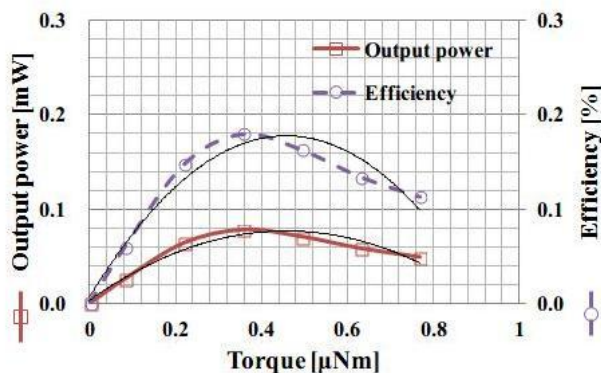

Figure 11. Output power and efficiency as a function of torque for reverse rotation.

The maximum efficiency was thus found to be about 0.8% and 0.2% in the forward and reverse rotation directions, respectively.

VI. CONCLUSIONS AND FUTURE WORK

We fabricated a Π-shaped CS-USM to improve the driving efficiency of CS-USMs for driving IVUS ultrasound sensors. The relationship between the revolution speed and torque of the fabricated Π-shaped CS-USM was measured. The driving efficiencies were calculated from the measurement data. The maximum driving efficiency was confirmed to be about 0.8%. In previous research, the maximum driving efficiency of a large single-transducer CS-USM was found to be about 0.1%. The observed improvement in driving efficiency shows the superiority of the closed-loop acoustic waveguide for Π-shaped CS-USM. However, the fabricated CS-USMs exhibited individual differences in driving frequency, revolution speed, and torque performance. These individual differences may be caused by poor fabrication accuracy and experimental conditions. Therefore, improvement in the manufacturing accuracy of the CS-USM is desired. To use the CS-USM in medicine, miniaturization and biocompatibility are required. Therefore, it is necessary to give sufficient consideration to the components and structure of the CS-USM. Optimization of the thickness and width of the closed acoustic waveguide is a problem for the future.

REFERENCES

[1] W. B. Keeling, et al, "Plaque excision with the Silverhawk catheter: Early results in patients with claudication or critical limb ischemia," J. Vasc. Surg., Vol. 45, Jan. 2007, pp. 25-31.

[2] Y. Saijo, A. Tanaka, N. Owada, and S. Nitta, "Tissue velocity imaging of coronary artery by rotating-type intravascular ultrasound," Ultrasonics, Vol. 42, Apr. 2004, pp. 753-757.

[3] Y. Saijo and A. F. W. van der Steen Eds., "Vascular Ultrasound," Tokyo: Springer-Verlag, Jul. 2003, p. 57.

[4] T. Maeno, T. Tsukimoto, and A. Miyake, "Finite-element analysis of the rotor/stator contact in a ring-type ultrasonic motor." IEEE Trans. Ultrason. Ferroelectr. Freq. Control., Vol. 39, Nov. 1992. pp. 668-674.

[5] C. H. Yun, T. Ishii, K. Nakamura, S. Ueha, and K. Akashi, "A high power ultrasonic linear motor using a longitudinal and bending hybrid bolt-clamped Langevin type transducer," Jpn. J. Appl. Phys., Vol. 40, May 2001, pp. 3773-3776.

[6] T. Yamazaki, J. Hu, K. Nakamura, and S. Ueha, "Trial construction of a noncontact ultrasonic motor with an ultrasonically levitated rotor." Jpn. J. Appl. Phys., Vol. 35, May 1996, pp. 3286-3288.

[7] T. Moriya and Y. Furukawa "Ultrasonic motor." U.S. Patent No. 7,602,103., Oct. 2009.

[8] T. Abe, T. Moriya, T. Irie, and S. Takeuchi, "Development of Hydrothermally Synthesized PZT Polycrystalline Film Transducers for CS-USM (Coiled Stator Ultrasound Motor)," Res. Bull. TOIN Univ. Yokohama, Dec. 2013, pp. 13-17. (In Japanese)

[9] T. Abe, T. Moriya, T. Irie, and S. Takeuchi, "Characteristic of Π-Shaped Coiled Stator Ultrasound Motor (CS-USM)," ICICE tech. rep, Vol. 114, May 2014, pp. 13-17. (In Japanese)

[10] T. Abe, T. Moriya, T. Irie, M. Sato, and S. Takeuchi, "Experimental study of the Π-shaped coiled stator ultrasound motor," Jpn. J. Appl. Phys., Vol. 53, Jun. 2014, pp. 07KE15-1-07KE15-5.

[11] A. Nakajima, Y. Furukawa, and T. Moriya, "Development of a New Traveling Wave Ultrasonic Micro Motor : Application to Catheter in Micro Blood Vessels(Nano/micro measurement and intelligent instrument)," Proc. Int. Conf. LEM21, Oct. 2005, pp. 371-374.

[12] K. Youhei, M. Yoshizawa, N. Tagawa, T. Irie, and T. Moriya, "Ultrasonic Power Circulation-type Quadratic Excitation Method for improvement in torque of Coiled Stator Ultrasonic Motor," Proc. Symp. Ultrason. Electron., Nov. 2012, pp. 475-476.

[13] M. Tanabe, S Xie, N. Tagawa, T. Moriya, and Y. Furukawa, "Development of a Mechanical Scanning-type Intravascular Ultrasound System Using a Miniature Ultrasound Motor," Jpn. J. Appl. Phys., Vol. 46, Jul. 2007, pp. 4805-4808.

[14] K. Uchino and J. R. Giniewicz, "Micromectronics" New York: Marcel Dekker, Apr. 2003, p. 423.

Development of a Vital Signs Monitoring System Using Radio Frequency Communication

Fábio Ferreira, Vítor Carvalho
School of Technology
Polytechnic Institute of Cávado and Ave (IPCA)
Barcelos, Portugal
vcarvalho@ipca.pt

Filomena Soares, José Machado, Filipe Pereira, Vítor Carvalho
Algoritmi Research Centre, CT2M (2nd author)
University of Minho
Guimarães, Portugal

Abstract—In this paper, the data transmission of an acquisition system for biomedical vital signs via Radio Frequency (RF) communication is explored. It was developed a platform capable of recording the patient´s physiological signals to check if any medical evolution/change occurred. The system allows also acquiring the environment data, as for example the room temperature and luminosity where the patient is. The main achievement of this paper is the patients' real-time health condition monitoring by the medical personnel or caregivers that will contribute to prevent health problems.

Keywords—ambient asssisted living (ALL); radio frequency (RF); medical care terminal (MCT)

I. INTRODUCTION

This work is part of a research and development project in Ambient Assisted Living (AAL) topic. Continuous monitoring of biomedical signals is crucial in diagnosis and clinical monitoring of patients. Nowadays, several biomedical signals are analyzed. The health assistant needs to have information of the patient's vital signs in order to be permanently informed about the patient heath status [1][2]. However, this procedure is not easy to accomplish. Regarding the acquisition of biomedical signals various sensors are placed on the patient including a series of cables to connect the sensors, which could be invasive and uncomfortable for the patient and his/her mobility [3]. At this moment, the commercial cost associated to the remote monitoring of biomedical variables in bedridden systems is expensive and unaffordable for most of families [4]. An example of a Medical Care Terminal (MCT) from BioPlux can be observed in Figure 1 [4].

Figure 1. Bioplux clinical biofeedback software GUI [4]

BioPlux clinical biofeedback software Graphical User Interface (GUI) is used in muscle rehabilitation allowing a more efficient medical intervention as well as a faster patient recovery. It is a web-based application, supported also by mobile operating systems.

The main objective of this work is the development of an electronic system using wireless transmission capable of registering the patient's vital signs. Moreover, this project gives also the possibility to the health aide to access the database of the patient, including the medical records and personal information. This project is a first step in order to achieve a minimum invasive biomedical data acquisition system, as it is further expected to integrate the sensors in the patients' clothes and/or in other common daily life tools.

This paper is organized as follows: Section II presents the biomedical sensors principle of operation used in the project; Section III presents the developed system, Section IV presents some results. Section V presents the conclusion and future perspectives of work.

II. BIOMEDICAL SENSORS

In this section, we describe some of the biomedical sensors used in this project.

A. Electrocardiogram (ECG)

During the electrical activation of the myocardium, the heart is swept by a "front activation" whose meaning and direction are modified in fractions of a second. The ECG detects the electrical activity of the heart, reflecting its activity, Figure 2 [5].
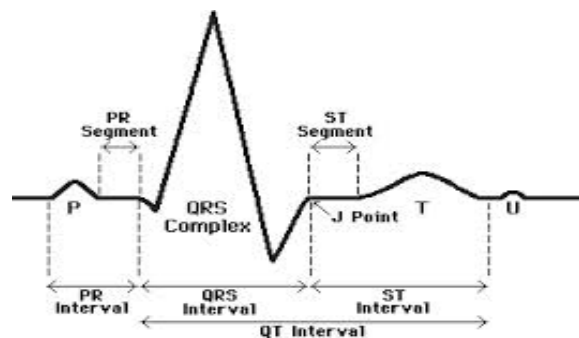

Figure 2. Electrocardiogram wave [5]

B. Body Temperature Sensor

The junction of two metals generates a temperature difference. The principle of operation of the temperature sensor is based on this process (thermocouple). Two materials of two different types are attached; the potential difference is measured between two points. Through this potential difference, it is possible to obtain the temperature. Figure 3 shows an example of the structure of the temperature sensor (thermocouple) used [6].
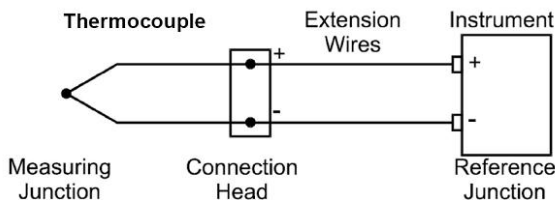

Figure 3. Thermocouple [6]

C. Airflow Sensor

The airflow is obtained by heating a wire by an electric current. The resistance of the wire increases as the temperature of the wire increases as a consequence of the airflow variation. Thus, it is possible to measure the airflow through the amount of current passing through the wire; see Figure 4 [7].
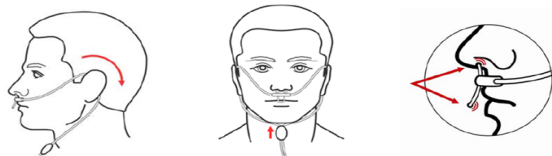

Figure 4. Airflow sensor [7]

Apart from these sensors, other sensors are considered in the project as the oximeter, the galvanic skin response, the patient position and the glucometer.

III. SYSTEM DEVELOPED

Figure 5 presents the overall block diagram of the system developed. This system registers the patient´s physiological signs; it allows the medical personnel to access the patient´s personal information and medical condition, as well as the applied treatment. Moreover, it also allows the remote access to monitor the patient's condition.

The database can store the data of the patient, medical personnel, health aid and health unit.
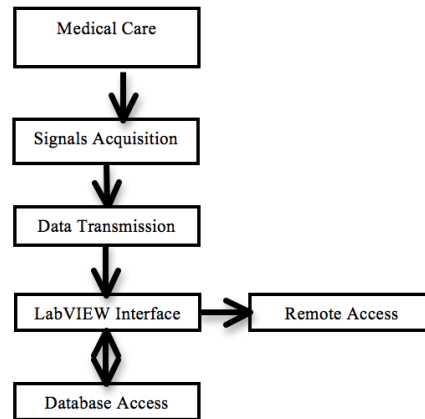

Figure 5. Block diagram of the program

A. System Hardware

The system hardware is based on the Arduino platform, including an Atmel microcontroller AVR [8]. The programming languages used are C and C++. Figure 6 presents an example of the connection between the room luminosity sensor, i.e., Light Dependent Resistor (LDR), the Arduino and the Radio Frequency (RF) module.
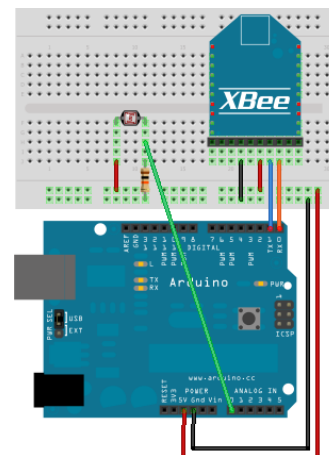
Figure 6. Room luminosity sensor (LDR) physical connection

The sensor (Figure 6) is plugged into the Arduino Analogue to Digital Converter (ADC) input (with a resolution of 12 bits [9]). After reading the sensor, the value is transmitted via the Arduino serial port (RX, TX) to the XBee and then to the acquisition system. This procedure is also used for the other system sensors.

B. Developed Database

The software used for data modeling was the Microsoft Access [10]. Figure 7 shows the developed database for data storage considering seven main tables plus one auxiliary table.

Figure 7. Data modeling

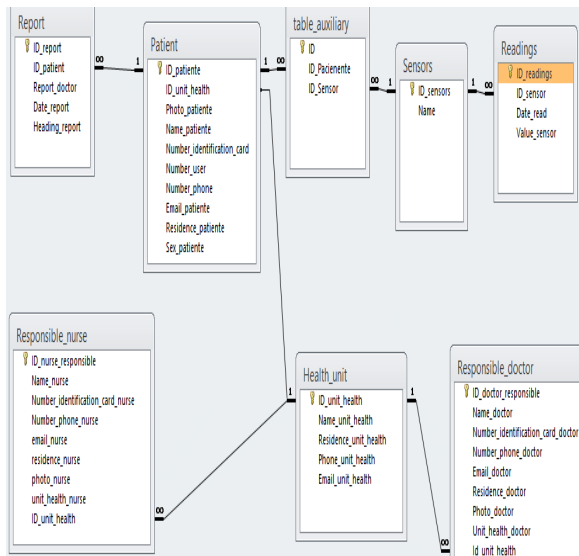The developed database records the data associated to the patient (tables Patient, Report, Sensors and Readings), the data associated to the medical personal responsible (tables Responsible_nurse and Responsible_doctor) as well as the data associated to the health unit (table Health_unit).

C. LabVIEW Interface

Figure 8 shows an example of the user interface developed in LabVIEW to consult information about a patient [11]. The database is accessed via a Universal Data Link (UDL) connection. UDL was created to store connections with databases. The serial port establishes the connection between LabVIEW and Xbee. A time period is defined for each sensor reading. The value is stored in the database along with the date and time when the acquisition was performed.
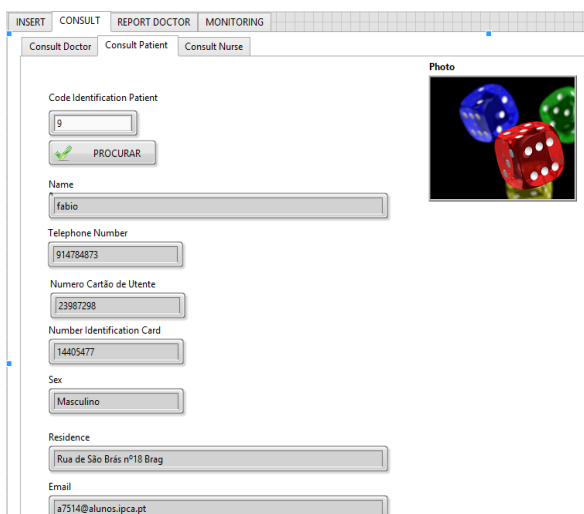

Figure 8. LabVIEW user interface – patient database consult

Figure 9 shows an example of the interface developed to register the light present in the patient's room [12].
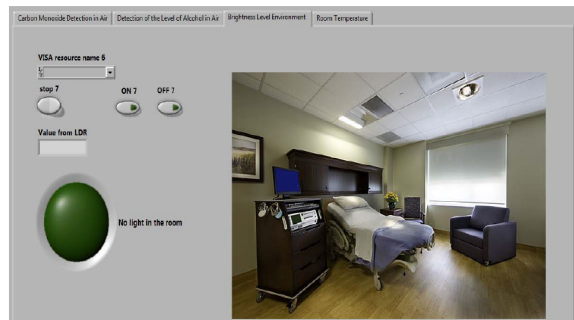

Figure 9. Light sensor LabVIEW interface [12]

Apart from the light intensity in the patient's room, the system also registers the air carbon monoxide level, the air alcohol level and the room temperature.

IV. EXPERIMENTAL RESULTS

In this section, three examples of the experimental results are presented, namely the temperature monitoring of the patient room, the access to the patient´s data and also the patient´s body temperature.

A. Temperature Room Sensor

In the menu from Figure 10, the medical personnel may choose to monitor the room temperature throughout the day by selecting the overall time of the acquisition. By observing Figure 10, it is verified that the patient room temperature was around 30ºC during the system measurement (one hour).
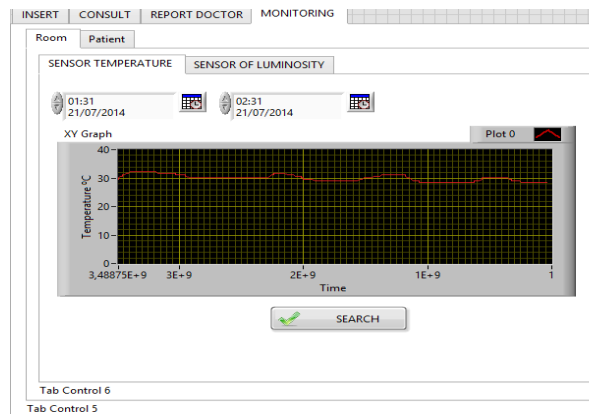

Figure 10. Room temperature monitoring

B. Medical Reports

As it is seen in Figure 11, the medical personnel can select a time interval and list the patient reports. To accomplish this, it has to insert the code of the patient and click on the "Search" button.
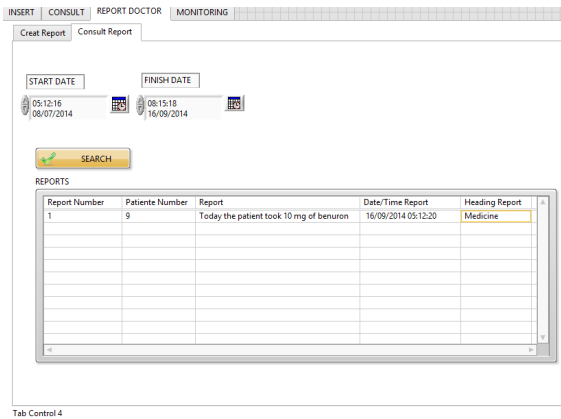
Figure 11. Consult reports

C. Biomedical Sensors

The system was first tested with two healthy persons: a) 28 years old, female, measuring 1.73 m and weighting 62 kg; b) 31 years old, male, measuring 1.76 m and weighting 79 kg. The first test was carried out to obtain the value of body temperature. Figure 12 refers to the sensor placement and Figure 13 shows the user interface where the temperature is acquired through wireless communication and registered in a chart.
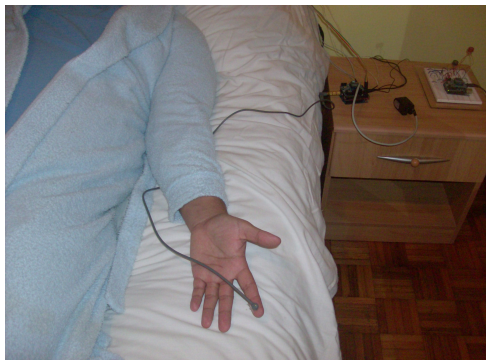

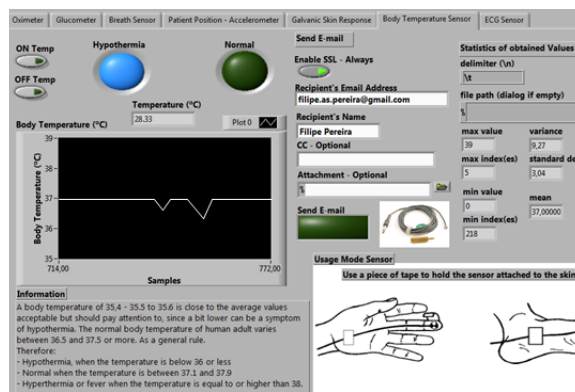Figure 12. Placement of the body temperature sensor in the patient [12]

Figure 13. Obtaining the body temperature profile in the MCT [12]

The conjunction of the biomedical sensors and the environmental sensors allows obtaining a very useful profile of the patients heath condition as well as the environment were he is exposed. The transmission of this information via RF allows a less invasive system to the users (patients and caregivers).

V. CONCLUSION AND FURTHER WORK

This paper described a system based on a medical care terminal using data transmission via RF. The physiological and environment data are acquired. An added value of this project is the real-time monitoring allowing the medical personnel to observe the patient healthcare condition at anytime and anywhere. All the data in registered in a database, allowing the physician to monitor the patient´s evolution over time.

So far, the system was tested in laboratory. In the near future, we aim to integrate all the sensors and test the system in clinical environment.

This work aims to develop a minimum invasive vital signs data acquisition system including the biomedical sensors either in the patients' clothes and/or in other common daily life tools.

ACKNOWLEDGMENT

REFERENCES

[1] Tianbing M. F. and Chuanzhi F., "Sensors state monitoring based on labview and wireless nodes", Procedia Engineering, Vol. 15, 2011, pp. 2639-2643.

[2] Alonso S. V., "Autonomous optical system for the measurement of biomedical parameters", Catalunya: Universitat Politécnica de Catalunya, 2010 (in spanish).

[3] Burns A. et al, "SHIMMER[TM]-A wireless sensor platform for noninvasive biomedical research", IEEE Sensors Journal, Volume 10, Issue 9, Sept. 2010, pp.1527-1534.

[4] bioPLUX research user manual, 2010, http://www.plux.info/biopluxresearch (acessed in September 2014):

[5] Prutkin J., ECG tutorial: Basic principles of ECG analysis, 2013, http://www.uptodate.com/contents/ecg-tutorial-basic-principles-of-ecg-analysis (acessed in September 2014)

[6] Thermocouples, An Introduction, http://www.omega.com/thermocouples.html (acessed in September 2014)

[7] How sensors work, mass air flow sensor, http://www.sensorland.com/HowPage060.html (acessed in September 2014)

[8] Arduino, http://www.arduino.cc (acessed in September 2014)

[9] Arduino, analog read resolution, http://arduino.cc/en/Reference/AnalogReadResolution (acessed in September 2014)

[10] Microsoft Access, http://office.microsoft.com/en-us/access/ (acessed in September 2014)

[11] NI LabVIEW, http://www.ni.com/labview (acessed in September 2014)

[12] Pereira F., Carvalho V., Soares F., Machado J., Bezerra K. and Matos D., "Development of a mechatronic system for bedridden people support", The Romanian Review Precision Mechanics, Optics & Mechatronics, 2013, no. 48, pp.138-14

LipoTool: Evaluation of Tissues Compressibility

Manuel Rodrigues Quintas, Tiago F. Andrade, Maria Teresa Restivo, Maria de Fátima Chouzal, Teresa Amaral

Institute of Mechanical Engineering (Faculty of Engineering, University of Porto branch)

Porto, Portugal

e-mail: mrq@fe.up.pt, tfa@fe.up.pt , trestivo@fe.up.pt, fchouzal@fe.up.pt, amaral.tf@gmail.com

Abstract—**Nowadays undernutrition, overweight and obesity are very common health problems, with high impact in society at individual, social and economic levels. Therefore, the quantification and screening of body fat composition is very important in the health area. The assessment method based on skinfold measurement has well-defined protocols but the commercial equipment, considered in the literature, lacks technical evolution. Present technologies do not integrate devices with novel characteristics and are not adequate for large scale studies. They are also limited for efforts in developing new algorithms, namely, if based in dynamic tissue response. The integrated LipoTool system intends to contribute for those goals. Some novel features of LipoTool are presented, i.e., end tips alignment and acquisition of the tissue compressibility. The paper highlights innovative capacities of LipoTool, which transform it into a powerful tool for assessing and tracking, training, study and research, with the potential to develop new models and different application domains.**

Keywords-skinfold calliper; data recording, skinfold compressibility, skinfold measurement protocol.

I. INTRODUCTION

Changes in the nutritional status of an individual are one of the most common health problems and with high impact in society at individual, social and economic levels [1]. Malnutrition, obesity or even the co-existence of both are a major world health problem documented by the World Health Organization (WHO) [2].

According to the WHO, over 50 % of the European adult population is overweight or obese. In fact, excess body fat may lead to the increase of coronary heart disease, high blood pressure, type 2 diabetes, obstructive lung disease, arthritis, and some types of cancer [3]. Malnutrition is also related to other diseases generating costs to the European Health System comparable to those associated with overweight and obesity [4].

Malnutrition is a global issue that affects billions of people. The term malnutrition refers to both undernutrition and overnutrition. Traditionally, undernutrition is prevalent in developing countries and obesity is an epidemic in developed countries. Recently, obesity has been increasing in developing countries, leading to a double burden of disease, especially in urban settings [5][6].

Therefore, the quantification and screening of Body Fat (BF) composition is very important in the health area. For monitoring BF, several techniques are used being based the most usual on the estimation of Body Mass Index (BMI). BMI estimation is based on height and weight evaluation, although leading to very inaccurate results according to the literature [7][8]. The measurement of skinfolds using a calliper and the Bioelectrical Impedance Analysis (BIA) measurement based in body resistance and reactance are techniques widely used. The Dual-energy X-ray Absorptiometry (DXA) for image evaluation is considered a valid body fat measuring device [9].

The BMI calculation is a highly empirical method that only gives a rough idea of body fat. The DXA method has great accuracy, but is invasive and requires very expensive bulky type equipment, adequate facilities, and expert technicians, resulting in high cost/test rate [10].

The BIA is the technique that competes directly with the skinfold calliper. The BF is calculated based in correlating impedance and reactance values obtained by passing an alternating electrical current through the body [11]. It is a recent and widely used method requiring a convenient preparation not often respected. Individual preparation before the test typically includes several requirements:

- Avoid exercising within 12 hours of the test.
- No alcoholic drinks within 48 hours of the test.
- Do not drink coffee within 48 hours of the test.
- Avoid diuretics within 24 hours of the test.
- Urinate completely prior to testing.
- Abstain from eating and drinking within 4 hours of the test.

Failure to meet these requirements leads to very poor, inaccurate results.

Skinfold calliper methodology has advantages over other techniques because it is a simple method (portable, easy to use and not requiring special individual preparation), non-invasive and low cost; it provides reliable results compared with the DXA [12].

The measurement protocol prescribes a uniform distributed pressure of 10 gf/mm^2 [13] to be applied to the skinfold by the end tips. After positioning the end tips, three seconds should be counted (as recommended), and then, the skinfold thickness value may be recorded. With the value of skinfold thickness and with the individual anthropometric data, the percentage of BF is estimated by selecting an equation from a huge set of equations (more than 60) related with individual data.

In fact, the assessment method based on the skinfold measurement has a well-defined protocol but the commercial equipment, considered in the literature and available in the market, lacks technical evolution.

The challenge of this work starts precisely from the lack of progress and precision that this type of device has experienced since its development in the 1960s and aims at overcoming these limitations. We designed and tested a dedicated BF measurement system called LipoTool. The integrated LipoTool system intends to achieve all requirements for this method: the pressure between end tips should be uniform and constant (10 gf/mm^2) as established by the protocol, to guaranty and to improve the precision and measurement resolution, to offer a larger measurement range, to minimize or even to discard subjective operator errors (thickness reading and measurement time counting), to facilitate the recording and monitoring of patient results (data recorded in database), to guide the technician through the complete procedure, and to provide a database for large scale studies. Additionally, the system also intends to allow further studies in the health and nutrition fields and even for other applications in distinct areas (now, it is possible to record the dynamic tissue response during the skinfold compression interval).

The work aims at highlighting new studies and some results already available due to the device unique features. We believe that new algorithms, namely, based on dynamic tissue response will be possible to be developed with LipoTool. However, these studies will need samples referred to a standard method (for example, to DXA).

In the present work, Section II describes the integrated system LipoTool, comprising a digital skinfold calliper, named Adipsmeter, and its communication system with the LipoSoft application, highlighting the used technology. Section III provides details of the LipoTool performance, namely, the constant pressure between end tips according with the followed measurement protocol and its novel capabilities for evaluating tissue compressibility. This allows accurate studies on the effect of the time interval duration for skinfold measurement and its significance in the final evaluation of %BF. Finally, in the conclusions, it is stressed how it can be a powerful tool in the assessing and tracking, training, study and research domains, such as nutrition and health, forensic sciences, veterinary science and sports.

II.   THE LIPOTOOL INTEGRATED SYSTEM

The technological solution of LipoTool, depicted in Figure 1, comprises a new digital skinfold calliper Adipsmeter (1), an antenna AirPCOn (2) for wireless communication with a computer and a software application LipoSoft (3).

A.   The Adipsmeter digital skinfold calliper

The Adipsmeter mechanical design was studied, conceived and implemented in order to guarantee a constant pressure value of 10 gf/mm^2 between end tips, to increase the calliper measurement range and to reduce the measurement subjectivity due to five novel features: a constant force actuator mechanism, a cam to compensate changes in force,
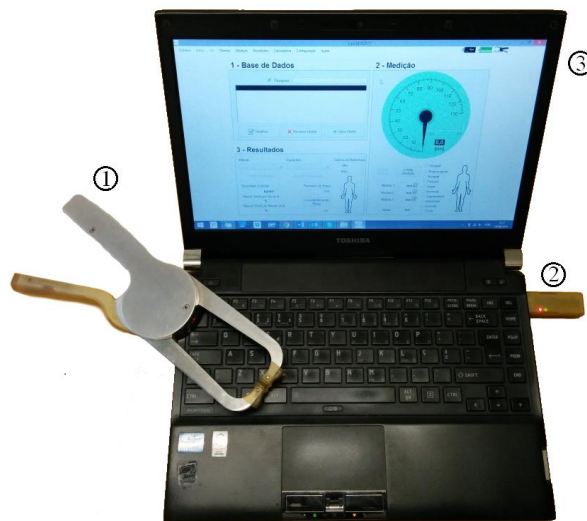

Figure 1.   LipoTool system.

a controlled end tips articulation for keeping their clamping surfaces parallel to each other over all its opening range, a large jaws centre distance permitting greater openings without increasing the device size and, finally, a symmetric design to make it independent of the operator dominant hand.

The entire mechanism can be seen in Figure 2. The two jaws (4) opening is accomplished by the operator through the manipulation of a fixed handle (1) and a lever (2). The simultaneous opening is achieved because the two jaws rotate around fixed axes and are interconnected by means of mechanical elements. Jaws closing action is operated by a transmission chain connected at the other end to a constant force actuator based on an elastic element. This actuator has the double effect of being the force element of the system while simultaneously eliminating all possible backlash in the transmission chain. The inclusion of a cam (3) whose profile compensates variations in the length of the applied force arm, guarantees the application of a constant force by the clamping surface of the end tips (5) to the skinfold under measurement. The end tips are hinged at the rotation axes in the extremities of the jaws, keeping their clamping surfaces parallel to each other at any opening level. This is achieved by a movement transmission mechanism that provides a constant and uniform pressure on the complete contact area between the end tip clamping surfaces and the skinfold.
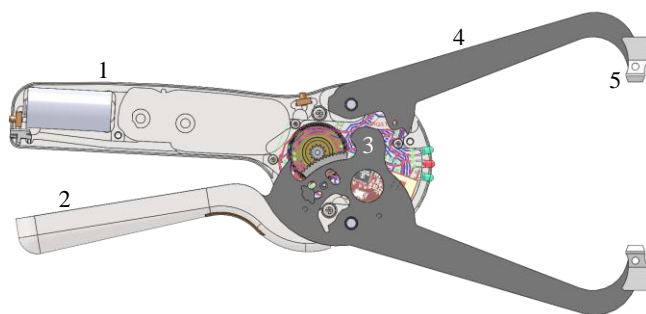

Figure 2.   Schematics of the transmission chain.

LipoTool is much more convenient and precise than any traditional skinfold calliper both in daily use and in large scale actions.

The integration of the mechanical design with electronics and informatics design enables to obtain a final resolution of 0.025 mm, to reduce the time measurement subjectivity, to reduce individual reading errors, to follow the tissue compressibility, to facilitate the use of the method by incorporation of all known equations, and also to integrate a database that enables the monitoring of individuals.

B. The communication and the LipoSoft application

The transmission rate for the wireless communication between the Adipsmeter and LipoSoft (60 samples/s) allows to register the dynamic tissue response for any skinfold under compression. It is also possible to monitor small changes in temperature during the compression process.

So, studies based on dynamic tissue response will be performed using traditional dynamic systems modelling techniques, such as time and frequency response, artificial neural networks, and genetic algorithms. We think that more flexible models could be achieved offering additional methods for BF evaluation, overcoming the use of more than 60 regression equations, at the present. In line with this idea, a study using neural networks has been reported by Barbosa, *et al.* [14].

The current electronic solution uses Microchip Technology Inc. [15] components for both processing and wireless communication. For the communication, data processing 8-bit microcontrollers were used. For the wireless communication, antennas were used with the communication protocol MiWi, based on the IEEE 802.15.4 standard for Wireless Personal Area Networks (WPANs) [16].

The digital measurement sensor of the calliper is an encoder of angular type and also includes a temperature sensor (miniaturized thermocouple bid). The angular encoder is connected directly to the microcontroller through two specific ports. The antenna and the temperature converter communicate with the microcontroller by Serial Peripheral Interface bus (SPI) and the set of buttons (included in the Adipsmeter) communicate through digital ports. In the AirPCOn antenna, two microcontrollers are used, communicating with Universal Synchronous/Asynchronous Receiver/Transmitter (USART) between them. One is used to communicate with the computer via Universal Serial Bus (USB) and the other with the antenna by SPI, as shown in Figure 3.

The LipoSoft application was developed in Visual Basic.NET and communicates with the antenna through the USB port. The interface is divided into three blocks: Database, Measurement and Results, as shown in Figure 4.

It is possible to introduce different settings through the LipoSoft user interface, as well as to turn off the Adipsmeter.

III. TESTING THE LIPOTOOL PERFORMANCE

This work presents two methods used for testing this novel calliper in terms of mechanical behaviour and dynamics evaluation of time interval during skinfold thickness evaluation.
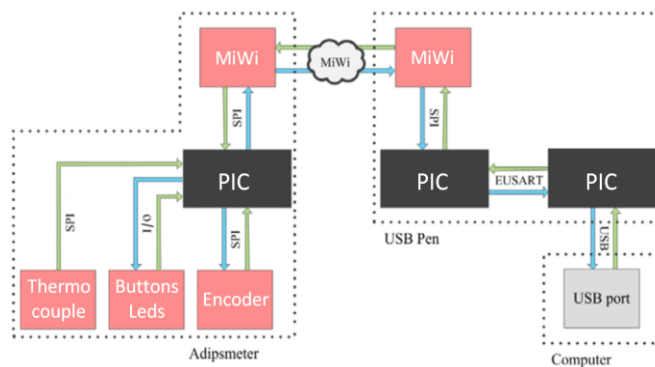

Figure 3. Communications diagram.

The first goal was achieved by comparing the pressure between calliper end tips within the measurement range for the Adipsmeter and the Harpenden calliper [17], the latter being the market reference. The second objective is to study the relevance of the protocol time interval value for measuring skinfolds.

A. Constant pressure between end tips

According to the protocol, the pressure between end tips should be 10 gf/mm^2 for the whole measurement range.

In order to compare the pressure values between end tips, their area and the force between them were digitally monitored and measured. A mechanical structure able to ensure repeatability and the same conditions in force measurements for both devices (Adipsmeter and Harpenden) was developed integrating a load cell of 5 LBS measurement range. An aluminium structure was built for housing the load cell (ensuring the force discharge without friction) and room for gauge blocks in order to measure force for different skinfold callipers accurate opening, from 15 mm to 120 mm.

The Adipsmeter end tips are articulated; so their surfaces are always parallel for any opening. For that reason, the measurement process is simple to carry out. In other cases in which there is no parallelism between end tips (and so between skinfold contact surfaces), which is the case of the Harpenden calliper, it is essential to use special care by introducing additional calculations for compensating the lack of parallelism. Once the force is equally distributed by careful design of the mechanical test system, this leads to uniformity in the pressure distribution on the surface of the end tips, and therefore, in the skinfold surface.

Figure 5 presents the results from lab tests for comparing the Adipsmeter and the Harpenden callipers in terms of pressure between the end tip surfaces at different openings.

Figure 5 shows the evolution of the pressure between end tips for different jaw opening along the measurement range of each calliper - Harpenden: 0-80 mm; Adipsmeter: 0-120 mm. It also shows a non-constant pressure between end tips, i.e., Harpenden calliper does not accomplish the protocol requirement exhibiting a decreasing pressure with the opening increase. On the other hand, the Adipsmeter offers an increase of 50 % in the measurement range and a constant pressure between end tips.
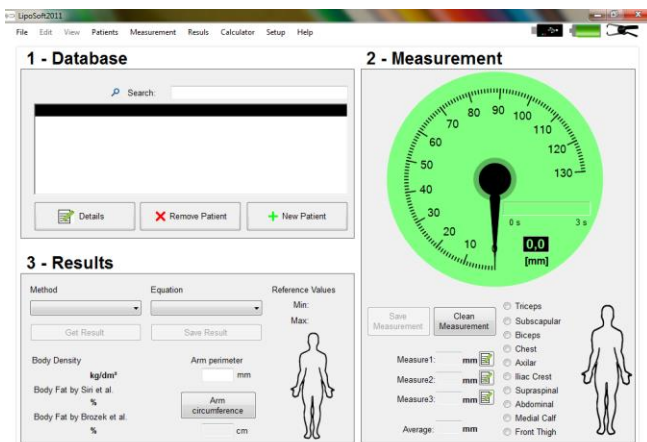
Figure 4.   LipoSoft interface.

B.   Time interval for skinfold measurement

LipoTool provides a unique ability by allowing to monitor and to register the skinfold behaviour along the skinfold measurement.

This LipoTool functionality permits to evaluate the time required for the skinfold measurement by observing the dynamic tissue response.

Studies of the protocol time interval have never been done based in an accurate procedure. The LipoTool system is able to read skinfold thickness and perform time evaluation in an intrinsic and precise digitally automatic way and to record them for later processing and evaluation. Nevertheless, Lohman [18] and Norton and Olds [19] have recommended the use of 2 s and 3 s after applying the callipers' end tips to the skinfold, as result of their empirical studies based in huge samples; but, it was impossible to read time and thickness with precision as it can be made by LipoTool.

In our study for evaluating tissue compressibility, the measurement procedure has followed the International Standards for Anthropometric Assessment recommendations [20]. A sample of 36 adults (50% women) aged between 21 and 49 years old was evaluated and all the participants were informed of the study purposes as well as the different procedures.
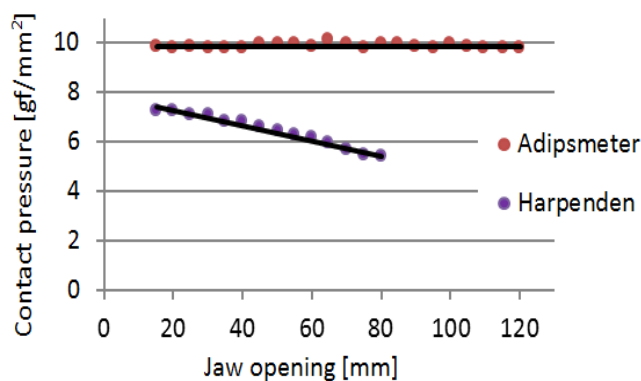
The tricipital skinfold was measured with the LipoTool system and the evolution of tissue compressibility during the initial 5 s was registered. The body density was estimated using the equations of Durnin and Womersley [21] and the % BF was estimated using the equation of Siri [22]. All these estimations were done in intervals of 0.5 s and the difference between these values in consecutive moments was calculated. The results are presented in Table 1.

Observing data from Table 1, it is evident that changes over 2.5 s are not meaningful when determining the % BF and this suggests the need for revision of the time interval for skinfold measurement.

Figure 6 shows an example of the information recorded during a skinfold measurement procedure for a heterogeneous set of 10 individuals. The data were processed in order to exhibit a normalized evolution of individual skinfolds during measuring time allowing a better comparison between individual skinfolds behaviour.

The dynamic evolution of tissue compressibility shows very different characteristics among individuals. We believe that for each individual it is possible to distinguishing two behaviours in the skinfold characteristic. One is related with the connective tissue and the other is related with the adipose tissue. The first decay rate is higher than the second one. For each individual, these decay rate values, respectively, must be related with his/her percentage of connective and adipose tissue, depicted in Figure 7.

Further studies may possibly conduct to offer a completely new functionality with skinfold callipers' measurement. However, for better characterization of these results, a higher resolution prototype must be used. These

TABLE I.   BODY FAT PERCENTAGES FOR TRICIPITAL SKINFOLD

		Time [s]										
		0	0,5	1	1,5	2	2,5	3	3,5	4	4,5	5
%BF (Siri)	Men	27,1	26,1	25,9	25,9	25,8	25,8	25,7	25,7	25,7	25,7	25,6
% dif*			1,0	0,1	0,1	0,1	0,0	0,0	0,0	0,0	0,0	0,0
%BF (Siri)	Women	26,6	25,4	25,2	25,2	25,1	25,1	25,0	25,0	25,0	25,0	24,9
% dif*			1,3	0,1	0,1	0,1	0,0	0,0	0,0	0,0	0,0	0,0

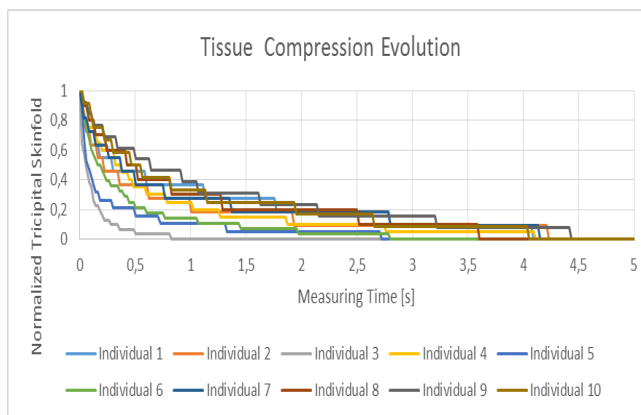Figure 5.   Pressure test between end tips for different jaw opening.

Figure 6.   Normalized tissue compression evolution of tricipital skinfolds.
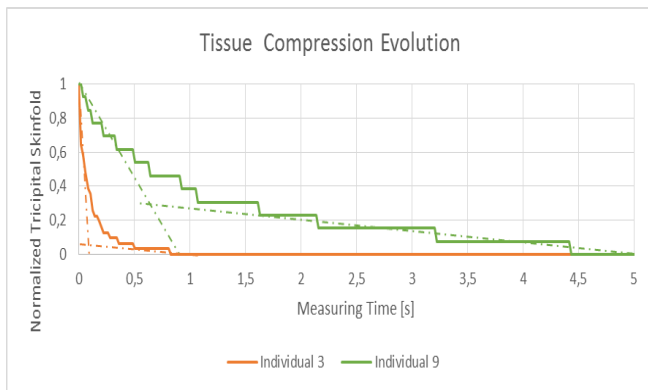
Figure 7.   Decay rate for distinct behaviours of a skinfold.

studies also need data simultaneously obtained by this device and with a DXA system in order to develop validated models.

These capabilities have been already used in preliminary studies in Forensic [23][24] and in Nutrition areas [25][26].

IV.   CONCLUSIONS

LipoTool presents innovations that allow its use for accurate and fast assessment of body composition by measuring skinfolds. While retaining the simplicity of any skinfold calliper, the innovative capacities of LipoTool transform it into a powerful tool for assessing and tracking, training, study and research, with the potential to help develop new models and different application domains which turns, once again, into additional innovation. To perform the associated research based on new studies, it is fundamental to get data not only from the LipoTool but also from a valid body fat measuring recognized standard systems. LipoTool is now under market development, which will bring later opportunities for new studies.

ACKNOWLEDGMENT

REFERENCES

[1]   European Parliament Resolution of 25 September 2008 on the White Paper on nutrition, overweight and obesity – related health issues (2007/2285(INI)) P6_TA(2008)0461.

[2]   World Health Organization (2009) Global health risks: mortality and burden of disease attributable to selected major risks. ISBN 978 92 4 156387 1 (NLM classification: WA 105).

[3]   Y. C. Wang, K. McPherson, T. Mars, S. L. Gortmaker, and M. Brown, "Health and economic burden of the projected obesity trends in the USA and the UK", The Lancet, vol. 378, Issue 9793, 2011, pp. 815 - 825, DOI: 10.1016/S0140-6736(11)60814-3.

[4]   C. A. Russell, "The impact of malnutrition on healthcare costs and economic considerations for the use of oral nutritional supplements", Clinical Nutrition Supplements, vol. 2, iss. 1, 2007, pp. 25–32, doi: 10.1016/j.clnu.2007.04.002.

[5]   A. M. Prentice, "The emerging epidemic of obesity in developing countries", Int. J. Epidemiol, 2006;35(1), pp. 93-9.

[6]   World Health Organization, "Global strategy on diet, physical activity and health", 57th World Health Assembly (WHA), 2004, ISBN 92 4 159222 2.

[7]   K. J. Rothman, "BMI-related errors in the measurement of obesity", Int J Obes (Lond), 2008, Suppl 3, pp. 56-59, doi: 10.1038/ijo.2008.87.

[8]   S. B. Heymsfield, T. G. Lohman, Z. Wong, and S. B. Going, "Human Body Composition - 2nd edition", Champaign, IL: Human Kinetics, 2005.

[9]   K. J. Ellis, "Human body composition: in vivo methods", Physiol Rev. 2000 Apr;80:2, pp. 649–680.

[10]   S. B. Heymsfield, "Development of imaging methods to assess adiposity and metabolism", Int J Obes (Lond) 2008;32:7, pp. 76-82.

[11]   A. Fürstenberg and A. Davenport, "Comparison of Multifrequency Bioelectrical Impedance Analysis and Dual-Energy X-ray Absorptiometry Assessments in Outpatient Hemodialysis Patients", American Journal of Kidney Diseases 57(1), 2010, pp. 123-129, doi: 10.1053/j.ajkd.2010.05.022. Epub.

[12]   H. J. Krämer and H. V. Ulmer, "Two-second standardization of the Harpenden Calliper", European Journal of Applied Physiology and Occupational Physiology, 46, 1981, pp. 103-104.

[13]   D. A. W. Edwards, W. H. Hammond, M. J. R. Healy, J. M. Tanner, and R. H. Whitehouse, "Design and Accuracy of Callipers for Measuring Subcutaneous Tissue Thickness", Br J Nutr. 1955, 9(2): pp. 133–143.

[14]   M. R. Barbosa, T. Amaral, M. F. Chouzal, and M. T. Restivo, "Neural Networks Based Approach to Estimate Body Fat (%BF)". In Controlo 2010, pp. 7-10.

[15]   Microchip Technology Inc. [Online]. Available from: http://www.microchip.com/ 2014.10.24

[16]   Y. Yang, "Microchip MiWi™ P2P Wireless Protocol", Microchip Technology Inc., 2010.

[17]   Baty International. Harpenden Skinfold Caliper. [Online]. Available from: http://www.harpenden-skinfold.com/ 2014.10.24

[18]   T. G. Lohman, "Advances in Body Composition Assessment: Current Issues in Exercise Science", Champaign, IL: Human Kinetics, vol. 5, iss. 2, 1992, pp. 3–4, Series Monograph No. 3.

[19]   K. Norton and T. Olds, "Anthropometrica", Sidney, Australia: University of New South Wales Press, 1996.

[20]   M. Marfell-Jones, T. Olds, A. Stewart, and L. Carter, "International standards for anthropometric assessment", Potchefstroom, South Africa: International Standards for Anthropometric Assessment, 2006.

[21]   J. V. Durnin and J. Womersley, "Body fat assessed from total body density and its estimation from skinfold thickness: measurements on 481 men and women aged from 16 to 72 years", British Journal of Nutrition, 32(1), 1974, pp. 77-97.

[22]   W. E. Siri, "Body composition from fluid spaces and density. Analysis of methods", In Techniques for Measuring Body Composition, Edited by: Brozek J, Henschel A., Washington, DC , National Academy of Sciences, 1961.

[23]   F. L. Ferreira, "Estimation of cadaveric rigidity – modifications of the mechanical properties", FEUP-MSc thesis in Bioengineering, 2013.

[24]   P. Martins, R. N. Jorge, M. Parente, and A. Santos, "Necromechanics: death induced changes on the mechanical properties of human tissues", submitted to Part H: Journal of Engineering in Medicine, 2014.

[25] M. T. Restivo, T. F. Amaral, M. F. Chouzal, C. P. Leão, R. S. Guerra, E. Marques, J. Mendes, M. Quintas, and J. Mota, "A digital Calliper for training and study purposes", Asia Pacific Journal of Clinical Nutrition, 2012, vol. 21(2), pp. 182-190.

[26] T. F. Amaral, T. Restivo, M. R. Quintas, F. Chousal, C. M. Silva, and T. F. Andrade, "LIPOTOOL – A New Integrated System for Assessment of Body Composition", XXXIV ESPEN Congress, 2012, vol. 7, iss. 1, pp. 177, DOI:10.1016/S1744-1161(12)70438-6.

[27] Portuguese Foundation for Science and Technology. [Online]. Available from: https://www.fct.pt/apoios/unidades/consulta/vglobal_projecto?idProjecto=132969&idElemConcurso=7579 2014.10.24

Bacterial Wetwood Detection in *Fagus grandifolia* and *Prunus serotina* Sapwood using a Conducting Polymer Electronic-nose Device

Alphus Dan Wilson

Forest Insect and Disease Research
USDA Forest Service, Southern Hardwoods Laboratory
Stoneville, MS, USA
e-mail: dwilson02@fs.fed.us

Abstract— **New electronic gas-detection methods were developed and tested for the diagnosis of bacterial wetwood disease in *Fagus grandifolia* (American beech) and *Prunus serotina* (black cherry) using a Conducting Polymer (CP)-type electronic nose (e-nose), the Aromascan A32S, based on detection of headspace volatile microbial and plant metabolites derived from sapwood. Diagnostic application-specific aroma signature patterns (profile databases), derived from e-nose analysis of known healthy and wetwood-infected sapwood cores of each hardwood tree species, were used to develop an aroma database library. The library was used as known references to screen aroma profiles of sapwood cores for the presence of wetwood in unknown samples. The Aromascan A32S e-nose effectively distinguished between headspace volatiles from tree cores of different wood types, correctly identifying them at frequencies ranging from 92.3-100%. Principal Component Analysis (PCA) and Quality Factor (QF) statistical values indicated the relatedness and significance of differences between headspace volatiles from aroma classes of each sample type. Significant differences were found between the aroma profiles of healthy vs. wetwood-infected sapwood of American beech and black cherry, and greater differences occurred between headspace wood volatiles released from healthy sapwoods of the two species.**

Keywords-artificial olfaction; disease diagnosis; electronic aroma detection; volatile organic compounds

I. INTRODUCTION

Bacterial wetwood is an important wood disease that is common primarily in bottomland hardwood tree species of seasonally-flooded forests of the lower Mississippi Delta region [1]. Wetwood bacteria are soil-inhabiting, facultative anaerobes that are taken up by trees via the roots in the water of the transpiration stream (xylem elements) where they attack the middle lamellae between wood cells and fibers in sapwood and heartwood in the main bole (trunk) by releasing pectolytic enzymes (pectolases) [2]. These enzymes damage the structural integrity of the wood and cause radial and lateral separations of wood fibers, resulting in cracks and splits (defects) in processed lumber during kiln drying [3]. The damage to processed kiln-dried lumber results in economic losses due to these defects that reduce lumber grade quality and the value of the lumber for commercial sale [4]. An electronic-nose (e-nose) instrument was first utilized to detect bacterial wetwood in the sapwood of

Populus deltoides (cottonwood) plantation trees and to identify host plants of the disease [5]-[7]. The current research focused on the detection of wetwood in two hardwood species, *Fagus grandifolia* (American beech) and *Prunus serotina* (black cherry), that occasionally become infected with wetwood bacteria in low-lying, seasonally-flood bottomland forest sites with anaerobic or water-saturated soils.

The objectives of this study were to 1) determine if an electronic-nose (e-nose) device, the Conducting Polymer (CP)-type Aromascan A32S e-nose, has the capability of detecting bacterial wetwood disease in the sapwood of two hardwood species, including *Fagus grandifolia* and *Prunus serotina*, and to 2) evaluate the effectiveness of this e-nose method to distinguished between the wood types (either healthy or uninfected and wetwood-infected sapwood) of these two species based on aroma signatures of Volatile Organic Compounds (VOCs) present in sample headspace derived from sapwood cores.

This paper is composed of an introduction to the wetwood problem in section 1, followed by e-nose experimental methods used in section 2, describing the specific materials and methods used in associated with e-nose run and analytical procedures, followed by results in section 3 that provide details of experimental research results and findings for CP e-nose analyses of wetwood samples, including sensor outputs, aroma map, and QF analysis of PCA data. Discussion and conclusions, based on the e-nose experimental results, are presented in section 4 to summarize the significance of findings and new discoveries resulting from this research.

II. MATERIALS AND METHODS

A. Collection and storage of sapwood core samples

Sapwood increment core samples (5 mm diameter × 5 cm length) were collected in spring from freshly-harvested *Fagus grandifolia* (American beech) and *Prunus serotina* (black cherry) logs deposited in piles within the Andersen Tully log and lumber mill yard at Vicksburg, Mississippi. A minimum of two core samples were extracted from the boles of at least twenty logs of each species using a Haglöf tree increment borer (Forest Suppliers, Inc., Jackson, MS) and placed into 14.8 mm glass vials. Increment cores were collected from healthy and bacterial wetwood-infected logs.

Wetwood logs were identified by the combined presence of water soaking, dark brown discoloration of sapwood tissue, and the acetic smell associated with this disease. Woody cores in all cases were frozen within 14.8 ml glass vials stored at -20 °C in long-term storage and thawed immediately prior to sample analysis. Cores that became desiccated in storage were rehydrated by soaking in sterile distilled water for 15 min followed by blotting on Chemwipe tissue paper to remove excess free moisture immediately prior to e-nose analysis.

B. Sample preparation and prerun procedures

Sapwood core samples in 14.8 ml glass vials were uncapped and placed into a 500 ml glass headspace sampling bottle fitted with reference air, sampling, and exhaust ports on a polypropylene bottle cap. Reference air entered the sampling bottle through a 3 mm polypropylene tube extending to the bottom of the sampling bottle. The sampling bottle was held at a constant air temperature of 25 ° C. The sampling bottle was purged with filtered, reference air (relative humidity $\leqslant$ 4%) for 2 min prior to building headspace. The sampling bottle was sealed and volatiles from the samples were allowed to build headspace and equilibrate for 30 min prior to each run. Prerun tests were performed as needed to determine sample air Relative Humidity (RH) compared with that of reference air. The sampling bottle cap and exhaust port were opened between runs to purge the previous sample with preconditioned reference air.

C. Instrument configuration and run parameters

The Aromascan A32S Conducting Polymer (CP) e-nose (Osmetech Inc.,Wobum, MA) with a 32-sensor array and 15 V across sensor paths was used for all analyses. Fourteen sensors, (including sensors 11, 12, 20-26, 28-32) that did not respond or did not contribute to the discrimination of sapwood volatiles, were turned off. The response sensitivities of the 18 active sensors used, measured as percent changes in electrical resistance responses across sensor paths relative to base resistance (%ΔR/Rbase), varied with the type of polymer used in the sensor-matrix coating, the type of proprietary ring substitutions used, and the type of metal ions used to dope the matrix to improve and modulate sensor response. Detailed analyses containing calibration data for the sensor array were reported previously [5]. The block temperature of the sensor array was maintained at 30 °C. Reference air was preconditioned by passing room air sequentially through a carbon filter, silica gel beads, inline filter, and Hepa filter [5] to remove organic compounds, moisture, and particulates prior to humidity control and introduction into the sampling bottle. The flow rate (suction) was maintained at -702 ml/min using an air flow-calibrated ADM 3000 flow meter (Agilent Technologies,Wilmington, DE). Sensors were purged between runs using a 2% isopropanol wash solution. The instrument was interfaced with a personal computer via an RS232 cable and controlled with Aromascan Version 3.51 software. The instrument plumbing was configured for static sampling of the headspace by allowing air flow out of the external vent port and closing the exhaust port on the sampling bottle so that headspace volatiles were taken from a homogeneous static air mass within the sampling bottle.

D. Data acquisition parameters and run schedules

Data from the sensor array were recorded at 1 s intervals using a 0.2 detection threshold (y-units), a 15–20 y-max graph scale, and pattern average of five data samples taken per run during data acquisition. A uniform run schedule consisted of reference air 20 s, sampling time 90 s, and wash 20 s, followed by 90 s of reference air for a total run time of 220 s. Data slices for processing and analysis were taken from a 20 s sampling interval (85–105 s) near the end of the sampling segment just before the sampling-valve closed. A 2 min reference air purge followed by a 30 min equilibration period was allowed between runs.

E. Construction of reference libraries and validation

An aroma signature reference library was constructed from wood types of known reference woods of hardwoods (angiosperm) species included in this study. All database files were linked to specific (designated) aroma classes defining each sample type or category. The following recognition network options (neural net training parameters) were used for each training session: training threshold = 0.60, recognition threshold = 0.60, number of elements allowed in error = 5, learning rate = 0.10, momentum = 0.60, error goal = 0.010 (P = 0.01), hidden nodes = 5, maximum iterations (epochs) = 10,000, using normalized input data, not actual intensity data. Some parameters were modified for improvement of recognition accuracy. A typical training required 2–35 min, depending on the size of the database applied, using an IBM-compatible personal computer with a minimum of 64 mb of RAM and 350 MHz run speed. Neural net trainings were validated by examining training results that compare individual database files for compatibility or by similarity matches to each specific odor classes by test-assigned odor class distributions among related odor classes included in each library. The specific detailed analytical methods used for identification of unknowns, data processing, and statistical determinations followed the procedures and specifications indicated by Wilson et al. [5].

F. Principal component analysis

Three-dimensional PCA was used to distinguish between headspace volatiles of all sapwood samples and to determine the relatedness of the four aroma classes derived from sapwood types of the two hardwood species, either healthy or wetwood-infected, based on PCA algorithms available with the Aromascan 3.51 software. The mapping parameters for three-dimensional PCA were: iterations = 30, units in Eigen values (%), and use of normalized input data.

III. RESULTS

A. Discrimination between e-nose aroma patterns of sapwood types

The A32S CP e-nose provided correct identifications of the majority of sapwood types tested based on differences in

the aroma profiles of headspace wood volatiles. Correct identifications of unknown sapwood cores were determined at rates above 90% (range 92.3-100%) for the four samples types of healthy and wetwood-infected sapwood of American beech and black cherry.

The sensor array of the Aromascan A32S electronic nose provided unique and significantly different aroma signature profiles for the four sapwood core types, representing healthy and wetwood-infected samples of the two hardwood species, including American beech (*F. grandifolia*) and Black Cherry (*P. serotina*) based on CP analysis of volatile organic compounds (Table 1). Sensor output values were statistically different (P<0.01) between sample types for each sensor with standard deviations for means generally <0.05 for all normalized sensor values of each sample type. Sensors 11, 12, 20-26, and 28-32 did not provide data values that significantly added to the discrimination of sample types in pretest runs, and therefore these sensors were turned off prior to analytical runs in order to exclude this data from the statistical analysis. Thus, 18 sensors were used in the data analysis of aroma profiles for each sensor type.

TABLE I. SENSOR OUTPUTS FROM THE A32S E-NOSE SENSOR ARRAY COMPARING HEALTHY AND WETWOOD-INFECTED SAPWOOD CORES OF TWO SPECIES

E-nose	*F. grandifolia*		*P. serotina*	
Sensor	Healthy	Wetwood	Healthy	Wetwood
1	6.83	6.74	7.45	7.15
2	6.15	6.06	6.74	6.46
3	6.94	6.86	7.54	7.31
4	3.48	3.41	3.81	3.69
5	3.46	3.39	3.78	3.67
6	3.48	3.42	3.83	3.70
7	3.84	6.88	7.20	7.13
8	3.99	6.99	7.26	7.15
9	5.46	5.53	5.57	5.51
10	5.09	5.16	5.28	5.20
13	4.93	4.91	5.05	4.89
14	4.52	4.53	4.74	4.51
15	5.09	5.15	5.36	5.14
16	4.77	4.81	4.95	4.75
17	6.09	6.09	4.47	5.12
18	6.32	6.28	4.77	5.40
19	6.10	6.09	4.68	5.24
27	7.47	7.68	7.53	7.98

Normalized sensor output values for wetwood cores were significantly lower than for healthy sapwood cores of both *F. grandifolia* and *P. serotina* species for sensors 1-6. Similar results were observed for sensors 7-27 in *P. serotina,* but these sensor output values were generally greater for wetwood cores than healthy cores of *F. grandifolia*. Sensor values 1-16 for *P. serotina* generally were greater than those of *F. grandifolia* for both wetwood and healthy cores, but the reverse was true for outputs of sensors 17-16. Normalized sensor output values for wetwood cores were significantly lower than for healthy sapwood cores of both *F. grandifolia* and *P. serotina* species for sensors 1-6.

Each sensor in the sensor array was coated with a different conducting polymer composed of polypyrrole, polyanaline, or polythiophene derivatives. Values for normalized and standard deviations of all means were ≤ 0.05, indicating high precision and a high level of statistical significant difference (P<0.01) between means of individual sensor outputs.

B. Principal component analysis

Principal Component Analysis (PCA) tests showed significant differences between wetwood-infected and healthy aroma profiles of beech and black cherry sapwood based on differences between headspace volatiles released from the two wood types of each species. PCA generated precise statistical numerical QF values (quality factors of significance) that provided precise indications of relatedness between aroma profiles of the four sapwood sample types. These QF values indicate the statistical differences between data clusters of all sapwood sample types, plotted as an aroma map in Figure 1. The aroma data plots of healthy and wetwood-infected beech (*F. grandifolia*) sapwood were closer together than healthy and wetwood-infected black cherry (*P. serotina*), although healthy sapwood was significantly different from wetwood-infected profiles for both species. These data plots for healthy black cherry were somewhat separated because one of the samples was considerably dryer and older that other samples of this species. The variability between samples likely indicates differences in the moisture content and amount of wood volatiles released from sapwood cores of healthy black cherry. PCA of this 3-dimensional aroma-map model, as indicated by the principal components in the sapwood volatiles, showed that principal component 1 (PC 1), represented by the x-axis, accounted for 96.4% of the sample variability in the data, while principal component 2 (PC 2), represented by the y-axis, accounted for only 3.5% of the sample variability. Thus, the percentages of the total variance, accounting for by PC 1 and PC 2, explained over 99% of the sample variability in these two orthogonal principal components. The percentage of the variance attributed to principal component 3 (PC 3), represented by the z axis, was negligible and explained less that 0.1% of the sample variance.

The clustering patterns of data points in the aroma for each sample type indicate the precision of the e-nose in

providing consistent data for multiple sample replications. The greater the distance between data clusters of each sample type, the less related the aroma signatures of headspace volatiles associated with each sample type.
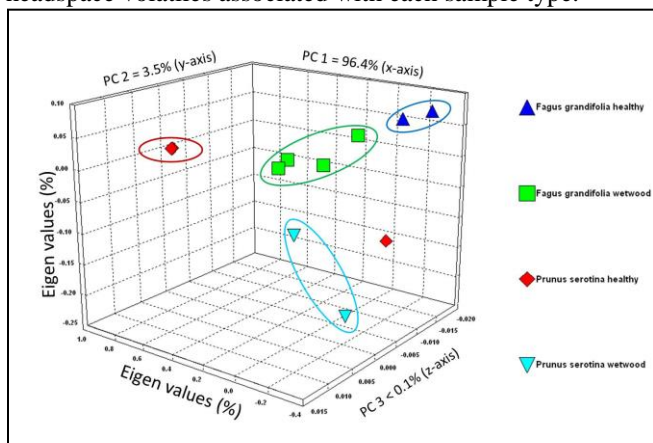

Figure 1. E-nose aroma map showing the differences in aroma profiles of headspace volatiles from healthy vs. wetwood-infected sapwood of *Fagus grandifolia* and *Prunus serotina* using Principal Component Analysis (PCA) of Volatile Organic Compounds (VOCs).

Pairwise comparisons of healthy and wetwood-infected sapwood aroma classes of the two wood types using Quality Factor (QF) significance values provided indications of levels of relatedness between the aroma profiles of healthy and wetwood-infected core types of the two wood species. The e-nose aroma profiles of healthy sapwood cores of American beech were highly significantly different from healthy black cherry (QF=1905.4) at P<0.0001 (Table II).

TABLE II. RELATEDNESS OF HEADSPACE VOLATILES RELEASED FROM HEALTHY AND WETWOOD-INFECTED SAPWOOD CORES OF TWO SPECIES

Aroma class	Aroma class	QF value
F. grandifolia healthy	F. grandifolia wetwood	5.7***
	P. serotina healthy	1905.4****
	P. serotina wetwood	4.5**
F. grandifolia wetwood	P. serotina healthy	32.3***
	P. serotina wetwood	12.3***
P. serotina healthy	P. serotina wetwood	256.4****

Statistical analysis symbols for quality factor (QF) significant difference levels between aroma classes were as follows: * = P < 0.05; ** = P < 0.01; *** = P < 0.001; **** = P < 0.0001. The percentages of the total variance, accounting for the variability explained by each orthogonal principal component (PC), were as follows: PC 1 = 96.40%; PC 2 = 3.51%; and PC 3 < 0.05%.

The aroma profile of healthy black cherry also was very significantly different from wetwood-infected black cherry (QF=256.4). However, differences in aroma profiles of

sapwood headspace volatiles between healthy cores of American beech and wetwood-infected beech and black cherry were much less significantly different at P < 0.001 and P < 0.01, respectively. By comparison, aroma profiles of wetwood-infected beech sapwood were different than healthy and wetwood-infected black cherry sapwood volatiles at intermediate levels of statistical difference (P<0.001). The lowest level of difference between sapwood aroma profiles occurred between healthy American beech and wetwood-infected black cherry (QF=4.5) at P < 0.01.

The large significant differences between healthy and wetwood-infected sapwood of both species provide evidence that the headspace volatiles derived from wetwood bacteria have a large effect on the aroma signature pattern, but not as great as the differences in healthy sapwood volatiles between the two hardwood species.

IV. DISCUSSION AND CONCLUSIONS

Analyses of data indicating unique aroma signature patterns, based on output results from the sensor array of the Aromascan A32S CP electronic-nose, provided effective discriminations between headspace volatiles derived from sapwood core samples of American beech and black cherry. Discriminations and correct identification of samples types were determined at high levels of statistical confidence.

These results are similar to those found for previous studies involving detections of plant disease infections using comparable e-nose analyses for bacterial diseases of onion [8][9], blueberry diseases [10], grain spoilage [11], mango fruit rot [12], wood decay [13]-[16], and other diseases [17][18].

E-nose analysis results of sapwood types in the current study were similar to those obtained from sapwood cores in related studies using different types of e-nose gas-detection technologies based on several different gas-sensing principles as summarized previously [19]-[22]. Wilson et al. [6] was able to distinguished between angiosperm and gymnosperm sapwood types using fresh tree cores frozen at -20 C and thawed immediately prior to analysis with a A32S CP e-nose. Baietto et al. [13] compared the performance of three different e-noses, including the PEN3 metal-oxide (MOS) e-nose, the LibraNose Quartz Microbalance (QMB) e-nose, and the Aromascan A32S CP e-nose to discriminate between healthy and decayed wood of different wood types, decayed by various wood-decay fungi. Other potential agricultural applications of e-nose instruments have been found in pesticide-residue identifications [23][24], environmental monitoring for agricultural wastes and pollutants [25], and disease-detection in fish culture [26].

The large differences between healthy sapwood of American beech and black cherry provide evidence that the headspace volatiles derived from healthy sapwood of these two species have a larger effect on the aroma signature pattern than do differences between wetwood-infected and healthy sapwood of the two hardwood species.

The aromascan A32S CP e-nose has been shown here to have the capability of identifying and discriminating between sapwood types and between healthy and wetwood-infected

sapwood of American beech and black cherry. These results provide additional corroborative evidence of the utility that e-nose devises provide for the diagnosis of bacterial wetwood in bottomland hardwood species. Previously, no consistently reliable methods for detecting the presence of wetwood in hardwoods have been developed [4]. The use of ultrasonic devices for wetwood detection [27] are unreliable and unfeasible due to the requirement for destructive sampling of sapwood logs to obtain measurements, the slow device recovery and setup time between log tests, and difficulties of distinguishing between wetwood and healthy sapwood, because wetwood does not significantly alter wood density unlike decayed wood that does physically soften woods, slowing the transmission rate of sound waves.

The diagnosis of bacterial wetwood in logs of hardwood species is an important first step for log and lumber processing in hardwood lumber mills. Wetwood can be effectively and rapidly detected with e-nose technologies in raw logs prior to cutting into lumber so that all boards derived from wetwood-infected logs can be treated with a different (slower) kiln-drying schedule to mitigate damage to wetwood lumber that results from damaged by shakes and splits during rapid kiln drying. This adjustment in the kiln drying schedule to a slower drying process is essential to preserve lumber value and minimize lumber defects to avoid commercial losses when the lumber is marketed.

ACKNOWLEDGMENT

REFERENCES

[1] A. D. Wilson, "Detection and diagnosis of bacterial wetwood in Tilia americana and Ulmus americana sapwood using a CP electronic-nose," in Industrial, Medical, and environmental applications of microorganisms, A. Méndes-Vilas, Ed., Wageningen Acad. Publishers: Wageningen, The Netherlands, 2014, pp. 209-214.

[2] J. C. Ward and W. Y. Pong, "Wetwood in trees: A timber resource problem," USDA Forest Service, General Technical Report PNW-112, Aug. 1980, pp. 1-57.

[3] B. Schink, J. C., Ward, and J. G. Zeikus, "Microbiology of wetwood: Importance of pectin degradation and Clostridium species in living trees," Appl. Environ. Microbiol., vol. 42, September 1981, pp. 526-532.

[4] Z. Xu, T. D. Leininger, A. W. C. Lee, and F. H. Tainter, "Chemical properties associated with bacterial wetwood in red oaks," Wood and Fiber Science, vol. 33, 2001, pp. 76-83.

[5] A. D. Wilson, D. G. Lester, and C. S. Oberle, "Development of conductive polymer analysis for the rapid detection and identification of phytopathogenic microbes," Phytopathology, vol. 94, 2004, pp. 419-431.

[6] A. D. Wilson, D. G. Lester, and C. S. Oberle, "Application of conductive polymer analysis for wood and woody plant identifications," For. Ecol. & Managem., vol. 209, 2005, pp. 207-224.

[7] A. D. Wilson, "Application of a conductive polymer electronic-nose device to identify aged woody samples," in Proceedings of The 3rd International IARIA Conference on Sensor Device Technologies and Applications, S. Yurish, I. Chilibon, V. Carvalho, S. Gervais-Ducouret, Eds. DE: Wilmington, Xpert Publishing Services, 2012, pp. 77–82.

[8] B. Prithiviraj, A. Vikram, A. C. Kushalappa, and V. Yaylayan, "Volatile metabolite profiling for the discrimination of onion bulbs infected by Erwinia carotovora spp. carotovora, Fusarium oxysporum, and Botrytis allii," Eur. J. Plant Pathol., vol. 110, 2004, pp. 371–377.

[9] A. Vikram, H. Hamzehzarghani, and A. C. Kushalappa, "Volatile metabolites from the headspace of onion bulbs inoculated with postharvest pathogens as a tool for disease discrimination," Can. J. Plant Pathol., vol. 27, 2005, pp. 194–203.

[10] C. Li, G. W. Krewer, P. Ji, H. Scherm, and S. J. Kays, "Gas sensor array for blueberry fruit disease detection and classification," Postharvest Biol. Technol., vol. 55, 2010, pp. 144–149.

[11] N. Magan and P. Evans, "Volatiles as an indicator of fungal activity and differentiation between species, and the potential use of electronic nose technology for early detection of grain spoilage," J. Stored Prod. Res., vol. 36, 2000, pp. 319–340.

[12] Z. Li, N. Wang, G. S. V. Raghavan, and C. Vigneault, "Ripeness and rot evaluation of "Tommy Atkins" mango fruit through volatiles detection," J. Food Eng., vol. 91, 2009, pp. 319-324.

[13] M. Baietto, A. D. Wilson, D. Bassi, and F. Ferrini, "Evaluation of three electronic noses for detecting incipient wood decay," Sensors, vol. 10, 2010, pp. 1062–1092.

[14] S. Hamilton, M. J. Hepher, and J. Sommerville, "Detection of Serpula lacrymans infestation with a polypyrrole sensor array", Sens. Actuator B Chem., vol. 113, 2006, pp. 989–997.

[15] M. A. Markoma, et al., "Intelligent electronic nose system for basal stem rot disease detection," Comput. Electron. Agric., vol. 66, 2009, pp. 140–146.

[16] M. Baietto, P. Letizia, A. D. Wilson, and D. Bassi, "Evaluation of a portable MOS electronic nose to detect root rots in shade tree species," Comput. Electron. Agric., vol. 96, 2013, pp. 117–125.

[17] J. Laothawornkitkul, et al., "Discrimination of plant volatile signatures by an electronic nose: A potential technology for plant pest and disease monitoring," Environ. Sci. Technol., vol. 42, 2008, pp. 8433–8439.

[18] R. M. C. Jansen, et al., "Detection of diseased plants by analysis of volatile organic compound emission," Annu. Rev. Phytopathol., vol. 49, 2011, pp.157–174.

[19] A D. Wilson and M. Baietto, "Applications and advances in electronic-nose technologies," Sensors, vol. 9, 2009, pp. 5099–5148.

[20] A D. Wilson and M. Baietto, "Advances in electronic-nose technologies developed for biomedical applications," Sensors, vol. 11, 2011, pp. 1105–1176.

[21] A. D. Wilson, "Future applications of electronic-nose technologies in healthcare and biomedicine," Chapter 15 in Wide Spectra of Quality Control. I. Akyar, Ed. Croatia: Rijeka, InTech Publishing, 2011, pp. 267-290.

[22] A. D. Wilson, "Diverse applications of electronic-nose technologies in agriculture and forestry," Sensors, vol. 13, 2013, pp. 2295–2348.

[23] A. D. Wilson, "Fungicide residue identification and discrimination using a conducting polymer electronic-nose," in: Proceedings of the Fourth International Conference on Sensor Device Technologies and Applications, DE: Wilmington, Xpert Publishing Services, 2013, pp. 116-121.

[24] A. D. Wilson, "Identification of insecticide residues with a conducting-polymer electronic nose," Chem. Sensors, vol. 4, 2014, pp. 1-10.

[25] A. D. Wilson, "Review of electronic-nose technologies and algorithms to detect hazardous chemicals in the environment," Proc. Technol., vol. 1, 2012, pp. 453-463.

[26] A. D. Wilson, C. S. Oberle, and D. F. Oberle, "Detection of off-flavor in catfish using a conducting polymer electronic-nose technology," Sensors, vol. 13, 2013, pp. 15968-15984.

[27] Z. Xu, T. D. Leininger, J. G. Williams, and F. H. Tainter, "Examination of the arborsonic decay detector for detecting bacterial wetwood in red oaks," S. J. Appl. Forestry, vol. 24, 2000, pp. 6-10.

Magnetic Flux Leakage Testing
for Back-side Defects Using a Tunnel Magnetoresistive Device

Yuya Tsukamoto, Keisyu Shiga,
Kenji Sakai, Toshihiko Kiwa, Keiji Tsukada

Graduate School of Natural Science and Technology,
Okayama University
Okayama, Japan
e-mail: (en421440, pcf45clo)@s.okayama-u.ac.jp
(sakai-k, kiwa, tsukada)@cc.okayama-u.ac.jp

Yasuhiro Honda
KONICA MINOLTA, INC.
Osaka, Japan
e-mail: yasuhiro.honda@konicaminolta.jp

Abstract— **Magnetic non-destructive testing is limited to surface inspection, however demand for the detection of deep defects is increasing. Therefore, we developed a magnetic flux leakage (MFL) system using a tunnel magnetoresistive (TMR) device that has high sensitivity and wide frequency range in order to detect deep defects. Using the developed system, back-side pits of steel plates having different depth and diameter were measured and 2D images were created. Moreover, we analyzed the detected vector signal with optimized phase data. As a result, the developed MFL system can detect a defect that has a wall thinning rate of more than 56 % of 8.6 mm thick steel plates. Furthermore, the defect's diameter size was estimated by spatial signal change.**

Keywords-MFL; magnetic imaging; TMR device; Low-Freaquency field; back-side pit.

I. INTRODUCTION

Accidents due to defects in steel structures such as power plants or pipe line cause serious injuries to humans and harm to the natural environment. Therefore, it is important to use non-destructive testing for detecting defects at an early stage. In many cases, it is difficult to find defects in the interior or on the back side, and thus a detection method for deep defects is desired. There are many non-destructive testing methods such as radiographic testing [1], ultrasonic testing [2], magnetic flux leakage (MFL) testing [3]-[9], and eddy current testing (ECT) [10]. Among them, MFL is commonly used for ferromagnetic material such as steel and it is a method for detecting flux with bypass defects due to differences in permeability and leakage from the sample's surface when an external field is applied to the sample.

MFL for deep defects needs to be operated at low frequency because the penetration of the applied external field becomes deeper with decreasing frequency. However, the conventional MFL method, which uses a detection coil as a magnetic sensor, cannot be operated at low frequency because it has low sensitivity at low frequency due to Faraday's law of induction. Therefore, it can detect only surface defects near the detection coil. Moreover, the

detection of deep defects also requires a high magnetic resolution because the change of flux generated by the deep defect is very small. The other problem of MFL is that the magnetic field intensity of MFL needs to be operated at the saturation region of the B-H curve in order to obtain measurable large magnetic flux leakage. However, a measurement system that gives such large magnetic field intensity is costly because a high power current source is necessary. One way to solve these problems is to use a high sensitivity magnetic sensor that can detect a low magnetic intensity field at low frequency such as a magnetoresistive (MR) sensor. If such a sensor were installed, we could operate MFL at extra low frequency, which would give deep skin depth and detect small magnetic flux leakage caused by a low power source. We reported a MFL system using an anisotropic magnetoresistive (AMR) sensor [11]. Recently, the tunnel magnetoresistive (TMR) sensor has progressed because it has a larger MR ratio than other MR devices with a wide frequency range.

In this study, we developed the MFL system using a TMR device having high sensitivity at extreme-low frequency in order to enable us to detect defects deeper and more clearly than the AMR sensor and other magnetic sensors. Moreover, we investigated the performance of the developed system using samples having various back-side pits.

II. TMR DEVICE

A TMR device is a kind of MR device and is usually applied in the magnetic head of a hard disk. It has a larger MR ratio than other MR devices. A common TMR device shows a step response to magnetic fields and has hysteresis. The TMR device used in this study was designed for sensor application [12]-[14]. It was annealed at different temperatures and directions two times in order to make easy directions of the pin layer and the free layer orthogonal. In this structure, the output is linear with respect to the magnetic field. In addition, it has a large MR ratio because of magnetic coupling of the free layer and the soft magnetic material layer. Figure 1 shows the TMR resistance as a function of an applied field. The range from -400 μT to
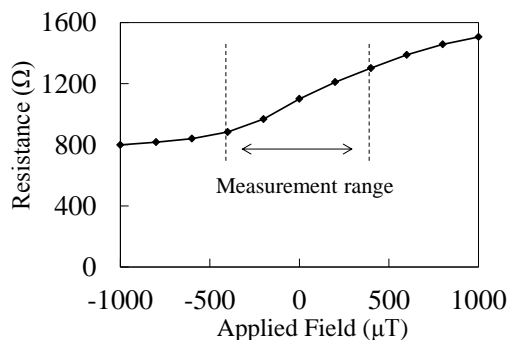
Figure 1. Resistance of the TMR device to an applied field.

400 µT, which is treated in MFL, can be applicable to the sensor application.

III.   EXPERIMENTAL

The developed MFL system (Figure 2) consists of a sensor probe with a TMR device, a lock-in amplifier, a current source, an oscillator, two excitation coils, a half shaped ferrite yoke, a sample stage, and a PC. Two excitation coils with 30 turns were connected to both ends of the yoke and an AC field was induced in the sample between both ends. The sensor probe was installed between the ends of the yoke and they were 1 mm away from the sample's surface. The TMR device measured magnetic flux leakage bypassing defects. In this study, the TMR device had sensitivity to the direction parallel to both ends of the yoke in order to obtain a larger output [11]. The excitation coils were operated by a sine wave of 1.2 A_{pp} and 5 Hz or 10 Hz from the current source controlled by the oscillator. The effect of the eddy current can be ignored in such an extreme-low frequency field. The output signal from the TMR device was detected by the lock-in amplifier, which is synchronized with the current source in order to obtain a high signal-to-noise ratio.

The signal from the lock-in amplifier contains the signal intensity R and the phase θ. In this measurement system, magnetic flux leakage is very small so that it is strongly affected by the phase shift of the entire measurement system. Therefore, we calculated the imaginary part of the signal intensity with the common phase φ [11].

$$R' = R \sin(\theta + \varphi). \qquad (1)$$

Here, φ is a common phase adjusting the phase shift of the entire measurement system.

The samples used in this study were two steel plates (SPHC) with four back-side pits as shown in Figure 3. Both samples were 8.6 mm thick. The pits of Sample (a) are of the same diameter (6 mm) and different wall thinning rates (23, 57, 70, 93 %). Sample (b) has the same wall thinning rate (70 %) and different diameters (4, 6, 8. 10 mm). Multipoint measurement was carried out in the range of 20 mm × 20 mm around a pit from front surface with an interval of 1 mm for 21 × 21 steps as shown in-Figure4.
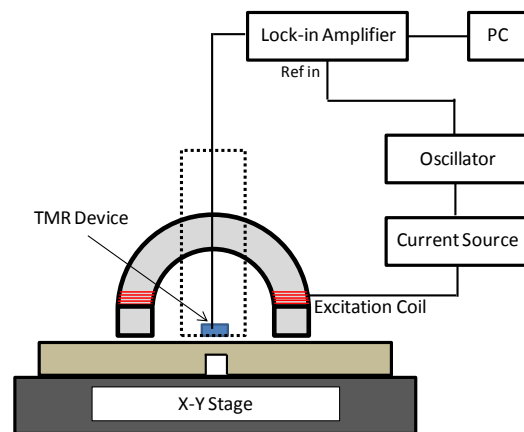

Figure 2. Schematic diagram of the developed MFL system.

We investigated the common phase φ in this measurement system. The measurement was carried out around a pit that has a wall thinning rate of 70% and a diameter of 4 mm. The excitation coils were operated by sine wave of 1.2 A_{pp} and 10 Hz or 5 Hz from the current source. The measurement results show as contour maps of calculated intensity (mV) with different common phases.

Figure 5 shows magnetic images with a frequency of 10 Hz and different common phases and Figure 6 shows that with 5 Hz and different common phases. Magnetic images with a common phase φ of 130 ° show the emphasis of the intensity change due to the pit in the center of the scanning range. The magnetic image with a frequency of 5 Hz shows the presence of the back-side pit more clearly than that of 10 Hz because the skin depth becomes deeper with decreasing frequency. Therefore, the frequency was 5 Hz and the optimized common phase φ was 130 ° for the measurement system.

Figure 7 shows the power spectrum of the developed system when the magnetic field was not applied and the sine field was applied at 100 µT and 5 Hz in the unshielded environment. The sensitivity at 5 Hz of the developed system is 2.44 mV/µT. We estimated the magnetic noise without an applied field that corresponds to the minimum magnetic field resolution at 5 Hz. As a result, the magnetic field resolution was 1.08 nT.
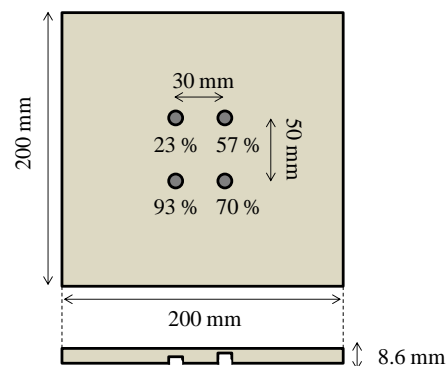
(a) Fixed diameter, different wall thinning rates.

(b) Fixed wall thinning rate, different diameters.
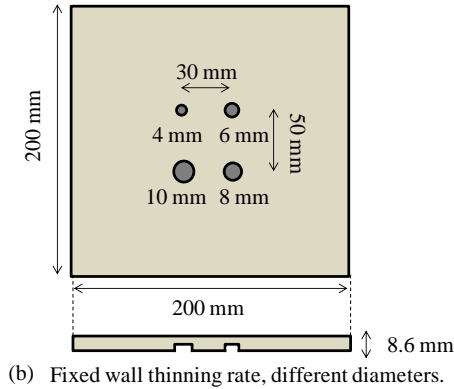
Figure 3. Schematic diagram of the test plates with pits.
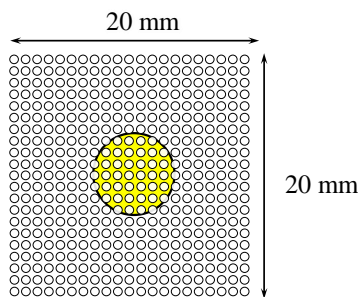

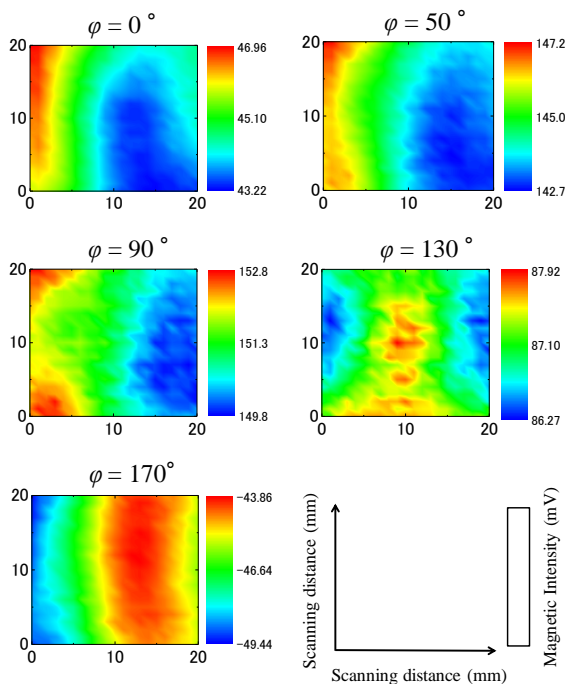Figure 4. Measuring points for back-side pits.

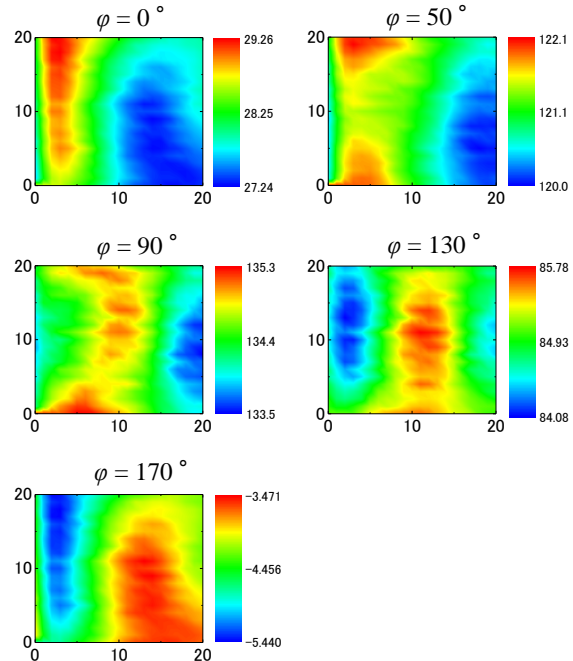Figure 5. Magnetic images with 10 Hz and different phase.

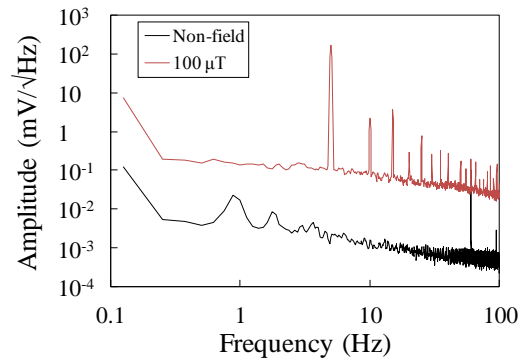Figure 6. Magnetic images with 5 Hz and different phase.

Figure 7. Power spectrum of the developed system.

To evaluate the performance of the developed MFL system, we analyzed the magnetic image change of a steel plate having different pit wall thinning rates and diameters under optimum conditions. The excitation coils were operated by a sine wave of 5 Hz and 1.2 A_{pp} from the current source. We calculated the signal vector with the optimized phase $\varphi = 130°$. The aforementioned Sample (a) and Sample (b) were measured and we made contour maps of the calculated signal vector.

IV.   RESULTS AND DISCUSSION

First, we used Sample (a) and investigated the change of magnetic images of the steel plates with different wall thinning rates. The map showed the existence of the pit and it becomes clear with increasing the actual pit's wall thinning rate (Figure 8). However, the magnetic image of a pit that has a wall thinning rate of 23 % is unclear. This was caused by the weak magnetic flux leakage from the small thinning rate of the wall. The detection limit was a thinning rate of

57 % corresponding to a wall thickness of 4.6 mm. Next, we used Sample (b) and investigated the changes of the magnetic images by changing the diameter (Figure 9). Apparent differences were observed in each figure. The contour map change became large according to the increment of the diameter.

Moreover, we quantitatively evaluated the magnetic field intensity change and examined the relationship of the defect's characteristics and the calculated intensity. The center line of the contour of the magnetic image was extracted as shown in Figure 10 and ΔB was defined as the value obtained by subtracting the minimum value from the maximum value as shown in Figure 10. Figure 11 shows the relationship of ΔB and the wall thinning rate and Figure 12 shows that of ΔB and the diameter. ΔB was increased with the increment of the wall thinning rate and the diameter. Therefore, we can estimate the defect's characteristics using the magnetic image and ΔB.

Figure 10. Example of the extracted line and the definition of ΔB.
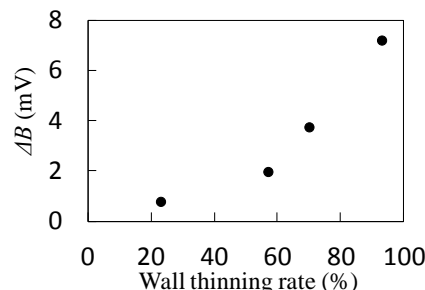

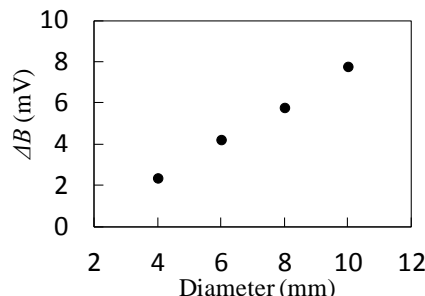Figure 11. Relationship of the defect's wall thinning rate and ΔB.

Figure 12. Relationship of the defect's diameter and ΔB.

Figure8. Magnetic images of pits with different wall thinning rate.

Figure 9. Magnetic images of pits with different diameter.

V. CONCLUSIONS

We developed a magnetic flux leakage (MFL) testing system using TMR for back-side defects. Analysis using the signal vector with optimized phase was effective for magnetic imaging of the back-side pits. The magnetic images reflected the actual defect's characteristics and were able to detect more than the wall thinning rate of 57%. The developed MFL system does not require a high power current source so that this measurement system is expected to be applicable to field testing.

REFERENCES

[1] T. W. Liao and Y. Li, "An automated radiographic NDT system for weld inspection," NDT&E Int 31, pp.183–192, 1998.

[2] E. T. Hall and D. I. Crecraft, "Bonded joints and non-destructive testing," Non-Destr. Test. 4, pp.181–191, 1971.

[3] G. Dobmann, G. Walle, and P. Hëller, "Magnetic leakage flux testing with probes: physical principles and restrictions for application," NDT Int 20, pp.101–104, 1987.

[4] A. I. Pashagin, N. P. Benklevskaya, and V. E. Shcherbinin, "Problems of evaluation of the flaw parameters in magnetic nondestructive testing," Russ J Nondestruct Test 38, pp.399–406, 2002.

[5] V. F. Muzhitskii and V. E. Shcherbinin, "Magnetic field of a short rectangular slot-type flaw," Russ J Nondestruct Test 42, pp.115–118, 2006.

[6] A. Z. Veksler, B. V. Gusev, A. M. Shanaurin, and V. E. Shcherbinin, "Comparison of results of measuring the magnetic field of a crack by flux-gate meters with calculated data obtained within a model of constant magnetic charge density," Russ J Nondestruct Test 44, pp.54–58, 2008.

[7] A. R. Ramírez, J. S. D. Mason, and N. Pearson, "Experimental study to differentiate between top and bottom defects for MFL tank floor inspections," NDT&E Int 42, pp.16–21, 2009.

[8] O. Stupakov, H. Kikuchi, T. Liu, and T. Takagi, "Applicability of local magnetic measurements," Measurement 42, pp.706–710, 2009.

[9] M. Katoh, K. Nishio, and T. Yamaguchi, "FEM study on the influence of air gap and specimen thickness on the detectability of flaws in the yoke method," NDT&E Int 33, pp.333–339, 2000.

[10] B. A. Auld and J. C. Moulder, "Review of advances in quantitative eddy current nondestructive evaluation," J Nondestruct Eval 18, pp.3–36, 1999.

[11] K. Tsukada, M. Yoshioka, Y. Kawasaki, and T. Kiwa. "Detection of back-side pit on a ferrous plate by magnetic flux leakage method with analyzing magnetic field vector," NDT&E Int 43, pp.323-328, 2010.

[12] K. Fujiwara, M. Oogane, S. Yokota, T. Nishikawa, H. Naganuma, and Y. Ando, "Fabrication of magnetic tunnel junctions with a bottom synthetic antiferro-coupled free layers for high sensitive magnetic field sensor devices," J. Appl. Phys. 111, 07C710, 2012.

[13] K. Fujiwara, M. Oogane, T. Nishikawa, H. Naganuma, and Y. Ando. "Detection of Sub-Nano-Tesla Magnetic Field by Integrated Magnetic Tunnel Junctions with Bottom Synthetic Antiferro-Coupled Free Layer," Japanese Journal of Applied Physics 52, 04CM07, 2013.

[14] D. Kato, M. Oogane, K. Fujiwara, T. Nishikawa, H. Naganuma, and Y. Ando, "Fabrication of Magnetic Tunnel Junctions with Amorphous CoFeSiB Ferromagnetic Electrode for Magnetic Field Sensor Devices," Applied Physics Express 6, 103004, 2013.

Reaction Distribution with Time in Fuel Cells
using a Terahertz Chemical Microscope

Tetsuya Kusaka, Kazuki Koiso, Kenji Sakai, Toshihiko Kiwa, and Keiji Tsukada

Graduate School of Natural Science and Technology,
Okayama University,
Okayama, Japan
E-mail: (pkta5jir, p4jh6yr8)@s.okayama-u.ac.jp
(sakai-k, kiwa, tsukada)@okayama-u.ac.jp

Abstract—**The visual evaluation of fuel cells by conventional means is impossible. To improve the power generation efficiency of fuels cells, the evaluation of catalytic reactions on the electrodes and ion propagation in the electrolyte are important. We developed a terahertz chemical microscope (TCM) to visualize the electric potential shift in the catalytic electrodes of fuel cells. The potential energy shift of the fuel cells due to the dissociation of gases was visualized using TCM during fuel cell operation.**

Keywords–TCM; THz; fuel cell; evaluation

I. INTRODUCTION

Energy and environmental issues have recently become crucial and require energy solutions of high efficiency and low environmental load. Thus, the use of hydrogen gas has attracted attention. Fuel cells are high-efficiency devices that transform chemical energy to electric energy. However, the power generation efficiency of fuel cells has to improve. Hence, evaluation methods and investigation of the catalytic reactions on the catalytic electrodes and ion propagation in the electrolyte are required.

Recently, we have developed a terahertz chemical microscope (TCM) to evaluate the distribution of the electric potential on a semiconductor-based device referred to as THz sensing plate. Terahertz (THz) waves radiating from the THz sensing plate can be related to the electric potential at the surface of the THz sensing plate [1]–[4].

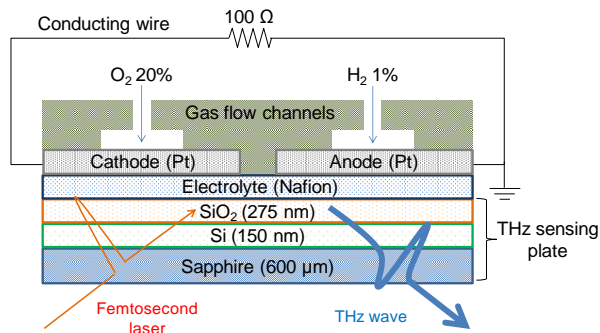Conventional evaluation methods of surfaces are atomic force microscopy [5], scanning electron microscopy [6], and transmission electron microscopy. Kelvin probe microscopy (KPM) can measure the electric potential distribution on the electrode surface [7]. However, KPM probe needs to closely touch the electrode surface; thus, in general, it is difficult for KPM to measure the electric potential while the fuel cell is in operation. On the other hand, the TCM can measure the electric potential of catalytic metals without coming to contact with the surface of metals.

In a previous study, the time variation of the THz signal during the fuel cell operation was measured [8], and the signal was observed to drift due to the diffusion of protons in the proton membrane. In this study, the two-dimensional imaging of the THz signal during the long operation of fuel cells is demonstrated, and the potential distribution on the electrodes is discussed.

II. EXPERIMENTS

Figure 1 shows the schematic diagram of the fuel cell on the THz sensing plate. The sensing plate consists of SiO_2 (275 nm) and Si (150 nm) layers on a sapphire substrate (600 μm). Because of its excellent mechanical and thermal stability, Nafion® (10%) membrane was applied on the surface of the SiO_2 layer by spin coating and baked for 90 s at 90 °C. Platinum (Pt) was deposited on the Nafion membrane to serve as catalytic metal electrodes by conventional sputtering techniques. Before the experiments, we confirmed that the fuel cell fabricated on the THz sensing plate generated voltage as well as the actual fuel cells.

Figure 2 shows the energy band diagram of the sensing plates, on which the Nafion membrane and the Pt thin film were fabricated. When femtosecond laser pulses were
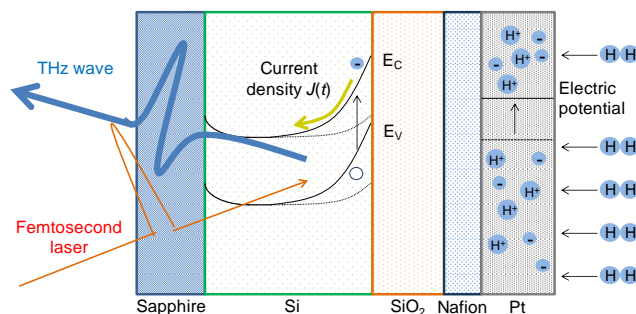

Figure 1. Schematic diagram of a fuel cell fabricated on the THz sensing plate.

Figure 2. Energy band diagram of the THz sensing plates. E_C is the conduction band and E_V is the valence band.

irradiated from the sapphire side of the THz sensing plate, photoexcited carriers were generated in the Si layer. The photoexcited carriers were accelerated by the electric field generated by the depletion layer, and THz waves were radiated to free space.

The relation between the radiated THz waves and the electric potential on the THz sensing plate is described with following equation:

$$E_{THz} \propto \frac{\partial J(t)}{\partial t} \propto e\frac{\partial n(t)}{\partial t}v(t) + en(t)\frac{\partial v(t)}{\partial t}, \qquad (1)$$

where $J(t)$ is the current density, e is the elementary charge, $n(t)$ is the excitation carrier density, and $v(t)$ is the carrier velocity. Hydrogen molecules are dissociated when hydrogen gas is exposed to the Pt electrodes. The hydrogen ions (H^+) diffuse into the Pt electrodes and then the Nafion membrane. The H^+ ions are adsorbed on the SiO_2 surface of the THz sensing plate. The carrier acceleration in the second term of (1) is equal to the local electric field E_{local} in the sensing plate; therefore, the amplitude of the THz wave emitted from the THz sensing plate is proportional to the local electric field.

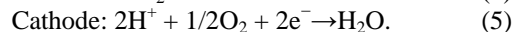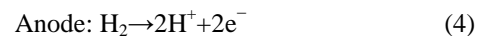The amplitude of the radiated THz wave is

$$E_{THz} \propto E_{local} = \sqrt{eN_D/2\varepsilon} \times \sqrt{\phi}, \qquad (2)$$

where E_{local} is the local electric field, N_D is the carrier density of the Si surface, ε is the dielectric constant of Si, and ϕ is the electric potential. The shift in the electric potential of Pt due to the reaction of hydrogen gas is expressed by using the Nernst equation:

$$\phi = const - (RT/zF) \ln P_{H_2}, \qquad (3)$$

where F is the Faraday constant, z is the number of electrons transferred in the cell reaction, R is the gas constant, T is the absolute temperature, and P_{H2} is the partial pressure of hydrogen. Equation (3) shows that the electric potential of the THz sensing plate shifts because of the adsorption of hydrogen gas to the Pt electrodes in the fuel cell. The visualization of the chemical reactions can be achieved by scanning the irradiation point of the femtosecond laser because the radiated THz wave depends on the local electric field of the depletion layer where the laser is irradiated. In the fuel cell, the chemical reaction at the anode and the cathode of the operating fuel cell can be expressed as follows:

$$\text{Anode: } H_2 \rightarrow 2H^+ + 2e^- \qquad (4)$$
$$\text{Cathode: } 2H^+ + 1/2O_2 + 2e^- \rightarrow H_2O. \qquad (5)$$

The electric potential shift because of the adsorption of hydrogen gas in the anode is obtained as the amplitude of the radiated THz wave by (3). At the anode, the hydrogen molecules, which reach Pt, dissociate to H^+ and electrons. H^+ reaches the cathode through the Nafion membrane. The electrons move to the cathode along the conducting wire. The THz amplitude from the anode increases with increasing electric potential because of the reduction of hydrogen. On the other hand, the amplitude of the radiated THz wave decreases due to the oxidation reaction of H^+ in the cathode.

Figure 3 shows the optical setup of TCM. The fuel cell fabricated on the THz sensing plate is fixed on the X–Y stage to scan the femtosecond laser. Before irradiating the THz sensing plate, the femtosecond laser pulses pass through the condensing lens to increase the spatial resolution. The Ti:sapphire laser is a femtosecond laser with a central wavelength of 780 nm, a pulse width of 100 fs, and a repetition frequency of 82 MHz. A conventional photoconductive antenna was used to detect the radiated THz waves whose amplitudes are related to the electric potential of the THz sensing plate. Figure 4 shows a photograph of
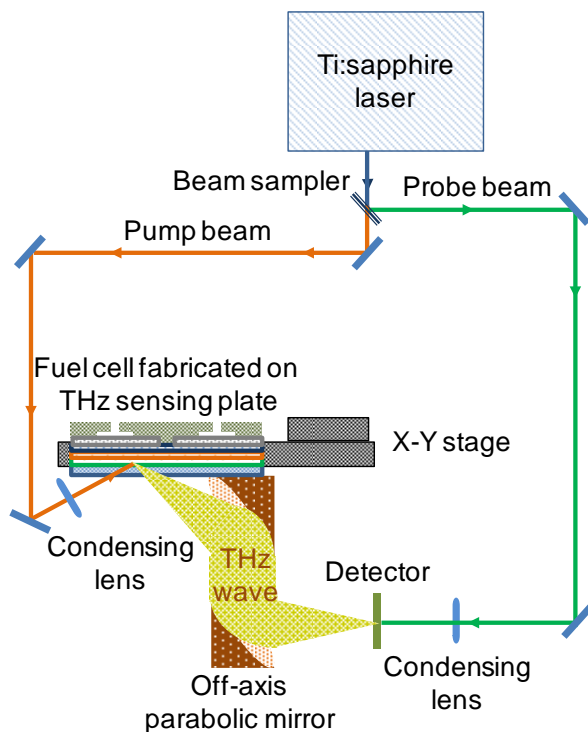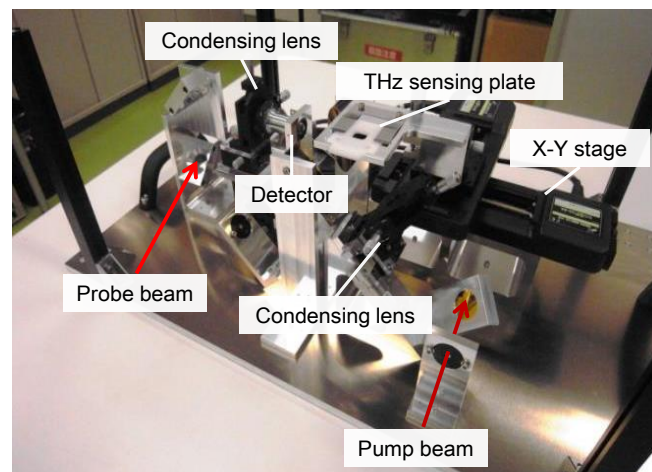

Figure 3. Setup of TCM.

Figure 4. Photograph of TCM.

TCM. All optical components were attached on the same platform sterically. The area of the platform is 628×379 mm^2.

III. RESULTS

Figure 5 shows the time variation of the distribution of the radiated THz amplitude from the THz sensing plate. The
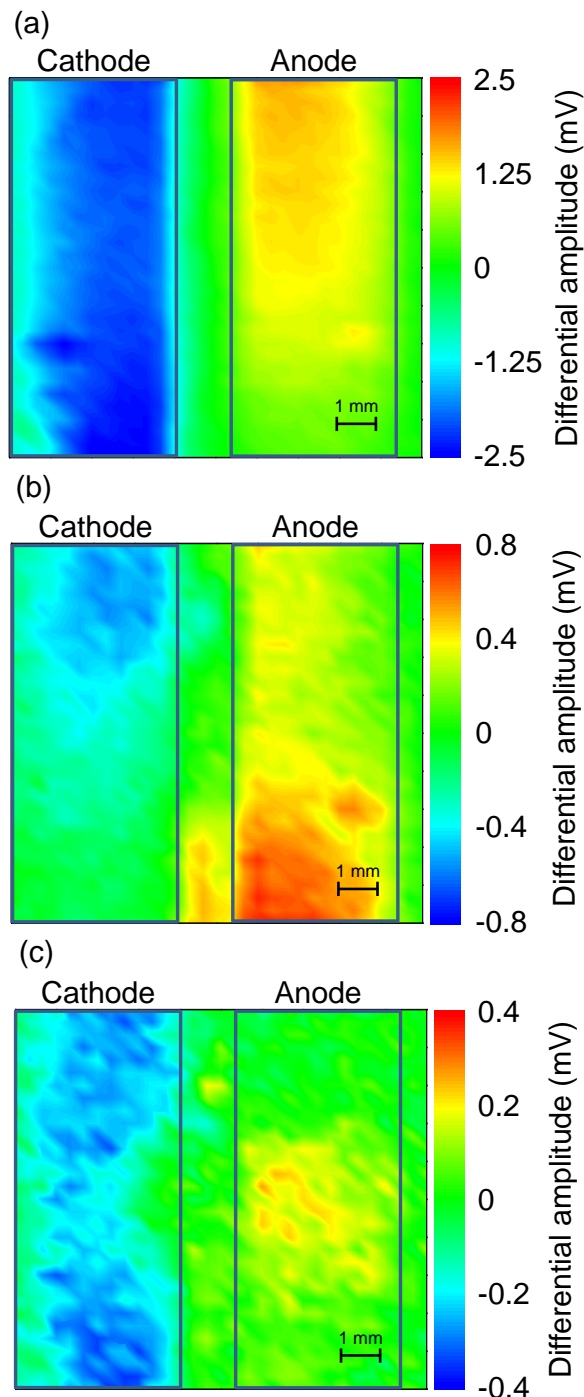

Figure 5. Variation of the THz amplitude distribution obtained after power generation (a) for 1 h, (b) between 1–2 h, and (c) between 2–3 h.

areas surrounded by the blue line show the catalytic electrodes. Hydrogen gas (1%) and oxygen gas (20%) in the nitrogen gas were, respectively, introduced to the anode and cathode to operate the fuel cell. Figures 5 (a), (b), and (c) show the change in the THz amplitude distribution obtained (a) before and after power generation for 1 h, (b) between 1–2 h, and (c) between 2–3 h. Initially, the THz amplitude at the cathode decreases, whereas the THz amplitude at the anode increases. The change in the THz signals was larger in magnitude at the upper parts of the electrodes. Subsequently, the THz amplitude was saturated across the electrodes.

The average values of the radiated THz amplitude from the anode and the cathode during the fuel cell operation are plotted in Figure 6. The electric potential in the anode increases, whereas that in the cathode decreases and, subsequently, both become saturated. This shows that TCM can measure the reaction amount in the catalytic electrodes.

IV. CONCLUSION AND FUTURE WORK

We mapped the radiated THz waves from a THz sensing plate, on which a fuel cell was fabricated, during fuel cell operation. The THz amplitude at the anode increased, whereas that at the cathode decreased. The nonuniformity of the THz amplitude can be seen at the anode and cathode. The results agree with past experiments. We also confirmed the reaction distribution in the catalytic electrodes with time, which shows that TCM can measure the reaction distribution in the catalytic electrodes. The radiated THz amplitude from the anode and cathode reach saturation with time. Evidently, TCM can measure the reaction amount in the catalytic metal electrodes. In conclusion, we showed that TCM can be used to evaluate fuel cells. When TCM is commercialized, we will be able to visually evaluate the uniformity of the electrolyte and electrodes. We conducted the experiments using only Nafion 10%; thus, we plan to measure the performance of fuel cells using Nafion with different concentrations or other electrolytes. The relation between TCM images and fuel cell efficiency is presently under investigation.
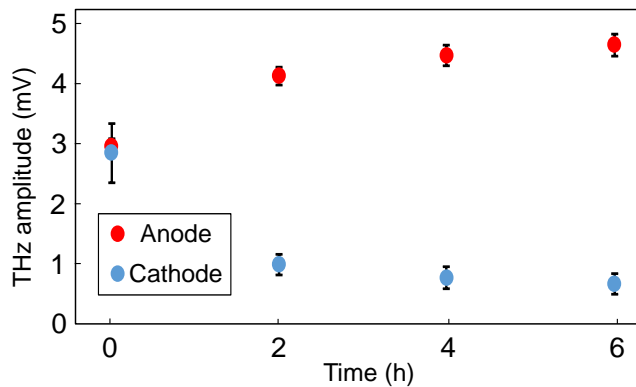

Figure 6. Time variation of the radiated THz amplitude due to the voltage generation in the fuel cell.

REFERENCES

[1] T. Kiwa, J. Kondo, S. Oka, I. Kawayama, H. Yamada, M. Tonouchi, and K. Tsukada, "Chemical sensing plate with a laser-terahertz monitoring system," Appl. Optics, 47, 18, pp. 3324–3327, 2008.

[2] T. Kiwa, S. Oka, J. Kondo, I. Kawayama, H. Yamada, M. Tonouchi, and K. Tsukada, "A terahertz chemical microscope to visualize chemical concentration in microfluidic chips," Jpn. J. Appl. Phys., 46, 41–44, pp. L1052–L1054, 2007.

[3] T. Kiwa, K. Tsukada, M. Suzuki, M. Tonouchi, S. Migitaka, and K. Yokosawa, "Laser terahertz emission system to investigate hydrogen gas sensors," Appl. Phys. Lett., 86, 261102, 2005.

[4] T. Kiwa, T. Hagiwara, M. Shinomiya, K. Sakai, and K. Tsukada, "Work function shifts of catalytic metals under hydrogen gas visualized by terahertz chemical microscopy," Opt. Express, 20, 11637–1164, 2012.

[5] H. Ghassemi, J. E. McGrath, and T. A. Zawodzinski Jr, "Multiblock sulfonated–fluorinated poly (arylene ether) s for a proton exchange membrane fuel cell," Polymer, 47, 4132–4139, 2006.

[6] J. Xie, D. L. Wood, K. L. More, P. Atanassov, and R. L. Borup, "Microstructural changes of membrane electrode assemblies during PEFC durability testing at high humidity conditions," J. Electrochem. Soc., 152, A1011–A1020, 2005.

[7] J. Zhang, G. Yin, and Z. Wang, and Y. Shao, "Effects of MEA preparation on the performance of a direct methanol fuel cell," J. Power Sources 160, 1035–1040, 2006.

[8] T. Kusaka, K. Koiso, K. Sakai, T. Kiwa, and K. Tsukada "Catalytic reactions of the fuel cells visualized by THz chemical microscope," In Laser Applications to Chemical, Security and Environmental Analysis (pp. LTu3D-6). Optical Society of America, 2014.

Sensor Platform for Measuring the Concentration in Aqueous Solutions by Cyclic Voltammetry and Impedance Spectroscopy

Dr. Thomas Frank, Manuel Fiedler, Dr. Ingo Tobehn, Arndt Steinke, Andrea Cyriax

Forschungsinstitut für Mikrosensorik und Photovoltaik GmbH, 99099 Erfurt, Germany

tfrank@cismst.de mfiedler@cismst.de itobehn@cismst.de asteinke@cismst.de acyriax@cismst.de

Abstract— **This article describes sensors for concentration measurement based on the electro-chemical properties of the liquid being measured. Herein two electrical methods, namely cyclic voltammetry and impedance spectroscopy, are being presented. The measurement can be performed quasi simultaneously using the same measurement medium. Further optimization of the combined methods are possible by adapting the geometric design of the electrode structure, the electrode material, the optional passivation and the electric coupling (galvanically or capacitively). In summary, by combining multiple sensory principles on a device it becomes possible to analyze mixtures of substances contained in a solution with respect to their composition.**

Keywords; interdigital structure; impedance spectroscopy; cyclic voltammetry; silicon.

I. INTRODUCTION

Sensors for concentration measurements are a very vast area of research. A concentration measurement is used when the components are known, but not their content. For their determination several substance-specific sensor principles are known. In this article, two electrical methods are presented using the implementation as the sensing element is reported. These methods are based on cyclic voltammetry and impedance spectroscopy. In cyclic voltammetry a rising and then sloping current is applied between the working electrode and the counter electrode in a solution. The potential is determined by a reference electrode. If there is a redox-active substance in the solution, it will be oxidized or reduced at a characteristic potential. The current is recorded as a function of voltage. The voltage in the oxidation and reduction and the corresponding maximum current are of interest. Impedance spectroscopy detects both the dielectric properties of a medium and its conductivity as a function of frequency. In aqueous solution, these properties are dependent on the concentration.

The base of the sensors is an interdigital structure. Figure 1 shows different variations of designs. The main features can be combined freely. A galvanic or capacitive coupling is possible. The DUT can be a liquid or a solid. The organic or inorganic sensitive solid is applied directly to the sensor surface. The thickness is only a few 100 nm and is micro- or nano-porous. This binds substances (DUT) by absorption from the surrounding atmosphere, such as water or carbon dioxide. The electrical properties change due to this and are determined by the spectroscopy. Table 1 shows the different materials for the sensor.
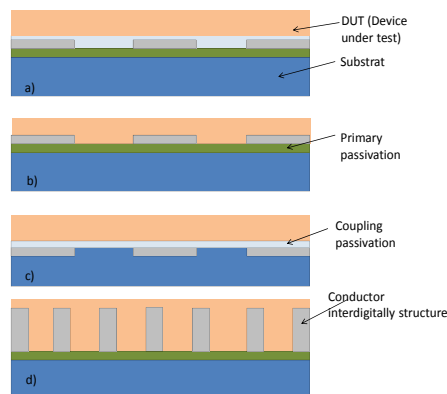

Figure 1. Various design options a) interdigital structure, passivated for a capacitive coupling, b) interdigitated structure without passivation, galvanic coupling, c) implanted in silicon interdigital structure, d) 3D interdigital structure

TABLE 1. OPTIONAL MATERIALS FOR THE SENSOR

Base material	Silicon, (optional) Borosilica
Passivation Base material	SiO_2
Conductor	Doped Silicon, MoSi, Gold Platinum
Passivation Conductor (optional)	Si_3N_4, ZrO_2, Al_2O_3 (20 nm to 500 nm)

In addition to the measurement of purely chemical parameters, such as concentration, measurement of biological media is possible. The evaluation of the measurement results, however, requires great experience. In [1] and [2], the dielectric measurement of a biological medium is described by some examples.

Often the signal is not very selective on the type of material. In the DUT (device under test) the selectivity of the sensor can be increased adding an indicator; using the mixing ratio and the associated change in impedance even a multi-component system can be analyzed. Further optimization of the combined methods are possible by the geometric design of the electrode structure, the electrode material, the optional passivation and the electric coupling.

The combination of multiple sensory principles on a device can be used to analyze a multicomponent system with a simple sensor.

Section II represents the principle for the combined impedance spectroscopy and cyclic voltammetry, the base of the sensor platform, the various of this and the electronic circuit. Section III represents the measurements for the evaluation and calibration of the sensor various. Section IV shows a sample application. Section V concludes the article.

II. EXPERIMENTAL SETUP

For the evaluation and adaptation of the sensor's design, a test setup was constructed. The design is configured such that the distances can be selected in a range of 200 microns with free a resolution of 5 microns. In Figure 2, the measuring principle is shown. By choosing the connections of the electrode gap can be selected. In [1] and [2], this method is described in detail.
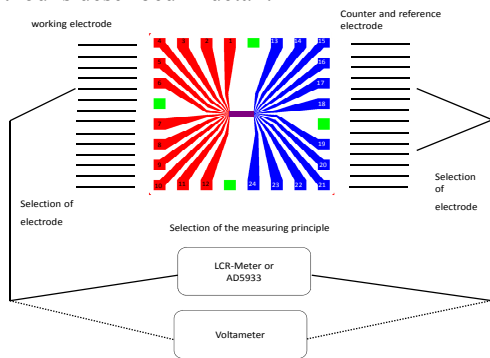
Figure 2. The principle for the combined impedance spectroscopy and cyclic voltammetry

The measurement setup for impedance spectroscopy can be seen in Figure 3. Here, the analysis-chip with the interdigital structure on it is seen in the middle. It is surrounded by 12 dual multiplexer, which can be used to select the 24 measurement channels (12 per page). On the left side of the figure there are SMA connectors for connecting an external LCR meter to chip, with which the impedance of the device can be measured.

Through the recess in the middle, the liquid which is to be investigated can be applied to the interdigital structure either directly, or a flow chamber can be installed to then perform the impedance spectroscopy using the desired channels.
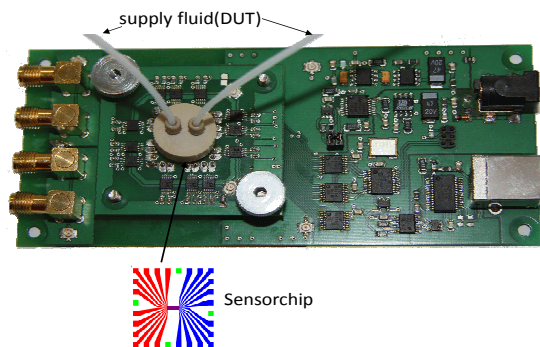

Figure 3. The electronic circuit for the combined impedance spectroscopy and cyclic voltammetry with die connector for the fluid

Figure 4 shows the sensor for the combined impedance spectroscopy and cyclic voltammetry. With the aid of a multiplexer array, a line-bound connection between the measuring object and the impedance spectrometer is established. Subsequently, the impedance spectroscopy is performed for the selected channel.
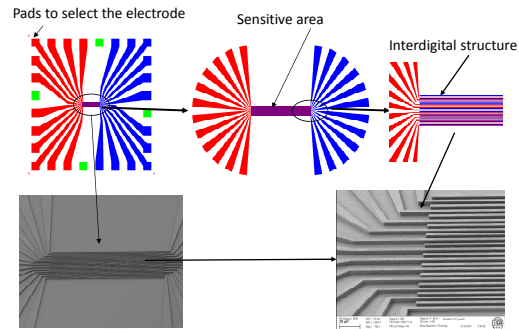

Figure 4. The sensor for the combined impedance spectroscopy and cyclic voltammetry

III. MEASUREMENTS FOR EVALUATION

For the evaluation and calibration of the sensor measurements are performed on an aqueous solution of KCl, ranging from 0.00002 mol/l to 1 mol/l. Figure 5 shows the frequency dependent measurement of the impedance |Z| of the aqueous KCl solution, the distance between the electrodes is constant.
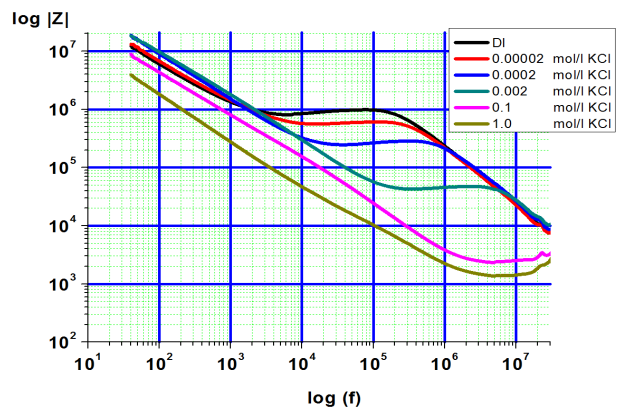

Figure 5. Concentration measurement, variation in the concentration

In Figure 6 the result when measurement is being performed at different distances of the electrodes is shown. In this way, the appropriate geometric structure is found for the measuring task.
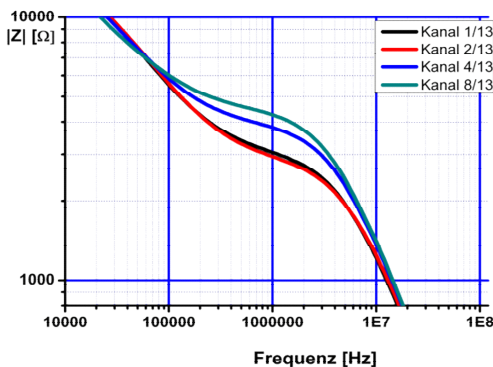
Figure 6. Concentration measurement, variation of the electrode distance

With the aid of the measured values, the amount and phase |Z|, an equivalent circuit diagram is developed. The values for the components are determined by a curve fitting. The results are shown in the Figure 7. The equivalent circuit is now allowing for the calculation of the resistor R1 from the measured values and the calibration of the sensor to the conductance. Figure 8 shows the graph of the curve fitting.

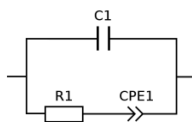| Parameters	Upper Limit	Lower Limit	Result/In.Val.	Error %	Fix
C1	6.7785e-13	6.7785e-13	6.7785E-13	1.016	☑
R1	1000000	0	2.4802E05	3.7676	☐
P1	0.0005	0	5.2288E-10	3.7702	☐
n1	1	0	0.83005	0.51933	☐

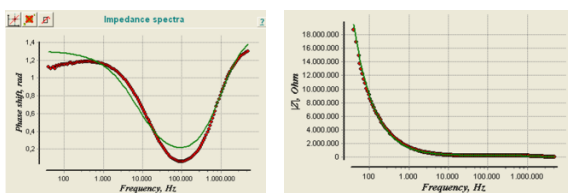Figure 7. Equivalent circuit diagram and the curve fitting

Figure 8. Graph of the curve fitting

In Figure 9 the resistances as a function of concentration from the curve fitting are plotted. Various layer structures, geometries and measurement strategies are explored. The aim is to explore a multi-component system with various sensors at the same location. The concentration of the components is derived from the signal pattern. If the sensor is calibrated, the concentration of the ingredients can be determined from the signal pattern. One application is the in-line measurement in biogas plants to optimize the output.
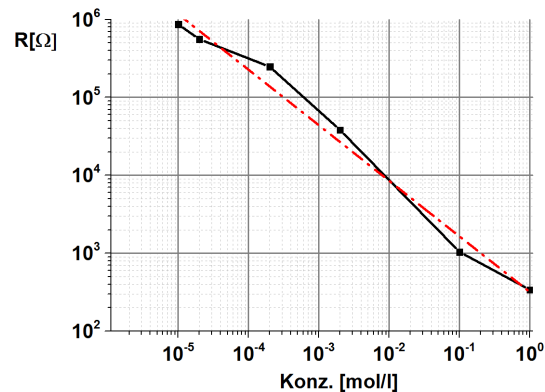

Figure 9. Concentration measurement, variation of the electrode distance

An overview of the previous work done is detailed in [3]-[5]. The cyclic voltammetry is partially used in micro-sensors, but not in combination with the impedance spectroscopy. The essential idea and novelty are related to the connection of several measurement principles and sensitivities to determine the concentration at the same location. In summary, by combining multiple sensory principles on a device it becomes possible to determine the composition of substances contained in solution.

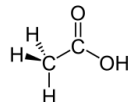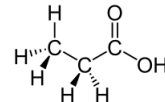IV. EXPERIMENTS ON THE TERNARY SYSTEM WATER-ACETIC ACID-PROPIONIC ACID

The ratio of acetic acid-propionic acid is a control parameter for the operation of biogas plants [6]. The sequence of processes in biogas plants is not explained here, an intrigued reader might take a look at [7]. The concentration measurement in this mixture is very challenging because acetic acid and propionic acid share similar chemical properties. The separate determination of the concentration of acetic acid and propionic acid in the mixture of the two materials is difficult because both materials differ structurally only by an additional-CH2-group, which is insignificant in terms of responsiveness and many physical properties

Cyclic voltammetry is preferably used to investigate redox processes in terms of their mechanism. It turns the electrode material used as a limit to the administrable voltage. Since acetic and propionic acid can be reduced only under very drastic conditions to the aldehyde, it can be expected that the cyclic voltammetry for the quantitative determination of these two components provides no useful results.

For the same reason, actually, no significant differences in the dielectric properties of both substances in the impedance spectroscopy arise. A variety of electrochemical processes are modeled in the equivalent circuit with a CPE (constant phase element). This reflects the ion mobility in the solution, which also depends on the mass of the moving particle. Thus the different molar masses of acetic and propionic-acid could be used for the analysis in this way. In Table 2, the two substances are shown.

R1 and C3 in this case represent the influence of the used multiplexer on the recorded spectra, while the remaining elements result from the properties of the comb structure used and of the measured liquid. First results show the practicability of this method. In addition, by varying the electrode spacing, all the other parameters which are characteristic of the liquid can be varied in order to eliminate them by a subsequent subtraction.

TABLE 2. COMPARISON OF ACETIC ACID AND PROPIONIC ACID

	acetic acid	propionic acid
Molmass (g mol^{-1})	60,05	74,08
pK$_s$	4,76	4,87
Refractive index	1,371	1,386

V. CONCLUSION SECTION

With the sensor platform described in the article could be shown that a combination by cyclic voltammetrie and impedance spectroscopy in a measuring system is possible and above all useful. Furthermore it could be shown by the various sensor adjustments (geometry, material, etc.) of the sensors used, and that this increased sensitivity liquids can be analyzed optimal. These optimizations are thus of crucial importance and represent an important decision process for the application areas of the sensor platform. These improvements will also enforce the ability to distinguish between liquids in a liquid mixture. For the sample application in Section IV, this means: To optimze the sensor, the geometrical layout will be modified increasing the sensitivity to discriminate better between acetic acid and propionic acid.

REFERENCES

[1] Westenthanner, M., Barthel, A., He, P., Beckmann, D., Steinke, A., Tobehn, I., Pliquett, U. (2013, April). Assessment of suspension medium conductivity by means of micro electrodes. In Journal of Physics: Conference Series (Vol. 434, No. 1, p. 012093). IOP Publishing.

[2] U. Pliquett, E. Gersing, F. Pliquett, Evaluation of Fast Time-domain Based Impedance Measurements on Biological Tissue, Biomed. Technik, 45(2000), 6-13, 2000

[3] L. Wahn, H. K. Trieu, L. Behrendt, S. Hemanth, Kohlenstoff-dotierter-Fotolack als Elektrodenmaterial für die in-situ Messung von Nitrit, , Mikrosystemtechnik Kongress 2013

[4] A. Rösner, Th. Frank, I. Tobehn,Bio instrument for determining the viability of cells on the basis of the impedance measurement, MME 2012 - Micromechanics and Microsystems Europe, 09.09.2012 - 12.09.2012, Ilmenau, Deutschland

[5] Ayliffe, H.E.; Bruno Frazier, A.; Rabbitt, R.D., Electric impedance spectroscopy using microchan-nels with integrated metal electrodes, Microelectrome-chanical Systems, Journal of , vol.8, no.1, pp.50,57, Mar 1999, doi: 10.1109/84.749402

[6] https://fbme.htwk-leipzig.de/fileadmin /fbme/ professoren/ jung/propionsaeure_uwe_jung.pdf

[7] http://pfi-biotechnology.de/fileadmin/templates/ PFI_Biotechnology/Abschlussbericht_FNR_Propionsaeure20 11-06-30.pdf.

[8] Th. Frank, I. Tobehn, A. Steinke, S. Päßler, W. Fichtner, Electric impedance spectroscopy using microchannels with integrated metal electrodes IMCS 2012 - The 14th International Meeting on Chemical Sensors, Nürnberg, Deutschland, 20.05.2012 - 23.05.2012